The study of the characteristics and structures of turbulent boundary layer flow using direct numerical simulation

by

Shevarjun Senthil

A thesis submitted to Monash University
for the degree of
Doctor of Philosophy (Engineering)

Main Supervisor: Professor Julio Soria
Associate Supervisor: Dr. Callum Atkinson

Laboratory for Turbulence Research in Aerospace and Combustion
Department of Mechanical and Aerospace Engineering
Monash University, Melbourne, Australia

November, 2021

Copyright notices

This thesis is dedicated to

my loving father Dr.Senthil Rajaram

and mother Dr.Radika Ponnuraj,

and

to the memory of my dear grandfather

Dr. Ponnuraj Ramalingam.

Abstract

Direct numerical simulations are performed for three incompressible turbulent boundary layer (TBL) cases with different streamwise pressure gradients, namely a zero pressure gradient (ZPG), a mild adverse pressure gradient (mild APG), and a strong adverse pressure gradient (strong APG) TBLs. The strong APG TBL can be characterized as being at the verge of separation and its domain of interest is the self-similar region in the flow. In the present study, the various factors and structures influencing the skin friction in TBLs are studied.

The contribution of the viscous effects and Reynolds shear stress to the skin friction and their variation with the pressure gradient are computed using the RD identity, which is based on the mean streamwise kinetic energy budget (Renard and Deck, 2016). With increasing pressure gradient, the viscous term in the RD identity plays a smaller role, while the contribution of the Reynolds shear stress increases. The Reynolds shear stress is the dominant positive contributor to the skin friction for all the pressure gradient cases. As the pressure gradient increases, the Reynolds shear stress contribution develops an outer peak, which is dominant in the strong APG case and is located around the displacement thickness height ($y/\delta_1 = 1$ or $y/\delta_\Omega = 0.2$), where δ_1 is the displacement thickness and δ_Ω is the boundary layer thickness. The dominant outer peak contribution from the Reynolds shear stress around the displacement thickness height has also been captured by the FIK identity (Fukagata et al., 2002), which, unlike the RD identity, is based on the mean streamwise momentum budget.

The contribution of the velocity-vorticity correlations to the skin friction are computed based on the YAHS identity presented by Yoon et al. (2016), which is based on the mean vorticity equation. For all the pressure gradient cases, the contribution of the advective vorticity transport term is negative, whereas the vortex stretching term provides a positive contribution to the skin friction. The combined contribution of the advective vorticity transport and the vortex stretching terms can be considered as the contribution from the Reynolds shear stress with a constant wall-normal weight for all the pressure gradient cases. When the flow reaches the verge of separation in the strong APG TBL, the combined contribution of these two terms also exhibits a dominant peak in the outer

region around the height of 20% of boundary layer thickness ($y/\delta_\Omega = 0.2$).

The turbulent contribution of the intense topological structures (dissipative and vortical) and the intense Reynolds stress quadrant structures to the skin friction are computed based on the Reynolds stress term in the RD identity. The intense structures of all the types in the strong APG TBL are smaller in scale than the intense structures in the ZPG TBL, which is evident from the reduction in their volume relative to the mean boundary layer volume (V_{BL}) and increase in their numbers. In the strong APG TBL, there is a greater propensity for detached intense structures than in the ZPG TBL. In the strong APG TBL, the intense structures are less streamwise elongated than the structures in the ZPG TBL. With increasing pressure gradient, the fractional contribution of the intense structures to the skin friction decreases, which is consistent with the reduction in their volume relative to V_{BL}. The contribution of all the intense structures to the skin friction in the ZPG TBL is from a broader part of the boundary layer, whereas, in the strong APG TBL, their contribution is from a dominant outer peak. The outer peak in the contribution of the intense structures in the strong APG TBL is also located around the displacement thickness height ($y/\delta_1 = 1$ or $y/\delta_\Omega = 0.2$). This shows that the vortical motions and turbulent mixing in the outer layer become more important with increasing pressure gradient, as it pertains to the contribution of the Reynolds shear stress and its negative wall-normal gradient to the skin friction.

Research output

Journal Articles

- **Shevarjun Senthil**, Vassili Kitsios, Atsushi Sekimoto, Callum Atkinson and Julio Soria (2020). Analysis of the factors contributing to the skin friction coefficient in adverse pressure gradient turbulent boundary layers and their variation with the pressure gradient. *International Journal of Heat and Fluid Flow*, 82:108531.

- **Shevarjun Senthil**, Callum Atkinson and Julio Soria (2020). Analysis of the spanwise extent and time persistence of uniform momentum zones in zero pressure gradient and adverse pressure gradient turbulent boundary layers. *Journal of Physics: Conference Series*, 1522:012013.

- **Shevarjun Senthil**, Callum Atkinson and Julio Soria (2021). Analysis of the contribution from velocity-vorticity correlations to the skin friction in turbulent boundary layers and its variation with the pressure gradient. *Physical Review Fluids* (under review).

- **Shevarjun Senthil**, Callum Atkinson and Julio Soria (2021). Investigation of the contribution of the intense structures to the skin friction in turbulent boundary layers. *Journal of Fluid Mechanics* (under review).

Conference Paper

- **Shevarjun Senthil**, Callum Atkinson, Vassili Kitsios, Atsushi Sekimoto and Julio Soria (2018). Investigation of the factors contributing to skin friction coefficient in adverse pressure gradient turbulent boundary layer flow using direct numerical simulation. *21st Australasian Fluid Mechanics Conference*.

Conference Presentations

- **Shevarjun Senthil**, Callum Atkinson, Vassili Kitsios, Atsushi Sekimoto and Julio Soria (2018). Investigation of the factors contributing to skin friction coefficient in a self-similar adverse pressure gradient (APG) turbulent boundary layer (TBL) flow using direct numerical simulation (DNS). *71st Annual Meeting of the APS Division of Fluid Dynamics.*

- **Shevarjun Senthil**, Callum Atkinson, Javier Jiménez and Julio Soria (2019). Spanwise extent and time persistence of uniform momentum zones in zero-pressure gradient turbulent boundary layers. *72nd Annual Meeting of the APS Division of Fluid Dynamics.*

- **Shevarjun Senthil**, Callum Atkinson, and Julio Soria (2020). Analysis of the contribution of velocity-vorticity correlations to skin friction coefficient in adverse pressure gradient turbulent boundary layers (APG-TBLs). *73rd Annual Meeting of the APS Division of Fluid Dynamics.*

Dataset contribution

- Julio Soria, Callum Atkinson, Vassili Kitsios, Atsushi Sekimoto, **Shevarjun Senthil** and Javier Jiménez. Statistics of Beta = 0, 1, 39 Turbulent Boundary Layer DNS (`https://doi.org/10.26180/5d1f2b59e66ea`).

Research workshop participated

- *Fourth Madrid Turbulence Workshop*, June-July 2019, Universidad Politécnica de Madrid, Madrid, Spain (`https://torroja.dmt.upm.es/summer19/group_foto.jpg`).

Declaration

I hereby declare that this thesis contains no material which has been accepted for the award of any other degree or diploma at any university or equivalent institution and that, to the best of my knowledge and belief, this thesis contains no material previously published or written by another person, except where due reference is made in the text of the thesis.

This thesis includes two original papers published in peer reviewed journals. The core theme of the thesis is centred on the analysis of incompressible turbulent boundary layer flows using direct numerical simulations. The ideas, development and writing up of all the papers in the thesis were the principal responsibility of myself, the student, working within the Department of Mechanical and Aerospace Engineering under the supervision of Professor Julio Soria and Dr. Callum Atkinson.

The inclusion of co-authors reflects the fact that the work came from active collaboration between researchers and acknowledges input into team-based research.

I have not renumbered sections of submitted or published papers in order to generate a consistent presentation within the thesis. In the case of Chapter 4 and Appendix A, my contribution to the work involved the following:

Title	Status	Student Contribution	Co-authors	Monash Student
Chapter 4: Analysis of the factors contributing to the skin friction coefficient in adverse pressure gradient turbulent boundary layers and their variation with the pressure gradient	Published journal paper	80%: Development of ideas, code development, performing simulations, data analysis, figure preparation, and manuscript writing.	Vassili Kitsios (6%: Input into manuscript), Atsushi Sekimoto (4%: Input into manuscript), Callum Atkinson (4%: Input into manuscript and supervision) and Julio Soria (6%: Input into manuscript and supervision)	No
Appendix A: Analysis of the spanwise extent and time persistence of uniform momentum zones in zero pressure gradient and adverse pressure gradient turbulent boundary layers	Published journal paper	85%: Development of ideas, code development, performing simulations, data analysis, figure preparation, and manuscript writing.	Callum Atkinson (7%: Input into manuscript and supervision), Julio Soria (8%: Input into manuscript and supervision)	No

Student signature: Shevarjun Senthil Date: 7 November, 2021

The undersigned hereby certify that the above declaration correctly reflects the nature and extent of the student's and co-authors' contributions to this work. In instances where I am not the responsible author I have consulted with the responsible author to agree on the respective contributions of the authors.

Main Supervisor signature: Julio Soria Date: 7 November, 2021

The journey matters as much as the goal.

–Kalpana chawla

Acknowledgments

This PhD journey has been a long, lonely, and daunting task filled with innumerable challenges. Chasing this dream alone has been an unnerving experience, especially because of being far away from my home and loved ones, which made the day-to-day activities difficult in ways that I have not experienced before. When I started this journey almost 4 years back, I was just filled with the eagerness to learn more about the subject of computational fluid dynamics. I believe that it was one of the main motivating factors which kept me going through this journey and I am grateful for being gifted with the passion for science and engineering. There are many people who have helped and supported me during the worst and the best moments of my candidature. I take this opportunity to sincerely thank every one of them.

First and foremost, it is a great pleasure to express my earnest gratitude and thanks to my main supervisor Professor Julio Soria for giving me the opportunity to perform this research study as a part of the LTRAC group. This achievement would not have been possible without his enormous support and never-ending guidance. I also owe my sincere thanks to my co-supervisor Dr. Callum Atkinson for his guidance and assistance throughout this endeavour. Getting continuous directions and suggestions from my supervisors had a profound impact on my research and the completion of this thesis. I would like to thank Dr. Shahram Karami for his continuous suggestions and assistance, especially in regards to high performance computing. I also thank Dr. Vassili Kitsios for his suggestions and particularly for his motivating words at the start of my candidature. I also thank Dr. Atsushi Sekimoto for his suggestions during the initial stage of my candidature.

I would also like to thank Professor Julio Soria for providing the financial support to attend international conferences, which gave me the opportunity to present my research work in a global arena and to see the work of other international researchers. I would like to acknowledge the computational resources and the support provided by the Pawsey Supercomputing Centre, the National Computational Infrastructure (NCI) and the Multimodal Australian ScienceS Imaging and Visualisation Environment (MASSIVE) through the National Computational Merit Allocation Scheme (NCMAS) funded by the Australian Government. I received a Faculty of Engineering International Postgraduate Research

Scholarship (FEIPRS) to cover my tuition fees and a Monash Graduate Scholarship (MGS) for my living expenses. Therefore, I would like to thank the Faculty of Engineering and Monash University Graduate Education (MGE) for their financial support. I would also like to thank TeamViewer for providing a free version of the remote control software to students as it proved to be a very useful tool in remotely accessing my workstation computer during the extended lock-down periods in 2019 due to the COVID-19 pandemic and helped in maintaining the research progress.

I am very grateful to my dear friend and colleague Shoaib Amjad for his continuous support, encouragement and numerous fruitful discussions. Meeting him is one of the best things that happened to me during my candidature. I would also like to thank all of my colleagues, especially Muhammad Shehzad, Zehuan Wu, Asif Ahmed, Bhavraj Thethy, Graham Bell, Rhiannon Kirby, Michael Eisfelder, Sean Lawrence, Joel Weightman, Dominic Tan, Thomas Knast, Marcus Wong, Seraj Alzhrani and Nick Mason-Smith for their support and suggestions.

I would like to specially thank my dear friends: Jagmohan Singh, Anchal Sareen, Shantanu Bhat, Meghana Kulkarni-Bhat, Methma Rajamuni, Shreyas Muralidaran, Manikandan Sachithanantham and Sewminda Kalana Samarasinghe for their countless support and for providing the feel of home in Melbourne. I also thank my friends Ezhilsabareesh Kannadasan and Udayakumar Dilly Bhaskar for their support.

I would like to thank Monash Residential Services (MRS) for offering me a room in Jackomos Hall, which gave me a sense of security and safety from the first day of my candidature and played a vital role in this journey by providing an environment to focus on my research.

I would like to extend my special thanks and gratitude to my family members Karthe Ponnuraj, Thilagavathi Karthe, Arun Tiilak Karthe, Annapoorani Ponnuraj and my late grandfather Ponnuraj Ramalingam for their endless support and encouragement since my childhood. Finally and most importantly, I extend my heartfelt gratitude to the pillars of my strength, my dear parents: Senthil Rajaram and Radika Ponnuraj. I simply would not have been capable of completing this journey without their unwavering support and encouragement. They stayed by my side from the very beginning and through the worst of the moments. Without their love and encouragement, my entire life wouldn't have been possible. They are my everything and I dedicate this thesis to my dear parents.

Contents

List of Tables

List of Figures

The task is, not so much to see what no one has yet seen; but to think what nobody has yet thought, about that which everybody sees.

–Erwin Schrödinger

Chapter 1

Introduction and Background

The time-line of evolution of the subject fluid mechanics starts from liquid statics, followed by fluid kinematics and moves to modern fluid dynamics. The problem of turbulence has intrigued mankind for several centuries. In the 15th century, Leonardo da Vinci (1452-1519), a great experimentalist who pioneered flow visualization and is known for his famous sketches of turbulent flows, described turbulence decomposition as (Lumley, 1992): "Observe the motion of the surface of the water, which resembles that of hair, which has two motions, of which one is caused by the weight of the hair, the other by the direction of the curls; thus the water has eddying motions, one part of which is due to the principal current, the other to the random and reverse motion."

It was not until the 19th century that this verbal description of fluid motions was transformed to the language of mathematics. Claude-Louis Navier (1785-1836) and Lord George Gabriel Stokes (1819-1903) successfully formulated the governing equations for real fluid motions by considering the fluid as a continuous media. These equations are famously called as the Navier-Stokes (N-S) equations. Although the N-S equations describe the fluid flows well, due to its non-linear nature, solving turbulence problems remains difficult. Richard Feynman, a famous theoretical physicist and a Nobel Laureate, once said "Turbulence is the most important unsolved problem of classical physics", which remains true until this day.

In the late 19th century, one of the seminal contributions of Osborne Reynolds (1842–1912) was the study of the flow transition from the laminar state to the turbulent state in pipe flow experiments (Reynolds, 1883; Anderson Jr, 2010). This led to the formulation of the famous non-dimensional quantity called the Reynolds number. He also made a breakthrough in calculating the distribution of the flow variables throughout a turbulent flow field in detail. Even though a turbulent flow is unsteady at any given point, Reynolds postulated that if a flow variable is taken a time average for a sufficient interval of time, that time average would be a steady value. This theory is commonly referred to as the

Reynolds decomposition, which states that each variable in a turbulent flow is locally composed of its time mean and its time wise fluctuating component (Reynolds, 1895). Introducing the Reynolds decomposition into the N-S equations and taking the time average transformed them into the well-known Reynolds-averaged Navier-Stokes (RANS) equations for turbulent flows.

However, the RANS equations are not without problems. In the process of Reynolds averaging, new unknown variables, namely the Reynolds stresses, are introduced in the RANS equations and this leads to the turbulence "closure problem" as there are more unknowns than the equations. This problem gave rise to the development of different statistical turbulence models. Despite the formulation of the RANS equations a century ago, it is a hard fact that the researchers are still trying to find the best and most appropriate closure model for turbulent flows (Marusic and Monty, 2019).

Complexity involved in finding a solution to the turbulent flows is due to the multi-scale nature of turbulence, where a range of spatial and temporal scales coexist in the flow, all interacting with one another. The idea of energy cascade from the largest eddies to the smaller scales was introduced by Richardson (1922), who is known for his rhyming verse "Big whorls have little whorls, Which feed on their velocity; And little whorls have lesser whorls, And so on to viscosity". In 1941, one of the significant achievements in the study of turbulence came from Kolmogorov (1941), who quantified the self-similar energy cascade for isotropic turbulence, based on the energy conservation arguments. Kolmogorov (1941) showed that the energy cascades from the inertial scale of the flow to the viscous length scale (Kolmogorov scale η) at which the kinetic energy is finally dissipated into internal energy (Pope, 2000; Jiménez, 2012). He showed that the characteristic length (η), time (τ_η) and velocity scales (u_η) of the smallest turbulent motions are $\eta = (\nu^3/\epsilon)^{1/4}$, $\tau_\eta = (\nu/\epsilon)^{1/2}$ and $u_\eta = (\nu\epsilon)^{1/4}$, respectively, where ν is the kinematic viscosity and ϵ is the rate of energy transfer. A detailed history and listing of some of the key developments in turbulence research are available in Davidson et al. (2011).

The study of turbulence becomes even more complex when the flow is confined by walls as it introduces new length scales and essentially changes the nature of turbulence itself (Smits and Marusic, 2013). This change takes place predominantly in a thin layer near the wall called the boundary layer. Boundary layer study has tremendous importance in many practical industrial applications. For instance, the energy loss in transporting oil through pipelines, and the drag force acting on automobiles, planes and ships depend on the behaviour of the turbulent eddies in the near-wall region. The turbulent boundary layer (TBL) accounts for the majority of the drag produced in these engineering applications. In order to overcome the drag and move things around, engines and pumps are employed, which results in burning of fuel and emission of carbon dioxide in the process. Therefore, an in-depth understanding of the mechanisms associated with the transport of mass, momentum and heat in wall-bounded turbulent flows is essential to predict and control drag, mixing rates and heat transfer experienced in the engineering applications.

In many engineering devices, TBLs are subjected to adverse streamwise pressure gradients. The efficiency of these devices is dependent on the TBL remaining attached to the curved surfaces. Adverse pressure gradient turbulent boundary layers (APG TBLs) are found in many aerodynamic devices such as internal expanding duct flows, and external flows over the diverging part of curved surfaces like turbine blades, the leeward side of aerofoil sections and diffusers. The separation of the TBLs in these practical flows reduces the efficiency and increases the operational cost of these engineering systems. The study of TBLs under the influence of adverse pressure gradient (APG) began as early as the 1950s, with the wind tunnel experiments by Clauser (1954). It still remains a challenging problem to understand the fluid physics of the onset of separation and subsequent reattachment of TBLs. A large mean velocity defect develops in a TBL when it is subjected to the influence of APG. In APG TBLs, the mean shear rates in the outer region are not insignificant when compared to those in the near-wall region. With increasing pressure gradient, the importance of the viscous forces in the near-wall region decreases. In contrast to the canonical zero pressure gradient turbulent flows, the turbulence activity reduces in the near-wall region and the outer layer plays a more important role as the adverse pressure gradient increases (Skåre and Krogstad, 1994; Na and Moin, 1998). Skåre and Krogstad (1994) observed that the peak of the turbulent stresses in the outer region scales linearly with the non-dimensional pressure gradient. However, our understanding of the influence of the adverse pressure gradient on the coherent structures in the TBLs is still limited.

When information-limited two-dimensional planar data, like particle image velocimetry (PIV) measurements, are used to study the spatial extent and orientation of coherent structures, the results and deductions obtained may be adversely affected by the lack of information from the third dimension (Soria et al., 2016). Direct numerical simulations (DNSs) overcome this information-limit and play a vital role in improving our understanding of wall-bounded flows by providing volumetric information of the full three-dimensional flow fields. In DNSs, all the important turbulent scales are resolved and quantified with a spatial and temporal resolution that cannot be matched by experiments. In the pioneering DNS of a turbulent channel flow by Kim et al. (1987), the turbulent statistical properties were studied without using any subgrid model at a Reynolds number of 3300, which was defined based on the channel half-width and mean centreline velocity. Since then, the advancement in computational power has enabled us to investigate the structures in wall-bounded flows at higher Reynolds numbers (Jiménez and Moser, 2007). These high fidelity simulations are being used to study the geometrical characteristics, arrangement and evolution of the spatially and temporally coherent structures. DNSs help in the development of computationally less demanding lower order models and test the stability of these structures to perturbations and control mechanisms.

Turbulent flows are usually studied from a statistical perspective like using the one-point and two-point statistics. The other approach is by investigating the properties of the structures in the turbulent flows. There are different types of coherent structures and eddying motions coexisting in a range of scales in turbulent flows and these structures are reviewed extensively in Robinson (1991); Adrian (2007); Jiménez (2012). Some of the brilliant and noteworthy contributions in the identification of the coherent structures are the experimental flow visualisations of fluid sweeps and ejections by Corino and Brodkey (1969), hairpin vortices by Head and Bandyopadhyay (1981), and uniform momentum zones (UMZs) by Meinhart and Adrian (1995); Adrian et al. (2000). Many of the past studies, as early as the investigation by Kline et al. (1967) in the 1960s, have focused on the analysis of the statistical properties of the Reynolds stresses. Kline et al. (1967) performed flow-visualisation and quantitative studies of turbulent boundary layers in a water channel and they found the presence of low-speed streaks in the regions close to the wall. They also showed that these streaks interacted with the outer part of the flow through a process comprising of a lift-up, then a sudden oscillation followed by a bursting and an ejection. Then, Kim et al. (1971) showed that the process of most of the turbulence production in the near-wall region occurs during the bursting events. In order to identify the structures involved in these phenomena, various conditional-sampling techniques were developed like the u'-level detection technique (Lu and Willmarth, 1973), the VITA (variable-interval time-averaged) technique (Blackwelder and Kaplan, 1976) and the VISA (variable-interval space-averaged) technique (Kim, 1985). One of the popular methods to classify the flow field is the quadrant analysis of Wallace et al. (1972); Willmarth and Lu (1972), which is based on the streamwise and wall-normal velocity fluctuations. After studying different techniques, Bogard and Tiederman (1986) concluded that the quadrant analysis of the velocity fluctuations gave the best balance between detection probability and false positives of these events. One of the types of coherent structures identified in turbulent flows is the intense structures. The intense structures can be generally defined as spatially coherent regions in the flow whose constituent points carry a higher magnitude of certain quantities than a threshold value. The intense Reynolds stress structures are of particular interest because they contribute to the majority of wall-normal momentum flux (Lozano-Durán et al., 2012). The detailed reviews and discussions of the quadrant analysis to investigate the sweep and ejection events in canonical wall-bounded turbulent flows are available in Robinson (1991); Lozano-Durán et al. (2012); Jiménez (2013).

Another way of classifying the flow to identify the structures is the topological methodology introduced by Chong et al. (1990); Soria and Cantwell (1994); Chong et al. (1998), which is based on the invariants of the velocity gradient tensor A_{ij} (VGT). For incompressible turbulent flows, as $P_A = 0$ from continuity, the (P_A,Q_A,R_A)-space reduces to the two-dimensional (R_A,Q_A)-plane, where P_A, Q_A, R_A are the first, second and third invariants of A_{ij}, respectively, and D_A is the discriminant of A_{ij}. According to the terminology of Chong et al. (1990), the four possible local topologies in the (R_A,Q_A)-plane are unstable focus/contracting (UF/C), stable focus/stretching (SF/S), unstable node/saddle/saddle (USN/S/S), and stable node/saddle/saddle (SN/S/S). In the (R_A,Q_A)-plane, regions in the flow field dominated by strain-rate are the local topologies with negative D_A values ($D_A < 0$), while vortex-like structures in the flow field have the local topologies with positive D_A values ($D_A > 0$). The topological methodology have been used in many of the past studies to investigate turbulent flows like the study of the dissipating motions in incompressible mixing layer by Soria et al. (1994), turbulent channel flow by Blackburn et al. (1996), homogeneous isotropic turbulence by Martın et al. (1998); Ooi et al. (1999), and low Reynolds number turbulent boundary layer by Chacin and Cantwell (2000).

To quantify the various factors contributing to the skin friction, Fukagata et al. (2002) introduced a theoretical decomposition based on the mean streamwise momentum equation. Following it, various decompositions based on different forms of the N-S equations were presented to investigate the mechanism of mean skin friction generation in turbulent flows (Mehdi and White, 2011; Mehdi et al., 2014; Renard and Deck, 2016; Yoon et al., 2016). An in-depth understanding of the factors and structures influencing the wall shear in TBLs is essential for the development of better flow control techniques and the design of efficient drag reduction devices, which will improve the performance of many engineering applications. Hence, in the present study, the contribution of the viscous effects, Reynolds stress, vortical motions and coherent structures to the wall shear are investigated using the skin friction decompositions presented by Renard and Deck (2016); Fukagata et al. (2002); Yoon et al. (2016). More details of these decompositions and their components are discussed in chapter 3. Direct numerical simulations are performed to address the following research questions.

- What is the contribution of the Reynolds stress and viscous effects to the skin friction and the role of pressure gradient in it?
- What is the contribution of the velocity-vorticity correlations to the skin friction and their variation with the pressure gradient?
- What is the turbulent contribution of the intense structures to the skin friction?

1.1 Organisation of the thesis

The present thesis is organized as follows. In chapter 2, brief details of the direct numerical simulations, various boundary conditions used in the simulations and the comparison of the characteristics of the turbulent boundary layer flows used in the current study are presented. In chapter 3, brief details of the basis of the skin friction decompositions and their components are presented. In chapter 4, the contribution of the Reynolds shear stress and viscous effects to the skin friction in incompressible turbulent boundary layers and the role of pressure gradient in it are analysed. Their contributions to the skin friction are computed based on the decomposition presented by Renard and Deck (2016), which is referred to as the RD identity. Chapter 5 reports on the contribution of the velocity-vorticity correlations to the skin friction and their variation with the streamwise pressure gradient. The contribution of the velocity-vorticity correlations to the skin friction coefficient are computed based on the decomposition presented by Yoon et al. (2016), which is referred to as the YAHS identity. In chapter 6, the contribution of the intense structures to the skin friction are analysed. The intense structures considered in the present study are intense topological structures (dissipative and vortical) and intense Reynolds stress structures. These intense structures are extracted from statistically independent velocity fields and their geometric properties are also investigated. The contribution from these coherent structures to the skin friction is quantified by using the Reynolds stress term in the RD identity. Finally, conclusions are presented.

Be the change that you want to see in the world.

–Mahatma Gandhi

Chapter 2

Numerical details

2.1 The numerical method

Direct numerical simulations are performed for three turbulent boundary layer cases with different pressure gradients, namely a zero pressure gradient (ZPG), a mild adverse pressure gradient (mild APG), and a strong adverse pressure gradient (strong APG) TBLs. An in-house DNS code solves the incompressible Navier-Stokes equation for pressure and velocity fields in Cartesian coordinates with the flow directions as streamwise (x), wall-normal (y) and spanwise (z). The instantaneous velocity components in these directions are denoted by (u, v, w). The mean velocity components are denoted by $(\langle u \rangle$, $\langle v \rangle$, $\langle w \rangle)$ and the corresponding fluctuating components are denoted by (u', v', w'). The instantaneous vorticity components are represented by $(\Omega_x, \Omega_y, \Omega_z)$ with the corresponding mean and fluctuating components given by $(\langle \Omega_x \rangle$, $\langle \Omega_y \rangle$, $\langle \Omega_z \rangle)$ and $(\omega'_x$, ω'_y, $\omega'_z)$, respectively. $\langle (\cdot) \rangle$ represents quantities averaged in time and the homogeneous spanwise direction and $(\cdot)'$ denotes fluctuating quantities.

The first version of the code developed by Simens et al. (2009); Simens (2008) used only Message Passing Interface (MPI) as a parallelisation technique and had one computational box. It was subsequently optimized by Borrell et al. (2013) by adding OpenMP (Open Multi-Processing) in addition to the MPI Parallelisation. It used two boundary layer boxes to achieve a higher Reynolds number and considered boundary layer flow with zero pressure gradient (ZPG). The current version of the code, which uses Hybrid OpenMP/MPI parallelisation, has one computational box and adverse pressure gradient is applied in the domain (Kitsios et al., 2016, 2017). The governing equations are solved by using the fractional step method as suggested in Harlow and Welch (1965) and in Perot (1993). The grid is staggered in x and y directions but not in the z direction. Compact finite difference is used for spatial discretization in x and y directions (Lele, 1992). Fourier decomposition is used in the spanwise direction. Time stepping is achieved using a 3-step

Runge Kutta method (Simens, 2008). The density ($\rho = 1$) and kinematic viscosity (ν) are taken as constants.

The computational domain is decomposed into yz planes and each node contains a number of these cross-flow planes. The OpenMP threads in these nodes further split the planes into sub-domains. In the cross-flow plane configuration, the operations in the y and z directions are performed. The derivatives and interpolations in the x direction are computed by applying a global transpose to the variables. After the transpose, each node contains pencils extending in the streamwise direction. Once the streamwise operations are finished, the results are transposed back to the cross-flow plane configuration. Full detail of the DNS code, plane to pencil domain decomposition and the parallelisation techniques used can be found in Sillero (2014); Borrell (2015); Borrell et al. (2013).

2.2 Boundary conditions used in the simulations

The current computational domain is a three-dimensional rectangular box with a no slip boundary condition on the bottom surface. The required pressure gradient is applied in the domain by specifying the wall-normal far-field velocity (v_∞) as shown in figure 2.1 for the three TBL cases. The domain of interest (DoI) for each TBL is highlighted with the markers. The spanwise vorticity (Ω_z) is zero in the far-field. Further details of the far-field boundary condition are presented in Kitsios et al. (2017, 2016).

The inflow boundary condition is obtained by recycling and mapping a yz plane (cross-plane) from a downstream position to the inflow (Kitsios et al., 2016, 2017). Mapping is essential because of the growth of the TBL in the wall-normal direction as it develops in the streamwise direction. For the mild APG and strong APG TBLs, the wall-normal far-field velocity is changed from suction ($v_\infty > 0$, fluid leaving the domain) to blowing ($v_\infty < 0$, fluid entering the domain) close to the outlet. Blowing is required to reduce the number of instantaneous reverse flow events at the outflow and to ensure numerical stability of the outflow boundary condition. Triangles on the left side of the figure 2.1 represent the position of the recycling plane for the respective TBL cases. Similarly, the triangles on the right side of the figure represent the position from which blowing starts for the respective TBL cases. Periodic boundary conditions are applied in the spanwise direction. The outflow is a convective boundary condition (Sillero, 2014; Simens, 2008) given by

$$\frac{\partial \boldsymbol{u}}{\partial t} + \langle u \rangle_\infty \, . \, \frac{\partial \boldsymbol{u}}{\partial x} = 0, \tag{2.1}$$

where $\boldsymbol{u}$ is the instantaneous velocity and t is the time. The schematic of the streamwise wall-normal domain of the strong APG TBL with an illustration of the farfield boundary condition is given in figure 2.2.

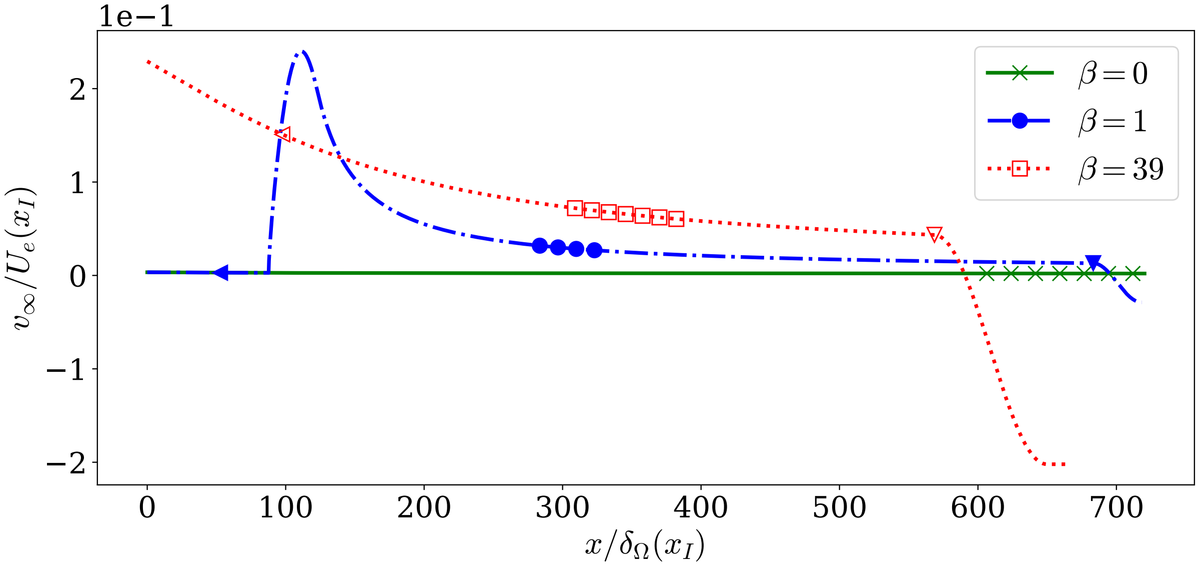

Figure 2.1: Farfield wall-normal velocity (v_∞) boundary condition for the three pressure gradient cases. x_I is the position of the inlet plane. β (non-dimensional streamwise pressure gradient), δ_1 (displacement thickness), Re_{δ_1} (Reynolds number based on displacement thickness), and U_e (reference velocity) are defined in the section 2.3. Triangles in the left side of the figure represent the position of the recycling plane for the respective TBL cases, while the triangles in the right side represent the position from which blowing starts.

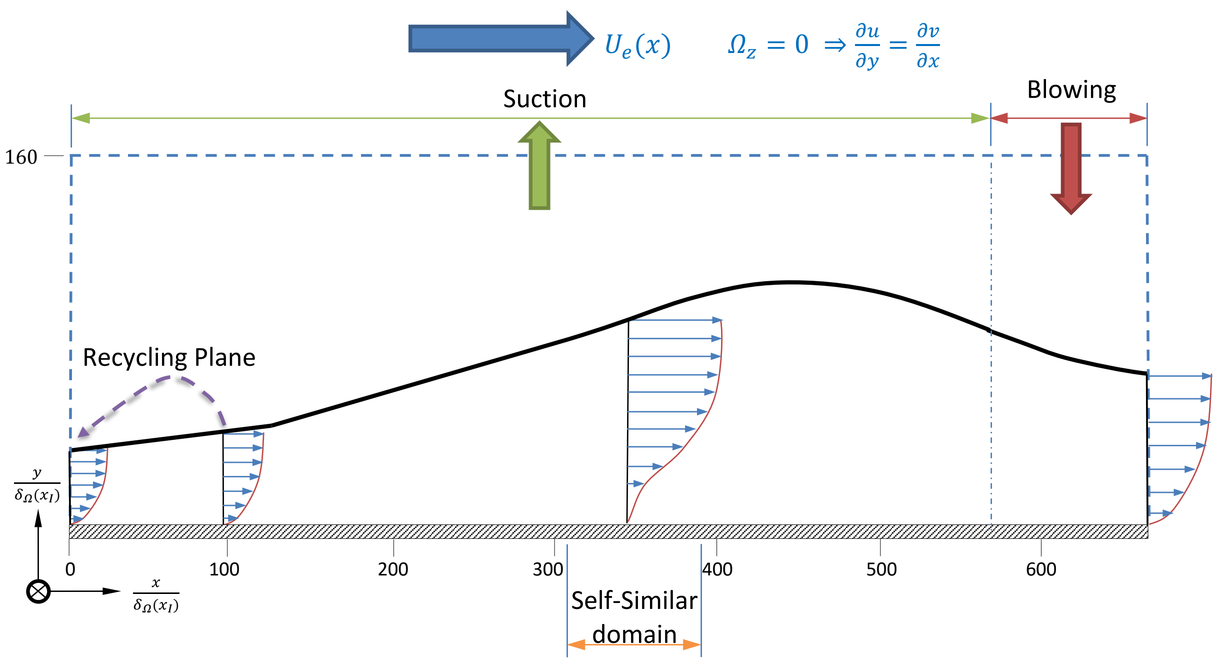

Figure 2.2: Schematic of the strong APG TBL.

2.3 Classification of the flows and the definition of the reference scales

The three turbulent boundary layer flows with different streamwise pressure gradients are classified based on the non-dimensional pressure gradient (β) as follows: ZPG - zero pressure gradient (β=0), mild APG (β=1) and strong APG (β=39). The non-dimensional pressure gradient is defined as

$$\beta = \frac{\delta_1}{{u_\tau}^2}\frac{P_{e,x}}{\rho} = \delta_1\frac{P_{e,x}}{\tau_w}, \tag{2.2}$$

where $u_\tau = \sqrt{\tau_w/\rho}$ is the friction velocity, δ_1 is the displacement thickness, $P_{e,x}$ is the far-field streamwise pressure gradient, ρ is the density, and τ_w is the mean wall shear stress.

For the mild APG and strong APG TBLs, as the wall-normal velocity is specified in the far-field boundary condition, $\partial v_\infty/\partial x$ has a negative value. In order to have zero spanwise vorticity (Ω_z) in the far-field boundary, $\partial u_\infty/\partial y$ must also have a negative value. This means that the profile of mean streamwise velocity ($\langle u \rangle$) has a maximum in the y direction and it does not approach a constant value. Therefore, the following definitions of reference velocity (U_e), displacement thickness (δ_1) and momentum thickness (δ_2) are used.

Based on the definition of Lighthill (1963), the reference velocity (U_e) used in the simulations is given as

$$U_e(x) = U_\Omega(x, \delta_\Omega), \tag{2.3}$$

where

$$U_\Omega(x,y) = -\int_0^y \langle\Omega_z\rangle(x,\tilde{y})\; d\tilde{y}, \tag{2.4}$$

$\langle\Omega_z\rangle$ is the mean spanwise vorticity, and δ_Ω is the wall-normal position where $\langle\Omega_z\rangle$ is 0.2% of the mean vorticity at the wall (Kitsios et al., 2017).

Based on the definition of Spalart and Watmuff (1993), the displacement thickness (δ_1) and the momentum thickness (δ_2) are given as

$$\delta_1(x) = \frac{-1}{U_e}\int_0^{\delta_\Omega} y\langle\Omega_z\rangle(x,y)dy, \tag{2.5}$$

and

$$\delta_2(x) = \frac{-2}{U_e^2}\int_0^{\delta_\Omega} yU_\Omega\langle\Omega_z\rangle(x,y)dy - \delta_1(x). \tag{2.6}$$

The flow dynamics of APG TBLs depend on the local environment and also on the flow history. The pressure forces and the shear stresses acting on a boundary layer are minute

	ZPG	Mild APG	Strong APG
Nominal β	0	1	39
N_x	8193	8193	8193
N_y	315	500	1000
N_z	1362	1362	1362
$L_x/\delta_1(x_\star)$	480	345	303
$L_y/\delta_1(x_\star)$	22.7	29.8	73.4
$L_z/\delta_1(x_\star)$	80.1	57.6	50.7
$\Delta x/\delta_1(x_\star)$	0.0585	0.0421	0.0370
$\Delta y_{wall}/\delta_1(x_\star)$	1.53×10^{-3}	1.10×10^{-3}	9.71×10^{-4}
$\Delta y_\infty/\delta_1(x_\star)$	0.0992	0.0714	0.254
$\Delta z/\delta_1(x_\star)$	0.0585	0.0421	0.0370
Re_{δ_1} range in DoI	4800→5280	4800→5280	22200→28800
$L_{x,DoI}/\delta_1(x_\star)$	82.0	20.0	37.0

Table 2.1: Numerical details of the DNS of the three pressure gradient cases: number of collocated grid points in the streamwise (N_x) and wall-normal (N_y) directions; number of spanwise Fourier modes after de-aliasing (N_z); domain size L_x, L_y and L_z in x, y and z directions respectively; uniform streamwise (Δx) and spanwise grid spacing (Δz); wall-normal grid spacing at the wall (Δy_{wall}) and at the far-field boundary (Δy_∞); Reynolds number based on displacement thickness (Re_{δ_1}) in the domain of interest (DoI); and streamwise extent of the DoI ($L_{x,DoI}$). δ_1 is the displacement thickness and $x_\star$ is the streamwise position where $Re_{\delta_1} = 4800$. Full details of the DNS of the three TBL cases are presented in Kitsios et al. (2016, 2017).

in nature and because of this, the boundary layer cannot react quickly to the changing environment (Clauser, 1954). This makes the dynamical properties of the boundary layer dependent on the flow history and on the specific pressure gradient distribution. In order to minimise the influence of these history effects, a self-similar APG TBL is studied. A TBL is considered self-similar if each of the terms in the governing equations has the same proportionality with the streamwise position (Mellor and Gibson, 1966; George and Castillo, 1993). Based on the definition in Mellor and Gibson (1966), the non-dimensional pressure gradient β must be independent of the streamwise position in a self-similar TBL. In the limiting case of zero mean wall shear stress, $\beta \to \infty$ and the TBL is at a point immediately prior to separation (Stratford, 1959; Townsend, 1960). In the self-similar region of the flow, statistical profiles at various streamwise positions collapse on to a single set of profiles under the appropriate length and velocity scaling (Stratford, 1959; Mellor, 1966; Mellor and Gibson, 1966; George and Castillo, 1993; Skåre and Krogstad, 1994; Kitsios et al., 2016, 2017). In the present strong APG flow, this self-similar flow is only possible in the domain of interest (DoI), where β has an average value of 39 (Kitsios et al., 2017). The $\beta = 39$ case can be characterized as being at the verge of separation as the wall shear stress approaches zero. The conditions of self-similarity and the magnitude of the similarity coefficients within the DoI of the TBLs are explained comprehensively in Kitsios et al. (2017, 2016). As shown in figure 2.3a, within the DoI, the Reynolds number based on displacement thickness (Re_{δ_1}) varies from 22,200 to 28,800 for the strong APG case, where $Re_{\delta_1} = U_e \delta_1/\nu$. Within DoI of the ZPG TBL, Re_{δ_1} varies from 4,800 to 5,280. The self-similar region of the mild APG TBL spans over a larger range of Re_{δ_1} (Kitsios et al., 2016). But, it is chosen to span over the same range of Re_{δ_1} as that of the ZPG TBL. This is done to reduce the effects of the Reynolds number and isolate the influence of the pressure gradient (Kitsios et al., 2017).

The numerical details of the simulations are given in Table 2.1. Figure 2.4a shows the displacement thickness, Figure 2.4b shows the shape factor ($H = \delta_1/\delta_2$), and Figure 2.4c shows δ_Ω, where δ_Ω is the boundary-layer thickness or the wall-normal position at which the mean spanwise vorticity ($\langle \Omega_z \rangle$) is 0.2% of the mean vorticity at the wall. $x_\star$ is the streamwise position where $Re_{\delta_1} = 4800$, $\delta_1(x_\star)$ is the displacement thickness at $x_\star$, and x_I is the location of the inlet plane. Figures 2.3a to 2.3c refer to the Reynolds number based on displacement thickness, momentum thickness ($Re_{\delta_2} = U_e \delta_2/\nu$), and δ_Ω based Reynolds number ($Re_{\delta_\Omega} = U_e \delta_\Omega/\nu$), respectively. The streamwise variation of the reference velocity (U_e), wall shear stress (τ_w), and skin friction coefficient ($C_f = 2\tau_w/\rho U_e^2$) are given in figures 2.5a to 2.5c, respectively. For all the three cases, the respective DoIs are highlighted with the markers in figures 2.3 to 2.5. To compare the three TBL cases in these figures, the independent variable is taken as $(x - x_\star)/\delta_1(x_\star)$. The independent axis is shifted by

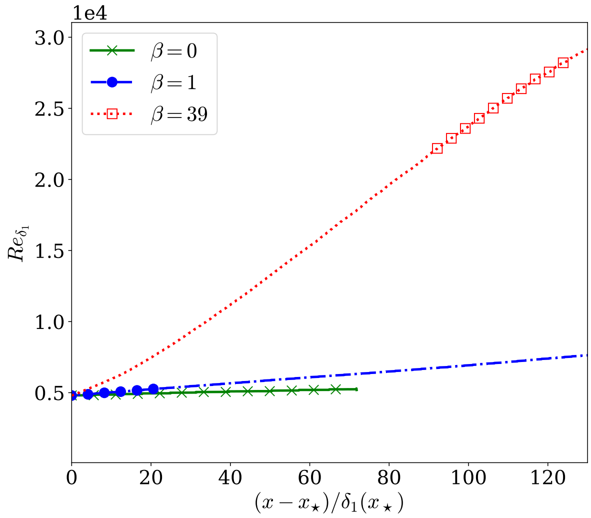

(a)

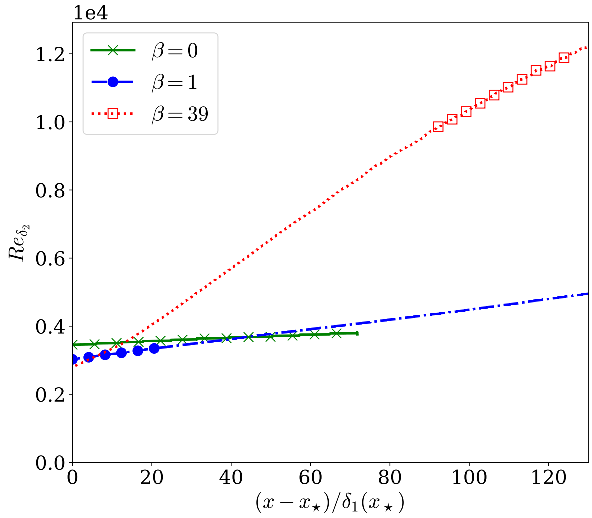

(b)

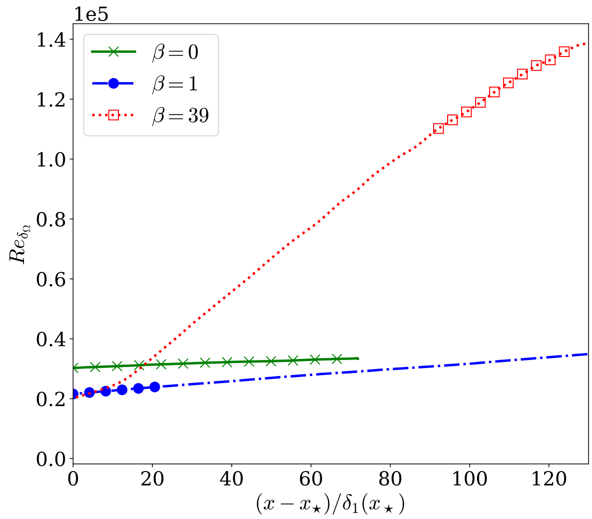

(c)

Figure 2.3: (a) Displacement thickness based Reynolds number (Re_{δ_1}); (b) momentum thickness based Reynolds number (Re_{δ_2}); (c) δ_Ω based Reynolds number (Re_{δ_Ω}); for each case of β and their respective DoI is highlighted with the markers. $x_\star$ is the streamwise position where $Re_{\delta_1} = 4800$.

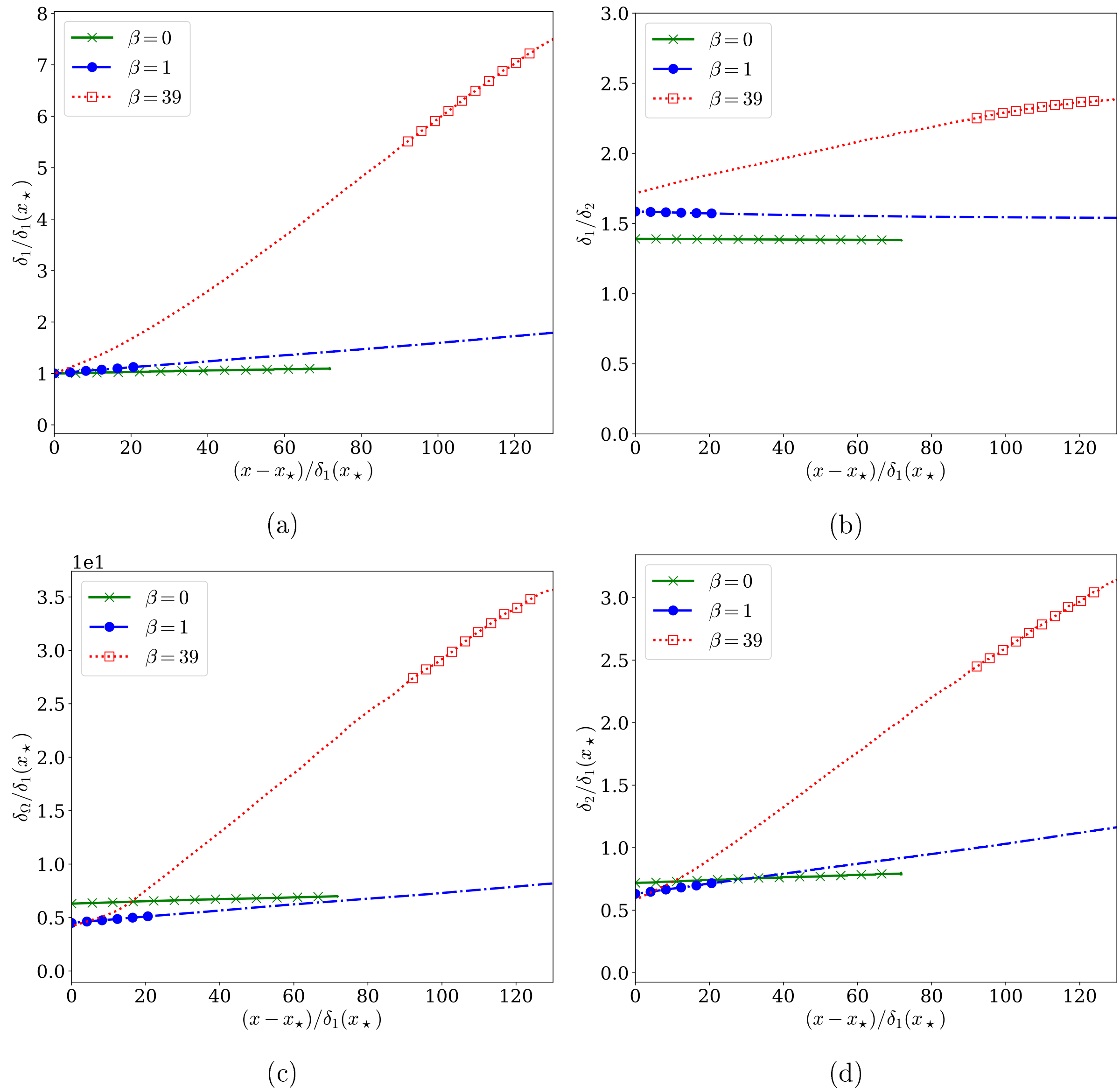

Figure 2.4: (a) Displacement thickness (δ_1); (b) shape factor ($H = \delta_1/\delta_2$), where δ_2 is the momentum thickness; (c) δ_Ω, where δ_Ω is the boundary-layer thickness or the wall-normal position at which the mean spanwise vorticity ($\langle\Omega_z\rangle$) is 0.2% of the mean vorticity at the wall; (d) momentum thickness (δ_2); for each case of β and their respective DoI is highlighted with the markers. $x_\star$ is the streamwise position where $Re_{\delta_1} = 4800$.

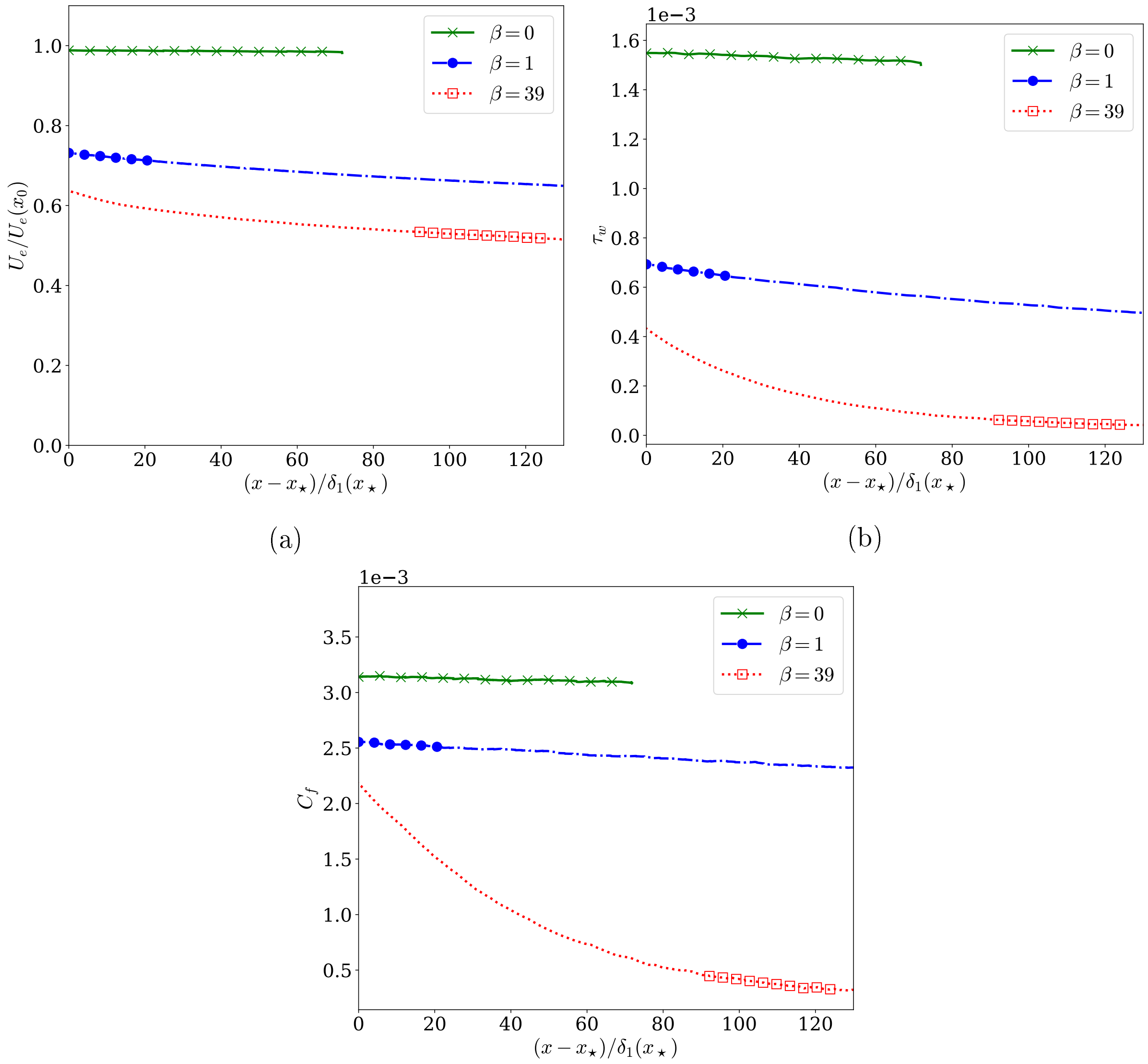

(a) (b) (c)

Figure 2.5: (a) Reference velocity (U_e); (b) wall shear stress (τ_w); (c) skin friction coefficient (C_f); for each case of β and their respective DoI is highlighted with the markers. $x_\star$ is the streamwise position where $Re_{\delta_1} = 4800$.

$x_\star$ to make sure that $Re_{\delta_1} = 4800$ at the origin for all the TBL cases. Full details of the DNS of the three TBL cases are presented in Kitsios et al. (2016, 2017) with the data of the statistical properties and turbulent kinetic energy budgets available in Soria et al. (2019).

2.4 Comparison of the TBL flow characteristics

As illustrated in figure 2.4, with increasing pressure gradient, the boundary layer expands more rapidly and the skin friction coefficient reduces and approaches zero in the strong APG TBL. This is also consistent with the reducing values of the wall shear stress and $\partial\langle u\rangle/\partial y$ at the wall illustrated in figures 2.5b and 2.6b, respectively. The profiles of the mean streamwise velocity ($\langle u\rangle$), $\partial\langle u\rangle/\partial y$ and $\partial^2\langle u\rangle/\partial y$ are illustrated in figure 2.6. The profiles are non-dimensionalised by the local values of the reference velocity (U_e) and the boundary layer thickness (δ_Ω). The profiles are streamwise averaged in the scaled coordinates within the DoI for each TBL case. The strong APG TBL has two inflection points in the profile of $\langle u\rangle$, one in the inner region and another at the approximate height of the displacement thickness ($y = \delta_1$ or $y = 0.2\delta_\Omega$). The inner region is defined as $y/\delta_1 < 10^{-1}$ or $y/\delta_\Omega < 10^{-2}$ (Pope, 2000) and the outer region is defined as $y/\delta_1 > 10^{-1}$ or $y/\delta_\Omega > 10^{-2}$.

The profiles of the Reynolds stresses and the wall-normal gradient of $\langle u'v'\rangle$ are shown in figures 2.7a to 2.7e, respectively. For the ZPG and mild APG TBLs, the Reynolds stresses $\langle u'u'\rangle$ and $\langle w'w'\rangle$ exhibit an inner peak. For all the TBL cases, no inner peak is seen in the profiles of $\langle u'v'\rangle$ and $\langle v'v'\rangle$. For the mild APG and strong APG TBLs, an outer peak is present for all the Reynolds stresses which becomes more dominant as the pressure gradient increases. For the strong APG TBL, the outer peak of all of the Reynolds stresses is present around the height of $y = \delta_1$ ($y = 0.2\delta_\Omega$), which coincides with the location of the outer inflection point in the mean streamwise velocity profile as shown in figure 2.6a. Similarly, for the mild APG TBL, the outer peaks of the Reynolds stresses located at the approximate height of $y = 1.3\delta_1$ ($y = 0.35\delta_\Omega$) also coincides with the outer inflection point in the mean streamwise velocity ($\langle u\rangle$).

In incompressible TBL flows, turbulent mixing and momentum transfer are related to $\partial\langle u'v'\rangle/\partial y$. All the three TBLs have an inner peak in the profile of $-\partial\langle u'v'\rangle/\partial y$ as illustrated in figure 2.7e, which decreases with the increasing pressure gradient. When adverse pressure gradient is applied in the mild APG TBL, an outer peak grows in $-\partial\langle u'v'\rangle/\partial y$ and it continues to grow in the strong APG TBL as illustrated in figure 2.7e. This is consistent with the narrowing of the outer peak of the Reynolds shear stress ($\langle u'v'\rangle$) in the strong APG TBL as shown in figure 2.7d.

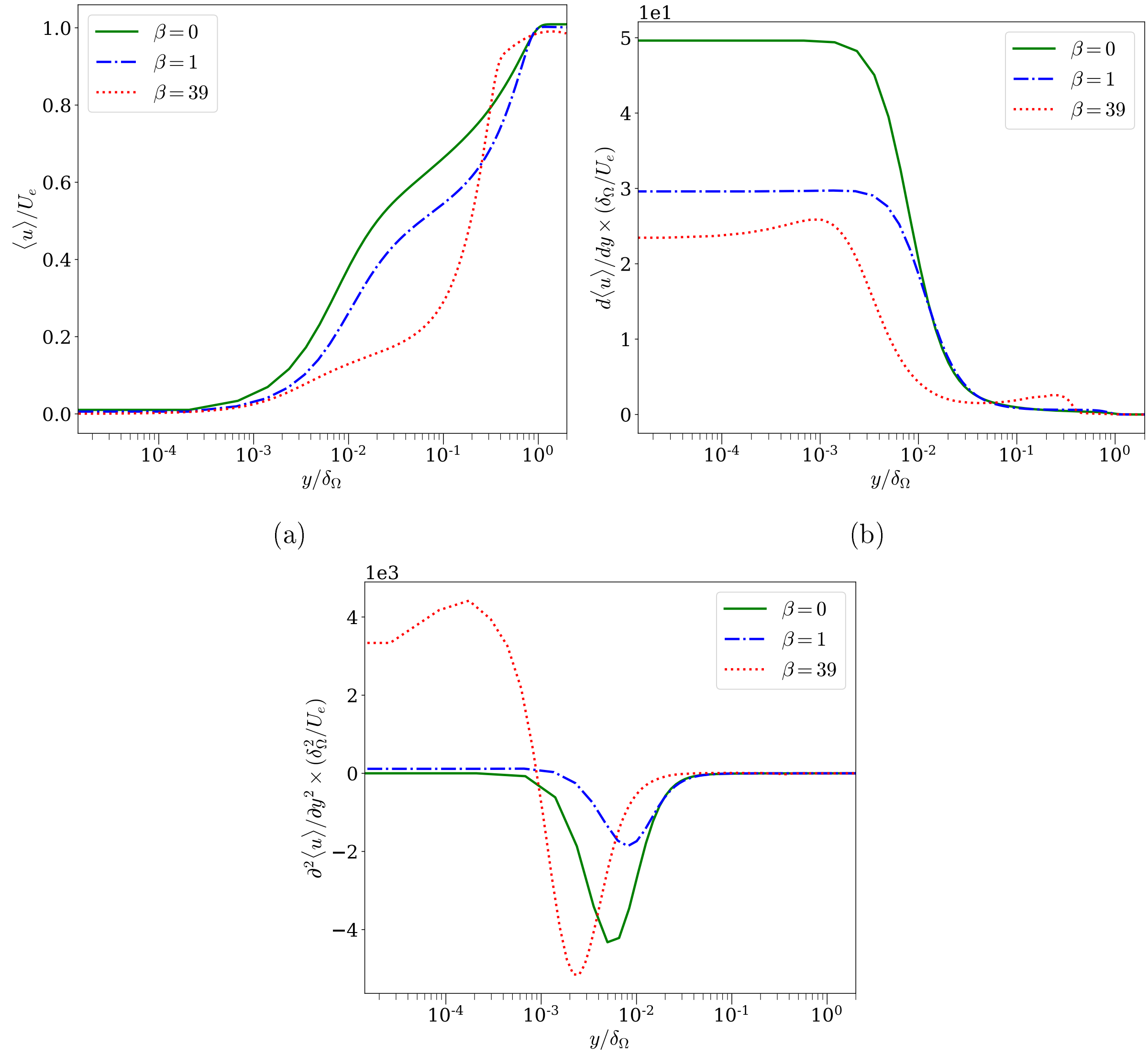

(a) (b) (c)

Figure 2.6: Variation of the (a) mean streamwise velocity $\langle u \rangle$, (b) wall-normal gradient of $\langle u \rangle$, and (c) $\partial^2 \langle u \rangle / \partial y^2$ with β. The profiles are averaged in streamwise direction within DoI and are non-dimensionalised by δ_Ω and U_e.

Figure 2.8 shows the instantaneous visualisation of regions of intense Reynolds stress in the entire flow domain of the TBLs. The isosurfaces correspond to the values of $\pm u'v'/{U_e}^2 = 0.006$, 0.0084 and 0.016 for the ZPG, mild APG and strong APG TBLs, respectively. The magnitude of each of these values is 4 times the respective peak of the Reynolds shear stress $\langle u'v' \rangle$ shown in figure 2.7d. The flow is from bottom-left to top-right as denoted by the arrow. The structures are coloured based on the distance from the wall $(y/\delta_\Omega(x_I))$. Figure 2.8 gives a qualitative indication of the differences in the size and complexity of the structures in the three TBLs. This figure clearly shows that more structures are found farther from the wall with increasing pressure gradient. This is also consistent with the rapid expansion of the boundary layer in the wall-normal direction with increasing pressure gradient as shown in figure 2.4c.

The turbulent kinetic energy budget of the TBLs is given by

$$\mathcal{M} + \mathcal{Z} + \mathcal{T} + \mathcal{P} + \mathcal{V} + \mathcal{D} = 0, \tag{2.7}$$

where $\mathcal{M}$ is the mean convection, $\mathcal{Z}$ is the pressure transport, $\mathcal{T}$ is the turbulent transport, $\mathcal{P}$ is the production, $\mathcal{V}$ is the viscous diffusion, and $\mathcal{D}$ is the pseudo-dissipation. As the TBL flows are statistically steady, the time derivatives are zero. Each of these budget terms are defined as

$$\mathcal{M} = -\partial \langle u_j \rangle \frac{\partial E}{\partial x_j}, \tag{2.8}$$

$$\mathcal{Z} = -\frac{\partial \langle p' u_i' \rangle}{\partial x_i}, \tag{2.9}$$

$$\mathcal{T} = -0.5 \frac{\partial \langle u_i' u_i' u_j' \rangle}{\partial x_j}, \tag{2.10}$$

$$\mathcal{P} = -\langle u_i' u_j' \rangle \frac{\partial \langle u_i \rangle}{\partial x_j}, \tag{2.11}$$

$$\mathcal{D} = -\nu \left\langle \frac{\partial u_i'}{\partial x_j} \frac{\partial u_i'}{\partial x_j} \right\rangle, \tag{2.12}$$

and

$$\mathcal{V} = \nu \frac{\partial^2 E}{\partial {x_j}^2}. \tag{2.13}$$

E is the turbulent kinetic energy given by

$$E = \frac{1}{2} \langle u_k' u_k' \rangle. \tag{2.14}$$

The kinetic energy budget profiles are streamwise averaged in the scaled coordinated within the DoI for each TBL as shown in figure 2.9. In the strong APG TBL, the inner and outer peaks of the turbulent production ($\mathcal{P}$) coincide with the respective inflection point in the profile of the mean streamwise velocity shown in figure 2.6a. For the strong APG TBL in figure 2.9c, the production ($\mathcal{P}$) and pseudo-dissipation ($\mathcal{D}$) has an outer peak around the height of $y = \delta_1$ ($y = 0.2\delta_\Omega$), which shows that the turbulent kinetic energy produced in the outer region is also locally dissipated. In the case of the ZPG TBL, the turbulent production has an inner peak without an outer peak. For the mild APG and strong APG TBL, both inner and outer peaks are present in the production and the outer peak becomes more evident with increasing pressure gradient. For the strong APG TBL, the outer inflection point in the mean streamwise velocity, the outer peaks of the Reynolds stresses, and the outer peaks of production and pseudo-dissipation coincide in the outer region around the height of $y = \delta_1$ ($y = 0.2\delta_\Omega$). Comparison of the momentum terms, two-point correlations, and streamwise velocity spectra for the three TBL cases are presented in Kitsios et al. (2017, 2016).

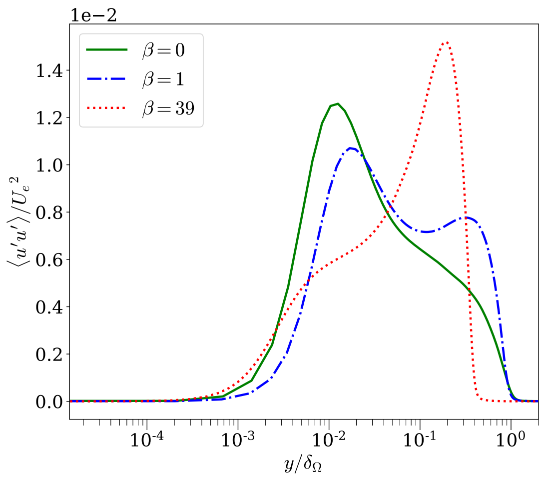

(a)

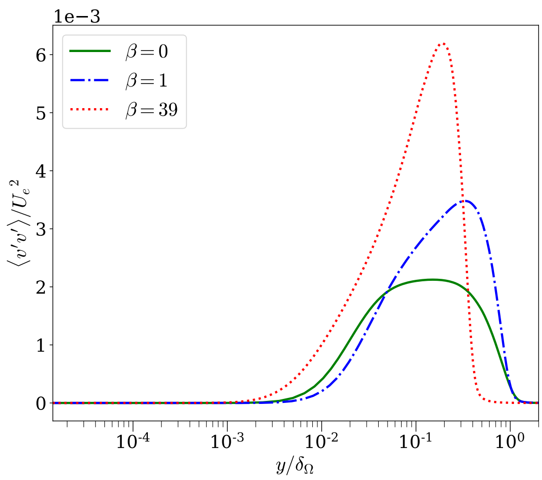

(b)

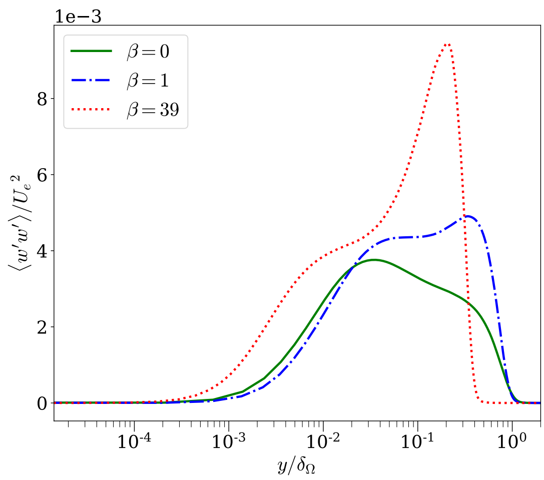

(c)

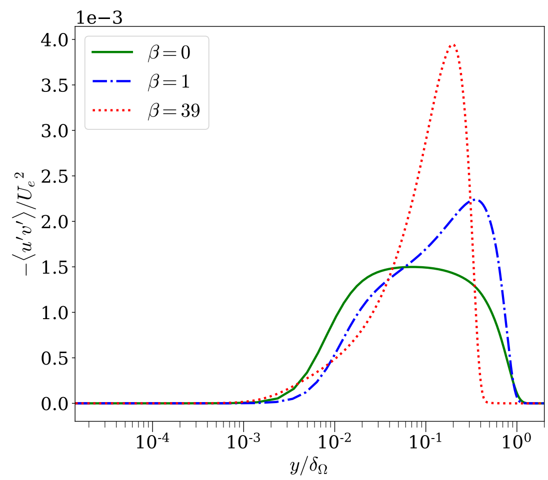

(d)

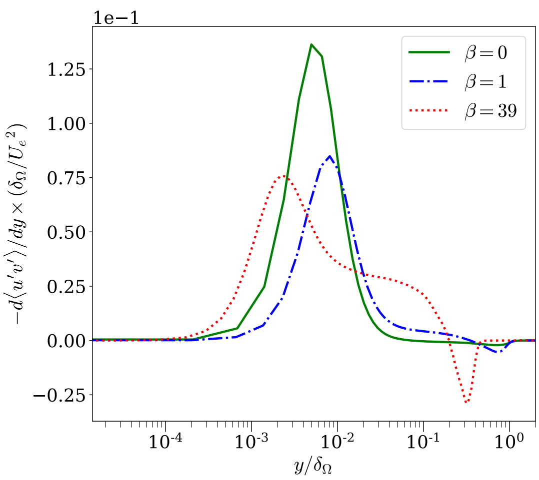

(e)

Figure 2.7: Variation of the Reynolds stress (a) $\langle u'u' \rangle$, (b) $\langle v'v' \rangle$, (c) $\langle w'w' \rangle$, (d) $\langle u'v' \rangle$, and (e) wall-normal gradient of $\langle u'v' \rangle$ with β. The profiles are averaged in streamwise direction within DoI and are non-dimensionalised by δ_Ω and U_e.

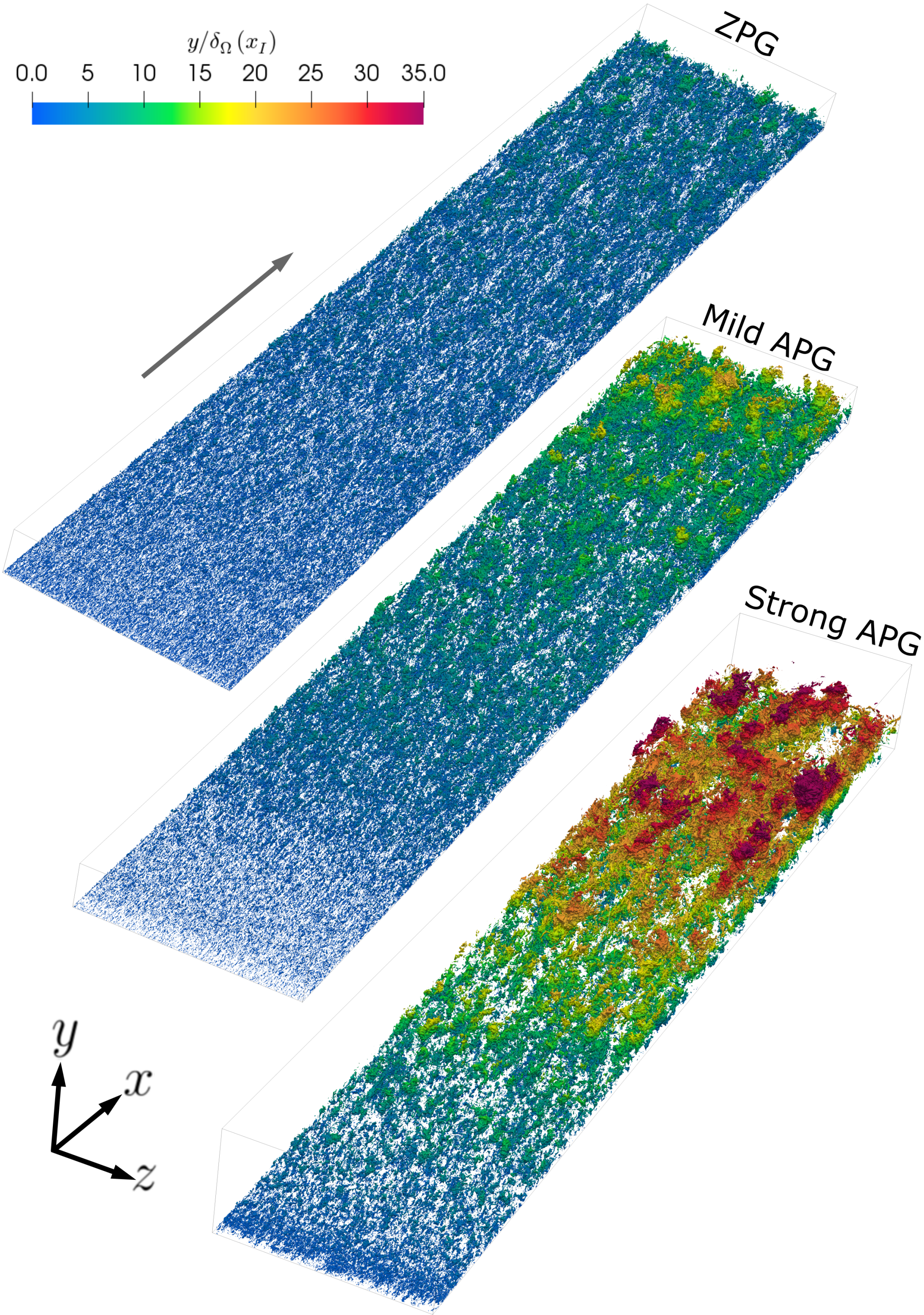

Figure 2.8: Instantaneous visualisation of regions of intense Reynolds stress in the entire flow domain of the TBLs. The isosurfaces correspond to the values of $\pm u'v'/{U_e}^2 = 0.006$, 0.0084 and 0.016 for the ZPG, mild APG and strong APG TBLs, respectively. The magnitude of these values is 4 times the respective peak of the Reynolds shear stress $\langle u'v' \rangle$ shown in figure 2.7d. The flow is from bottom-left to top-right as denoted by the arrow. The structures are coloured based on the distance from the wall.

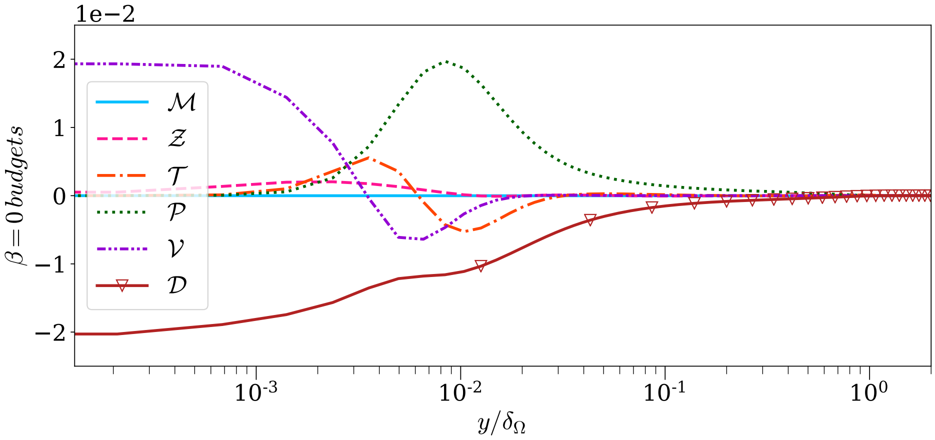

(a)

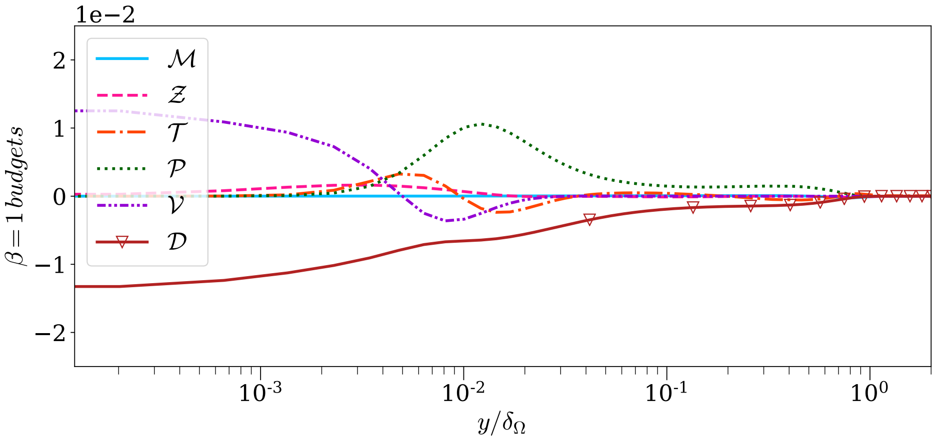

(b)

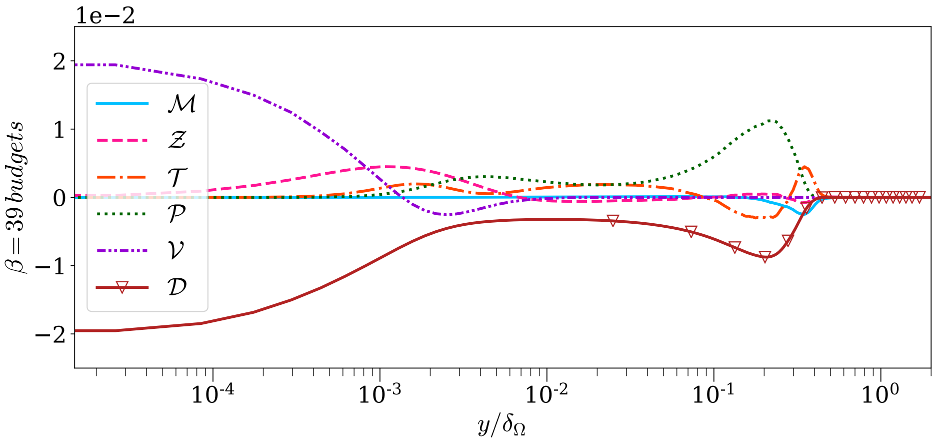

(c)

Figure 2.9: The kinetic energy budget profiles for (a) ZPG, (b) mild APG and (c) strong APG TBLs. The profiles are averaged in streamwise direction within DoI and are non-dimensionalised by δ_Ω and U_e. The kinetic energy budget terms are defined in Equations (2.8) to (2.13).

Not only is the Universe stranger than we think, it is stranger than we can think.

–Werner Heisenberg

Chapter 3

Decomposition of the skin friction coefficient

In the present study, the contribution of the viscous effects, Reynolds stress, vertical motions and coherent structures to the wall shear are investigated using the skin friction decompositions presented by Renard and Deck (2016); Fukagata et al. (2002); Yoon et al. (2016). The basis of these decompositions and the details of their components are briefly discussed in this chapter.

3.1 The RD identity

Renard and Deck (2016) proposed a theoretical decomposition for the mean skin friction coefficient in turbulent boundary layer flows. In the present study, this decomposition is referred to as "the RD identity" after the authors. The RD identity is based on the mean kinetic energy budget in the streamwise direction and is given by

$$C_{f_{RD}} = \underbrace{\frac{2}{U_e^3}\int_0^\infty \nu\Big(\frac{\partial\langle u\rangle}{\partial y}\Big)^2\,dy}_{C_{f_a}} \;+\; \underbrace{\frac{2}{U_e^3}\int_0^\infty -\langle u'v'\rangle\frac{\partial\langle u\rangle}{\partial y}\,dy}_{C_{f_b}} \;+ \\ \underbrace{\frac{2}{U_e^3}\int_0^\infty (\langle u\rangle - U_e)\frac{\partial}{\partial y}\Big(\frac{\tau}{\rho}\Big)\,dy,}_{C_{f_c}} \tag{3.1}$$

where

$$\frac{\tau}{\rho} = \nu\Big(\frac{\partial\langle u\rangle}{\partial y}\Big) - \langle u'v'\rangle. \tag{3.2}$$

The RD identity is compatible with spatially developing flows as it decomposes the mean skin friction coefficient into physical phenomena at every local streamwise position and corresponding wall-normal positions. Renard and Deck (2016) performed their analysis from an absolute reference frame, which travels with the undisturbed far-field fluid at the speed $\langle u \rangle_\infty$ in the streamwise direction when seen from the wall. The undisturbed fluid will appear to be stationary in this absolute reference frame. Renard and Deck (2016) derived the decomposition by integrating the mean streamwise kinetic energy budget once in the absolute reference frame. Full detail of the derivation of the RD identity is available in Renard and Deck (2016).

When seen from the stationary reference frame fixed to the wall, the term C_{f_a} represents the contribution of the viscous effects to the skin friction coefficient. The term C_{f_b} refers to the contribution of the Reynolds shear stress $-\langle u'v' \rangle$. The term C_{f_c} signifies the spatial growth in the flow. The variation of the components of the RD identity with the pressure gradient is discussed in chapter 4.

3.2 The FIK identity

The decomposition of the skin friction coefficient proposed by Fukagata et al. (2002), known as "the FIK identity", was derived by integrating the mean streamwise momentum budget three times in the wall-normal direction. For turbulent boundary layer flows, the FIK identity is given by

$$C_{f_{FIK}} = \underbrace{\frac{4(1-\delta_1/\delta_\Omega)}{Re_{\delta 1}}}_{C_{f_I}} + \underbrace{4\int_0^1 \frac{\langle -u'v' \rangle}{U_e^2}\left(1-\frac{y}{\delta_\Omega}\right) d\left(\frac{y}{\delta_\Omega}\right)}_{C_{f_{II}}} + \\ \underbrace{2\int_0^1 -\left(1-\frac{y}{\delta_\Omega}\right)^2 \left(\frac{1}{\rho}\frac{\partial \langle P \rangle}{\partial x} + \langle I_x \rangle + \frac{\partial \langle u \rangle}{\partial t}\right)\frac{\delta_\Omega}{U_e^2}\, d\left(\frac{y}{\delta_\Omega}\right)}_{C_{f_{III}}}, \tag{3.3}$$

where

$$\langle I_x \rangle = \frac{\partial \langle u \rangle^2}{\partial x} + \frac{\partial (\langle u \rangle \langle v \rangle)}{\partial y} - \nu \frac{\partial^2 \langle u \rangle}{\partial x^2} + \frac{\partial \langle u'u' \rangle}{\partial x}. \tag{3.4}$$

The term C_{f_I} represents the laminar contribution to the skin friction coefficient. The term $C_{f_{II}}$ refers to the contribution of the Reynolds shear stress $-\langle u'v' \rangle$. The term $C_{f_{III}}$ represents the inhomogeneous and transient contribution, where $\partial\langle u \rangle/\partial t$ is zero for statistically steady TBL flows. Full detail of the derivation of the FIK identity is available in Fukagata et al. (2002). The comparison of the FIK identity with the RD identity and the variation of its components with the pressure gradient are presented in chapter 4.

3.3 The YAHS identity

The decomposition of the skin friction coefficient presented by Yoon et al. (2016), referred to as "the YAHS identity" after the authors, was derived from the mean vorticity equation. Using the continuity equation and the divergence of the vorticity, the spanwise component of the mean vorticity equations was simplified. Further triple integration of the equation in wall-normal direction yielded the YAHS identity as

$$C_{f_{YAHS}} = \underbrace{\int_0^1 2\Big(1-\frac{y}{\delta_\Omega}\Big)\frac{\delta_\Omega\langle v'\omega_z'\rangle}{U_e^2}\,d\Big(\frac{y}{\delta_\Omega}\Big)}_{C_{f_1}} + \underbrace{\int_0^1 2\Big(1-\frac{y}{\delta_\Omega}\Big)\frac{\delta_\Omega\langle -w'\omega_y'\rangle}{U_e^2}\,d\Big(\frac{y}{\delta_\Omega}\Big)}_{C_{f_2}} + \underbrace{\frac{\nu\delta_\Omega}{U_e^2}\frac{\partial\langle\Omega_z\rangle}{\partial y}\bigg|_{y=0}}_{C_{f_3}} + \underbrace{\int_0^1 \frac{-2\nu}{U_e^2}\langle\Omega_z\rangle\,d\Big(\frac{y}{\delta_\Omega}\Big)}_{C_{f_4}} + \underbrace{\int_0^1 \Big(1-\frac{y}{\delta_\Omega}\Big)^2 \frac{\delta_\Omega^2\langle I_{x,YAHS}\rangle}{U_e^2}\,d\Big(\frac{y}{\delta_\Omega}\Big)}_{C_{f_5}}, \tag{3.5}$$

where

$$\langle I_{x,YAHS}\rangle = \frac{\partial}{\partial x}\Big(\langle u\rangle\langle\Omega_z\rangle + \langle u'\omega_z'\rangle - \langle w'\omega_x'\rangle\Big) + \frac{\partial}{\partial y}\Big(\langle v\rangle\langle\Omega_z\rangle\Big) - \nu\frac{\partial^2\langle\Omega_z\rangle}{\partial x^2}. \tag{3.6}$$

The term C_{f_1} refers to the contribution of the body forces resulting from the advective vorticity transport. The term C_{f_2} refers to the contribution of the body forces resulting from the vortex stretching. The term C_{f_3} refers to the contribution from the molecular diffusion at the wall, whereas the term C_{f_4} represents the contribution of the molecular transfer due to the mean vorticity. The fifth term C_{f_5} corresponds to the contribution of the inhomogeneous effects arising from the spatial development of the flow in the streamwise direction. Full detail of the derivation of the YAHS identity is available in Yoon et al. (2016). The variation of the components of the YAHS identity with the pressure gradient is discussed in chapter 5.

Excellence is a continuous process and not an accident.

–A. P. J. Abdul Kalam

Chapter 4

Analysis of the contribution of the Reynolds stress and viscous effects to the skin friction

In this chapter, the contribution of the Reynolds shear stress and the viscous effects to the skin friction and their variation with the pressure gradient are analysed from the perspective of the mean streamwise kinetic energy budget using the skin friction decomposition given by Renard and Deck (2016) (RD identity). This chapter is presented in the form of a journal paper published in the *International Journal of Heat and Fluid Flow* (Senthil et al., 2020b).

International Journal of Heat and Fluid Flow 82 (2020) 108531

Contents lists available at ScienceDirect

International Journal of Heat and Fluid Flow

journal homepage: www.elsevier.com/locate/ijhff

Analysis of the factors contributing to the skin friction coefficient in adverse pressure gradient turbulent boundary layers and their variation with the pressure gradient

Shevarjun Senthil[*,a], Vassili Kitsios[b,a], Atsushi Sekimoto[c,a], Callum Atkinson[a], Julio Soria[a,d]

[a] Laboratory for Turbulence Research in Aerospace and Combustion, Department of Mechanical and Aerospace Engineering, Monash University, Melbourne 3800, Australia
[b] CSIRO Oceans and Atmosphere, Castray Esplanade, Battery Point, Tasmania 7004, Australia
[c] Department of Materials Engineering Science, Osaka University, Osaka 560–8531, Japan
[d] Department of Aeronautical Engineering, King Abdulaziz University, Jeddah 21589, Kingdom of Saudi Arabia

ARTICLE INFO

Keywords:
Turbulent boundary layer
Adverse pressure gradient
Skin friction

ABSTRACT

This paper reports on a study of the various factors contributing to the skin friction in incompressible adverse pressure gradient turbulent boundary layer (APG-TBL) flows. Specifically, it deals with the contributions to the skin friction coefficient from the Reynolds stresses and the viscous effects and the role of the pressure gradient. The skin friction coefficient is calculated based on the theoretical decomposition for mean skin friction generation introduced by Renard and Deck (2016). This decomposition is compatible with spatially developing flows as it is applicable to every local streamwise position. The turbulent flows are generated through the direct numerical simulation of a TBL on a smooth flat plate with the desired farfield pressure gradient. It is observed that the Reynolds shear stress provides the dominant positive contribution to the skin friction coefficient for all the pressure gradient cases. However, with increasing adverse pressure gradient, the skin friction coefficient continues to decrease and approaches zero as the positive contribution from the Reynolds shear stress is diminished by the negative contribution of the pressure gradient. When the flow reaches the verge of separation, the predominant Reynolds shear stress contribution to the skin friction coefficient is from a spatially localized outer peak at an approximate height of the displacement thickness ($y=\delta_1$) which coincides with the inflection point of the mean streamwise velocity. Even though, the decompositions in Renard and Deck (2016) and Fukagata et al. (2002) give a different distribution for the skin friction coefficient in the zero pressure gradient (ZPG) and the mild APG cases, both of the identities capture the dominant outer peak of the Reynolds shear stress contribution when the flow reaches the verge of separation. This emphasizes the growing importance of the outer layer dynamics with increasing pressure gradient as it pertains to skin friction generation.

1. Introduction

Adverse pressure gradient turbulent boundary layers (APG-TBLs) are found in internal expanding duct flows, and external flows like those over the diverging part of curved surfaces such as turbine blades and the leeward side of aerofoil sections. Separation of the TBL in many of these practical flows results in reduced efficiency and increases the operational cost of these engineering systems. It is a challenging problem to understand the fluid physics of the detachment of the TBLs and our understanding of the influence of the adverse pressure gradient on the TBLs is still limited (Clauser, 1954). Wall shear stress (τ_w) plays a fundamental role in the flow as it is related to the characteristic friction velocity (u_τ) which is used for scaling wall-bounded turbulent flows. Orlandi and Jiménez (1994) showed that the formation of the near-wall streaks results in higher wall friction in the turbulent boundary layers. But the contribution of turbulent fluctuations to the mean skin friction was not quantified as a function of wall distance. It has also been shown by Skåre and Krogstad (1994) that the outer layer plays a more important role in wall-bounded flows as the adverse pressure gradient increases. Skåre and Krogstad (1994) observed that the peak of the turbulent stresses in the outer region scales linearly with the non-dimensional pressure gradient (β is defined in Section 2.3).

Fukagata et al. (2002) came up with a decomposition, known as the FIK identity, to relate the wall-normal distribution of the Reynolds shear stress to the skin friction coefficient in incompressible channel, pipe and ZPG boundary layer flows. It is based on the mean streamwise momentum equation and has explicit streamwise gradient terms. They decomposed the skin friction coefficient into different dynamical

* Corresponding author.
E-mail address: shevarjun.senthil@monash.edu (S. Senthil).

https://doi.org/10.1016/j.ijheatfluidflow.2019.108531
Received 3 September 2019; Received in revised form 11 December 2019; Accepted 24 December 2019
Available online 21 February 2020
0142-727X/

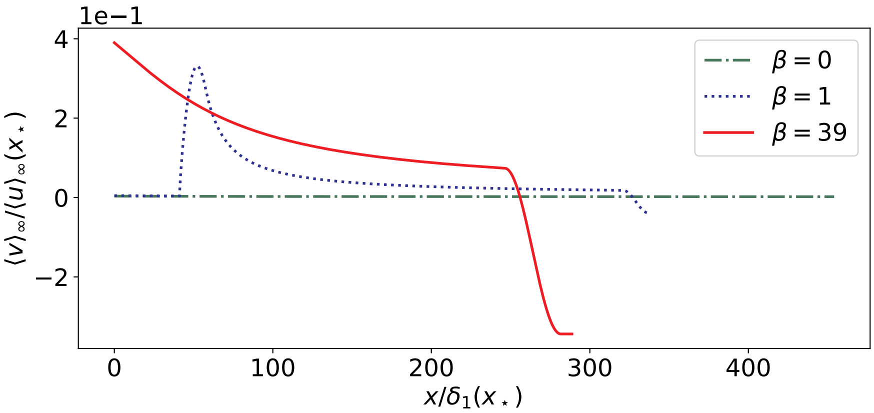

Fig. 1. Farfield wall-normal velocity boundary condition for the three pressure gradient cases. $x_\star$ is the streamwise position where $Re_{\delta 1}$ = 4800 and $\langle u \rangle_\infty$ is the far-field mean streamwise velocity. β (the non-dimensional streamwise pressure gradient), δ_1 (displacement thickness) and $Re_{\delta 1}$ (Reynolds number based on displacement thickness) are defined in the Section 2.3.

contributions. However, the terms in the decomposition did not have a simple and direct physical interpretation.

Mehdi and White (2011) presented a direct integral method to compute the wall shear stress similar to that of Fukagata et al. (2002). The mean momentum equation was integrated to the boundary layer edge and the streamwise gradients were replaced with the wall-normal gradients of the total shear stress. This decomposition was found to be useful when the flow statistics at different streamwise positions are not available especially in experimental data. Following it, Mehdi et al. (2014) presented a direct method to compute the wall shear stress based on a full momentum integral approach. Their decomposition did not have direct streamwise gradient terms. Their expression depends only on the inner wall boundary conditions as they integrated up to an arbitrary height in the wall-normal direction. This method is useful when it is not feasible to measure the outer boundary condition or when it is not clearly defined. They tested the effect of changing the integration limits on the wall shear stress. Still, their upper integration bound was restricted within the boundary layer edge. More recently, Renard and Deck (2016) formulated a theoretical decomposition for the skin friction coefficient based on a mean streamwise kinetic energy budget across the entire boundary layer. This decompositon is hereafter referred as the "RD identity" (named after its authors Renard and Deck (2016)). This formulation decomposes the skin friction coefficient at every streamwise position into a physical phenomena.

The present study focuses on analysing the contributions to the skin friction coefficient from the Reynolds shear stress and the viscous effects in an incompressible turbulent boundary layer flow using the RD identity. The contribution to skin friction coefficient from different regions of the boundary layer and the role of the pressure gradient in it is also investigated. Brief details of the direct numerical simulation and the characteristics of the flows considered for this study are presented in Section 2. In Section 3, the details and interpretation of the components of the RD decomposition introduced by Renard and Deck (2016) are discussed. The variation of the components of the RD identity with the pressure gradient is presented in Section 4. The wall-normal distribution of the RD components are analyzed in Section 5. Then, the explicit relationship between the RD identity and the pressure gradient is established in Section 6. In Section 7, the effects of varying one of the limits of integration in the RD identity to an arbitrary limit while keeping the other limit fixed are discussed. Components of the RD identity is qualitatively compared with the corresponding components of the FIK identity in Section 8. Finally, concluding remarks are presented in Section 9.

2. Details of the direct numerical simulation

2.1. The numerical method

The in-house direct numerical simulation (DNS) code solves the incompressible Navier-Stokes equation for pressure and velocity fields in Cartesian coordinates with the flow directions as streamwise (x), wall-normal (y) and spanwise (z). In this paper, the mean velocity components are denoted by ($\langle u \rangle$, $\langle v \rangle$, $\langle w \rangle$) and the corresponding fluctuating components are denoted by (u', v', w'). The first version of the code was developed by Simens et al. (2009); Simens (2008) and subsequently improved by Borrell et al. (2013). The fractional step method is used to solve the governing equations as suggested in Harlow and Welch (1965) and in Perot (1993). The grid is staggered in x and y directions but not in the z direction. Compact finite difference is used for spatial discretization in x and y directions (Lele, 1992), while Fourier decomposition is used in the spanwise direction. Time stepping is achieved using a 3-step Runge Kutta method (Simens, 2008). The density (ρ = 1) and kinematic viscosity (ν) are taken as constants. Full detail of the DNS code and the parallelisation techniques used can be found in Sillero (2014); Borrell et al. (2013).

2.2. Boundary conditions used in the simulations

The current computational domain is a three dimensional rectangular box with a no slip boundary condition on the bottom surface. It uses a modified far-field boundary condition to apply the required adverse pressure gradient in the domain. This is achieved by specifying the wall-normal suction velocity ($\langle v \rangle_\infty$) in the far-field as shown in Fig. 1. The spanwise vorticity (Ω_z) is zero in the far-field. Details of the far-field boundary condition are presented in Kitsios et al. (2017).

The inflow boundary condition is obtained by recycling and mapping a yz plane (cross-plane) from a downstream position to the inflow (Kitsios et al., 2016; 2017). Mapping is essential because of the growth of the TBL in the wall-normal direction as it develops in the streamwise direction. Periodic boundary conditions are applied in the spanwise direction. The outflow is a convective boundary condition given as (Sillero, 2014; Simens, 2008)

$$\frac{\partial \boldsymbol{u}}{\partial t} + \langle u \rangle_\infty \cdot \frac{\partial \boldsymbol{u}}{\partial x} = 0, \tag{1}$$

where $\boldsymbol{u}$ is the instantaneous velocity and t is the time.

2.3. Classification of the flows and the definition of the reference scales

Boundary layer flows with three different streamwise pressure gradients are considered in this study and are classified based on β as follows: ZPG - zero pressure gradient (β=0), mild APG (β=1) and strong APG (β=39). The non-dimensional pressure gradient (β) is defined as

$$\beta = \frac{\delta_1}{{u_\tau}^2}\frac{P_{e,x}}{\rho} = \delta_1 \frac{P_{e,x}}{\tau_w}, \tag{2}$$

where $u_\tau = \sqrt{\tau_w/\rho}$ is the friction velocity, δ_1 is the displacement thickness, $P_{e,x}$ is the far-field streamwise pressure gradient, ρ is the density, and τ_w is the mean wall shear stress.

Based on the definition of Lighthill (1963), the reference velocity (U_e) used in the simulations is given as

$$U_e(x) = U_\Omega(x, \delta_\Omega), \tag{3}$$

where

$$U_\Omega(x, y) = -\int_0^y \langle \Omega_z \rangle (x, \tilde{y})\, d\tilde{y}, \tag{4}$$

$\langle \Omega_z \rangle$ is the mean spanwise vorticity, and δ_Ω is the wall-normal position where $\langle \Omega_z \rangle$ is 0.2% of the mean vorticity at the wall.

Based on the definition of Spalart and Watmuff (1993), the displacement thickness (δ_1) and the momentum thickness (δ_2) are given as

$$\delta_1(x) = \frac{-1}{U_e} \int_0^{\delta_\Omega} y \langle \Omega_z \rangle (x, y) dy, \tag{5}$$

and

$$\delta_2(x) = \frac{-2}{U_e^2} \int_0^{\delta_\Omega} y U_\Omega \langle \Omega_z \rangle (x, y) dy - \delta_1(x). \tag{6}$$

The flow dynamics of APG TBLs depend on the local environment and also on the flow history. The pressure forces and the shear stresses acting on a boundary layer are minute in nature and because of this, the boundary layer cannot react quickly to the changing environment (Clauser, 1954). This makes the dynamical properties of the boundary layer dependent on the flow history and on the specific pressure gradient distribution. In order to minimise the influence of these history effects, a self-similar APG TBL is studied. Moreover, this self-similar flow is only possible in the domain of interest (DoI) of the strong APG flow, where β has an average value of 39. The conditions of self-similarity are explained comprehensively in Kitsios et al. (2017, 2016). The $\beta = 39$ case can be characterized as being at the verge of separation. Within the DoI, the Reynolds number based on displacement thickness ($Re_{\delta 1}$) varies from 22,200 to 28,800 for the strong APG case where $Re_{\delta 1} = U_e \delta_1 / \nu$.

The numerical details of the simulations are given in Table 1. Fig. 2a shows the displacement thickness, Fig. 2b shows the shape factor ($H = \delta_1/\delta_2$), and Fig. 2c shows δ_Ω, where δ_Ω is the boundary-layer thickness or the wall-normal position at which the mean spanwise vorticity ($\langle \Omega_z \rangle$) is 0.2% of the mean vorticity at the wall. $x_\star$ is the streamwise position where $Re_{\delta 1} = 4800$ and $\delta_1(x_\star)$ is the displacement thickness at $x_\star$. Fig. 3a and b refer to the Reynolds number based on displacement thickness and momentum thickness ($Re_{\delta 2} = U_e \delta_2 / \nu$) respectively. For all the three cases, the respective DoIs are highlighted with the markers. Full details of the DNS of the three TBL cases are presented in Kitsios et al. (2016, 2017) with the data of the statistical properties available in Soria et al. (2019).

3. Decomposition of the skin friction coefficient

Friction drag and shear are the major cause of energy dissipation in a TBL flow. Thus, it is of great importance to understand the mechanism of generation of mean skin friction in wall bounded turbulent flows. Renard and Deck (2016) proposed a theoretical decomposition for the mean skin friction in boundary layer flows. The RD decomposition (named after its authors Renard and Deck (2016)) is based on mean kinetic energy budget in the streamwise direction and gives the mean skin friction coefficient as

$$C_{f_{RD}} = \underbrace{\frac{2}{U_e^3} \int_0^\infty \nu \left(\frac{\partial \langle u \rangle}{\partial y} \right)^2 dy}_{C_{f_a}} + \underbrace{\frac{2}{U_e^3} \int_0^\infty -\langle u'v' \rangle \frac{\partial \langle u \rangle}{\partial y} dy}_{C_{f_b}} + \underbrace{\frac{2}{U_e^3} \int_0^\infty (\langle u \rangle - U_e) \frac{\partial}{\partial y} \left(\frac{\tau}{\rho} \right) dy}_{C_{f_c}}, \tag{7}$$

where

$$\frac{\tau}{\rho} = \nu \left(\frac{\partial \langle u \rangle}{\partial y} \right) - \langle u'v' \rangle. \tag{8}$$

Table 1
Numerical details of the DNS of the three pressure gradient cases: number of collocated grid points in the streamwise (N_x) and wall-normal (N_y) directions; number of spanwise Fourier modes after de-aliasing (N_z); domain size L_x, L_y and L_z in x, y and z directions respectively; uniform streamwise (Δx) and spanwise grid spacing (Δz); wall-normal grid spacing at the wall (Δy_{wall}) and at the far-field boundary (Δy_∞); Reynolds number based on displacement thickness ($Re_{\delta 1}$) in the domain of interest (DoI); and the time taken to accumulate the statistics (T). δ_1 is the displacement thickness and $x_\star$ is the streamwise position where $Re_{\delta 1} = 4800$. The eddy-turnover time ($\delta_1(x_\star)/U_e(x_\star)$) is defined at $x_\star$. Full details of the DNS of the three TBL cases are presented in Kitsios et al. (2016), Kitsios et al. (2017).

	ZPG	Mild APG	Strong APG
Nominal β	0	1	39
N_x	8193	8193	8193
N_y	315	500	1000
N_z	1362	1362	1362
$L_x/\delta_1(x_\star)$	480	345	303
$L_y/\delta_1(x_\star)$	22.7	29.8	73.4
$L_z/\delta_1(x_\star)$	80.1	57.6	50.7
$\Delta x/\delta_1(x_\star)$	0.0585	0.0421	0.0370
$\Delta y_{wall}/\delta_1(x_\star)$	1.53×10^{-3}	1.10×10^{-3}	9.71×10^{-4}
$\Delta y_\infty/\delta_1(x_\star)$	0.0992	0.0714	0.254
$\Delta z/\delta_1(x_\star)$	0.0585	0.0421	0.0370
$Re_{\delta 1}$ range in DoI	3800 → 5280	3800 → 5280	22200 → 28800
$TU_e(x_\star)/\delta_1(x_\star)$	621	720	1160

This decomposition is local in the streamwise position and is compatible with spatially developing flows. Renard and Deck (2016) presented the skin friction generated in both laminar and turbulent flows. Their analysis is considered from an absolute reference frame which travels with the undisturbed far-field fluid at the speed $\langle u \rangle_\infty$ in the x-direction when seen from the wall. The undisturbed fluid will appear to be stationary in this absolute reference frame. Only the instantaneous streamwise velocity at the wall is considered as zero. There are no restrictions on the velocity in wall-normal and spanwise directions which allows blowing or suction at the wall, though neither is present in the current TBL cases. As the absolute reference frame moves at a constant speed, it is an inertial reference frame and so the pressure coincides in both the wall and the absolute reference frames. The RD identity decomposes the mean skin friction coefficient into physical phenomena at every local streamwise position and corresponding wall normal positions for a spatially developing flow. The Reynolds shear stress is weighted by the wall normal gradient of the mean streamwise velocity. This weight increases as we move closer to the wall for ZPG TBL flows as the velocity gradient increases towards the wall. Renard and Deck (2016) showed that in high Reynolds number ZPG TBL flows, the excess friction induced by turbulence is mostly located in the logarithmic layer.

When seen from the absolute reference frame, $C_{f_{RD}}$ is represented as the mean power supplied to the fluid by the wall and C_{fa} refers to direct viscous dissipation. Similarly, C_{fc} can be interpreted as the mean streamwise kinetic energy gained by the fluid in the absolute reference frame or the fraction of the mean skin friction power that is not dissipated into turbulent kinetic energy and heat. In the absolute reference frame, Renard and Deck (2016) referred to C_{fb} as the “dissipation” because of production of turbulent kinetic energy. The RD identity considers the contribution to $C_{f_{RD}}$ from the whole boundary layer.

4. Variation of skin friction coefficient and its components with adverse pressure gradient

The dependence of the skin friction coefficient ($C_{f_{RD}}$) on the pressure gradient and the friction Reynolds number (Re_τ) is illustrated in Fig. 4. The friction Reynolds number is defined as $Re_\tau = u_\tau \delta_\Omega / \nu$ where u_τ is the friction velocity, and ν is the kinematic viscosity. Table 2 shows the streamwise and spanwise averaged values of $C_{f_{RD}}$ within the DoI for the three pressure gradient cases. The skin friction coefficient based on the

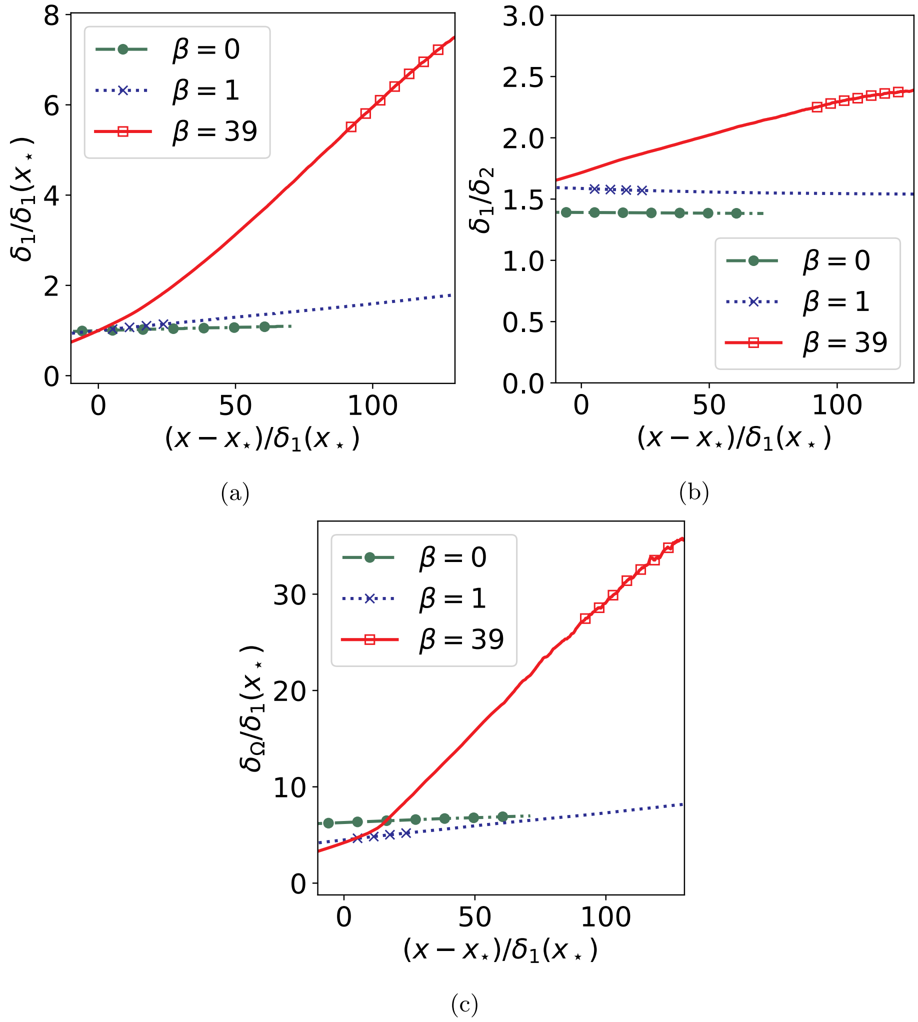

Fig. 2. (a) Displacement thickness (δ_1); (b) shape factor ($H = \delta_1/\delta_2$), where δ_2 is the momentum thickness; (c) δ_Ω, where δ_Ω is the boundary-layer thickness or the wall-normal position at which the mean spanwise vorticity ($\langle\Omega_z\rangle$) is 0.2% of the mean vorticity at the wall; for each case of β and their respective DoI is highlighted with the markers. $x_\star$ is the streamwise position where $Re_{\delta 1} = 4800$.

wall shear stress (C_{f_w}) is given by

$$C_{f_w} = \frac{\tau_w}{\frac{1}{2}\rho U_e^2}, \tag{9}$$

where

$$\tau_w = \mu \frac{d\langle u\rangle}{dy}|_{y=0}. \tag{10}$$

Fig. 4 shows that $C_{f_{RD}}$ and C_{f_w} are in close agreement with each other as expected. With increasing pressure gradient, $C_{f_{RD}}$ keeps reducing and approaches zero as shown in Fig. 4 and Table 2. As illustrated in Fig. 3a, $Re_{\delta 1}$ increases with the pressure gradient. This is due to the fact that the displacement thickness (δ_1) increases with the pressure gradient as shown in Fig. 2a. The displacement thickness has a larger value for the strong APG TBL when compared to the mild APG TBL, which in turn has a larger value than that of the ZPG TBL. This shows that the boundary layer expands more in the wall-normal direction with increasing adverse pressure gradient. The expansion of the boundary layer also coincides with the reduction of the skin friction coefficient (C_{f_w} and $C_{f_{RD}}$) with increasing pressure gradient as shown in Fig. 4. The reduction in skin friction coefficient is because of the reduction of the mean wall shear stress with increasing pressure gradient. This in turn coincides with the reduction of mean velocity gradient at the wall with increasing pressure gradient as shown in Fig. 8e. As the adverse pressure gradient is increased, the flow becomes more like a free shear layer with the wall shear stress tending to

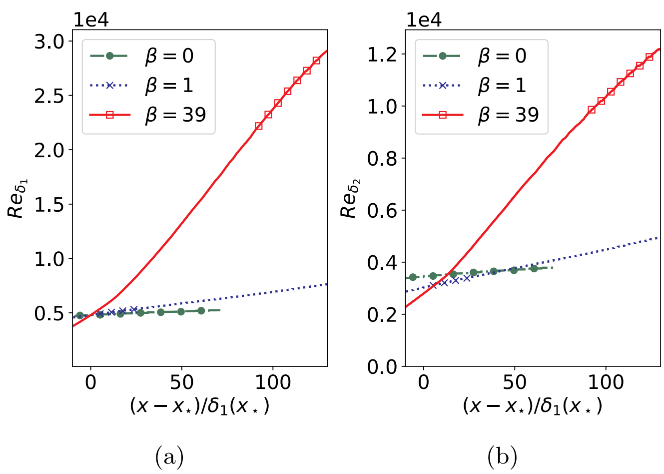

Fig. 3. (a) Reynolds number based on displacement thickness ($Re_{\delta 1}$); (b) momentum thickness ($Re_{\delta 2}$); for each case of β and their respective DoI is highlighted with the markers. $x_\star$ is the streamwise position where $Re_{\delta 1} = 4800$.

zero. The skin friction coefficient is given as a function of Reynolds number based on momentum thickness ($Re_{\delta 2}$) in Appendix A.

When seen from the usual wall reference frame, C_{fa} signifies the contribution of viscous effects, C_{fb} refers to the contribution from the

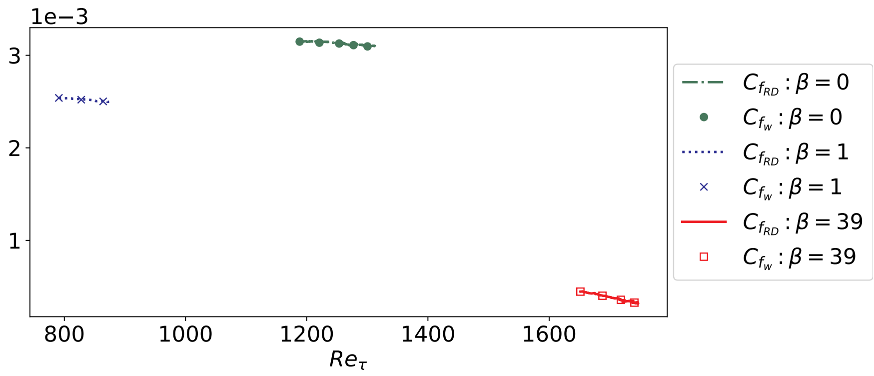

Fig. 4. Dependence of $C_{f_{RD}}$ and C_{f_w} on β and the friction Reynolds number (Re_τ) in the respective DoI.

Table 2
Variation of the streamwise and spanwise averaged values of $C_{f_{RD}}$ with β in the respective DoI.

β	0	1	39
$C_{f_{RD}} \times 10^3$	3.127	2.520	0.377

Table 3
Variation of the streamwise and spanwise averaged values of the three components of $C_{f_{RD}}$ with β in the respective DoI.

β	0	1	39
$C_{fa} \times 10^3$	1.111	0.795	0.064
$C_{fb} \times 10^3$	1.705	2.289	4.370
-$C_{fc} \times 10^3$	− 0.311	0.563	4.057

Reynolds shear stress and C_{fc} signifies the spatial growth in the flow or the contribution from the pressure gradient. But in the absolute reference frame, C_{fc}/C_f is seen as the efficiency at which the wall supplies energy to the fluid. For all the pressure gradient cases, C_{fa} and C_{fb} are positive. Note that C_{fc} is positive only for the ZPG case while it is negative for the other two adverse pressure gradient cases.

Fig. 5 shows the dependence of the components of the $C_{f_{RD}}$ on the friction Reynolds number (Re_τ) and their variation with the pressure gradient. Table 3 shows the variation of the streamwise and spanwise averaged values of the components of the $C_{f_{RD}}$ with β in the respective DoIs. As β increases, the contribution of the viscous effects (C_{fa}) reduces and approaches zero in Fig. 5 and Table 3. With increase of β, the absolute values of C_{fb} and C_{fc} increases. It is also apparent that the absolute values of C_{fb} and C_{fc} develops with a sharp gradient as Re_τ increases for the $\beta = 39$ case when compared to the other two pressure gradient cases in Fig. 5. The positive contribution to C_f from the Reynolds shear stress (through C_{fb}) is diminished by the negative contribution from C_{fc}. However, the dominant contribution to the skin friction coefficient for all the pressure gradient cases is from the Reynolds shear stress (C_{fb}).

The variation of the proportion of each component in $C_{f_{RD}}$ with β and its dependence on the friction Reynolds number (Re_τ) is seen in Fig. 6. These ratios refer to the relative contribution of each of the terms for the various pressure gradient cases. The variation of the streamwise and spanwise averaged values of the ratios of the components of $C_{f_{RD}}$ with β in the respective DoIs is given in Table 4. On average, the proportion of the Reynolds shear stress ($C_{fb}/C_{f_{RD}}$) increases by around 21.6 times when β varies from 0 to 39 as seen in Table 4. The proportion of C_{fb} and C_{fc} increases drastically with Re_τ for $\beta = 39$ whereas they do not have steep gradients for $\beta = 0$ and $\beta = 1$ in Fig. 6. But, C_{fc} acts to cancel out the effect of C_{fb}. As shown in Table 4, the proportion of C_{fa} in C_f reduces with the pressure gradient. The ratio $C_{fa}/C_{f_{RD}}$ is approximately 0.5 times smaller for $\beta = 39$ compared to $\beta = 0$. On average, the viscous contribution accounts for 35.5% of $C_{f_{RD}}$ for $\beta = 0$ and it drops to 16.9% for $\beta = 39$.

5. Wall-normal distribution of the components of $C_{f_{RD}}$ and the role of the adverse pressure gradient

The streamwise averaged profiles of the premultiplied integrands in Figs. 7, 8 and 9 show the distribution of each of the terms of $C_{f_{RD}}$ in the wall-normal direction within the DoI. The wall normal position is

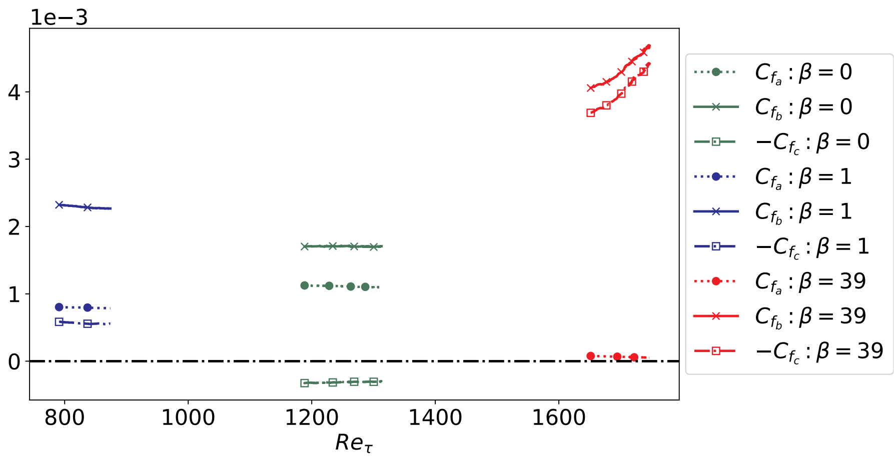

Fig. 5. Dependence of the three components of $C_{f_{RD}}$ on β and the friction Reynolds number (Re_τ) in the respective DoI.

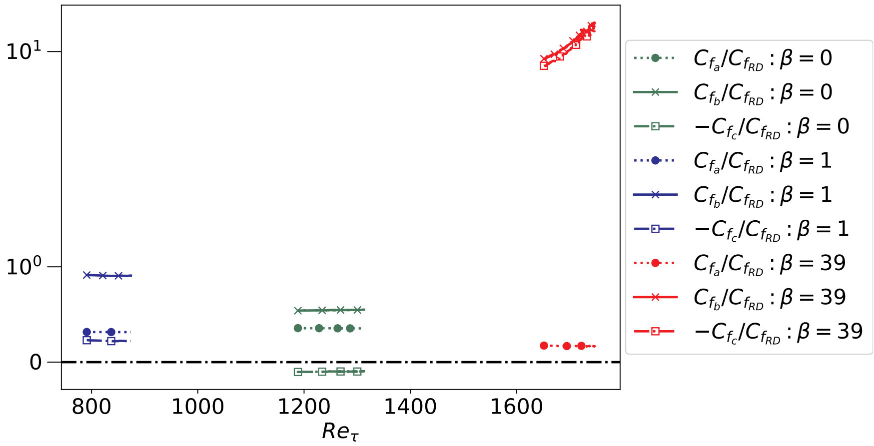

Fig. 6. Dependence of the proportion of the components of $C_{f_{RD}}$ on β and the friction Reynolds number (Re_τ) in the respective DoI.

Table 4
Variation of the streamwise and spanwise averaged values of the proportion of the components of C_{fRD} with β in the respective DoI.

β	0	1	39
C_{fa}/C_{fRD}	0.355	0.300	0.169
C_{fb}/C_{fRD}	0.545	0.908	11.760
$-C_{fc}/C_{fRD}$	− 0.100	0.223	10.930

non-dimensionalised by the outer scale δ_1. Deck et al. (2014) and Renard and Deck (2016) also studied the wall-normal distribution of the skin friction coefficient for a ZPG boundary layer flow. The premultiplied integrand of each term of $C_{f_{RD}}$, given by

$$c_{f\,a*} = \frac{y}{\delta_1} \times \frac{2\nu\delta_1}{U_e^3}\left(\frac{\partial\langle u\rangle}{\partial y}\right)^2, \tag{11}$$

$$c_{f\,b*} = \frac{y}{\delta_1} \times \frac{-2\langle u'v'\rangle\delta_1}{U_e^3}\frac{\partial\langle u\rangle}{\partial y}, \tag{12}$$

and

$$c_{f\,c*} = \frac{y}{\delta_1} \times \frac{2(\langle u\rangle - U_e)\delta_1}{U_e^3}\frac{\partial}{\partial y}\left(\frac{\tau}{\rho}\right) \tag{13}$$

is denoted in lowercase and by the subscript of *.

The premultiplied integrand c_{fa^*} refers to the contribution from the viscous effects to the skin friction coefficient and its profiles are given in Fig. 7. There is an inner peak for the ZPG case around $y^+ = 6.6$ with negligible contribution in the outer region. The inner region is defined as $y/\delta_1 < 0.1$ (Pope, 2000) while the outer region as $y/\delta_1 > 0.1$. As the pressure gradient increases, for the mild APG case, the inner peak diminishes while a small outer peak develops. When the pressure gradient increases to the point of the flow being at the verge of separation as in the $\beta = 39$ case, the contribution from c_{fa^*} is almost negligible throughout the boundary layer with two tiny inner and outer peaks.

The premultiplied integrand c_{fb^*} describes the contribution to the skin friction coefficient from the Reynolds shear stress which represents turbulent momentum transport and its profile occupies a broader region for the ZPG case as shown in Fig. 8a. It has an inner and an outer peak. When the pressure gradient increases to the $\beta = 1$ case, the inner peak reduces while the outer peak grows. For the $\beta = 39$ case, the value of c_{fb^*} is almost negligible in the inner region while it is concentrated in the outer region with a dominant peak. For the strong APG case, c_{fb^*} has the outer peak at approximately the displacement thickness height ($y = \delta_1$). The C_{fb} integrand in Eq. 7 is composed of the Reynolds shear stress and the wall-normal gradient of the mean streamwise velocity and their profiles are given in Fig. 8b and 8 e respectively. Similar to the profile of c_{fb^*} for the ZPG case, the profile of Reynolds shear stress is widely spread over the domain. For the $\beta = 39$, the Reynolds shear stress develops a dominant outer peak like that of c_{fb^*} at an approximate height of displacement thickness ($y = \delta_1$). The profile of the mean streamwise velocity in Fig. 8d develops an inflection point as the pressure gradient reaches $\beta = 39$ and this inflection point is also around the displacement thickness height ($y = \delta_1$) as shown in Fig. 8e. In incompressible turbulent boundary layer flows, turbulent momentum transport is represented by $-\partial\langle u'v'\rangle/\partial y$ (Fig. 8c). This gradient accelerates the mean flow near the wall but decelerates the mean flow in the wake of the boundary layer (Renard and Deck, 2016). The integral of the gradient of the Reynolds shear stress in the wall-normal direction vanishes when integrated over all $y \geq 0$. The peak of this gradient is almost the same for all the pressure gradient cases and it shifts down in the inner region for the β= 39 case.

The premultiplied integrand c_{fc^*} refers to the contribution from the pressure gradient or the effect of the spatial growth of the flow. In Fig. 9, for the ZPG case, the c_{fc^*} contribution is virtually negligible throughout the boundary layer as expected. For $\beta = 1$, a negative and a positive peak start to develop in the outer region. These peaks become more pronounced for the flow at the verge of separation ($\beta = 39$ case) and it changes sign close to the displacement thickness height (y= δ_1).

The peak of the premultiplied integrand c_{fb^*}, the peak of the Reynolds shear stress, the inflection point of the mean streamwise velocity as well as the point where the premultiplied integrand c_{fc^*} changes sign coincide at the approximate height of the displacement thickness (y= δ_1) for $\beta = 39$ case. Fig. 10 shows the comparison of the three premultiplied integrands of $C_{f_{RD}}$ for $\beta = 39$ case.

The total premultiplied integrand $c_{f_{RD_*}}$ in Fig. 11 shows the cumulative effect of the three components. For the ZPG case, the contribution

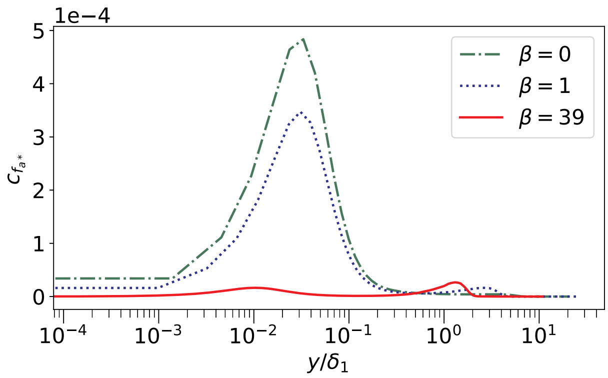

Fig. 7. Variation of the premultiplied integrand c_{fa^*} with β. The profiles are averaged in streamwise direction within DoI and are non-dimensionalised by δ_1.

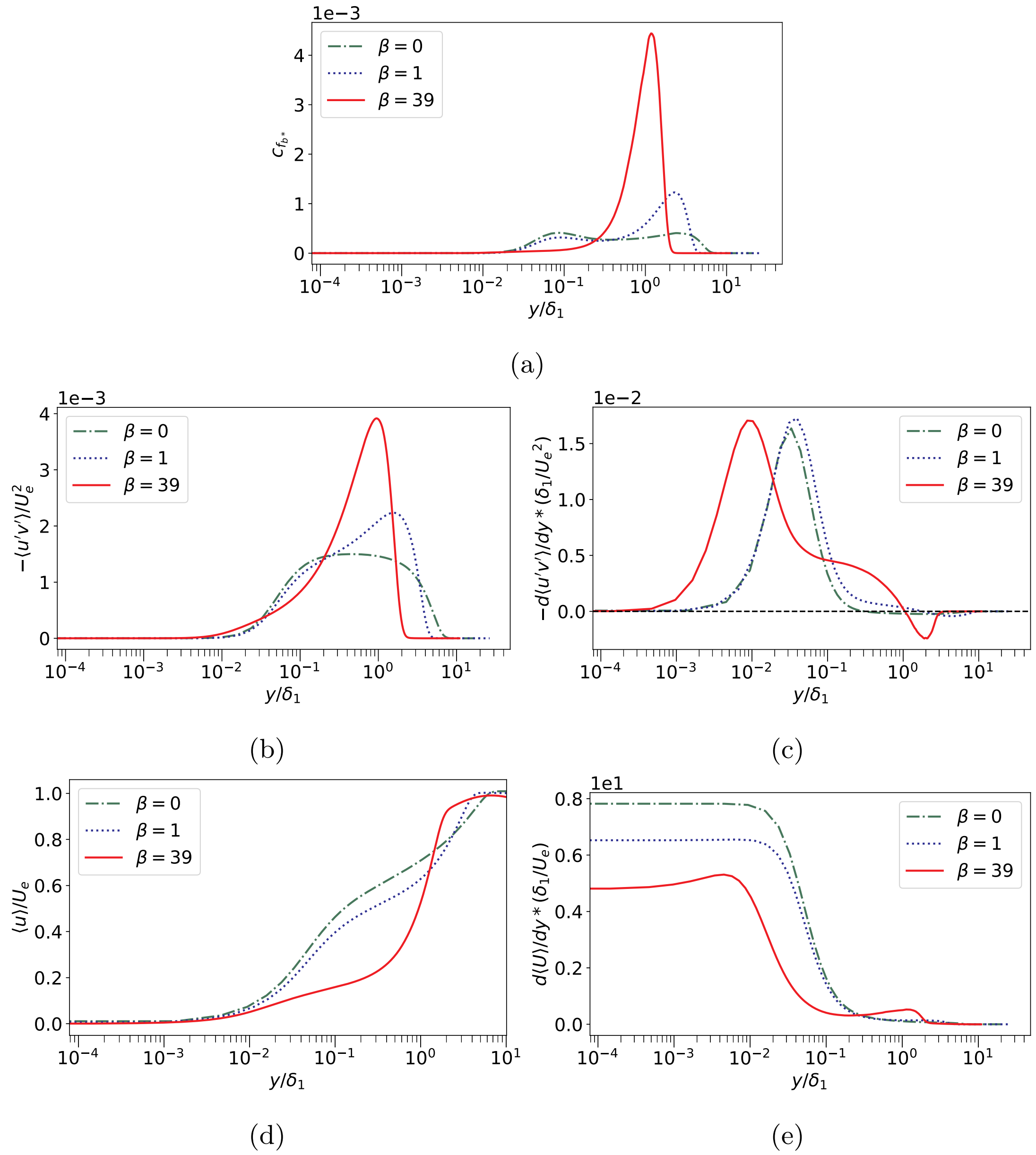

Fig. 8. Variation of the (a) premultiplied integrand c_{fb^*}, (b) reynolds shear stress ($\langle u'v'\rangle$), (c) wall-normal gradient of $-\langle u'v'\rangle$, (d) mean streamwise velocity ($\langle u\rangle$), and (e) wall-normal gradient of $\langle u\rangle$ with β. The profiles are averaged in streamwise direction within DoI and are non-dimensionalised by δ_1.

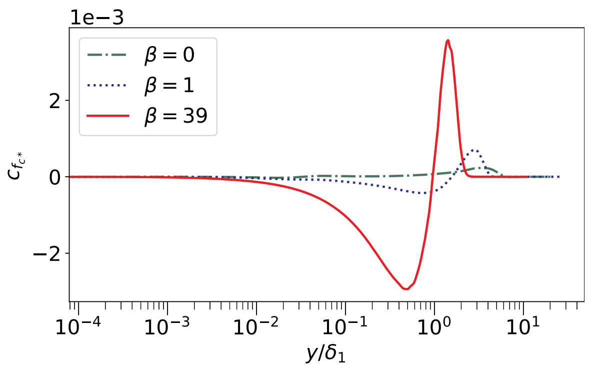

Fig. 9. Variation of the premultiplied integrand c_{fc^*} with β. The profiles are averaged in streamwise direction within DoI and are non-dimensionalised by δ_1.

to the skin friction coefficient has a positive inner and outer peak. For the $\beta = 1$ case, the inner peak decreases and the outer peak increases. The behaviour of $c_{f_{RD_*}}$ is same as c_{fb^*} for the ZPG and the $\beta = 1$ cases. For the $\beta = 39$ case, it has negative peak in the inner region similar to c_{fc^*} and it is because of the contribution from the pressure gradient. The major contribution to the total $C_{f_{RD}}$ is from the dominant positive outer peak in the strong APG case. However, the net effect of the negative and the positive peaks of $c_{f_{RD_*}}$ makes the total $C_{f_{RD}}$ almost insignificant for the $\beta = 39$ case and so $C_{f_{RD}}$ approaches zero. For all the three pressure gradient cases, the premultiplied integrands c_{fa^*}, c_{fb^*}, c_{fc^*}, and $c_{f_{RD_*}}$ in viscous units are given in Appendix B.

6. Relationship between C_{fc} and the pressure gradient

The C_{fc} term in Eq. 7, given by

$$C_{f_c} = \frac{2}{U_e^3}\int_0^\infty (\langle u\rangle - U_e)\frac{\partial}{\partial y}\left(\frac{\tau}{\rho}\right) dy, \tag{14}$$

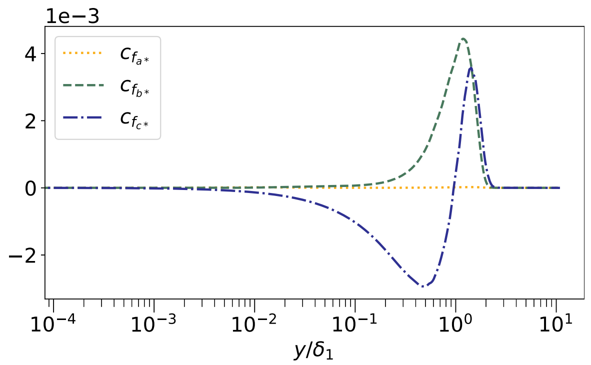

Fig. 10. Comparison of the premultiplied integrands c_{fa^*}, c_{fb^*}, and c_{fc^*} for $\beta = 39$ case. The profiles are averaged in streamwise direction within DoI and are non-dimensionalised by δ_1.

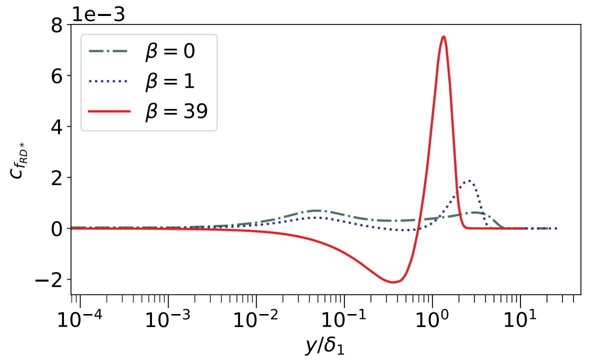

Fig. 11. Variation of the total premultiplied integrand $c_{f_{RD_*}}$ with β. The profiles are averaged in streamwise direction within DoI and are non-dimensionalised by δ_1.

can be related to the streamwise pressure gradient ($\partial\langle P\rangle/\partial x$) using the mean streamwise momentum equation as follows. The wall-normal gradient of the total shear stress in Eq. 14 is related to the streamwise pressure gradient and the inhomogeneous terms ($\overline{I_x}$) via

$$\frac{\partial}{\partial y}\left(\frac{\tau}{\rho}\right) = \frac{1}{\rho}\frac{\partial\langle P\rangle}{\partial x} + \overline{I_x}, \tag{15}$$

where

$$\overline{I_x} = \frac{\partial\langle u\rangle^2}{\partial x} + \frac{\partial(\langle u\rangle\langle v\rangle)}{\partial y} - \nu\frac{\partial^2\langle u\rangle}{\partial x^2} + \frac{\partial\langle u'u'\rangle}{\partial x}. \tag{16}$$

The term C_{fc} can therefore be decomposed into five components which are defined as

$$C_{f\,1c} = \frac{2}{U_e^3}\int_0^\infty(\langle u\rangle - U_e)\frac{1}{\rho}\frac{\partial\langle P\rangle}{\partial x}\,dy, \tag{17}$$

$$C_{f\,2c} = \frac{2}{U_e^3}\int_0^\infty(\langle u\rangle - U_e)\frac{\partial\langle u\rangle^2}{\partial x}\,dy, \tag{18}$$

$$C_{f\,3c} = \frac{2}{U_e^3}\int_0^\infty(\langle u\rangle - U_e)\frac{\partial(\langle u\rangle\langle v\rangle)}{\partial y}\,dy, \tag{19}$$

$$C_{f\,4c} = -\frac{2}{U_e^3}\int_0^\infty(\langle u\rangle - U_e)\nu\frac{\partial^2\langle u\rangle}{\partial x^2}\,dy, \tag{20}$$

and

$$C_{f\,5c} = \frac{2}{U_e^3}\int_0^\infty(\langle u\rangle - U_e)\frac{\partial\langle u'u'\rangle}{\partial x}\,dy. \tag{21}$$

C_{f1c} is the pressure gradient term. C_{f2c} and C_{f3c} are the convective terms. C_{f4c} is the viscous diffusion term and C_{f5c} is the Reynolds stress term.

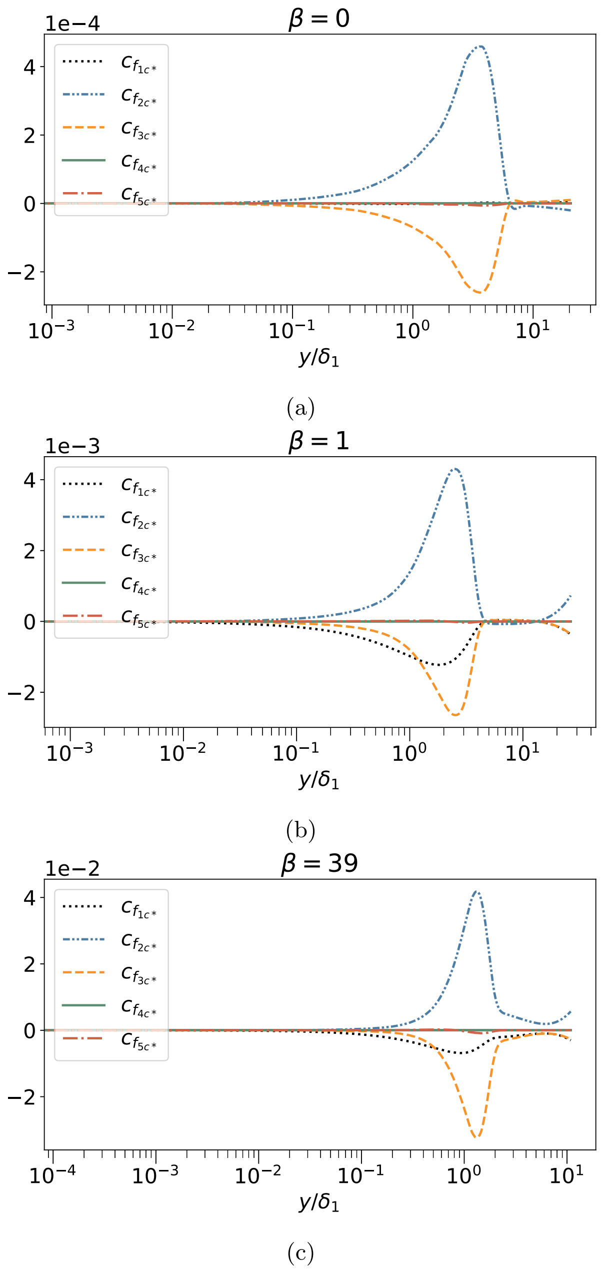

Fig. 12. The premultiplied integrands of the components of C_{fc} for (a) ZPG, (b) mild APG, and (c) strong APG. The profiles are averaged in streamwise direction within DoI and are non-dimensionalised by δ_1.

Variation of the premultiplied integrands of the five components of C_{fc} with β for the three cases is given in Fig. 12. c_{f4c^*} and c_{f5c^*} are negligible for the three pressure gradient cases and in line with the boundary layer hypothesis. The convective terms (c_{f2c^*} and c_{f3c^*}) have peaks of opposite signs in the outer region for all the three cases, which grow in magnitude with increasing pressure gradient. When compared to the contribution of c_{f1c^*}, the cumulative contribution of these peaks becomes less significant as they almost cancel each other out with increasing pressure gradient. As the pressure gradient increases, C_{f1c} becomes the major contributor and hence, C_{fc} can be seen as the representation of the pressure gradient contribution in $C_{f_{RD}}$. The magnitude of c_{f1c^*} increases by around two orders of magnitude from the ZPG case (Fig. 12a) to the strong APG case (Fig. 12c). For the strong APG case, the peak of the pressure gradient term (c_{f1c^*}), and the peaks of the convective terms are located around the displacement thickness height ($y = \delta_1$). The wall-normal distribution of the five premultiplied integrands c_{f1c^*}, c_{f2c^*}, c_{f3c^*}, c_{f4c^*}, and c_{f5c^*} in viscous units are shown in Appendix B for the three pressure gradient cases.

7. Effects of varying the limits of integration

In boundary layer flows, the extent of the flow domain in the wall-normal direction is $0 < y < \infty$. However, in most practical cases, it is difficult to get data points close to the wall in the viscous sublayer ($y^+ < 5$) and the outer boundary conditions are not clearly defined. Hence, it is important to consider the error associated with the computed skin friction coefficient due to lack of reliable data either close to the wall or far from the wall by varying one of the integration limits of the RD identity to an arbitrary value while keeping the other fixed.

$\zeta(y_u)$ is defined as

$$\zeta(y_u) = \underbrace{\frac{2}{U_e^3}\int_0^{y_u} \nu\left(\frac{\partial\langle u\rangle}{\partial y}\right)^2 dy}_{\zeta_a(y_u)} + \underbrace{\frac{2}{U_e^3}\int_0^{y_u} -\langle u'v'\rangle\frac{\partial\langle u\rangle}{\partial y}dy}_{\zeta_b(y_u)} + \underbrace{\frac{2}{U_e^3}\int_0^{y_u} (\langle u\rangle - U_e)\frac{\partial}{\partial y}\left(\frac{\tau}{\rho}\right)dy}_{\zeta_c(y_u)}, \tag{22}$$

which represents the sum of the three terms of the RD identity integrated from the wall to an arbitrary upper limit (y_u). Fig. 13 shows the percentage error of the computed skin friction coefficient ($\zeta(y_u)$), relative to C_{f_w}, for the three pressure gradient cases. For the ZPG case, it is observed that the error approaches zero around the height of $y_u = 6\delta_1$ while, for the $\beta = 39$ case, it is close to $y_u = 3\delta_1$. Therefore, with the increase of the pressure gradient, $c_{f_{RD_*}}$ converges quicker for smaller y_u and the skin friction coefficient is recovered at a lower height in the wall-normal direction.

Analogous to $\zeta(y_u)$, $\zeta(y_l)$ is defined as

$$\zeta(y_l) = \underbrace{\frac{2}{U_e^3}\int_{y_l}^{\infty} \nu\left(\frac{\partial\langle u\rangle}{\partial y}\right)^2 dy}_{\zeta_a(y_l)} + \underbrace{\frac{2}{U_e^3}\int_{y_l}^{\infty} -\langle u'v'\rangle\frac{\partial\langle u\rangle}{\partial y}dy}_{\zeta_b(y_l)} + \underbrace{\frac{2}{U_e^3}\int_{y_l}^{\infty} (\langle u\rangle - U_e)\frac{\partial}{\partial y}\left(\frac{\tau}{\rho}\right)dy}_{\zeta_c(y_l)}, \tag{23}$$

which represents the sum of the terms of the RD identity integrated from an arbitrary lower limit (y_l) to infinity. Fig. 14 shows the percentage error of the computed skin friction coefficient ($\zeta(y_l)$), relative to C_{f_w}, for the three cases of β. For the ZPG case, when $y_l^+ \in [0, 3]$, the percentage error varies from 0 to 10%. As the pressure gradient increases, specifically for the strong APG case, the error diverges much quicker in the viscous sublayer and the 10% error occurs around a lower height of $y_l^+ = 1$ or $y_l/\delta_1 = 3 \times 10^{-3}$.

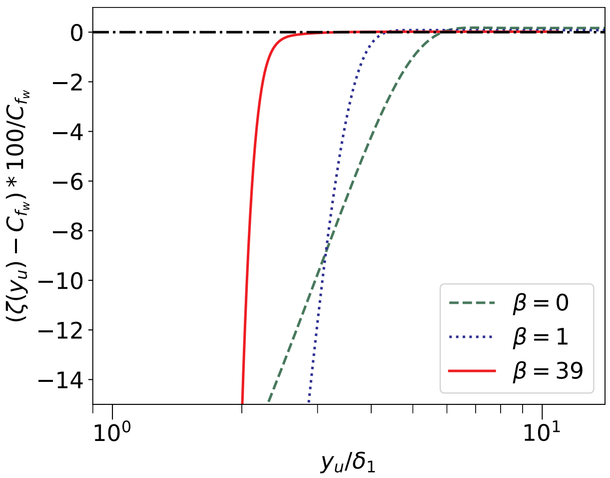

Fig. 13. Variation of the percentage error of $\zeta(y_u)$, relative to C_{f_w}, with β. The terms are integrated from the wall to an arbitrary height (y_u). The profiles are averaged in streamwise direction within DoI and are non-dimensionalised by δ_1.

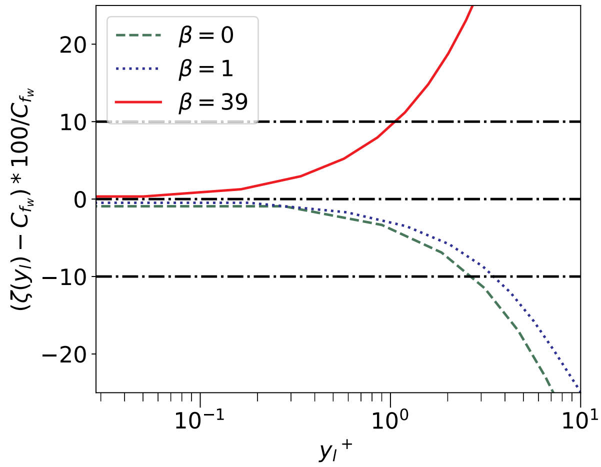

Fig. 14. Variation of the percentage error of $\zeta(y_l)$, relative to C_{f_w}, with β. The terms are integrated from an arbitrary height (y_l) to infinity. The profiles are averaged in streamwise direction within DoI and are non-dimensionalised by δ_1.

Fig. 15 shows the percentage of the components of $\zeta(y_u)$, relative to C_{f_w}, for all the pressure gradient cases. Fig. 15a shows that, for the ZPG case, the predominant contribution to C_{f_w} is from $\zeta_a(y_u)$ (viscous contribution) in the viscous sublayer while the contribution from $\zeta_b(y_u)$ and $\zeta_c(y_u)$ are negligible. $\zeta_a(y_u)$ accounts for around 10% contribution to C_{f_w} when $y_u^+ = 3$. However, for the strong APG case in Fig. 15c, the primary contribution to C_{f_w} is from $\zeta_c(y_u)$ (pressure gradient contribution) in the viscous sublayer. $\zeta_c(y_u)$ accounts for around 10% contribution to C_{f_w} when $y_u^+ = 1$. For the strong APG case, the effect of pressure gradient is felt till the wall.

This analysis shows that if the viscous sublayer is not included to compute the integrals of the RD identity, the percentage error of the computed skin friction coefficient ($\zeta(y_l)$) is over 10% for all the cases. Hence, it is important to get data points in the viscous sublayer for all the pressure gradient cases when employing the RD identity to compute the skin friction coefficient. For the ZPG case, the predominant contribution in the viscous sublayer is from the viscous term while for the flow at the verge of separation, it is from the pressure gradient term.

8. Comparison with the FIK identity

Fukagata et al. (2002) also proposed a decomposition for the skin friction coefficient ($C_{f_{FIK}}$), known as the FIK identity, given by

$$C_{f_{FIK}} = \underbrace{\frac{4(1-\delta_1/\delta_\Omega)}{Re_{\delta 1}}}_{c_{f_1}} + \underbrace{4\int_0^1 \frac{\langle -u'v'\rangle}{U_e^2}\left(1-\frac{y}{\delta_\Omega}\right)d\left(\frac{y}{\delta_\Omega}\right)}_{c_{f_2}} + \underbrace{2\int_0^1 -\left(1-\frac{y}{\delta_\Omega}\right)^2\left(\frac{1}{\rho}\frac{\partial\langle P\rangle}{\partial x} + \overline{I_x} + \frac{\partial\langle u\rangle}{\partial t}\right)\frac{\delta_\Omega}{U_e^2}\,d\left(\frac{y}{\delta_\Omega}\right)}_{c_{f_3}}, \tag{24}$$

where δ_Ω is the boundary-layer thickness at which the mean spanwise vorticity ($\langle\Omega_z\rangle$) is 0.2% of the mean vorticity at the wall, with $\overline{I_x}$ defined by Eq. 16.

It is important to compare the RD identity with the FIK identity as the latter has been used extensively in the previous studies and various

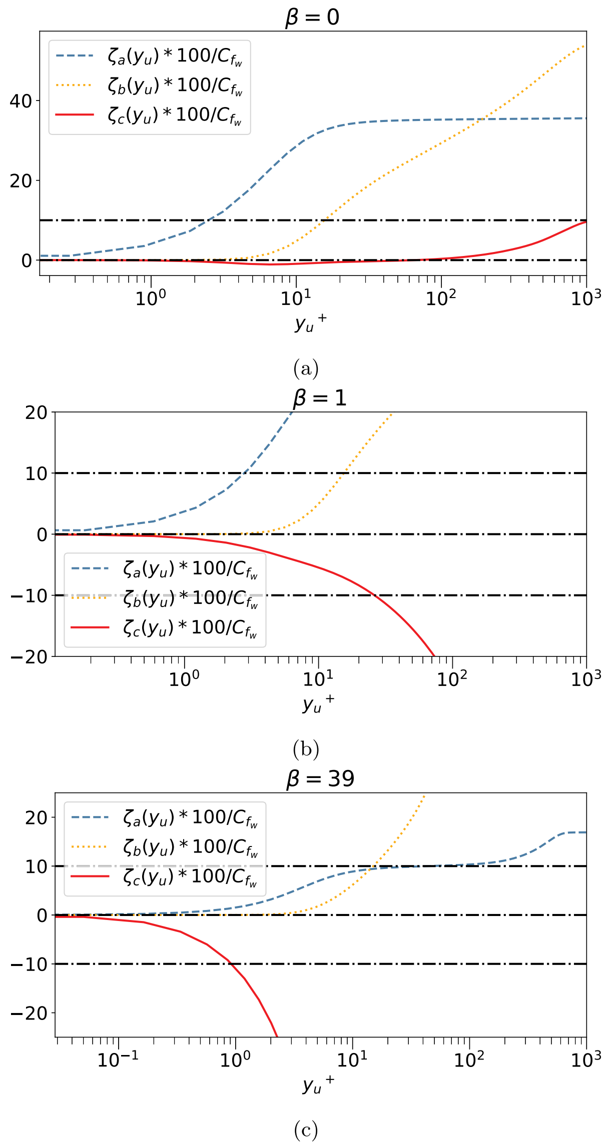

Fig. 15. The percentage of the components of $\zeta(y_u)$, relative to C_{f_w}, for (a) ZPG, (b) mild APG, and (c) strong APG. The terms are integrated from the wall to an arbitrary height (y_u). The profiles are averaged in streamwise direction within DoI and are non-dimensionalised by δ_1.

flow control techniques have also been suggested based on it. The main differences between the FIK identity and the RD formulation are as follows. The FIK identity is based on mean streamwise momentum budget while the RD identity is based on the mean streamwise kinetic energy budget. The FIK analysis is performed from the wall reference frame while the RD decomposition is based on the absolute reference frame. When seen from the absolute reference frame, the moving wall develops non-zero power in the RD identity whereas in the FIK identity, the wall is stationary and doesnâ;;t produce any power. The FIK identity involves three integrations by parts while the RD formulation has only one integration in the wall normal direction.

Moreover, the Reynolds shear stress is weighted by a linear function in the wall normal direction in the FIK identity while the RD identity uses the wall normal gradient of mean streamwise velocity as the weight. The FIK identity considers the turbulent fluctuations only within the conventional boundary layer edge while the RD formulation takes into account the entire boundary layer profile. Even though the values of the Reynolds shear stress $\langle u'v'\rangle$ located above the conventional boundary layer edge are small, it is not logically satisfying to simply disregard their direct contribution as the definition of the boundary layer thickness is arbitrary. It was shown by Renard and Deck (2016) that the suggested flow control techniques for ZPG TBL flows by the FIK identity focuses on the wake region while the RD decomposition emphasis control on the logarithmic layer.

C_{f_1} can be expressed in the integral form as given by

$$C_{f_1} = \frac{4\nu}{\delta_\Omega U_e^2}\int_0^1 \langle u\rangle\, d\left(\frac{y}{\delta_\Omega}\right). \tag{25}$$

In order to compare with the components of $C_{f_{RD}}$, the wall-normal direction in $C_{f_{FIK}}$ can be non-dimensionalized using the displacement thickness (δ_1) which results in Eq. 26. Note that the upper integration limit has become as δ_Ω/δ_1.

$$C_{f_{FIK}} = \underbrace{\int_0^{\frac{\delta_\Omega}{\delta_1}} \frac{4\nu\langle u\rangle}{\delta_\Omega U_e^2}\times\frac{\delta_1}{\delta_\Omega}\, d\left(\frac{y}{\delta_1}\right)}_{C_{f_1}} + \underbrace{\int_0^{\frac{\delta_\Omega}{\delta_1}} \frac{4\langle -u'v'\rangle}{U_e^2}\left(1-\frac{y}{\delta_\Omega}\right)\times\frac{\delta_1}{\delta_\Omega}\, d\left(\frac{y}{\delta_1}\right)}_{C_{f_2}} + \underbrace{\int_0^{\frac{\delta_\Omega}{\delta_1}} -2\left(1-\frac{y}{\delta_\Omega}\right)^2\left(\frac{1}{\rho}\frac{\partial\langle P\rangle}{\partial x}+\overline{I_x}+\frac{\partial\langle u\rangle}{\partial t}\right)\frac{\delta_\Omega}{U_e^2}\times\frac{\delta_1}{\delta_\Omega}\, d\left(\frac{y}{\delta_1}\right)}_{C_{f_3}} \tag{26}$$

Fig. 16 a shows that the contribution from c_{f1^*} is almost zero in the wall-normal direction for all the pressure gradient cases. c_{f2^*} (Fig. 16b), which is the Reynolds shear stress contribution, has a peak in the wake region ($y/\delta_1 > 1$) for the ZPG case. As the pressure gradient increases to $\beta = 1$, the peak continues to grow in the wake region. Whereas, c_{fb^*} in the RD identity, has an inner and a outer peak for the ZPG and the mild APG cases. The linear weight of the Reynolds shear stress in the FIK identity has shifted the peaks to the wake region for the above two cases. As the pressure gradient increases so that the flow is at the verge of separation, the peak of c_{f2^*} increases and moves to a point around the height of the displacement thickness ($y = \delta_1$) which is similar to the behaviour observed in c_{fb^*} of the RD identity.

The overall behaviour of c_{f3^*} is similar to that of c_{fc^*} in Fig. 16c. c_{f3^*} has negligible contribution for the ZPG case. For the $\beta = 1$ case, a negative peak develops around $y = \delta_1$ and a positive peak in the wake region. For the strong APG case, these peaks grow stronger and c_{f3^*} changes sign around the displacement thickness height ($y = \delta_1$).

When the flow reaches the verge of separation, it is observed that the behaviour of c_{f2^*} and c_{f3^*} in the FIK identity matches with the corresponding components of the RD identity. Fig. 17 shows the variation of the total premultiplied integrand $c_{f_{FIK*}}$ with the pressure gradient. Similar to the observation made by Renard and Deck (2016), the peak of $c_{f_{FIK*}}$ is in the wake region for the ZPG case whereas $c_{f_{RD_*}}$ has contribution from almost the entire boundary layer with an inner and a outer peak. For the $\beta = 1$ case, the peak of $c_{f_{FIK*}}$ still grows in the wake region. But, for the $\beta = 39$ case, $c_{f_{FIK*}}$ develops a negative and a positive peak and it changes its sign around an approximate height of displacement thickness ($y = \delta_1$). This behaviour of $c_{f_{FIK*}}$ is similar to that of $c_{f_{RD_*}}$ for the flow at the verge of separation. But, it is also observed that the positive and the negative peak of the skin friction coefficient ($c_{f_{FIK*}}$) in the FIK identity has roughly increased by two orders of magnitude when compared to the corresponding ones in the RD identity ($c_{f_{RD_*}}$).

Even though, the FIK identity and the RD identity suggest different distribution for the Reynolds shear stress contribution in the ZPG and the mild APG cases, both of the decompositions have captured the dominant outer peak contribution around the height of $y = \delta_1$ in the strong APG case.

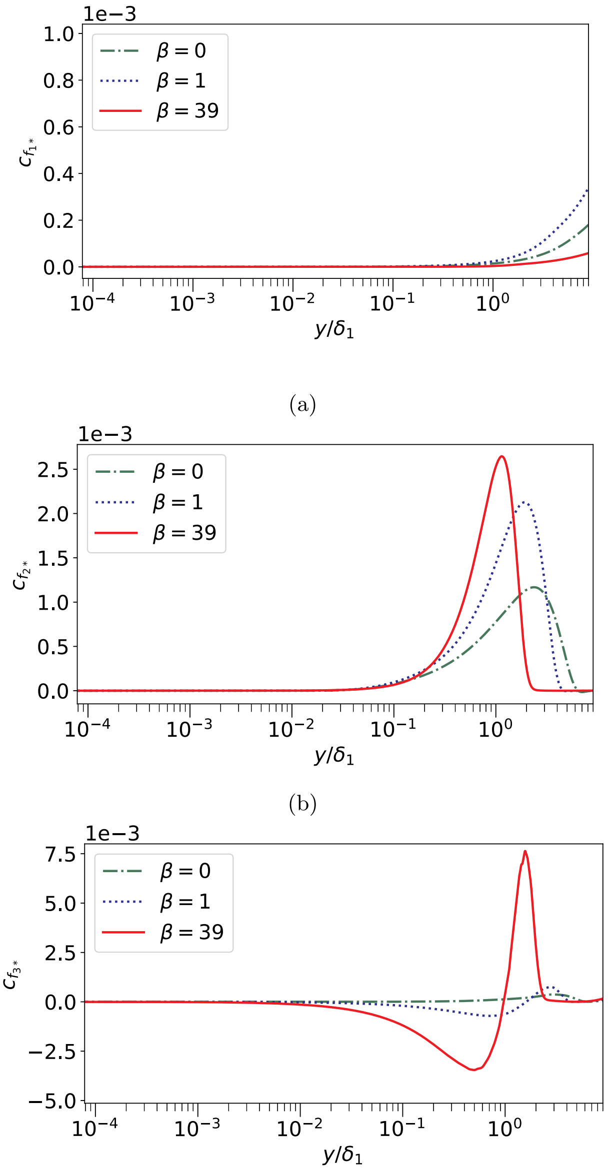

(a)

(b)

(c)

Fig. 16. Variation of the premultiplied integrand (a) c_{f1^*}, (b) c_{f2^*}, and (c) c_{f3^*} with β. The profiles are averaged in streamwise direction within DoI and are non-dimensionalised by δ_1.

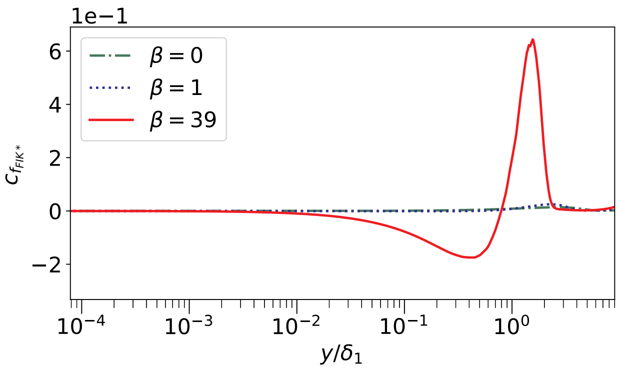

Fig. 17. Variation of the total premultiplied integrand $c_{f_{FIK*}}$ with β. The profiles are averaged in streamwise direction within DoI and are non-dimensionalised by δ_1.

9. Conclusion

As the adverse pressure gradient increases such that the turbulent boundary layer is at the point of verge of separation, the skin friction coefficient ($C_{f_{RD}}$) reduces and approaches zero. This is the result of the more rapid expansion of the boundary layer in the wall-normal direction with increasing pressure gradient. At the verge of separation, the dominant positive contribution to the total skin friction ($c_{f_{RD_*}}$) is from the outer peak while its contribution is diminished by the negative peak and hence, the total skin friction becomes negligible.

All the components of the RD identity are positive for the ZPG case while C_{fc} is negative for the mild and the strong APG cases. As β increases from 0 to 39, the percentage of viscous contribution ($C_{fa}/C_{f_{RD}}$) drops by half and its absolute value (C_{fa}) becomes negligible for the strong APG case. With increasing β, the wall-normal distribution of the viscous contribution becomes more uniform and negligible. Hence, with increasing pressure gradient, the viscous term plays a smaller role.

When β changes from 0 to 39, the relative contribution of the Reynolds shear stress ($C_{fb}/C_{f_{RD}}$) increases by around 21.6 times while its positive contribution is reduced by the negative contribution from C_{fc} for the mild and the strong APG cases. However, the Reynolds shear stress (C_{fb}), remains as the dominant positive contributor to skin friction for all the pressure gradient cases. As the pressure gradient increases, the Reynolds shear stress contribution develops an outer peak which is dominant in the strong APG case and is located around the displacement thickness height ($y = \delta_1$). For the strong APG case, it is observed that the peak of the Reynolds shear stress, the peak of the premultiplied integrand c_{fb^*} (Reynolds shear stress contribution), the negative peak of the pressure gradient premultiplied integrand (c_{f1c^*}), the inflection point of the mean streamwise velocity and the point where the premultiplied integrand c_{fc^*} changes sign coincide around the displacement thickness height (y = δ_1). This shows that the outer layer has a more important role to play in the skin friction contribution with increasing pressure gradient.

The relative significance of the turbulent fluctuations depends on whether its contribution to the mean momentum (FIK identity) is considered or its contribution to the mean kinetic energy (RD identity) is considered. The FIK identity suggests that, for the ZPG and the mild APG cases, the peak contribution of the Reynolds shear stress (c_{f2^*}) is in the wake region, while its contribution is negligible in the inner region. This observation is in contrast to the inner peak identified by the RD identity for the ZPG and the mild APG cases. However, when the flow reaches the verge of separation, in the strong APG case, the outer peak of the Reynolds shear stress contribution in the FIK and the RD identities (c_{f2^*} and c_{fb^*} respectively) coincide at the approximate height of the displacement thickness ($y = \delta_1$). Both the decompositions manage to capture the outer peak of the Reynolds shear stress contribution which again emphasizes the importance of outer layer dynamics with increasing pressure gradient.

CRediT authorship contribution statement

Shevarjun Senthil: Writing - original draft, Conceptualization, Methodology, Software, Validation, Formal analysis, Data curation. **Vassili Kitsios:** Methodology, Software, Data curation, Supervision. **Atsushi Sekimoto:** Methodology, Software, Data curation, Supervision. **Callum Atkinson:** Conceptualization, Funding acquisition, Supervision. **Julio Soria:** Conceptualization, Funding acquisition, Data curation, Supervision, Project administration.

Declaration of Competing Interest

None.

Acknowledgements

The authors would like to acknowledge the research funding from the

Australian Government through the Australian Research Council. This work was supported by the computational resources provided by the Pawsey Supercomputing Centre, the National Computational Infrastructure (NCI) and the Multi-modal Australian ScienceS Imaging and Visualisation Environment (MASSIVE) through the National Computational Merit Allocation Scheme (NCMAS) funded by the Australian Government. Julio Soria gratefully acknowledges the support of an Australian Research Council Discovery Outstanding Researcher Award fellowship and Callum Atkinson the support of an Australian Research Council Discovery Early Career Researcher Award.

Appendix A. Skin friction coefficient as a function of Reynolds number based on momentum thickness

The skin friction coefficient is given as a function of Reynolds number based on momentum thickness ($Re_{\delta 2}$) in Fig. A.18. $C_{f_{RD}}$ and C_{f_w} are in close agreement with each other as expected. The skin friction coefficient keeps decreasing with the increase of the pressure gradient.

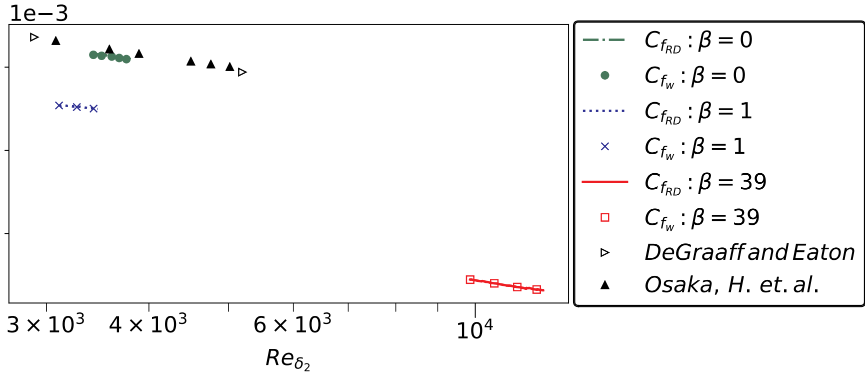

Fig. A.18. Dependence of $C_{f_{RD}}$ and C_{f_w} on β and the Reynolds number based on momentum thickness ($Re_{\delta 2}$) in the respective DoI. De Graaff and Eaton (2000) and Osaka et al. (1998) - black triangles.

Appendix B. Premultiplied integrands of the components of $C_{f_{RD}}$ in viscous units

The premultiplied integrand of each of the components of $C_{f_{RD}}$ and the total premultiplied integrand $c_{f_{RD_*}}$ in viscous units are shown in Fig. B.19 for all the three pressure gradient cases. Similarly, the premultiplied integrand of the five components of C_{fc} in viscous units are illustrated in Fig. B.20.

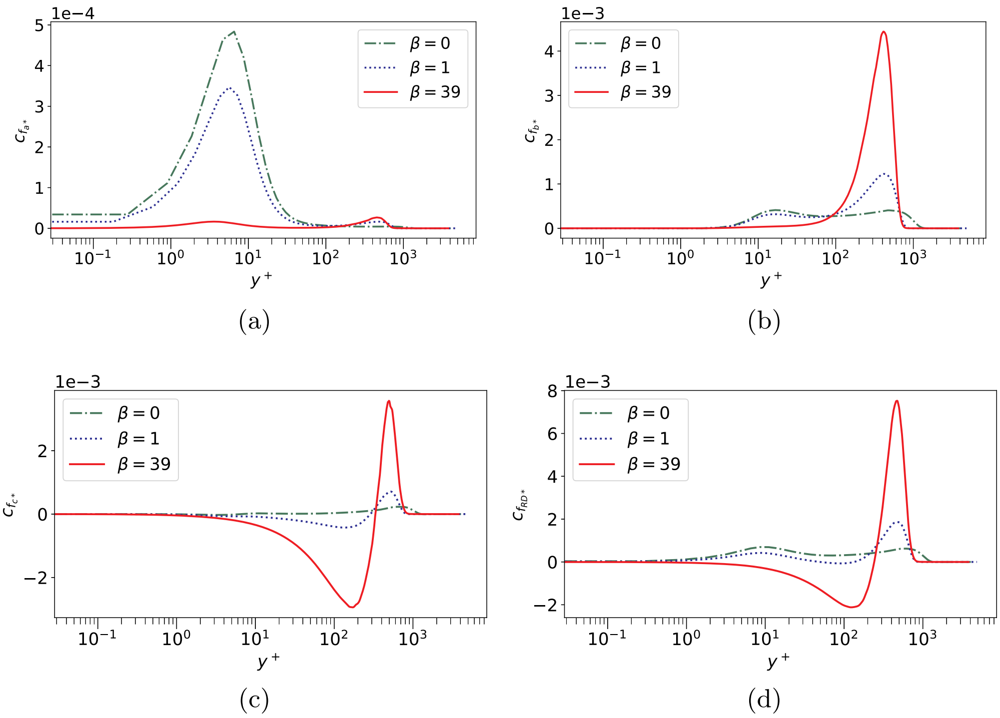

Fig. B.19. Variation of (a) c_{fa^*}, (b) c_{fb^*}, (c) c_{fc^*}, and (d) the total premultiplied integrand $c_{f_{RD_*}}$ with β in viscous units. The profiles are averaged in streamwise direction within DoI.

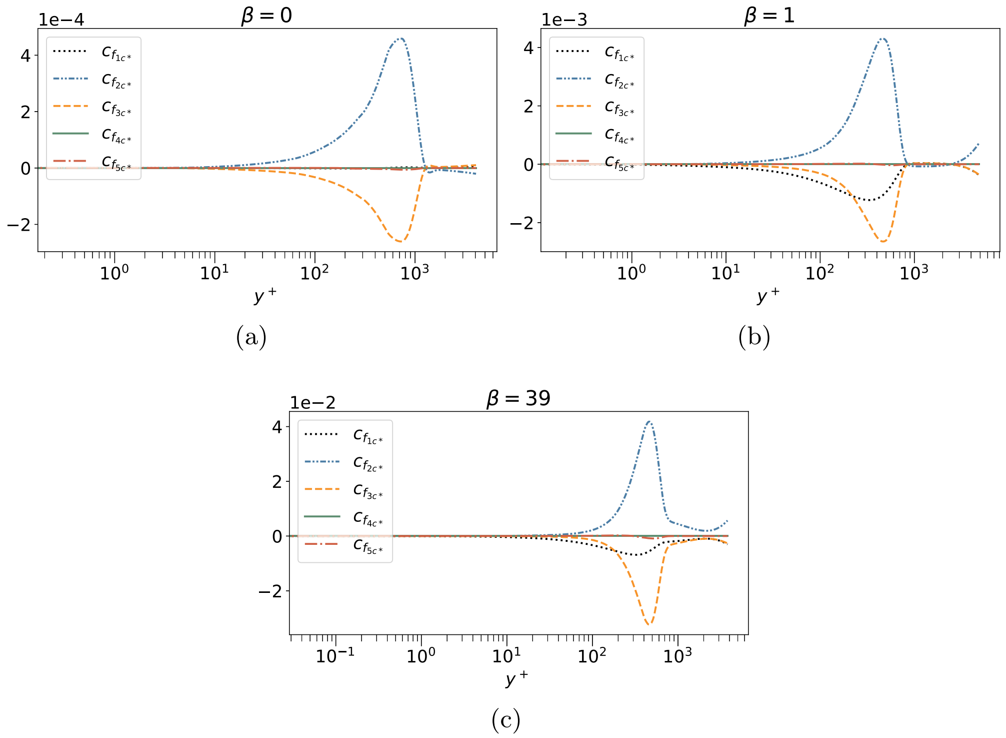

Fig. B.20. The premultiplied integrands of the components of C_{fc} for (a) ZPG, (b) mild APG, and (c) strong APG in viscous units. The profiles are averaged in streamwise direction within DoI.

References

Borrell, G., Sillero, J.A., Jiménez, J., 2013. A code for direct numerical simulation of turbulent boundary layers at high reynolds numbers in bg/p supercomputers. Comput. Fluids 80, 37–43.

Clauser, F.H., 1954. Turbulent boundary layers in adverse pressure gradients. J. Aeronautical Sci. 21 (2), 91–108.

De Graaff, D.B., Eaton, J.K., 2000. Reynolds-number scaling of the flat-plate turbulent boundary layer. J. Fluid Mech. 422, 319–346.

Deck, S., Renard, N., Laraufie, R., Weiss, P.-É., 2014. Large-scale contribution to mean wall shear stress in high-Reynolds-number flat-plate boundary layers up to 13650. J. Fluid Mech. 743, 202–248.

Fukagata, K., Iwamoto, K., Kasagi, N., 2002. Contribution of reynolds stress distribution to the skin friction in wall-bounded flows. Phys. Fluids 14 (11), L73–L76.

Harlow, F.H., Welch, J.E., 1965. Numerical calculation of time-dependent viscous incompressible flow of fluid with free surface. Phys. Fluids 8 (12), 2182–2189.

Kitsios, V., Atkinson, C., Sillero, J.A., Borrell, G., Gungor, A.G., Jiménez, J., Soria, J., 2016. Direct numerical simulation of a self-similar adverse pressure gradient turbulent boundary layer. Int. J. Heat Fluid Flow 61, 129–136.

Kitsios, V., Sekimoto, A., Atkinson, C., Sillero, J.A., Borrell, G., Gungor, A.G., Jiménez, J., Soria, J., 2017. Direct numerical simulation of a self-similar adverse pressure gradient turbulent boundary layer at the verge of separation. J. Fluid Mech. 829, 392–419.

Lele, S.K., 1992. Compact finite difference schemes with spectral-like resolution. J Comput Phys 103 (1), 16–42.

Lighthill, M.J., 1963. Introduction. Boundary layer theory. In: Rosenhead, L. (Ed.), Laminar boundary layers. Oxford University Press.

Mehdi, F., Johansson, T.G., White, C.M., Naughton, J.W., 2014. On determining wall shear stress in spatially developing two-dimensional wall-bounded flows. Exp. Fluids 55 (1), 1656.

Mehdi, F., White, C.M., 2011. Integral form of the skin friction coefficient suitable for experimental data. Exp. Fluids 50 (1), 43–51.

Orlandi, P., Jiménez, J., 1994. On the generation of turbulent wall friction. Phys. Fluids 6 (2), 634–641.

Osaka, H., Kameda, T., Mochizuki, S., 1998. Re-examination of the reynolds-number-effect on the mean flow quantities in a smooth wall turbulent boundary layer. JSME Int. J. Series B FluidsThermal Eng. 41 (1), 123–129.

Perot, J.B., 1993. An analysis of the fractional step method. J Comput Phys 108 (1), 51–58.

Pope, S.B., 2000. Turbulent Flows. Cambridge University Press, Cambridge. https://doi.org/10.1017/CBO9780511840531.

Renard, N., Deck, S., 2016. A theoretical decomposition of mean skin friction generation into physical phenomena across the boundary layer. J. Fluid Mech. 790, 339–367.

Sillero, J.A., 2014. High Reynolds number turbulent boundary layers. Universidad Politénica de Madrid Ph.D. thesis.

Simens, M.P., 2008. The study and control of wall bounded flows. Universidad Politénica de Madrid Ph.D. thesis.

Simens, M.P., Jiménez, J., Hoyas, S., Mizuno, Y., 2009. A high-resolution code for turbulent boundary layers. J. Comput. Phys. 228 (11), 4218–4231.

Skåre, P.E., Krogstad, P.-Å., 1994. A turbulent equilibrium boundary layer near separation. J. Fluid Mech. 272, 319–348.

Soria, J., Atkinson, C., Kitsios, V., Sekimoto, A., Senthil, S., Jimenez, J., 2019. Statistics of Beta = 0, 1, 39 Turbulent Boundary Layer DNS, URL: https://monash.figshare.com/articles/Statistics_of_Beta_0_1_39_Turbulent_Boundary_Layer_DNS/8790785. doi:10.26180/5d1f2b59e66ea.

Spalart, P.R., Watmuff, J.H., 1993. Experimental and numerical study of a turbulent boundary layer with pressure gradients. J. Fluid Mech. 249, 337–371.

I learned that courage was not the absence of fear, but the triumph over it. The brave man is not he who does not feel afraid, but he who conquers that fear.

–Nelson Mandela

Chapter 5

Analysis of the contribution of the velocity-vorticity correlations to the skin friction

5.1 Introduction

In wall-bounded flows, it is important to detect and characterise the vortical structures to understand their complex three-dimensional motions and their ability to transport momentum across the mean flow (Robinson, 1991; Klewicki, 1989; Klewicki et al., 1994). Quasi-streamwise vortices cause the low momentum fluid to lift up from the wall resulting in the formation of the near-wall low-speed streaks (Kline et al., 1967; Adrian et al., 2000). Kim (2011) showed that the near-wall streamwise vortical structures, which are regenerated autonomously by a self-sustaining process, are primarily related to the skin friction drag in the wall-bounded flows. It is observed in recent experiments and numerical studies that numerous hairpin vortical structures travel at a similar convective velocity. These vortical structures align in the streamwise direction into packets resulting in the formation of large-scale motions (Adrian, 2007; Smits et al., 2011). Therefore, it is important to quantify the contributions of the vortical motions to the wall shear in turbulent flows.

As discussed in chapter 4, the contribution of the Reynolds shear stress to the skin friction increases with the pressure gradient and its contribution remains as the dominant positive contributor for all the pressure gradient cases. In this chapter, the contribution of the velocity-vorticity correlations to the skin friction and their variation with the pressure gradient are analysed using the skin friction decomposition given by Yoon et al. (2016) (YAHS identity). In incompressible TBL flows, turbulent mixing and momentum transfer are related to the gradient of the Reynolds shear stress $\langle u'v' \rangle$. Therefore, it is important to investigate the contribution of the velocity-vorticity correlations as they can be related to the gradients of the Reynolds stresses (Hinze, 1975; Klewicki, 1989). This chapter is organised as follows. In section 5.2, the variation of the components of the YAHS identity with the pressure gradient is discussed. In section 5.3, the relationship between the velocity-vorticity correlations and the Reynolds stress gradients are investigated with regards to the variation with the pressure gradient. In section 5.4, the wall-normal distribution of the terms in the YAHS identity is analysed. In section 5.5, a new method (based on the decomposition of Renard and Deck (2016)) to compute the contribution of the velocity-vorticity correlations to the skin friction coefficient is discussed.

5.2 Variation of the components of the YAHS identity with pressure gradient

The YAHS identity given in Equation 3.5 has five components. The terms C_{f_1} and C_{f_2} refer to the contribution of the body forces resulting from the advective vorticity transport and the vortex stretching, respectively. The term C_{f_3} refers to the contribution from the molecular diffusion at the wall, whereas the term C_{f_4} represents the contribution of the molecular transfer due to the mean vorticity. The fifth term C_{f_5} corresponds to the contribution of the inhomogeneous effects arising from the spatial development of the flow in the streamwise direction.

The variation of the components of the YAHS identity in Equation 3.5 with the pressure gradient is shown in figure 5.1. The contribution of the molecular transfer due to the mean vorticity (C_{f_4}) is negligible when compared to the other components for all the pressure gradient cases. The advective vorticity transport term (C_{f_1}) reduces the skin friction coefficient by giving a negative contribution irrespective of the pressure gradient in the flow. Whereas, the vortex stretching term (C_{f_2}) gives a positive contribution for all the TBL cases. Similar influence in the contributions of C_{f_1} and C_{f_2} is also observed in channel and pipe flows (Yoon et al., 2016). The term C_{f_1} gives negative contribution for all the pressure gradients because of the negative contribution from the quadrant motions $(+v', -\omega_z')$ and $(-v', +\omega_z')$, where $(+v', -\omega_z')$ represents the lifting motion of hairpin vortices in the outward direction (Klewicki et al., 1994).

The term C_{f_3} is related to the wall-normal gradient of the spanwise vorticity at the wall as shown in Equation 3.5. With increasing pressure gradient, the magnitude of the mean spanwise vorticity at the wall ($\langle\Omega_z\rangle(y=0)$) decreases, while the magnitude of the wall-normal gradient of the spanwise vorticity increases as shown in figures 5.2a and 5.2b respectively. The molecular diffusion at the wall (C_{f_3}) provides a positive contribution

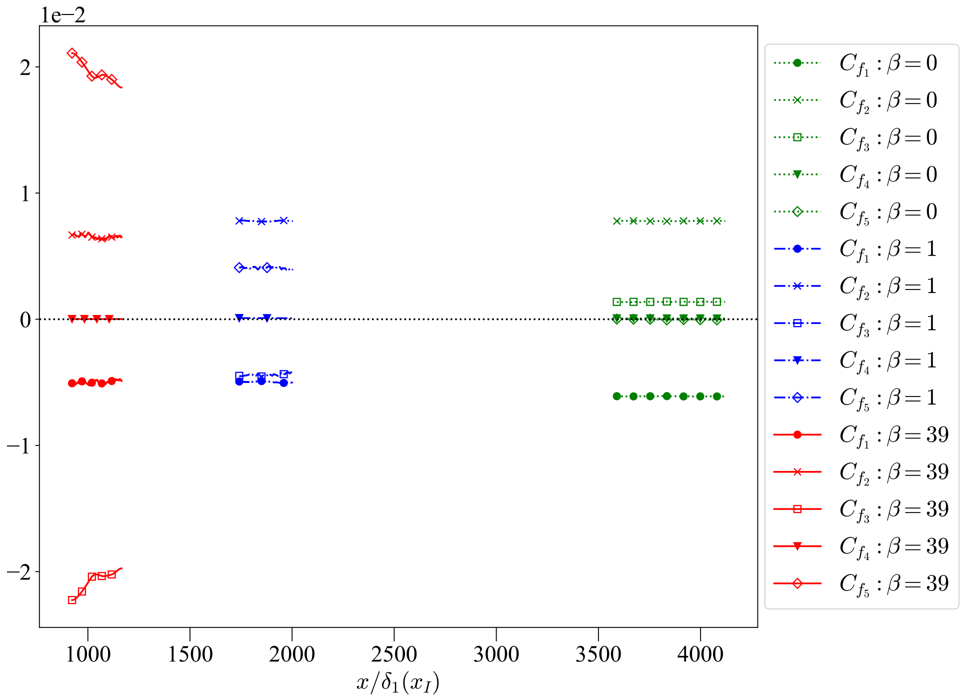

Figure 5.1: Variation of the components of the YAHS identity with β in the respective DoI. x_I is the position of the inlet plane.

to the skin friction coefficient in the case of the ZPG TBL, similar to what is observed in channel and pipe flows (Yoon et al., 2016). However, C_{f_3} reduces the skin friction coefficient for both of the APG TBLs. The wall-normal gradient of the spanwise vorticity is related to $-\partial^2\langle u\rangle/\partial y^2$ and its value is negative at the wall for both the APG TBLs because of the inflection point in the profile of $\langle u\rangle$ in the near wall region as illustrated in figure 2.6a. The profiles of $\partial^2\langle u\rangle/\partial y^2$ for the three TBL cases are shown in figure 2.6c. For the strong APG TBL, as the wall-normal gradient of the spanwise vorticity is significantly higher, the molecular diffusion at the wall (C_{f_3}) becomes a dominant negative contributor in reducing the skin friction coefficient.

The contribution from the streamwise inhomogeneous term (C_{f_5}) increases with the pressure gradient. The terms C_{f_1} and C_{f_2} are dominant contributors in the ZPG and mild APG TBL. However, when the flow reaches the verge of separation in the strong APG TBL, the dominant contributors are the terms C_{f_3} and C_{f_5}. The variation of the proportion of each component in the YAHS identity is shown in figure 5.3. For the strong APG TBL, the proportion of the components are higher than the other two TBLs as the skin friction coefficient decreases with increasing pressure gradient and tends to zero in the strong APG case. Within the DoI, the proportion of the molecular diffusion term (C_{f_3}/C_f) is 0.44 in the ZPG TBL and its magnitude increases by almost 115 times to 50.45 in the strong APG TBL which reduces the overall skin friction when the flow reaches the

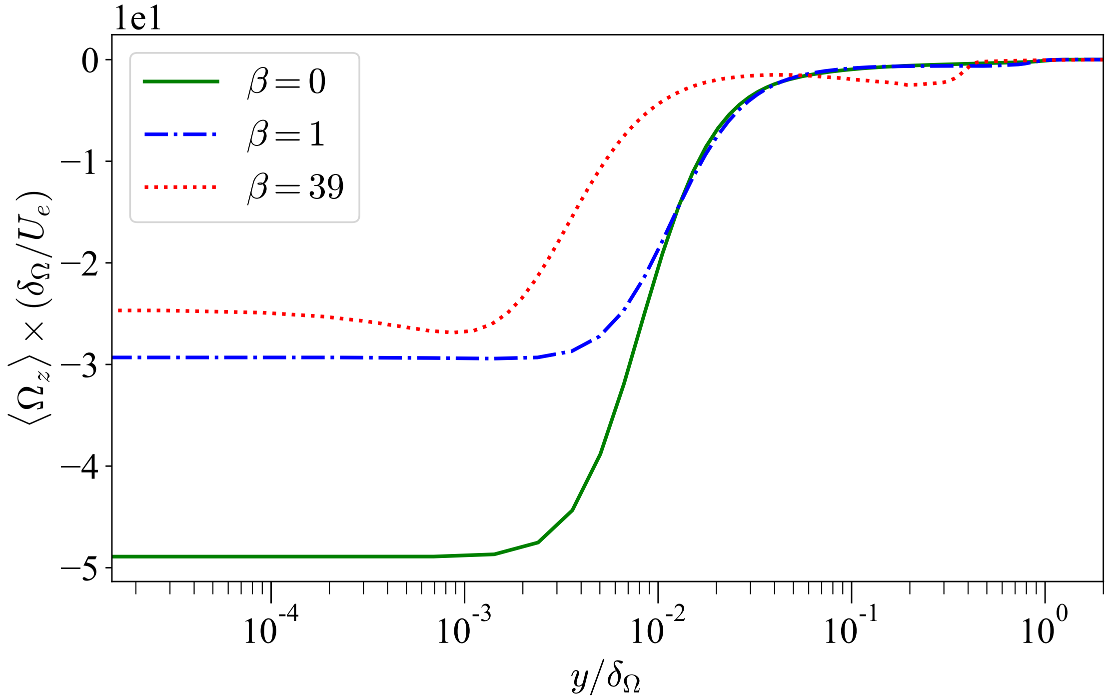

(a)

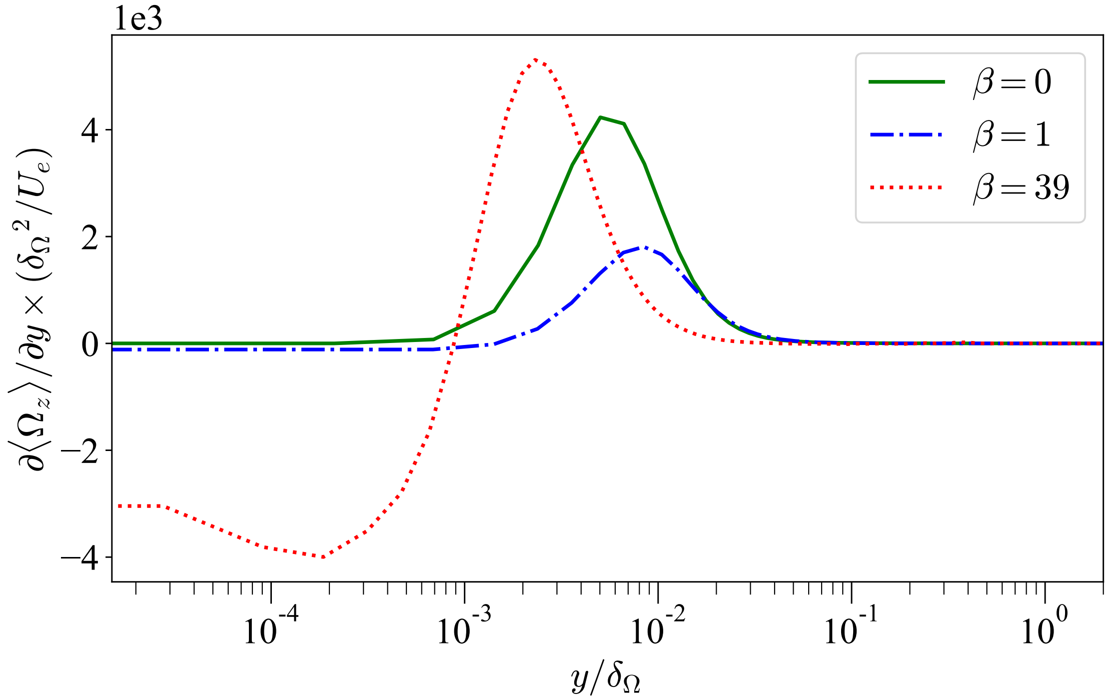

(b)

Figure 5.2: Variation of the (a) mean spanwise vorticity ($\langle \Omega_z \rangle$), and (b) wall-normal gradient of the mean spanwise vorticity with β. The profiles are averaged in streamwise direction within DoI and are non-dimensionalised by δ_Ω and U_e.

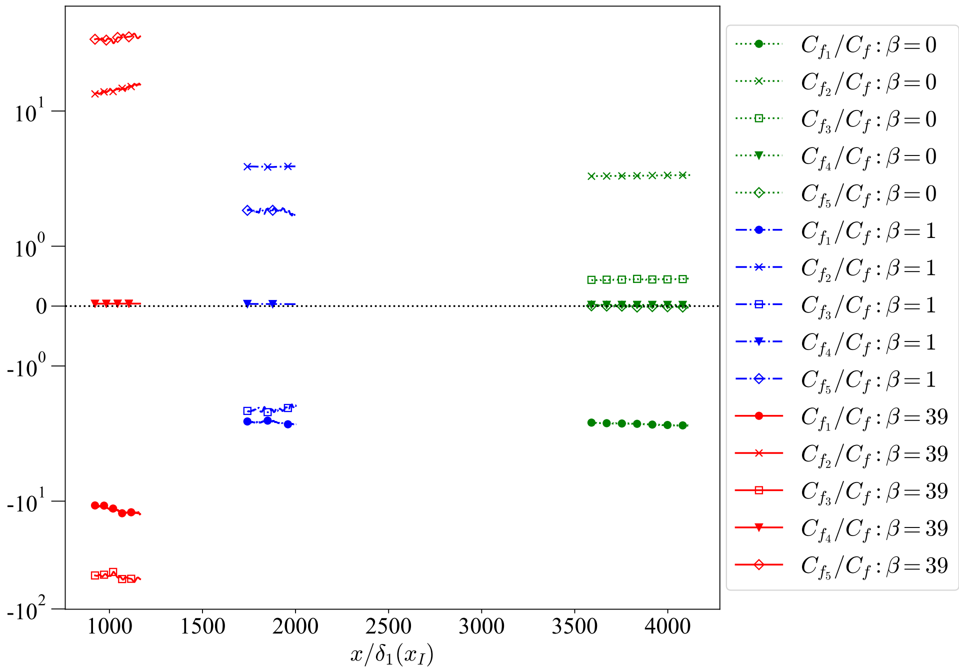

Figure 5.3: Variation of the proportion of the components of the YAHS identity with β in the respective DoI. x_I is the position of the inlet plane.

verge of separation.

5.3 Relationship between the velocity-vorticity correlations and Reynolds stresses

There are four velocity-vorticity correlations in the YAHS identity given in Equation 3.5. The profiles of the velocity-vorticity correlations are shown in figure 5.4 and they are non-dimensionalised by the local values of U_e and δ_Ω. The profiles are streamwise averaged in the scaled coordinates within the DoI. Even though the contribution of the advective vorticity term (C_{f_1}) is negative, the velocity-vorticity correlation $\langle v'\omega_z' \rangle$ has a positive peak for all the pressure gradient cases in the inner region. The inner region is defined as $y/\delta_1 < 10^{-1}$ or $y/\delta_\Omega < 10^{-2}$. The positive values of $\langle v'\omega_z' \rangle$ in near wall region are physically understood as the motion of the sublayer streaks in the outward direction (Klewicki et al., 1994). For the strong APG TBL, the positive peak of $\langle v'\omega_z' \rangle$ moves closer to the wall when compared to the ZPG TBL. In the case of the ZPG TBL, the dominant negative peak is in the outer layer and the peak reduces with increasing pressure gradient. The mild APG TBL develops a second negative peak in the outer region which becomes more pronounced in the strong APG TBL. The outer region is defined as $y/\delta_1 > 10^{-1}$ or $y/\delta_\Omega > 10^{-2}$. As shown in figure 5.4a, the third zero crossing of $\langle v'\omega_z' \rangle$ occurs around the

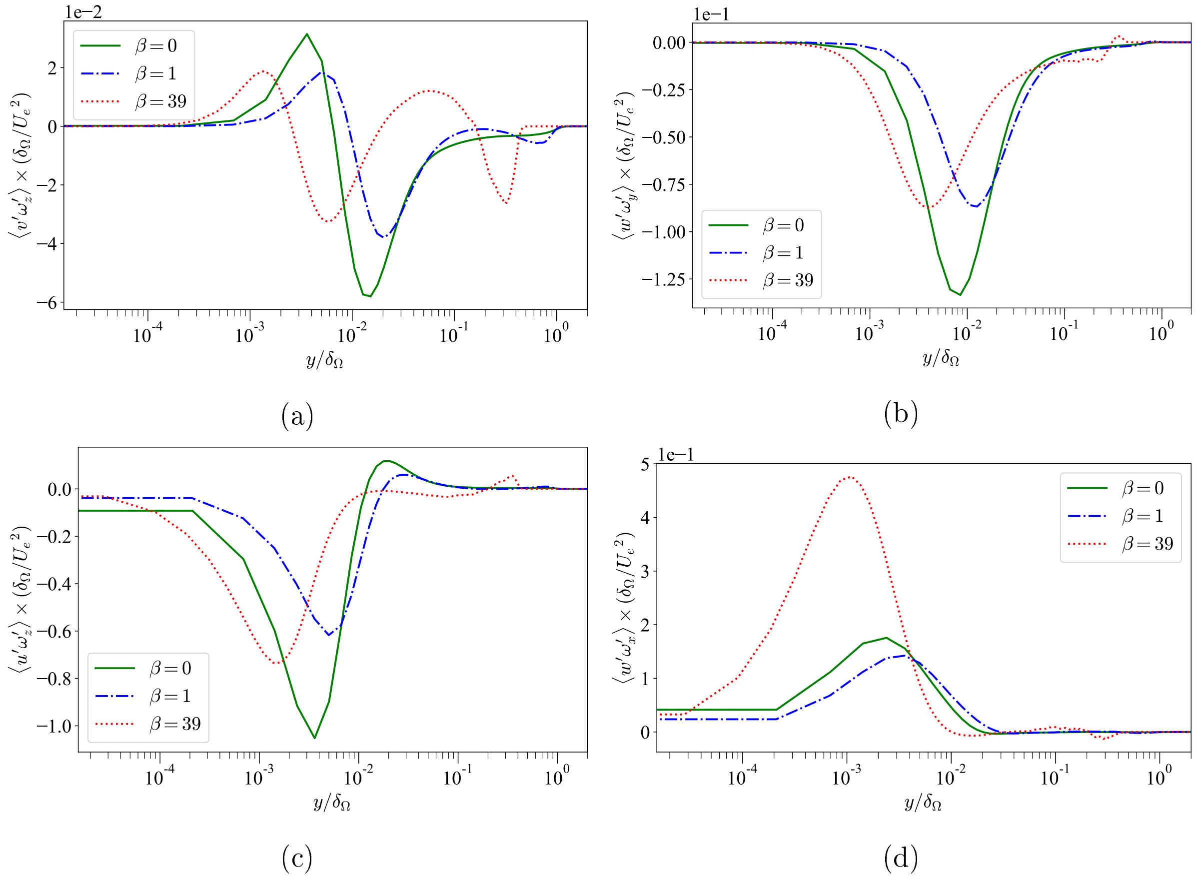

Figure 5.4: Variation of the velocity-vorticity correlations (a) $\langle v'\omega_z'\rangle$, (b) $\langle w'\omega_y'\rangle$, (c) $\langle u'\omega_z'\rangle$, and (d) $\langle w'\omega_x'\rangle$ with β. The profiles are averaged in streamwise direction within DoI and are non-dimensionalised by δ_Ω and U_e.

height of $y/\delta_\Omega = 0.2$ in the outer region, which matches with the position of the outer peak of $\langle u'v'\rangle$ illustrated in figure 2.7d. The second negative peak of $\langle v'\omega_z'\rangle$, which comes after the third zero crossing, is located at the height of $y/\delta_\Omega = 0.3$ and it coincides with the location of the negative outer peak in $-\partial\langle u'v'\rangle/\partial y$ as shown in figure 2.7e. The growth of the outer negative peak in $-\partial\langle u'v'\rangle/\partial y$ with the pressure gradient shows that the outer peak of the Reynolds stress $-\langle u'v'\rangle$ becomes narrower and steeper with increasing pressure gradient as shown in figures 2.7d and 2.7e.

The velocity-vorticity correlation $\langle w'\omega_y'\rangle$ has one dominant negative peak for the ZPG TBL and it has reduced in the strong APG TBL as illustrated in figure 5.4b. The velocity-vorticity correlation $\langle u'\omega_z'\rangle$ has a dominant negative peak and a small outer peak for all the pressure gradient cases as illustrated in figure 5.4c. For the strong APG TBL, both the peaks in $\langle u'\omega_z'\rangle$ have reduced in magnitude when compared to that of the ZPG TBL as shown in figure 5.4c. The velocity-vorticity correlation $\langle w'\omega_x'\rangle$ has one dominant positive peak in the inner region for all the TBLs and in the case of the strong APG TBL, it is located around the height of $y/\delta_\Omega = 10^{-3}$ as illustrated in figure 5.4d.

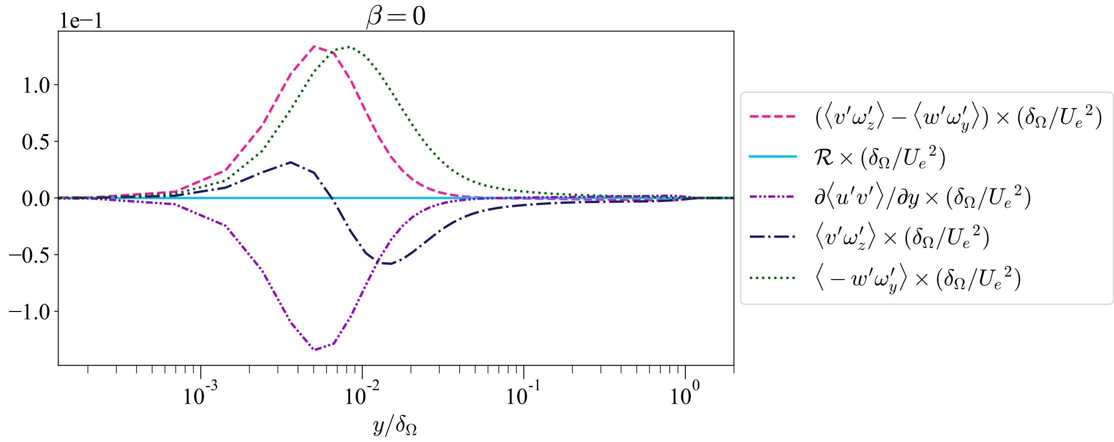

(a)

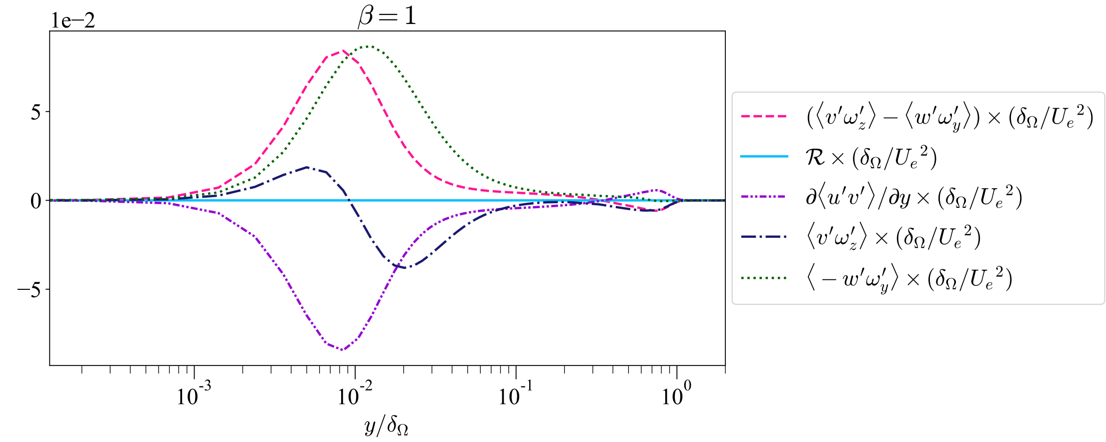

(b)

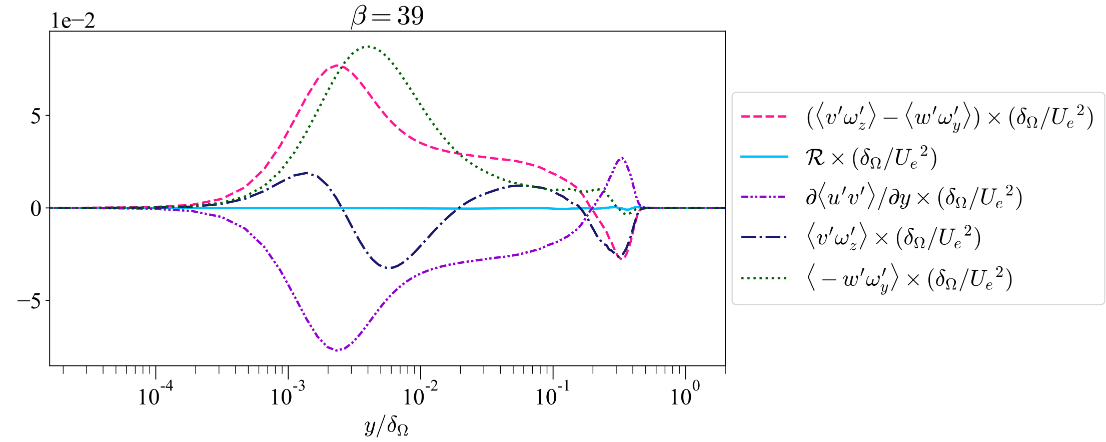

(c)

Figure 5.5: Profiles of the velocity-vorticity correlations ($\langle v'\omega'_z\rangle$ and $-\langle w'\omega'_y\rangle$) and gradients of the corresponding Reynolds stresses in Equation 5.2 for (a) ZPG, (b) mild APG, and (c) strong APG. The profiles are averaged in streamwise direction within DoI and are non-dimensionalised by δ_Ω and U_e.

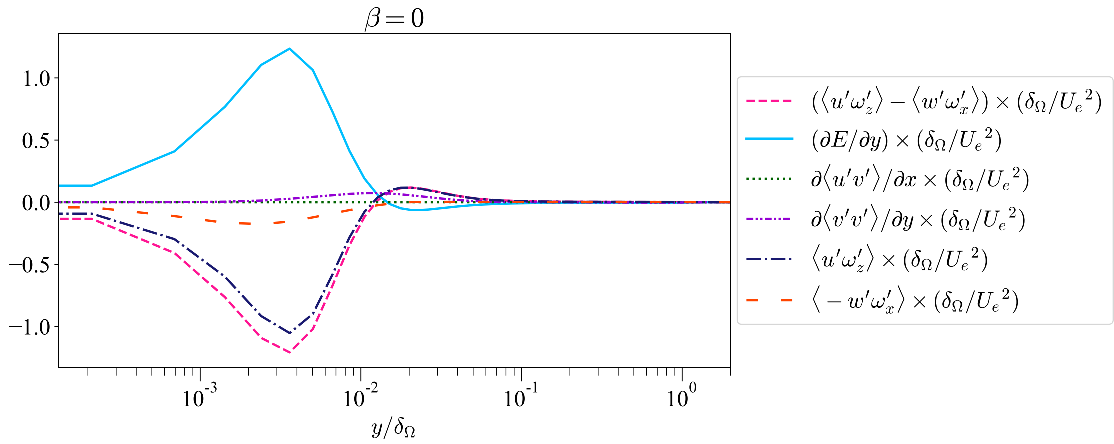

(a)

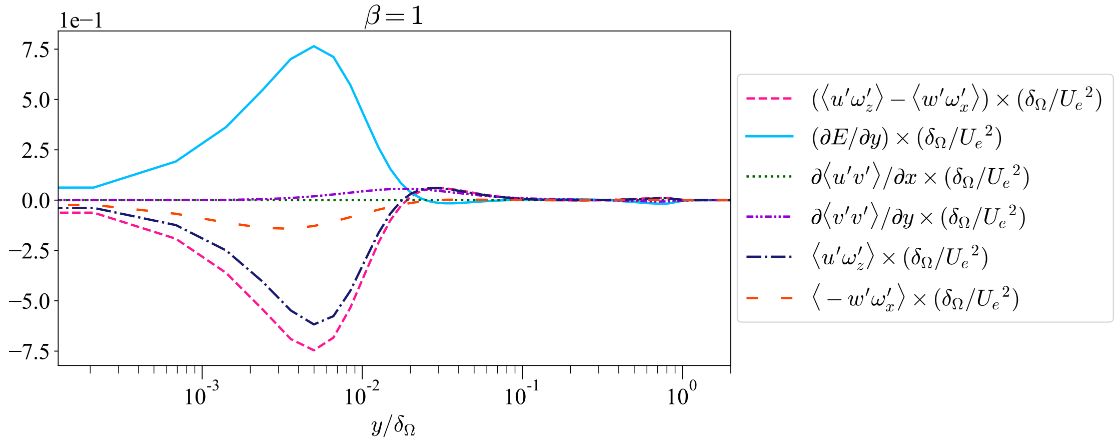

(b)

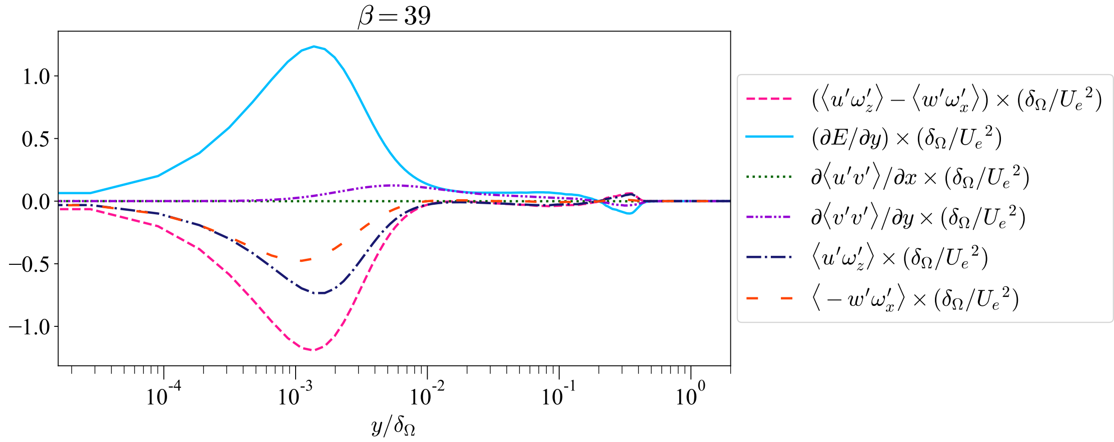

(c)

Figure 5.6: Profiles of the velocity-vorticity correlations ($\langle u'\omega_z'\rangle$ and $-\langle w'\omega_x'\rangle$) and gradients of the corresponding Reynolds stresses in Equation 5.3 for (a) ZPG, (b) mild APG, and (c) strong APG. The profiles are averaged in streamwise direction within DoI and are non-dimensionalised by δ_Ω and U_e.

It can be shown that the velocity-vorticity correlations can be related to the gradients of the Reynolds stresses (Hinze, 1975; Klewicki, 1989) as given by

$$\frac{\partial\langle u'_j u'_i\rangle}{\partial x_j} = -\epsilon_{ijk}\langle u'_j \omega'_k\rangle \ + \ \frac{1}{2}\frac{\partial\langle u'_j u'_j\rangle}{\partial x_i}. \tag{5.1}$$

By setting $i = 1$ and $i = 2$ in Equation 5.1, the velocity-vorticity correlations $\langle v'\omega'_z\rangle - \langle w'\omega'_y\rangle$ and $\langle u'\omega'_z\rangle - \langle w'\omega'_x\rangle$ are expressed as

$$\langle v'\omega'_z\rangle - \langle w'\omega'_y\rangle = \mathcal{R} - \frac{\partial\langle u'v'\rangle}{\partial y} \tag{5.2}$$

and

$$\langle u'\omega'_z\rangle - \langle w'\omega'_x\rangle = -\frac{\partial E}{\partial y} + \frac{\partial\langle u'v'\rangle}{\partial x} + \frac{\partial\langle v'v'\rangle}{\partial y}, \tag{5.3}$$

where $\mathcal{R}$ refers to the streamwise gradient terms given by

$$\mathcal{R} = \frac{\partial}{\partial x}\left(\frac{(-\langle u'u'\rangle + \langle v'v'\rangle + \langle w'w'\rangle)}{2}\right) \tag{5.4}$$

and E is the turbulent kinetic energy given by

$$E = \frac{1}{2}\langle u'_j u'_j\rangle = \frac{1}{2}(\langle u'u'\rangle + \langle v'v'\rangle + \langle w'w'\rangle). \tag{5.5}$$

The profiles of the terms in Equations 5.2 and 5.3 are illustrated in figures 5.5 and 5.6 respectively. Across the boundary layer, for all the pressure gradient cases illustrated in figure 5.5, the correlation $\langle v'\omega'_z\rangle - \langle w'\omega'_y\rangle$ can be considered as the dominant contributor to the term $-\partial\langle u'v'\rangle/\partial y$ as the streamwise gradient terms ($\mathcal{R}$) in Equation 5.2 are negligible when compared to the other terms. The streamwise gradient terms are usually referred to as the inactive component contributions Townsend (1961); Klewicki et al. (1994). As illustrated in figures 2.7e and 5.5, the wall-normal gradient of $\langle u'v'\rangle$ has an inner peak for all the TBL cases and also an outer peak develops when APG is applied in the domain. The outer peak of $\partial\langle u'v'\rangle/\partial y$ becomes more significant for the strong APG TBL case and is located at the height of $y/\delta_\Omega = 0.3$. For all the TBLs, the significant contribution to the inner peak of $-\partial\langle u'v'\rangle/\partial y$ is from the velocity-vorticity correlation $-\langle w'\omega'_y\rangle$, whereas the outer peak contribution is primarily from the correlation $\langle v'\omega'_z\rangle$. This is also consistent with the value of $\langle v'\omega'_z\rangle - \langle w'\omega'_y\rangle$ matching with the value of $\langle v'\omega'_z\rangle$ at the height of $y/\delta_\Omega = 0.3$ for the strong APG TBL as shown in figure 5.5c.

In all the TBL cases, the combined effect of $\langle u'\omega'_z\rangle$ and $\langle w'\omega'_x\rangle$ in Equation 5.3 can be considered as the contribution from the wall-normal gradient of the turbulent kinetic energy (E) as illustrated in figure 5.6. The dominant peak of $\langle u'\omega'_z\rangle - \langle w'\omega'_x\rangle$ in the inner region coincides with the inner peak of $\partial E/\partial y$ for all the pressure gradient cases. When the velocity-vorticity correlations $\langle u'\omega'_z\rangle$ and $-\langle w'\omega'_x\rangle$ are compared, it is observed that $\langle u'\omega'_z\rangle$ is more significant than $-\langle w'\omega'_x\rangle$ in all the TBLs. However, the peak of $\langle u'\omega'_z\rangle$ has reduced for the strong APG TBL when compared to the ZPG TBL as shown in figure 5.4c.

5.4 Variation of the premultiplied integrands with pressure gradient

The variation of the contribution of the advective vorticity transport and vortex stretching terms are further analysed by investigating the wall-normal distribution of their integrands for the three TBL cases. The integrands of the terms C_{f_1} and C_{f_2} are denoted by I_1 and I_2 respectively. In the present study, the premultiplied integrands are denoted by the subscript of $*$. The y coordinate is non-dimensionalised by the outer scale δ_Ω and the premultiplied integrands are streamwise averaged within the DoI. The profiles of the premultiplied integrands of C_{f_1} and C_{f_2} (I_{1*} and I_{2*}) are shown in figure 5.7.

It is shown in section 5.2 that the term C_{f_1} gives a negative contribution to the skin friction coefficient for all the pressure gradient cases. As illustrated in figure 5.7a, the premultiplied integrand I_{1*} has two negative peaks in the outer region for the ZPG TBL. The first outer peak decreases with increasing pressure gradient, whereas the second negative peak continues to grow. When the flow reaches the verge of separation in the strong APG TBL, the dominant negative contribution is from the second peak which is located around the height of $y/\delta_\Omega = 0.3$. The location of the dominant outer peak in I_{1*} coincides with the outer peak in $-\partial\langle u'v'\rangle/\partial y$ as illustrated in figures 2.7e and 5.5c.

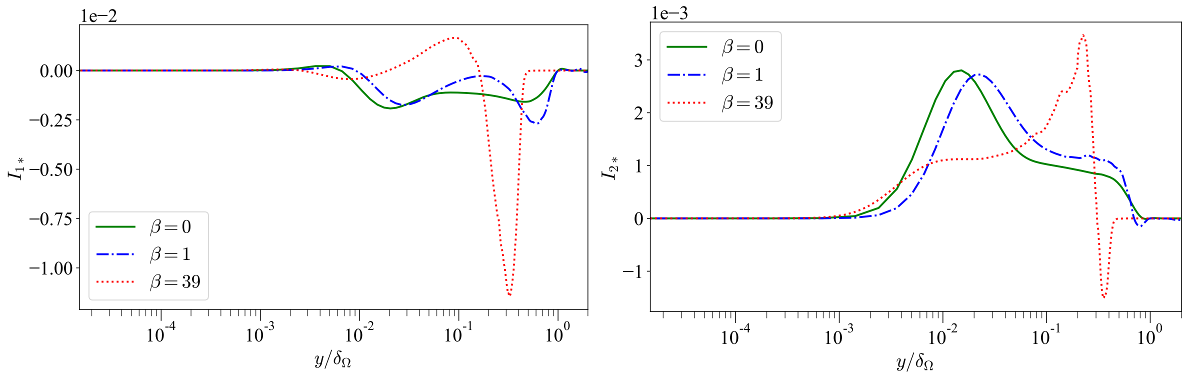

(a) (b)

Figure 5.7: Variation of the premultiplied integrand (a) I_{1*}, and (b) I_{2*} of the YAHS identity (Equation 3.5) with β. The profiles are averaged in streamwise direction within DoI.

The vortex stretching term (C_{f_2}) provides a positive contribution in all the three TBL cases as shown in figure 5.1. In the ZPG TBL, the dominant positive contribution is from the outer peak located at the height of $y/\delta_\Omega = 1.5 \times 10^{-2}$ as illustrated in figure 5.7b. As the pressure gradient increases, a second positive outer peak develops, while the first peak reduces. The second outer peak becomes the dominant positive contributor in the strong APG TBL and its location coincides with the position of the outer peak in $\langle u'v'\rangle$

around the height of $y/\delta_\Omega = 0.2$ as shown in figure 2.7d. It is also to be noted that there is a negative peak present around the height of $y/\delta_\Omega = 0.35$ in the strong APG TBL.

As shown in Equation 5.2, $\langle v'\omega_z'\rangle - \langle w'\omega_y'\rangle$ can be expressed in terms of the Reynolds stress gradients. Therefore, the sum of the terms C_{f_1} and C_{f_2} is given by

$$\underbrace{\int_0^1 \frac{2\delta_\Omega}{{U_e}^2}\Big(1-\frac{y}{\delta_\Omega}\Big)\left(\langle v'\omega_z'\rangle + \langle -w'\omega_y'\rangle\right)\, d\Big(\frac{y}{\delta_\Omega}\Big)}_{C_{f_1}+C_{f_2}} =$$
$$\underbrace{\int_0^1 \frac{2\delta_\Omega}{{U_e}^2}\Big(1-\frac{y}{\delta_\Omega}\Big)\frac{\partial}{\partial x}\left(\frac{(-\langle u'u'\rangle + \langle v'v'\rangle + \langle w'w'\rangle)}{2}\right)\, d\Big(\frac{y}{\delta_\Omega}\Big)}_{C_{f_{12a}}}$$
$$+ \underbrace{\int_0^1 \frac{2\delta_\Omega}{{U_e}^2}\Big(1-\frac{y}{\delta_\Omega}\Big)\frac{-\partial\langle u'v'\rangle}{\partial y}\, d\Big(\frac{y}{\delta_\Omega}\Big)}_{C_{f_{12b}}}. \tag{5.6}$$

The contribution from the term $C_{f_{12a}}$ is insignificant for all the TBL cases as the Reynolds stress gradients ($\mathcal{R}$) in the term $C_{f_{12a}}$ are negligible, which is illustrated in figure 5.5. The profiles of the premultiplied integrands of the terms $C_{f_{12b}}$ and $C_{f_1}+C_{f_2}$ are shown in figure 5.8. The profile of the premultiplied integrand $I_{1*}+I_{2*}$ match closely with the profile of I_{12b*} for all the pressure gradient cases. This shows that the combined effect of the advective vorticity transport and vortex stretching terms ($C_{f_1}+C_{f_2}$) can be considered as the contribution from the negative wall-normal gradient of the Reynolds shear stress ($C_{f_{12b}}$). This is also consistent with the profile of $\langle v'\omega_z'\rangle - \langle w'\omega_y'\rangle$ matching with the profile of $-\partial\langle u'v'\rangle/\partial y$ in all the TBLs, as observed in figure 5.5.

The term $C_{f_{12b}}$ can be further integrated by parts and applying the no slip condition $\langle u'v'\rangle(y/\delta_\Omega = 0) = 0$ leads to

$$\begin{aligned}
C_{f_{12b}} &= \int_0^1 \frac{2\delta_\Omega}{{U_e}^2}\Big(1-\frac{y}{\delta_\Omega}\Big)\frac{\partial\langle -u'v'\rangle}{\partial y}\, d\Big(\frac{y}{\delta_\Omega}\Big) \\
&= \left[\frac{2\delta_\Omega}{{U_e}^2}\Big(1-\frac{y}{\delta_\Omega}\Big)\frac{\langle -u'v'\rangle}{\delta_\Omega}\right]_0^1 + \int_0^1 \frac{2\delta_\Omega}{{U_e}^2}\frac{\langle -u'v'\rangle}{\delta_\Omega}\, d\Big(\frac{y}{\delta_\Omega}\Big) \\
&= \underbrace{\int_0^1 \frac{-2}{{U_e}^2}\langle u'v'\rangle\, d\Big(\frac{y}{\delta_\Omega}\Big)}_{C_{f_{12c}}}.
\end{aligned} \tag{5.7}$$

The term $C_{f_{12c}}$ can be considered as the Reynolds stress contribution in the YAHS identity and the Reynolds shear stress in the term $C_{f_{12c}}$ is weighted by a constant $(2/{U_e}^2)$ in the wall-normal direction. The profiles of the premultiplied integrand of $C_{f_{12c}}$ is illustrated in figure 5.8. The premultiplied integrand I_{12c*} has an outer peak in all the TBL cases. Even though the wall-normal distribution of the integrands of the terms $C_{f_{12b}}$ and $C_{f_{12c}}$

look different, their integration in the wall-normal direction is the same as shown in Equation 5.7.

As discussed in chapters 3 and 4, the RD identity and the FIK identity have three components each. From these two decompositions, the terms of interest to the current analysis are C_{f_b} and $C_{f_{II}}$. The term C_{f_b} in the RD identity and the term $C_{f_{II}}$ in the FIK identity refer to the contribution from the Reynolds shear stress ($\langle u'v' \rangle$) in the respective decompositions. The term C_{f_b} is given by

$$C_{f_b} = \int_0^\infty \frac{-2}{U_e^3} \frac{\partial \langle u \rangle}{\partial y} \langle u'v' \rangle \; dy \tag{5.8}$$

and the term $C_{f_{II}}$ is given by

$$C_{f_{II}} = \int_0^1 \frac{-4}{U_e^2} \Big(1 - \frac{y}{\delta_\Omega}\Big) \langle u'v' \rangle \; d\Big(\frac{y}{\delta_\Omega}\Big). \tag{5.9}$$

The premultiplied integrands of the terms C_{f_b} and $C_{f_{II}}$ are denoted by I_{b*} and I_{II*}, respectively, and their wall-normal profiles are given in figure 5.8.

The Reynolds shear stress contribution from the three decompositions, namely the YAHS identity, the FIK identity, and the RD identity are compared for the three TBL cases in figure 5.8. The notable difference between the Reynolds stress components in the three identities ($C_{f_{12c}}$, $C_{f_{II}}$, C_{f_b}) is the wall-normal weight of the Reynolds shear stress. The terms $C_{f_{12c}}$, $C_{f_{II}}$ and C_{f_b} have a constant weight ($2/{U_e}^2$), a linear weight ($1{-}y/\delta_\Omega$) and a $\partial\langle u \rangle/\partial y$ weight, respectively. For the ZPG TBL, I_{b*} of the RD identity has an inner and an outer peak whereas, the premultiplied integrands in the other two decompositions (I_{II*} and I_{12c*}) have only an outer peak. As the pressure gradient increases, the inner peak of I_{b*} decreases while the outer peak grows. For the strong APG TBL, the components from all the three decompositions have a dominant outer peak around the height of $y/\delta_\Omega = 0.2$ as illustrated in figure 5.8c. The dominant outer peak in the premultiplied integrands I_{12c*}, I_{b*} and I_{II*} coincide with the outer peak of the Reynolds shear stress ($\langle u'v' \rangle$) and the outer inflection point in the mean streamwise velocity ($\langle u \rangle$) for the strong APG TBL illustrated in figure 2.7d and figure 2.6a, respectively. This emphasizes the increasing influence of the outer layer dynamics on the skin friction with increasing pressure gradient.

The terms $C_{f_1}{+}C_{f_2}$ and $C_{f_{12b}}$ of the YAHS identity are related as shown in Equation 5.6. For the strong APG TBL, the zero crossing of the premultiplied integrands $I_{1*}{+}I_{2*}$ and I_{2b*}, illustrated in figure 5.8c, is also around the height of $y/\delta_\Omega = 0.2$ and it is also consistent with the zero crossing of $-\partial\langle u'v' \rangle/\partial y$, signifying the position of the outer peak in the Reynold shear stress ($\langle u'v' \rangle$) as shown in figures 2.7d and 2.7e. For the ZPG TBL, the premultiplied integrands $I_{1*}{+}I_{2*}$ and I_{2b*} have a positive peak in the inner region and a negative peak in the outer region. As the pressure gradient increases,

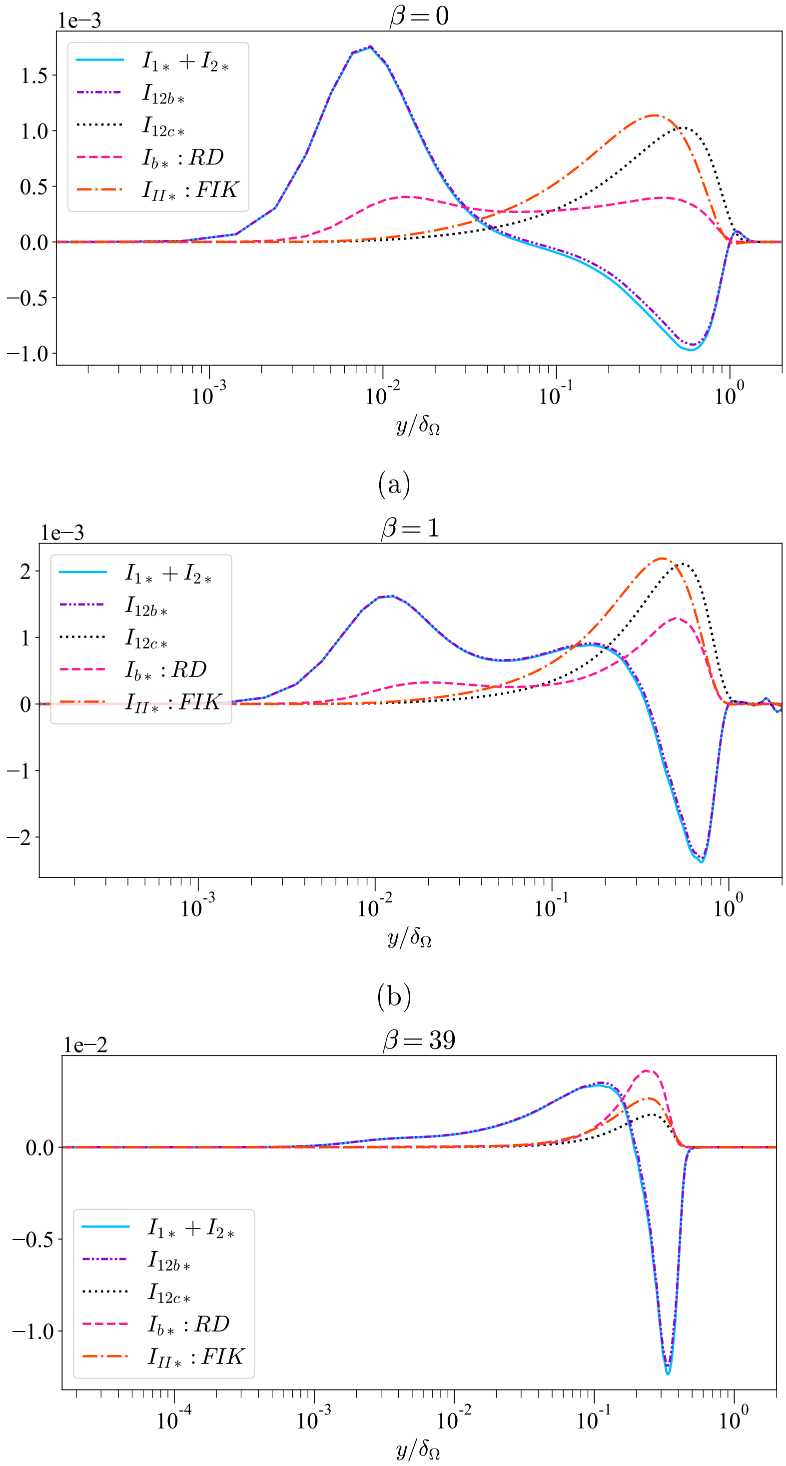

(a)

(b)

(c)

Figure 5.8: Profiles of the premultiplied integrands corresponding to the Reynolds shear stress components in the three decompositions, namely the YAHS identity (I_{12c*}), the FIK identity (I_{II*}), and the RD identity (I_{b*}) for (a) ZPG, (b) mild APG, and (c) strong APG. The profiles are averaged in streamwise direction within DoI and are non-dimensionalised by δ_Ω and U_e.

the inner peak continues to decrease and disappears in the strong APG TBL case. As the adverse pressure gradient is applied, a second positive outer peak grows in the mild APG TBL and it continues to grow in the case of the strong APG TBL. The outer negative peak in the profiles of $I_{1*}+I_{2*}$ and I_{2b*} continues to grow significantly with increasing pressure gradient and becomes a dominant negative contributor when the flow reaches the verge of separation in the strong APG TBL case. The negative peak of $I_{1*}+I_{2*}$ and I_{2b*} is around the height of $y/\delta_\Omega = 0.3$ in the strong APG case, which coincides with the outer peak in the profile of $-\partial\langle u'v'\rangle/\partial y$ illustrated in figure 2.7e. The above observations in the strong APG TBL imply the increased significance of the vortical motions and turbulent mixing in the outer layer as it pertains to the contribution of the Reynolds shear stress and $-\partial\langle u'v'\rangle/\partial y$ to the skin friction coefficient.

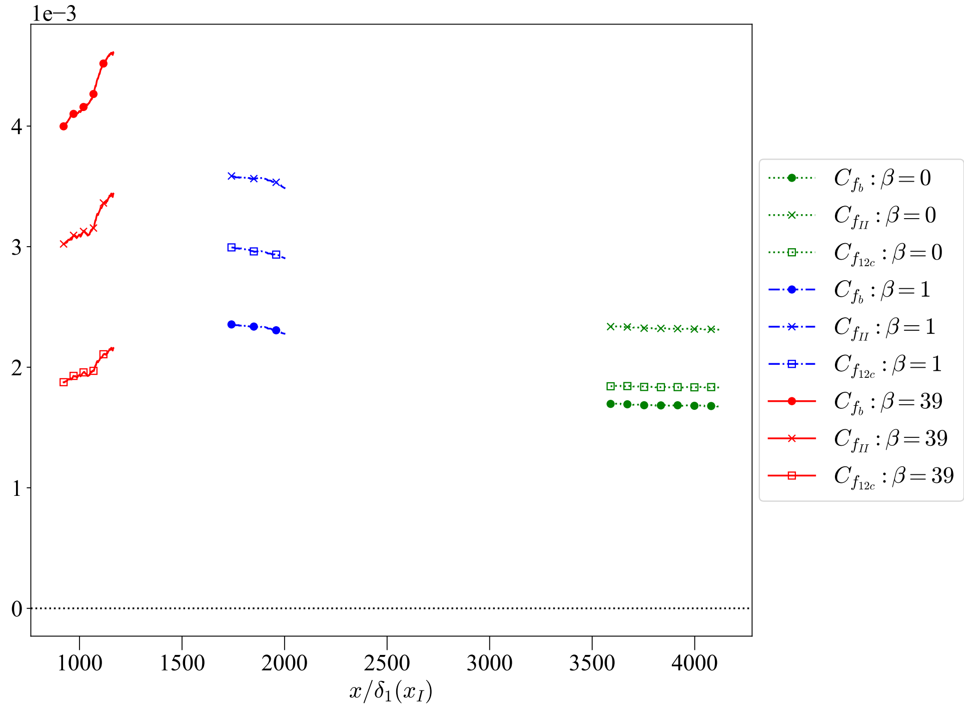

Figure 5.9: Variation of the contribution of the Reynolds shear stress components in the three decompositions, namely the YAHS identity ($C_{f_{12c}}$), the FIK identity ($C_{f_{II}}$), and the RD identity (C_{f_b}) with β in the respective DoI.

The variation of the contribution of the Reynolds stress components from the three decompositions with β is given in figure 5.9. As the pressure gradient increases, the terms $C_{f_{12c}}$ and $C_{f_{II}}$ have a similar trend, while the term C_{f_b} continues to increase. On average, the term C_{f_b} is about 2.1 times the term $C_{f_{12c}}$ within the DoI for the strong APG TBL, which also coincides with the ratio of the outer peaks in I_{b*} and I_{2c*} shown in figure 5.8c.

5.5 Relationship between the RD identity and velocity-vorticity correlations

One of the main advantages of the RD identity is that it does not have any inhomogeneous terms (Renard and Deck, 2016). As the RD identity is local in the streamwise direction, it can also be used when the data at different streamwise locations are not available. Therefore, it is useful and important to quantify the contribution of the velocity-vorticity correlations to the skin friction coefficient without having to compute any streamwise gradients that are significant. The original RD identity is given in Equation 3.1.

At $y = 0$, the no-slip condition gives $\langle u'v'\rangle(y = 0) = \langle u\rangle(y = 0) = 0$. In the far-field, the flow becomes irrotational leading to $\langle u'v'\rangle(y \to \infty) = 0$. With these conditions, integrating by parts the term C_{f_b} in the RD identity (Equation 3.1) gives

$$
\begin{aligned}
C_{f_b} &= \frac{2}{U_e^3}\int_0^\infty -\langle u'v'\rangle \frac{\partial\langle u\rangle}{\partial y}\,dy \\
&= \frac{2}{U_e^3}\left(\Big[-\langle u'v'\rangle\langle u\rangle\Big]_0^\infty - \int_0^\infty \langle u\rangle \frac{\partial(-\langle u'v'\rangle)}{\partial y}\,dy\right) \\
&= \underbrace{\frac{2}{U_e^3}\int_0^\infty \langle u\rangle \frac{\partial\langle u'v'\rangle}{\partial y}\,dy}_{C_{f_{bIV}}}\,.
\end{aligned} \tag{5.10}
$$

As shown in Equation 5.2, the Reynolds stress gradients can be related to the velocity-vorticity correlations $\langle v'\omega_z'\rangle$ and $\langle w'\omega_y'\rangle$. As discussed in Soria (2020), substituting Equation 5.2 into the term $C_{f_{bIV}}$ in Equation 5.10 gives

$$
\begin{aligned}
C_{f_b} &= \frac{2}{U_e^3}\int_0^\infty \langle -u'v'\rangle \frac{\partial\langle u\rangle}{\partial y}\,dy \\
&= \underbrace{\frac{2}{U_e^3}\int_0^\infty \langle u\rangle \frac{\partial\langle u'v'\rangle}{\partial y}\,dy}_{C_{f_{bIV}}} \\
&= \underbrace{\frac{2}{U_e^3}\int_0^\infty \langle u\rangle\langle -v'\omega_z'\rangle\,dy}_{C_{f_{bI}}} + \underbrace{\frac{2}{U_e^3}\int_0^\infty \langle u\rangle\langle w'\omega_y'\rangle\,dy}_{C_{f_{bII}}} \\
&\quad \underbrace{+\frac{2}{U_e^3}\int_0^\infty \langle u\rangle \frac{\partial}{\partial x}\left(\frac{(-\langle u'u'\rangle + \langle v'v'\rangle + \langle w'w'\rangle)}{2}\right)dy}_{C_{f_{bIII}}}\,.
\end{aligned} \tag{5.11}
$$

The contribution from the term $C_{f_{bIII}}$ is insignificant for all the TBL cases as the Reynolds stress gradients ($\mathcal{R}$) in it are negligible, which is illustrated in figure 5.5. The

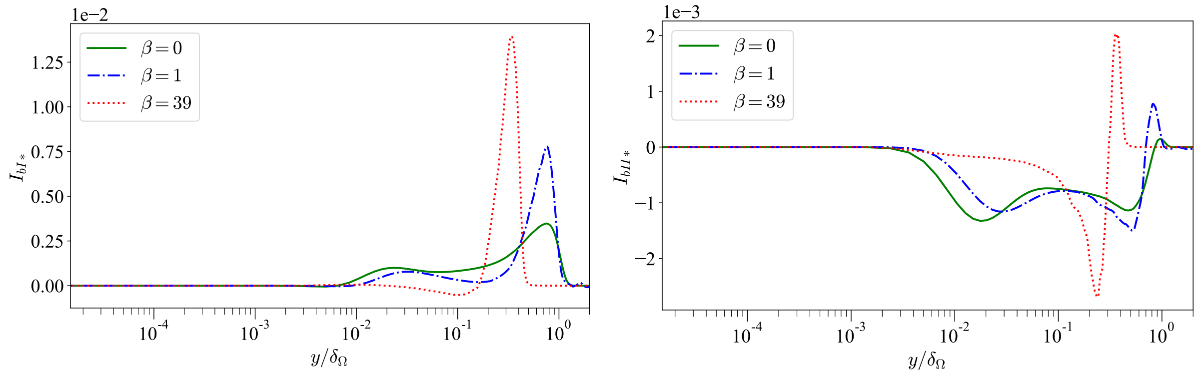

(a) (b)

Figure 5.10: Variation of the premultiplied integrand (a) I_{bI*}, and (b) I_{bII*} in Equation 5.11 of the RD identity with β. The profiles are averaged in streamwise direction within DoI and are non-dimensionalised by δ_Ω and U_e.

term $C_{f_{bI}}$ refers to the contribution of the body force arising from the transport of ω'_z by v' in the RD identity, whereas the term $C_{f_{bII}}$ is interpreted as the contribution of the vortex stretching force. The variation of the premultiplied integrand of these two terms (I_{bI*} and I_{bII*}) with the pressure gradient is illustrated in figure 5.10. The premultiplied integrand I_{bI*} has two positive outer peaks for the ZPG TBL. As the pressure gradient increases, the first peak decreases and vanishes in the case of the strong APG TBL. The second outer peak continues to grow with the pressure gradient and becomes a dominant contributor in the strong APG TBL. The outer peak of I_{bI*} in the strong APG TBL is present around the height of $y/\delta_\Omega = 0.3$ which matches with the location of the outer peak in $\partial\langle u'v'\rangle/\partial y$ as shown in figure 2.7e. The premultiplied integrand of the vortex stretching term (I_{bII*}) has two negative peaks in the outer region. With increasing pressure gradient, the first peak reduces in magnitude, whereas the second peak grows. For the strong APG TBL, there is a dominant negative peak in I_{bII*} around the height of $y/\delta_\Omega = 0.2$. For the ZPG TBL, the vortex stretching term in the YAHS identity (I_{2*}) has only one outer peak as illustrated in figure 5.7b whereas, a clear second peak is evident in I_{bII*} of the RD identity as shown in figure 5.10b.

The contribution of the velocity-vorticity correlations $\langle v'\omega'_z\rangle$ and $\langle w'\omega'_y\rangle$ in the RD identity are in the opposite sense to that of the corresponding terms in the YAHS identity. This is because the term C_{f_b} of the RD identity is related to the positive wall-normal gradient of the Reynolds shear stress ($\partial\langle u'v'\rangle/\partial y$) in Equation 5.11 whereas, the terms in the YAHS identity are related to the negative wall-normal gradient of the Reynolds shear stress ($-\partial\langle u'v'\rangle/\partial y$) as shown in Equation 5.6.

The variation of the terms $C_{f_{bI}}$ and $C_{f_{bII}}$ of the RD identity with the pressure gradient is presented in figure 5.11. The term $C_{f_{bI}}$ gives a positive contribution for all the cases,

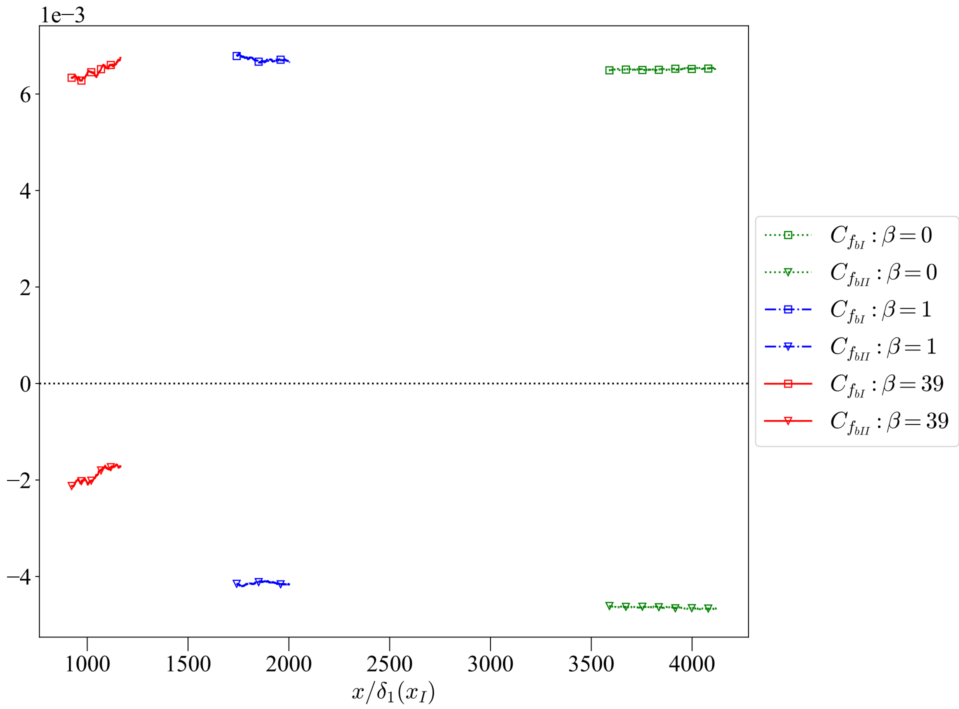

Figure 5.11: Variation of the contribution of the advective vorticty transport term ($C_{f_{bI}}$) and the vortex stretching ($C_{f_{bII}}$) term in Equation 5.11 of the RD identity with β in the respective DoI.

while $C_{f_{bII}}$ gives a negative contribution. The contribution of the term $C_{f_{bII}}$ in the strong APG TBL is approximately 60% lower than that in the ZPG case. This is consistent with the negative peak of I_{bII*} being narrow for the strong APG case as illustrated in figures 5.10 and 5.12c. The comparison of the profiles of the premultiplied integrand of the terms in Equation 5.11, which shows the relationship of the term C_{f_b} in the RD identity with the velocity-vorticity correlations, is shown in figure 5.12 for each TBL case. Although the profiles of the premultiplied integrands I_{b*} and I_{IV*} look different, their integrated value in the wall-normal direction is the same as shown in Equation 5.11. The premultiplied integrands are wider for the ZPG TBL and become narrower with increasing pressure gradient. For the strong APG TBL, their profiles are concentrated in the outer region as illustrated in figure 5.12c. When the flow reaches the verge of separation in the strong APG case shown in figure 5.12c, the dominant outer peak in the premultiplied integrand I_{bIV*} (contribution of $\partial\langle u'v'\rangle/\partial y$) matches with the peak of I_{bI*} (contribution of $-\langle v'\omega_z'\rangle$) around the height of $y/\delta_\Omega = 0.3$, which again indicates that the velocity-vorticity correlation $\langle v'\omega_z'\rangle$ is the dominant contributor to the outer peak of $-\partial\langle u'v'\rangle/\partial y$ in the strong APG TBL as observed in section 5.3.

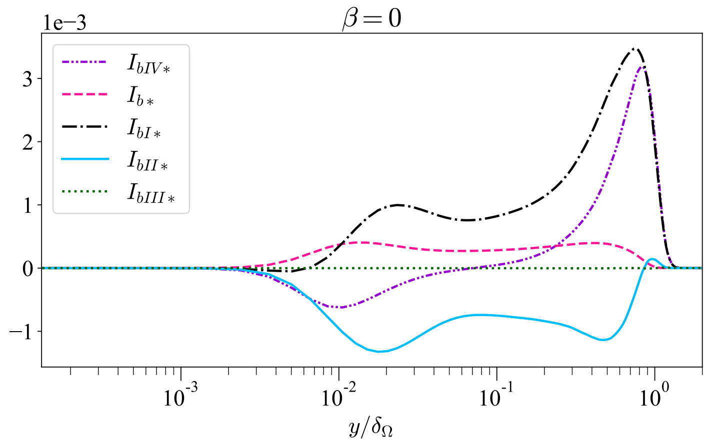

(a)

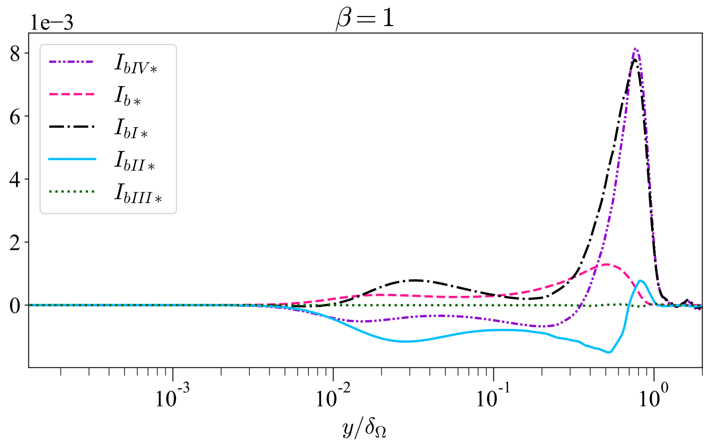

(b)

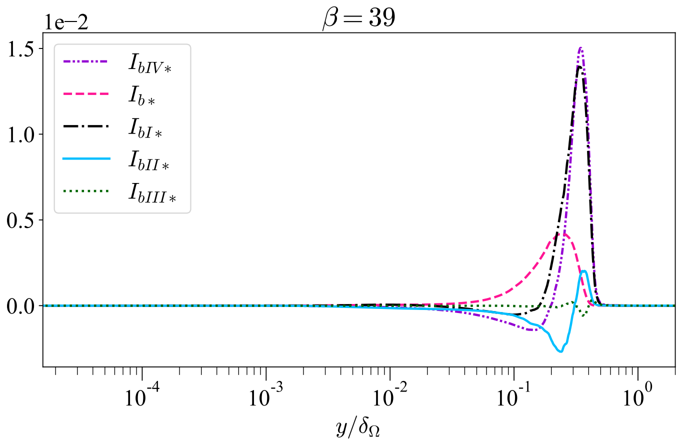

(c)

Figure 5.12: Profiles of the premultiplied integrand of the terms in Equation 5.11 of the RD identity for (a) ZPG, (b) mild APG, and (c) strong APG. The profiles are averaged in streamwise direction within DoI and are non-dimensionalised by δ_Ω and U_e.

5.6 Conclusion

The contribution of the velocity-vorticity correlations to the skin friction coefficient and their variation with the pressure gradient are investigated using the YAHS identity (Yoon et al., 2016). For both the mild and the strong APG TBLs, the molecular diffusion term (C_{f_3}) reduces the skin friction coefficient as $\partial\langle\Omega_z\rangle/\partial y = \partial^2\langle v\rangle/\partial y\partial x - \partial^2\langle u\rangle/\partial y^2$ is negative at the wall because of the inflection point in the mean streamwise velocity profile in the near wall region. The contribution of the molecular diffusion at the wall (C_{f_3}) increases with the pressure gradient. For the strong APG TBL, the term C_{f_3} becomes a dominant negative contributor which is consistent with a larger negative value of the wall-normal gradient of the mean spanwise vorticity at the wall. The contribution of the molecular transfer due to the mean vorticity (C_{f_4}) is negligible for all the pressure gradient cases.

Across the boundary layer in all the three pressure gradient cases, the combined effect of $\langle v'\omega_z'\rangle$ and $-\langle w'\omega_y'\rangle$ can be considered as the dominant contributor to $-\partial\langle u'v'\rangle/\partial y$. In the case of the strong APG TBL, the velocity-vorticity correlation $\langle v'\omega_z'\rangle$ is the primary contributor to the outer peak of the negative wall-normal gradient of $\langle u'v'\rangle$ located around the height of $y/\delta_\Omega = 0.3$. For all the pressure gradient cases, the combined effect of the advective vorticity transport term (C_{f_1}) and the vortex stretching term (C_{f_2}) represents the contribution from the Reynolds shear stress with a constant weight ($C_{f_{12c}}$) as shown in Equations 5.6 and 5.7. When the flow reaches the verge of separation in the strong APG TBL, the integrand of the term $C_{f_{12c}}$ exhibits an outer peak which coincides with the outer peak of the Reynolds stress terms in the RD identity (C_{f_b}) and the FIK identity ($C_{f_{II}}$) around the height of 20% of boundary layer thickness ($y/\delta_\Omega = 0.2$). This shows the significance of the outer layer vortical motions and turbulent mixing in regards to the contribution from the Reynolds shear stress ($\langle u'v'\rangle$) and its negative wall-normal gradient ($-\partial\langle u'v'\rangle/\partial y$) to the skin friction coefficient when the flow reaches the verge of separation. The important distinction between the Reynolds stress components in the three identities is the wall-normal weight of the Reynolds shear stress ($-\langle u'v'\rangle$). The term $C_{f_{12c}}$ of the YAHS identity has a a constant weight ($2/{U_e}^2$), the term $C_{f_{II}}$ of the FIK identity has a linear weight ($1 - y/\delta_\Omega$) and the term C_{f_b} of the RD identity has a $\partial\langle u\rangle/\partial y$ weight for the Reynolds shear stress.

A new method, using the RD identity (Renard and Deck, 2016), to quantify the contribution of the advective vorticity transport and the vortex stretching force is introduced. One of the benefits of the RD identity is that it does not have inhomogeneous terms and therefore, it is helpful to express the contribution of the velocity-vorticity correlations to the skin friction in a way that does not involve the computation of significant streamwise gradients. The premultiplied integrands of the terms in Equation 5.11 are wide for the ZPG TBL and they continue to shrink with increasing pressure gradient. In the strong APG TBL, when the flow reaches the verge of separation, the premultiplied integrand I_{bIV*} (contribution of $\partial\langle u'v'\rangle/\partial y$) has a dominant outer peak around the height of $y/\delta_\Omega = 0.3$ which coincides with the peak of I_{bI*} (contribution of $-\langle v'\omega_z'\rangle$). This observation again implies that the velocity-vorticity correlation $\langle v'\omega_z'\rangle$ is the dominant contributor to the outer peak of $-\partial\langle u'v'\rangle/\partial y$.

The two most important days in your life are the day you are born and the day you find out why.

–Mark Twain

Chapter 6

Analysis of the turbulent contribution of the intense structures to the skin friction

6.1 Introduction

One of the types of coherent structures identified in turbulent flows is the intense structures or clusters. The intense structures can be generally defined as spatially coherent regions in the flow whose constituent points carry a higher magnitude of certain quantities than a threshold value. The optimum threshold to identify the intense structures is chosen based on the percolation analysis, which gives an equilibrium between detecting only a few very large structures and detecting only a few small and very intense structures. The percolation analysis was first used by Moisy and Jiménez (2004) to identify intense vortical and dissipative structures in isotropic turbulence followed by Del Álamo et al. (2006) to identify vortex clusters in turbulent channel flows. Subsequently, several studies used percolation analysis to identify coherent structures like the study of intense Reynolds stress structures in turbulent channel flows by Lozano-Durán et al. (2012); Soria et al. (2016), in TBLs by Maciel et al. (2017b,a) and to identify clusters of streamwise velocity fluctuations in TBLs by Yoon et al. (2020).

As discussed in chapter 4, the Reynolds shear stress ($\langle u'v' \rangle$) provides the predominant positive contribution to the skin friction irrespective of the pressure gradient in the flow. The Reynolds shear stress contribution (C_{f_b}) exhibits an outer peak with increasing adverse pressure gradient. In the case of the strong APG TBL, the major part of the contribution is from a dominant outer peak located around the displacement thickness height ($y/\delta_1 = 1$). In chapter 5, it is shown that the combined contribution of the velocity-vorticity correlations $\langle v'\omega_z' \rangle$ and $-\langle w'\omega_y' \rangle$ represents the contribution from the Reynolds shear stress with a constant wall-normal weight, which also develops an outer peak around the displacement thickness height ($y/\delta_1 = 1$) in the strong APG TBL. These results from the last two chapters emphasize the significance of the Reynolds shear stress contribution from the outer region to the skin friction with increasing pressure gradient. As the Reynolds shear stress contribution from the entire flow is analysed in chapters 4 and 5, the focus of the present chapter is to investigate the contribution of the Reynolds shear stress only from the intense structures in the flow. The types of intense structures considered in the present study are intense topological structures and intense Reynolds stress structures. This chapter is organised as follows. In section 6.2, the methodology used to identify the intense structures (intense dissipative structures, intense vortical structures and intense Reynolds stress structures) is discussed. In section 6.3, the number and volume proportions, and geometric characteristics of these intense structures are presented. In section 6.4, the turbulent contribution of these intense structures to the skin friction is analysed using the Reynolds stress term (C_{f_b}) in the RD identity (Renard and Deck, 2016).

6.2 Identification methodology of the intense structures

Three types of intense structures, namely intense dissipative structures, intense vortical structures and intense Reynolds stress structures are investigated in the DoI of the ZPG and strong APG TBLs. For the detection of these structures in the strong APG TBL, a buffer domain of streamwise extent $2.8\overline{\delta_1}$ is used on both the sides of the self-similar DoI. This is done to ensure that the full streamwise extent of the intense structures within the self-similar DoI is captured. $\overline{\delta_1}$ is the mean displacement thickness within the DoI. The identification methodologies of these structures are outlined below.

6.2.1 Intense dissipative structures

Following Chong et al. (1990); Soria and Cantwell (1994); Chong et al. (1998), the flow can be classified into different topologies based on the invariants in the (R_A,Q_A)-plane, where Q_A is the second invariant of the velocity gradient tensor $A_{ij} = \partial u_i/\partial x_j$ and R_A is the third invariant of the A_{ij}. The velocity gradient tensor A_{ij} can be split into two components as given by

$$A_{ij} = S_{ij} + W_{ij}, \tag{6.1}$$

where S_{ij} is the symmetric rate of strain tensor and W_{ij} is the skew symmetric rate of rotation tensor. The symmetric and anti-symmetric parts of A_{ij} are given by

$$S_{ij} = \frac{1}{2}\left(\frac{\partial u_i}{\partial x_j} + \frac{\partial u_j}{\partial x_i}\right) \tag{6.2}$$

and

$$W_{ij} = \frac{1}{2}\left(\frac{\partial u_i}{\partial x_j} - \frac{\partial u_j}{\partial x_i}\right), \tag{6.3}$$

respectively. Q_A and R_A are given by

$$Q_A = -\frac{1}{2}A_{ij}A_{ji} = Q_s + Q_w \tag{6.4}$$

and

$$R_A = -\frac{1}{3}A_{ij}A_{jk}A_{ki}, \tag{6.5}$$

where Q_s is the second invariant of the symmetric rate of strain tensor (S_{ij}) and Q_w is the second invariant of the skew symmetric rate of rotation tensor (W_{ij}). Q_s is always a negative quantity, while Q_w is always a positive quantity. The discriminant of the velocity gradient tensor A_{ij} is defined as

$$D_A = \frac{27}{4}R_A^2 + Q_A^3. \tag{6.6}$$

As illustrated in figure 6.1, the tent-like curve in the (R_A,Q_A)-plane corresponds to $D_A = 0$ (Soria and Cantwell, 1994; Chong et al., 1998). For any point in the flow, Q_A gives a measure of the relative intensity of the local strain and vorticity. The two topologies used to identify the intense dissipative structures are unstable node/saddle/saddle (USN/S/S) and stable node/saddle/saddle (SN/S/S) and they lie below the tent-like curve in the (R_A,Q_A)-plane.

The intense dissipative structures, which lie below and farther away from the $D_A = 0$ curve, have large negative values of Q_A indicating regions of strong local strain. The negative contribution to Q_A is from the second invariant of S_{ij} (Q_s), which is always a negative quantity. Q_s can be related to the dissipation of kinetic energy into heat per unit mass (ϕ) as given by

$$Q_s = -\frac{1}{2}S_{ij}S_{ij} = \frac{-1}{4\nu}\phi, \tag{6.7}$$

where $\phi = 2\nu S_{ij}S_{ij}$ and ν is the kinematic viscosity. The intense dissipative structures are defined as regions of connected points in the flow that satisfy two conditions simultaneously. The first condition is given by

$$-D_A(x, y, z) > \alpha_s \sigma_{D_A}(x, y), \tag{6.8}$$

where α_s is a constant threshold and $\sigma_{D_A} = \sqrt{\overline{(D_A{}')^2}}$ is the standard deviation of D_A. The threshold α_s is chosen based on the percolation analysis as outlined in Lozano-Durán

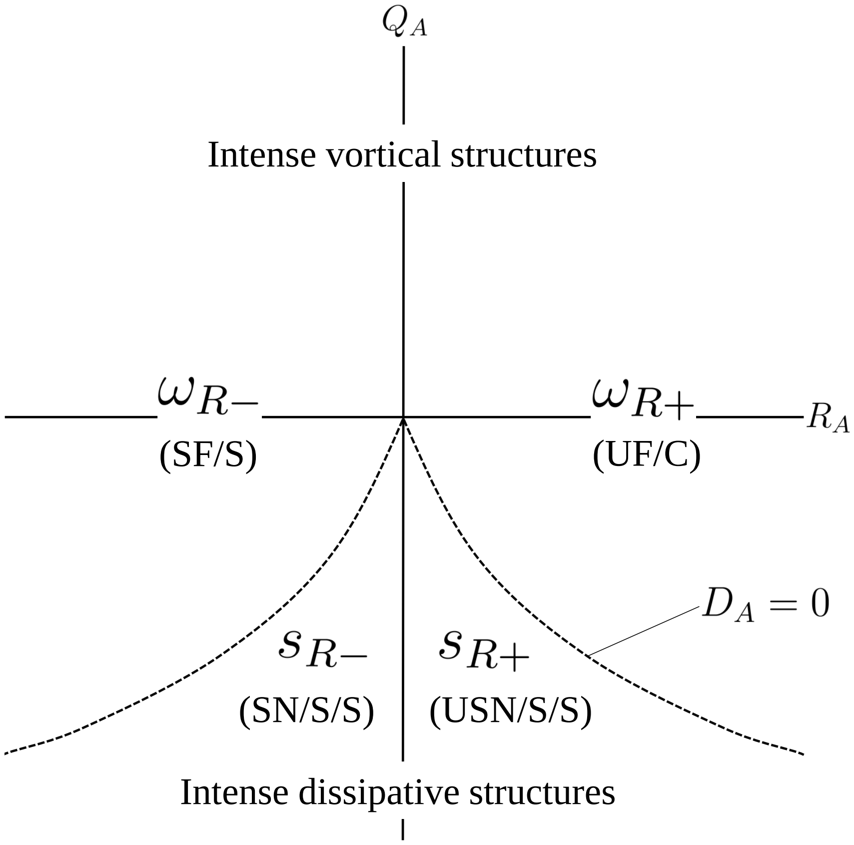

Figure 6.1: Notations of the intense vortical and dissipative structures. The local non-degenerate topologies in the (R_A,Q_A)-plane are stable focus/stretching (SF/S), unstable focus/contracting (UF/C), stable node/saddle/saddle (SN/S/S), and unstable node/saddle/saddle (USN/S/S). The tent-like curve corresponds to $D_A = 0$ (Soria and Cantwell, 1994; Chong et al., 1998). Based on the sign of R_A, intense dissipative structures belonging to USN/S/S topology is denoted as s_{R+} and those in SN/S/S topology as s_{R-}. Similarly, intense vortical structures belonging to UF/C topology is denoted as ω_{R+} and those in SF/S topology as ω_{R-}.

et al. (2012); Del Álamo et al. (2006); Moisy and Jiménez (2004). The second condition is that all the points within a dissipative structure should belong to the same topology in the (R_A,Q_A)-plane. The two topologies considered here are unstable node/saddle/saddle (USN/S/S) given by $D_A < 0$, $R_A > 0$ and stable node/saddle/saddle (SN/S/S) given by $D_A < 0$, $R_A < 0$. Both of these topologies have negative D_A values ($D_A < 0$). Therefore, based on the sign of R_A, intense dissipative structures belonging to USN/S/S topology are denoted as s_{R+} and those in SN/S/S topology as s_{R-}. The s_{R+} and s_{R-} structures are referred to as $s_{R,both}$. Connectivity of the points is defined based on the six orthogonal neighbours in the Cartesian coordinate system. The structures or clusters or objects are identified using an efficient in-house 3D implementation of the Hoshen–Kopelman (HK) algorithm (Hoshen and Kopelman, 1976).

A percolation analysis is performed separately for each topological structure to obtain a separate threshold for each structure type. The percolation diagrams for the identification of s_{R+} and s_{R-} structures in the ZPG and the strong APG TBLs are shown in figure 6.2. As illustrated in figure 6.2a of the ZPG TBL, $N_{s_{R+}}/N_{max,s_{R+}}$ refers to the number of identified s_{R+} structures normalised by its maximum over the range of α_s, and $V_{lar,s_{R+}}/V_{tot,s_{R+}}$ refers to the ratio of the volume of the largest identified s_{R+} structure to the total volume of all identified s_{R+} structures. For the s_{R+} structures in the ZPG TBL, when $\alpha_s \gtrsim 4 \times 10^{-4}$, only a few small and intense objects are detected. As α_s is reduced, new objects are introduced, while previously identified objects grow in size. Eventually, they merge together resulting in a rapid increase of $V_{lar,s_{R+}}/V_{tot,s_{R+}}$. For the s_{R+} structures, this percolation crisis takes place in the approximate range $8\times10^{-8} \lesssim \alpha_s \lesssim 4\times10^{-4}$. For lower values of $\alpha_s \lesssim 8 \times 10^{-8}$, $V_{lar,s_{R+}}/V_{tot,s_{R+}} \approx 1$ as one large object contributes to most of the total volume. The percolation threshold is defined as the value of α_s for which the gradient of $V_{lar,s_{R+}}/V_{tot,s_{R+}}$ is maximum. For the s_{R+} structures, the maximum gradient occurs at a value of 8×10^{-5} and it falls within the range of the percolation crisis. Therefore, the chosen threshold for the s_{R+} structures in the present study is $\alpha_{s_{R+}} = 8 \times 10^{-5}$ and it is denoted by the vertical dotted line in figure 6.2a.

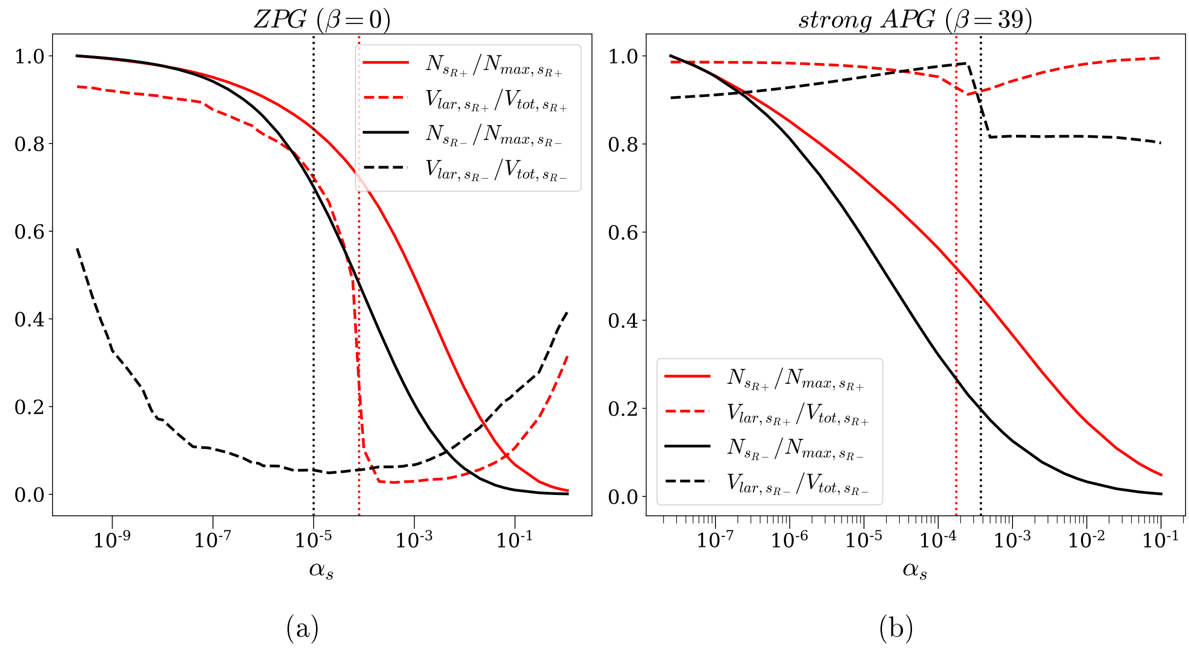

Figure 6.2: Percolation diagram for the identification of intense dissipative structures in (a) the ZPG TBL and (b) the strong APG TBL. The vertical dotted lines indicate the chosen thresholds ($\alpha_{s_{R+}}, \alpha_{s_{R-}}$) for each topological structures, respectively.

Similarly, for the s_{R-} structures, $N_{s_{R-}}/N_{max,s_{R-}}$ refers to the number of identified s_{R-}

Case	ZPG	strong APG
$\alpha_{s_{R+}}$	8×10^{-5}	1.75×10^{-4}
$\alpha_{s_{R-}}$	1×10^{-5}	3.75×10^{-4}

Table 6.1: The chosen thresholds, within the respective percolation crisis range, for the intense dissipative structures in the ZPG TBL and the strong APG TBL.

structures normalised by its maximum over the range of α_s, and $V_{lar,s_{R-}}/V_{tot,s_{R-}}$ refers to the ratio of the volume of the largest identified s_{R-} structure to the total volume of all identified s_{R-} structures. For the s_{R-}, the maximum gradient of $V_{lar,s_{R-}}/V_{tot,s_{R-}}$ occurs at a value of 2×10^{-10} as shown in figure 6.2a. As this threshold value is close to zero, almost all the points belonging to the particular topology type are selected. Therefore, for the s_{R-} structures in the ZPG TBL, a threshold value of $\alpha_{s_{R-}} = 1 \times 10^{-5}$ is chosen, which also lies within the respective percolation crisis range. In the strong APG TBL, all of the chosen thresholds correspond to the value for which the gradient of $V_{lar,k}/V_{tot,k}$ is maximum, where 'k' refers to each dissipative structure type considered in the present study. The chosen thresholds for all the intense dissipative structures in the ZPG and the strong APG TBLs are summarised in table 6.1 and are denoted by vertical dotted lines in their respective percolation diagrams illustrated in figure 6.2.

6.2.2 Intense vortical structures

The intense vortical structures, which lie above and farther away from the $D_A = 0$ curve, have large positive values of Q_A indicating regions of strong local vorticity. As given by Equation 6.4, Q_A is the sum of Q_s and Q_w. The positive contribution to Q_A is from the second invariant of W_{ij} (Q_w), which is always a positive quantity. Q_w is proportional to the enstrophy density (the square of the vorticity), given by

$$Q_w = -\frac{1}{2} W_{ij} W_{ij}. \tag{6.9}$$

Case	ZPG	strong APG
$\alpha_{\omega_{R+}}$	6×10^{-5}	7.5×10^{-6}
$\alpha_{\omega_{R-}}$	0.002	0.0001

Table 6.2: The chosen thresholds, within the respective percolation crisis range, for the intense vortical structures in the ZPG TBL and the strong APG TBL.

Based on the relation in Equation 6.9, intense vortical structures are defined as regions of connected points in the flow that satisfy two conditions simultaneously. The first

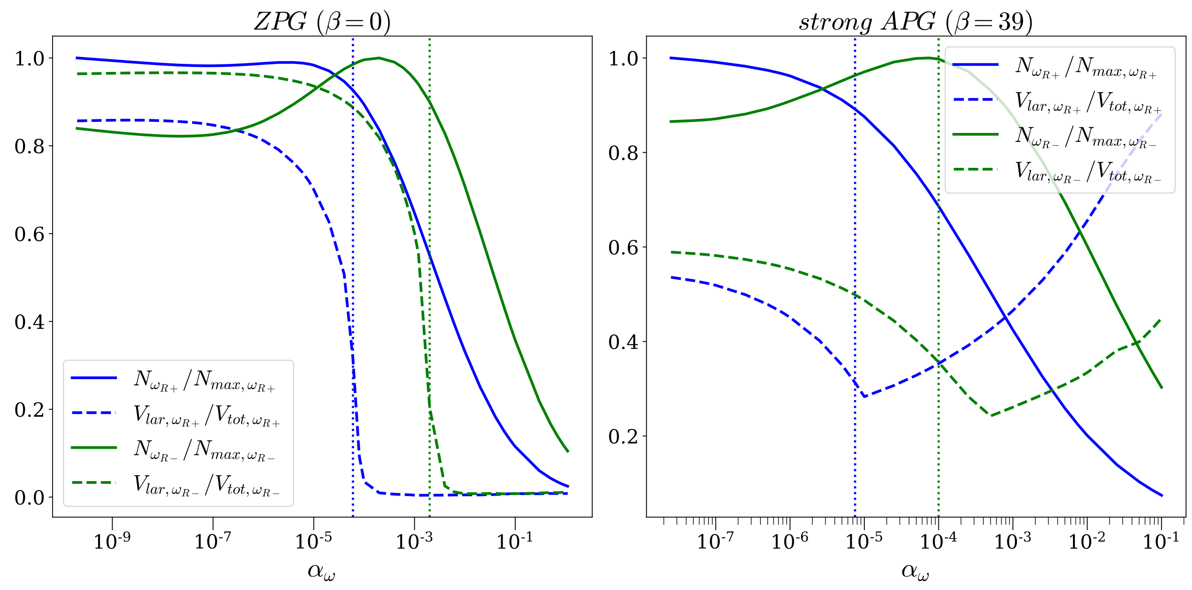

(a) (b)

Figure 6.3: Percolation diagram for the identification of intense vortical structures in (a) the ZPG TBL and (b) the strong APG TBL. The vertical dotted lines indicate the chosen thresholds ($\alpha_{\omega_{R+}}, \alpha_{\omega_{R-}}$) for each topological structures, respectively.

condition is given by

$$D_A(x, y, z) > \alpha_\omega \sigma_{D_A}(x, y), \tag{6.10}$$

where α_ω is a constant threshold and $\sigma_{D_A} = \sqrt{\overline{(D_A{}')^2}}$ is the standard deviation of D_A. The second condition is that all the points within a vortical structure should belong to the same topology in the (Q_A,R_A)-plane. The two topologies (Chong et al., 1998, 1990) considered here are unstable focus/contracting (UF/C) given by $D_A > 0$, $R_A > 0$ and stable focus/stretching (SF/S) given by $D_A > 0$, $R_A < 0$. Both of these topologies have positive D_A values ($D_A > 0$). Therefore, based on the sign of R_A, intense vortical structures belonging to UF/C topology are denoted as ω_{R+} and those in SF/S topology as ω_{R-}. The ω_{R+} and ω_{R-} structures are referred to as $\omega_{R,both}$. Similar to the intense dissipative structures, point connectivity is defined based on the six orthogonal neighbours and α_ω is obtained from a similar percolation analysis for each vortical structure type. The percolation diagrams for the identification of ω_{R+} and ω_{R-} structures in both the TBLs are shown in figure 6.3 and the vertical dotted lines refer to the values for which the gradient of $V_{lar,k}/V_{tot,k}$ is maximum in each case. The chosen thresholds for all the vortical structures ($\alpha_{\omega_{R+}}, \alpha_{\omega_{R-}}$) are summarised in table 6.2.

6.2.3 Intense Reynolds stress structures

Intense Reynolds stress quadrant structures are defined as regions of connected points in the flow that satisfy two conditions simultaneously. The first condition (Lozano-Durán et al., 2012) is given by

$$|u'v'(x,y,z)| > Hu'_{rms}(x,y)v'_{rms}(x,y), \tag{6.11}$$

where u'_{rms} and v'_{rms} represent the root mean square of the respective velocity fluctuations u' and v', and H is a constant threshold known as the hyperbolic-hole size. The second condition is that all the points within a Reynolds stress structure should belong to the same quadrant in the (u',v')-space. Following Wallace et al. (1972), the quadrants are defined as follows: Q1 represents $u' > 0, v' > 0$, Q2 represents $u' < 0, v' > 0$, Q3 represents $u' < 0, v' < 0$, and Q4 represents $u' > 0, v' < 0$. All of the intense quadrant structures (Q1, Q2, Q3, Q4) are referred to as Q_{uv}. Based on the sign of the product $u'v'$, the Q2 and Q4 structures are denoted as Q_{uv-} and, the Q1 and Q3 structures as Q_{uv+}. Point connectivity is defined based on the six orthogonal neighbours and the threshold H is obtained from a similar percolation analysis for each quadrant type.

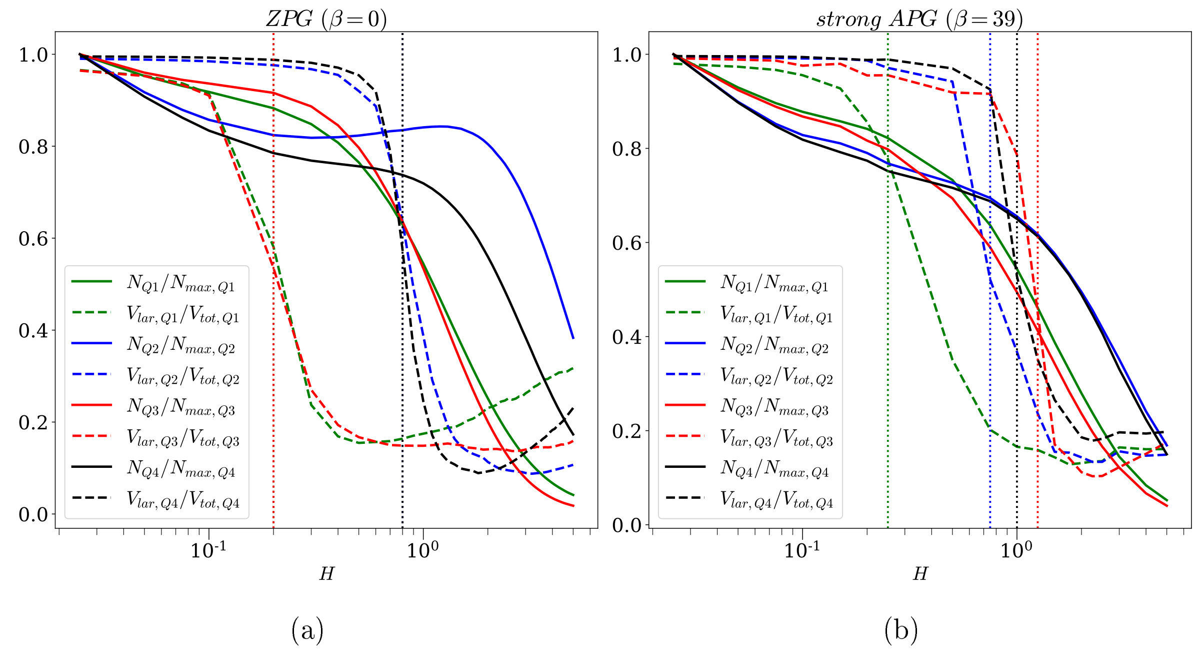

Figure 6.4: Percolation diagram for the identification of intense Reynolds stress quadrant structures in (a) the ZPG TBL and (b) the strong APG TBL. The vertical dotted lines indicate the chosen thresholds (H_1, H_2, H_3, H_4) for each quadrant structures, respectively.

The percolation diagrams for the identification of Q_{uv} structures in both the TBLs are shown in figure 6.4 and the vertical dotted lines refer to the threshold values for which the gradient of $V_{lar,k}/V_{tot,k}$ is maximum in each quadrant type. The chosen thresholds,

Case	ZPG	strong APG
H_1	0.20	0.25
H_2	0.80	0.75
H_3	0.20	1.25
H_4	0.80	1.0

Table 6.3: The chosen thresholds, within the respective percolation crisis range, for the intense Reynolds stress structures in the ZPG TBL and the strong APG TBL.

which lie within the respective percolation crisis range, for all the quadrant structures (H_1, H_2, H_3, H_4) are summarised in table 6.3.

6.3 Geometric characteristics of the intense structures

In this section, the geometric characteristics of the intense structures identified by the above procedures are investigated. Each structure is circumscribed by a rectangular box aligned with the Cartesian axes, whose streamwise, wall-normal and spanwise extents are denoted by l_x, l_y and l_z, respectively. The minimum and maximum distances of each structure from the wall are denoted by y_{min} and y_{max}, respectively. The position of the mid-height of the circumscribing box is denoted as y_c and $l_y = y_{max} - y_{min}$. Following Maciel et al. (2017b), very small intense structures with a volume $V_{struct} < (3\Delta x)^3$ are disregarded as their sizes are not well resolved on the grid. The structures that touch the boundaries of the flow domain are also rejected as their sizes are indeterminate. In this study, wall-attached structures are defined as those for which $y_{min} < 0.2\overline{\delta_1}$, where $\overline{\delta_1}$ is the mean displacement thickness within the DoI. The number of statistically independent flow fields (n_f) used to identify the intense structures in the ZPG TBL and the strong APG TBL are respectively 50 and 40. The reference volume V_{BL} is defined as the volume from the wall up to the mean boundary layer thickness within the DoI.

6.3.1 Geometric characters of the intense dissipative structures

With the present identification methodology, a total of 3.42×10^6 $s_{R,both}$ structures are identified in the ZPG TBL and 7.13×10^6 $s_{R,both}$ structures in the strong APG TBL.

The relative volume and number of intense dissipative structures (s_{R+} and s_{R-}) are summarised in table 6.4, where $V_{tot,s_{R,both}}$ is the total volume occupied by the s_{R+} and s_{R-} structures, and $N_{s_{R,both}}$ is the total number of identified s_{R+} and s_{R-} structures. In the ZPG TBL, the s_{R+} structures occupy 83.6% of the total volume occupied by all the

Case	ZPG	strong APG
s_{R+}	83.6% of $V_{tot,s_{R,both}}$ 69.1% of $N_{s_{R,both}}$	89.0% of $V_{tot,s_{R,both}}$ 79.4% of $N_{s_{R,both}}$
attached s_{R+}	29.8% of $V_{tot,s_{R+}}$ 15.3% of $N_{s_{R+}}$	14.1% of $V_{tot,s_{R+}}$ 9.4% of $N_{s_{R+}}$
s_{R-}	16.4% of $V_{tot,s_{R,both}}$ 30.9% of $N_{s_{R,both}}$	11.0% of $V_{tot,s_{R,both}}$ 20.6% of $N_{s_{R,both}}$
attached s_{R-}	0.3% of $V_{tot,s_{R-}}$ 0.6% of $N_{s_{R-}}$	8.7% of $V_{tot,s_{R-}}$ 12.5% of $N_{s_{R-}}$
$s_{R,both}$	6.07% of V_{BL}	1.58% of V_{BL}

Table 6.4: Number and volume proportion of the intense dissipative structures (s_{R+} and s_{R-}) in the ZPG TBL and the strong APG TBL, where $V_{tot,s_{R,both}}$ is the total volume occupied by the s_{R+} and s_{R-} structures.

intense dissipative structures and represent 69.1% of $N_{s_{R,both}}$. Similarly, the strong APG TBL also shows less propensity for the s_{R-} structures, where the relative volume and number of the s_{R+} structures have increased to 89.0% and 79.4%, respectively.Figure 6.5 shows instantaneous 3D isosurfaces of the s_{R+} and s_{R-} structures in the ZPG TBL and similarly, figure 6.6 shows the $s_{R,both}$ structures in the strong APG TBL. In all the following 3D visualisations, isosurfaces are for the values above the chosen thresholds from the respective percolation analysis. The wall-normal extent of the domain shown in all the 3D visualisations are $14.7\overline{\delta_1}$ and $5.9\overline{\delta_1}$ for the ZPG and strong APG TBLs, respectively. The isosurfaces are coloured based on the distance from the wall. The flow is from top-left to bottom-right in all the 3D visualisations. The isosurfaces in figures 6.5 and 6.6 clearly show that there is a greater propensity for the s_{R+} structures than the s_{R-} structures in both the TBLs.

The volume occupied by the $s_{R,both}$ structures relative to the reference volume V_{BL} is 6.07% in the ZPG TBL as shown in table 6.4 and it has reduced to 1.58% in the strong APG TBL. However, the number of identified $s_{R,both}$ structures ($N_{s_{R,both}}$) has increased by 2.1 times in the strong APG TBL when compared to the ZPG TBL. This shows that the intense dissipative structures have become finer in the strong APG TBL.

As shown in table 6.4, the wall-attached s_{R+} structures in the ZPG TBL represent 29.8% of the total volume of s_{R+} structures and 15.3% of their total number. In the strong APG TBL, the relative volume and number of wall-attached s_{R+} structures has decreased

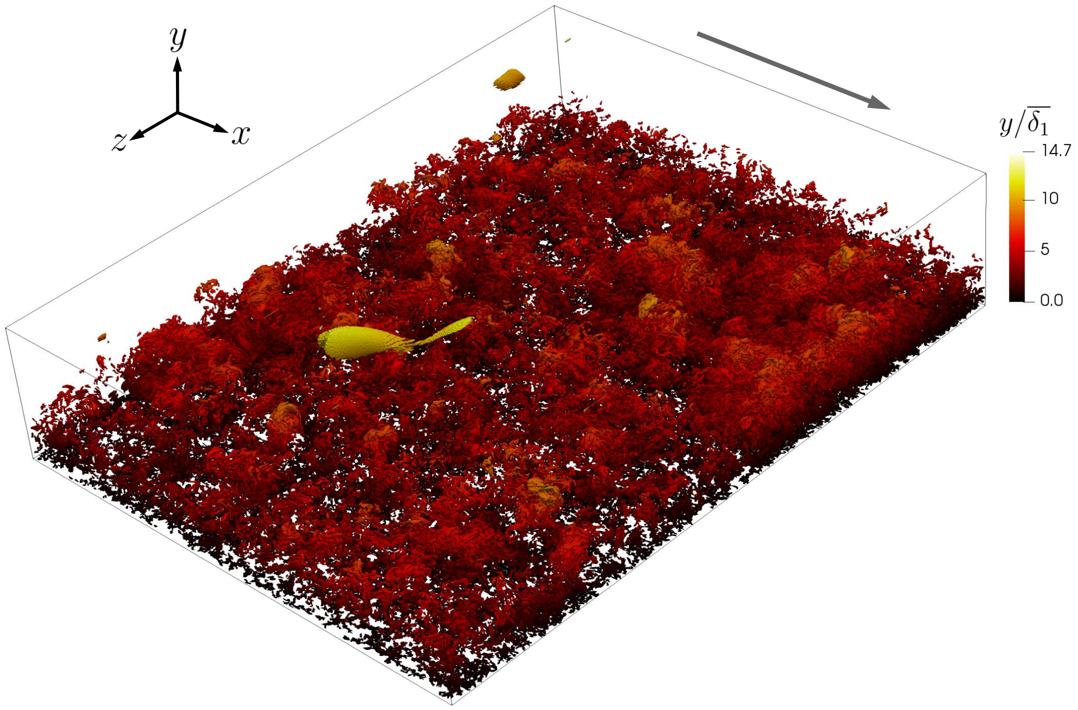

(a)

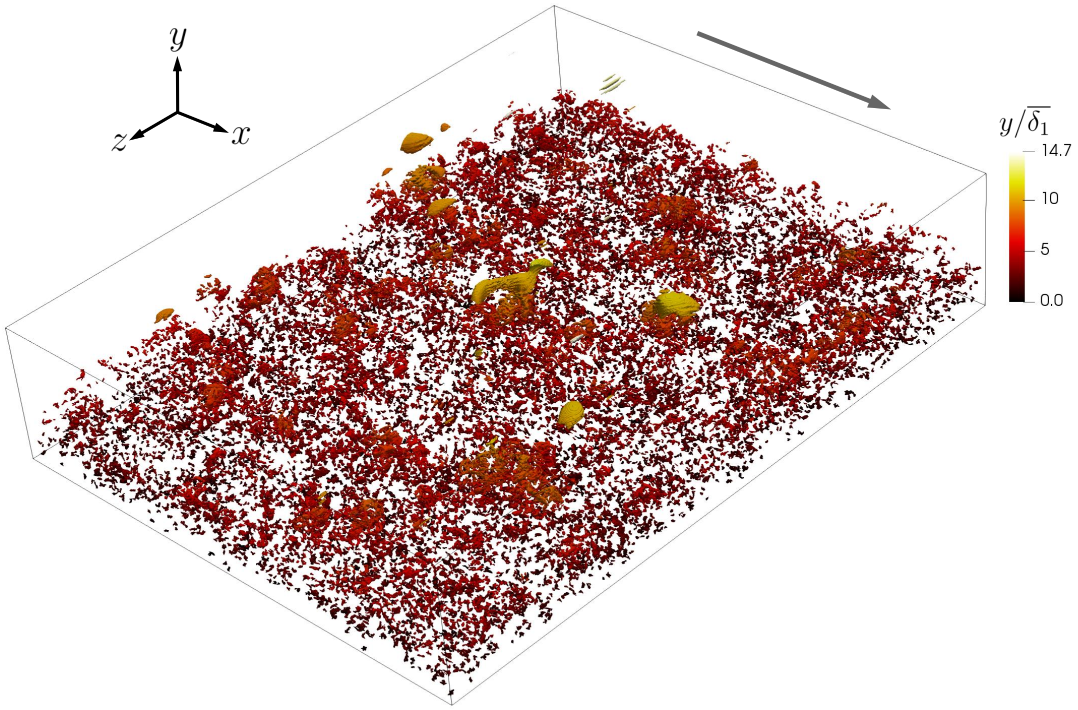

(b)

Figure 6.5: Instantaneous isosurfaces of (a) s_{R+} and (b) s_{R-} structures in the DoI of the ZPG TBL. The flow is from top-left to bottom-right as denoted by the arrow. The structures are coloured based on the distance from the wall. The size of the box in x, y and z directions are $54.4\overline{\delta_1}$, $14.7\overline{\delta_1}$ and $72.0\overline{\delta_1}$, respectively.

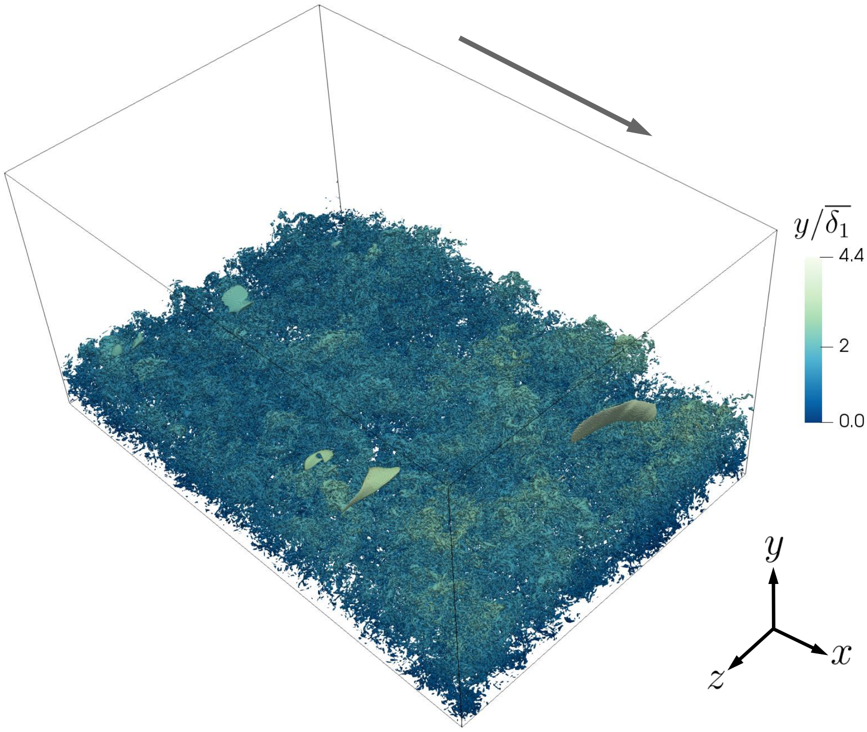

(a)

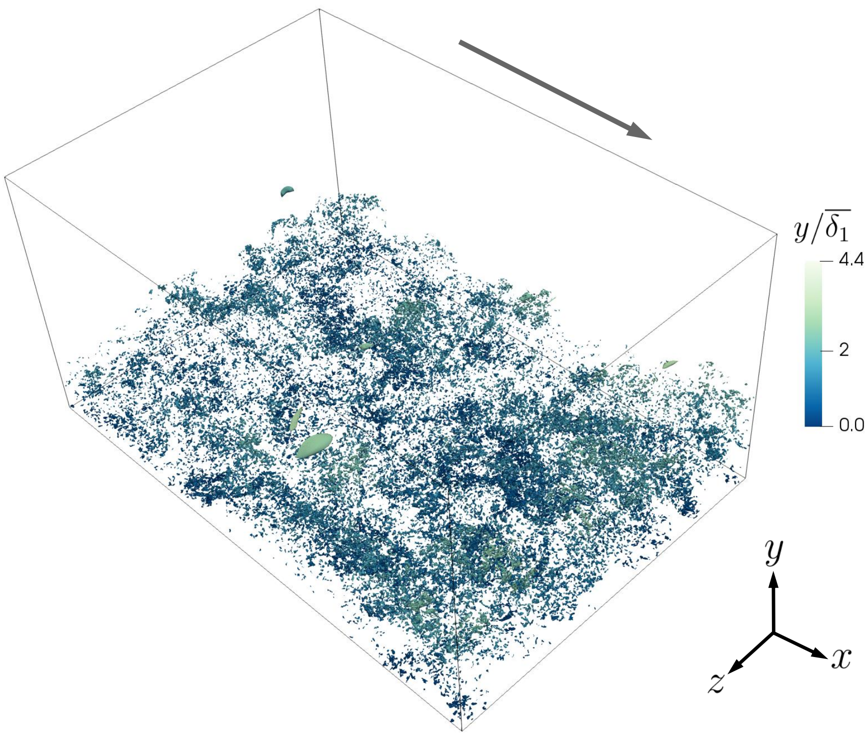

(b)

Figure 6.6: Instantaneous isosurfaces of (a) s_{R+} and (b) s_{R-} structures in the DoI and buffer domain of the strong APG TBL. The flow is from top-left to bottom-right as denoted by the arrow. The structures are coloured based on the distance from the wall. The size of the box in x, y and z directions are $11.3\overline{\delta_1}$, $5.9\overline{\delta_1}$ and $7.7\overline{\delta_1}$, respectively.

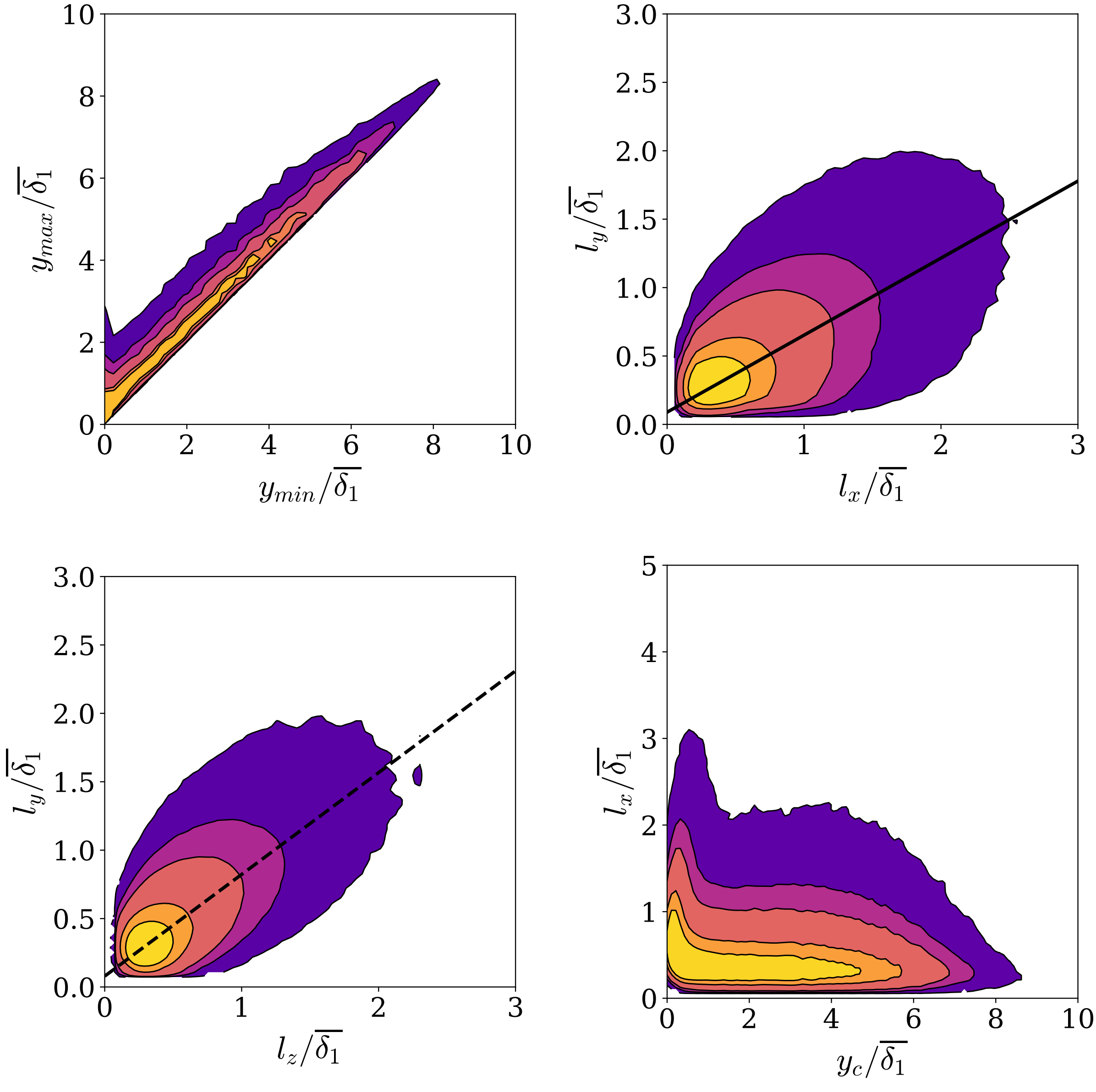

Figure 6.7: Geometrical characteristics of s_{R+} structures in the ZPG TBL. The contour lines contain 50, 70, 90, 95, and 99% of the data. Solid line represents $l_y \approx 0.56 l_x$. Dashed line represents $l_y \approx 0.74 l_z$.

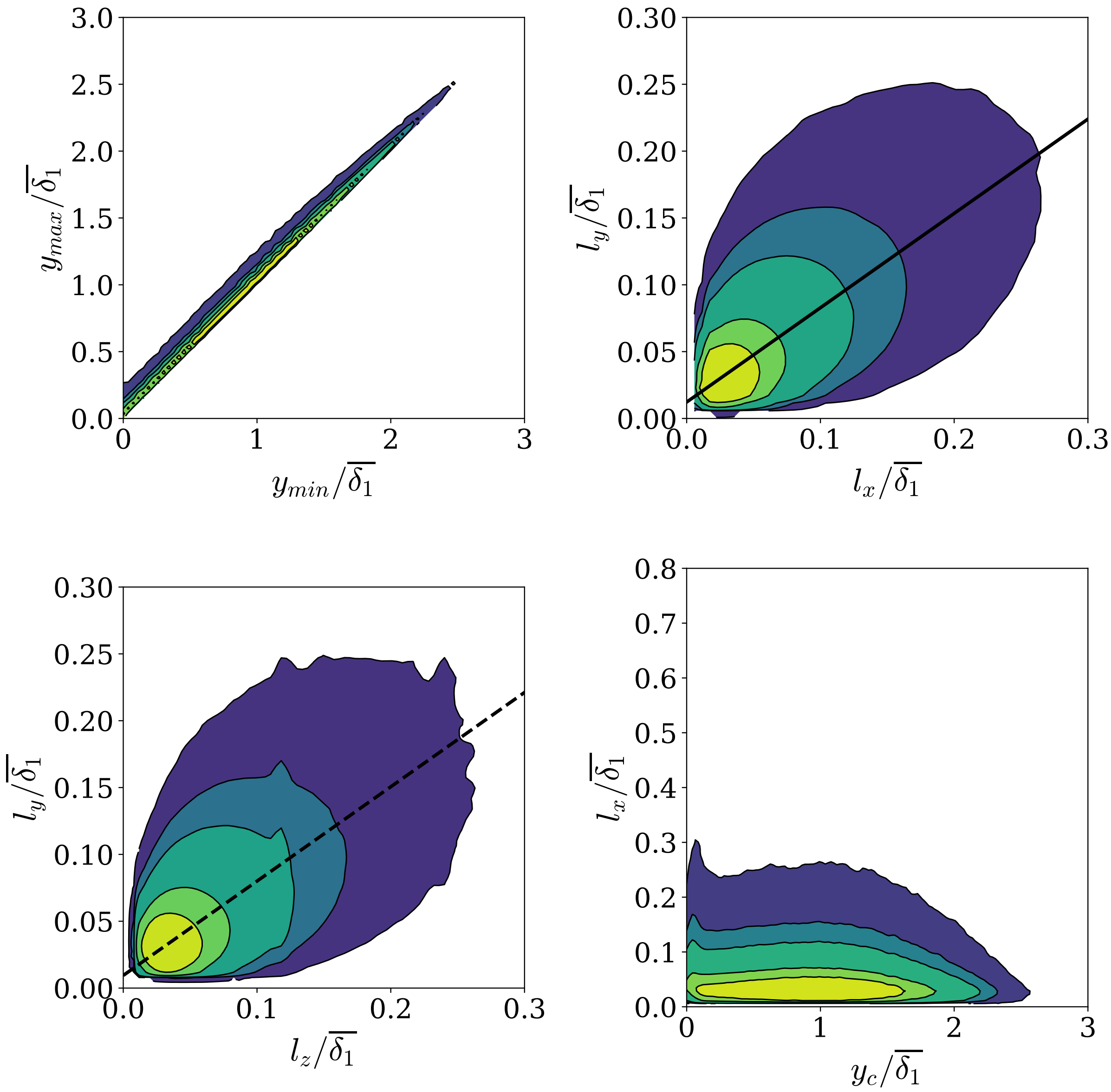

Figure 6.8: Geometrical characteristics of s_{R+} structures in the strong APG TBL. The contour lines contain 50, 70, 90, 95, and 99% of the data. Solid line represents $l_y \approx 0.71 l_x$. Dashed line represents $l_y \approx 0.71 l_z$.

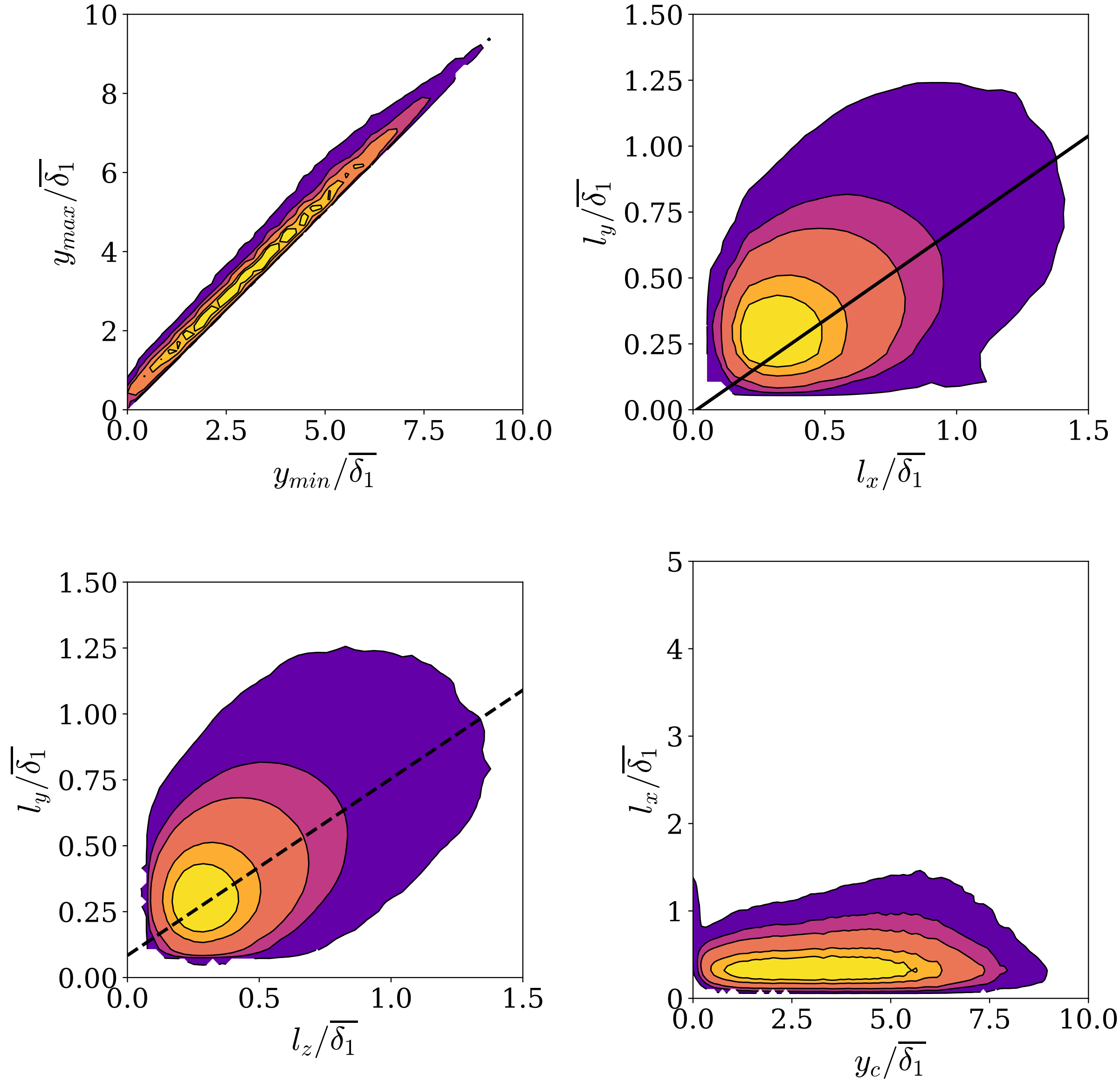

Figure 6.9: Geometrical characteristics of s_{R-} structures in the ZPG TBL. The contour lines contain 50, 70, 90, 95, and 99% of the data. Solid line represents $l_y \approx 0.70 l_x$. Dashed line represents $l_y \approx 0.67 l_z$.

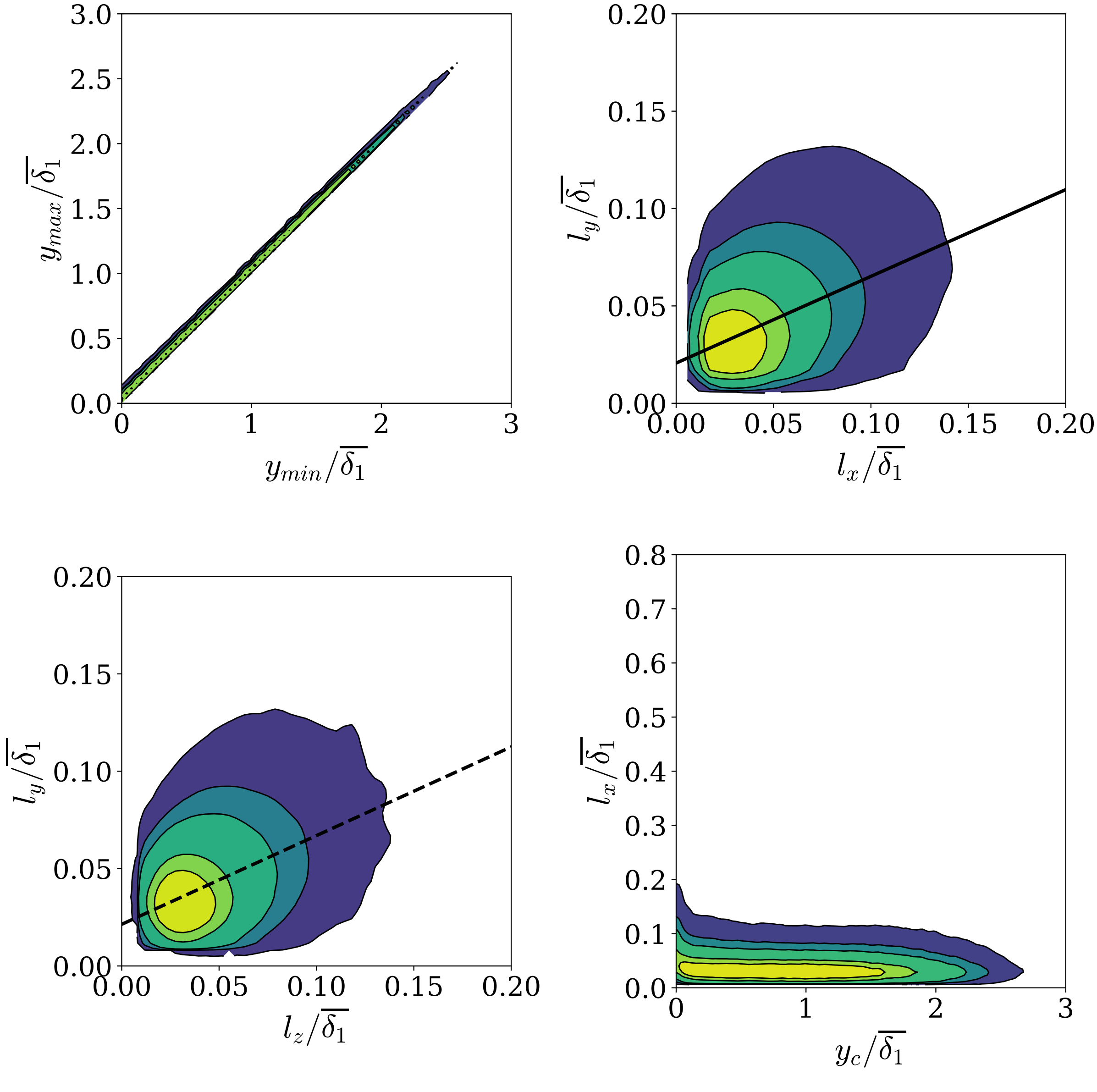

Figure 6.10: Geometrical characteristics of s_{R-} structures in the strong APG TBL. The contour lines contain 50, 70, 90, 95, and 99% of the data. Solid line represents $l_y \approx 0.45 l_x$. Dashed line represents $l_y \approx 0.46 l_z$.

to 14.1% and 9.4%, respectively, showing that the volume and number proportion of detached s_{R+} structures have increased in the strong APG TBL. Figure 6.7 shows the joint probability density functions (JPDFs) of y_{min} and y_{max}, l_x and l_y, l_z and l_y, and between l_x and y_c for the s_{R+} structures in the ZPG TBL. Similarly, figure 6.8 shows the JPDFs associated with the s_{R+} structures in the strong APG TBL. In all the JPDFs between the streamwise (l_x) and wall-normal (l_y) extents, the solid line represents the mean l_y at a given l_x. Similarly, in all the JPDFs between spanwise (l_z) and wall-normal (l_y) extents, the dashed line represents the mean l_y at a given l_z. The colormap used for the JPDFs in the ZPG TBL is different from that of the strong APG TBL for easy identification. When compared to the strong APG TBL, the s_{R+} structures in the ZPG TBL are generally bigger in all the directions relative to the mean displacement thickness ($\overline{\delta_1}$). As illustrated by the JPDFs of the ZPG TBL in figure 6.7, the s_{R+} structures form a self-similar family of streamwise elongated structures with the aspect ratio of their sizes following the linear law $l_x \approx 1.8 l_y \approx 1.3 l_z$. However, as shown in figure 6.8, the s_{R+} structures in the strong APG TBL are less streamwise extended than the ZPG TBL following the ratio $l_x \approx 1.4 l_y$, while the relationship between the wall-normal and spanwise extents remains the same as $l_y \approx 0.7 l_z$. As illustrated by the JPDF of l_x and y_c, it is less likely to find the streamwise elongated s_{R+} structures closer to the wall in the strong APG TBL than in the ZPG TBL, which is consistent with the higher relative volume and number of detached s_{R+} objects in the strong APG TBL.

In the ZPG TBL, the wall-attached s_{R-} structures represent only 0.3% of the total volume of s_{R-} structures and 0.6% of their total number as shown in table 6.4. In the strong APG TBL, these percentages of the wall-attached s_{R-} structures are respectively 8.7% and 12.5%. However, in both the TBLs, the s_{R-} structures represent a lesser relative volume and number of all the $s_{R,both}$ structures, which is apparent from the instantaneous isosurfaces of the s_{R-} objects illustrated in figures 6.5b and 6.6b. As illustrated by the JPDFs of the ZPG TBL in figure 6.9, the sizes of the s_{R-} structures follow the law $l_x \approx 1.4 l_y \approx 1.0 l_z$. However, the sizes of the s_{R-} structures in the strong APG TBL follow the ratio $l_x \approx 2.2 l_y \approx 1.0 l_z$ as shown in figure 6.10. As shown by the narrower JPDF of y_{min} and y_{max} in the strong APG TBL, the s_{R-} structures in the strong APG TBL are longer objects with a shorter wall-normal extent than those in the ZPG TBL.

6.3.2 Geometric characters of the intense vortical structures

With the present identification methodology, a total of 4.99×10^6 $\omega_{R,both}$ structures are identified in the ZPG TBL and 12.85×10^6 $\omega_{R,both}$ structures in the strong APG TBL.

The relative volume and number of the intense vortical structures (ω_{R+} and ω_{R-}) are summarised in table 6.5, where $V_{tot,\omega_{R,both}}$ is the total volume occupied by the ω_{R+} and

Case	ZPG	strong APG
ω_{R+}	51.8% of $V_{tot,\omega_{R,both}}$ 52.7% of $N_{\omega_{R,both}}$	60.9% of $V_{tot,\omega_{R,both}}$ 58.7% of $N_{\omega_{R,both}}$
attached ω_{R+}	24.1% of $V_{tot,\omega_{R+}}$ 8.6% of $N_{\omega_{R+}}$	14.8% of $V_{tot,\omega_{R+}}$ 10.8% of $N_{\omega_{R+}}$
ω_{R-}	48.2% of $V_{tot,\omega_{R,both}}$ 47.3% of $N_{\omega_{R,both}}$	39.1% of $V_{tot,\omega_{R,both}}$ 41.3% of $N_{\omega_{R,both}}$
attached ω_{R-}	36.2% of $V_{tot,\omega_{R-}}$ 8.9% of $N_{\omega_{R-}}$	14.4% of$V_{tot,\omega_{R-}}$ 12.9% of $N_{\omega_{R-}}$
$\omega_{R,both}$	11.85% of V_{BL}	3.61% of V_{BL}

Table 6.5: Number and volume proportion of the intense vortical structures (ω_{R+} and ω_{R-}) in the ZPG TBL, where $V_{tot,\omega_{R,both}}$ is the total volume occupied by the ω_{R+} and ω_{R-} structures.

ω_{R-} structures, and $N_{\omega_{R,both}}$ is the total number of identified ω_{R+} and ω_{R-} structures. In the ZPG TBL, the ω_{R+} structures occupy 51.8% of the total volume occupied by all the intense vortical structures and represent 52.7% of $N_{\omega_{R,both}}$. Similarly, the strong APG TBL shows less inclination towards the ω_{R-} structures, where the relative volume and number of the ω_{R+} structures have increased to 60.9% and 58.7%, respectively. Figure 6.11 shows instantaneous 3D isosurfaces of the ω_{R+} and ω_{R-} structures in the ZPG TBL and similarly, figure 6.12 shows the $\omega_{R,both}$ structures in the strong APG TBL.

The volume occupied by the $\omega_{R,both}$ structures relative to the reference volume V_{BL} is 11.85% in the ZPG TBL as shown in table 6.5 and it has reduced to 3.61% in the strong APG TBL. However, the number of identified $\omega_{R,both}$ structures ($N_{\omega_{R,both}}$) has increased by 2.6 times in the strong APG TBL when compared to the ZPG TBL. This shows that the intense vortical structures have also become finer in the strong APG TBL.

As shown in table 6.5, in the ZPG TBL, the wall-attached ω_{R+} structures represent 24.1% of the total volume of the ω_{R+} structures. In the strong APG TBL, the relative volume of the wall-attached structures has decreased to 14.8%, showing that the volume proportion of the detached ω_{R+} structures have increased in the strong APG TBL. The joint probability density functions (JPDFs) associated with the ω_{R+} structures in the ZPG TBL and the strong APG TBL are shown in figures 6.13 and 6.14, respectively. When compared to the strong APG TBL, the ω_{R+} structures in the ZPG TBL are generally bigger in all the directions relative to the mean displacement thickness ($\overline{\delta_1}$). As illustrated

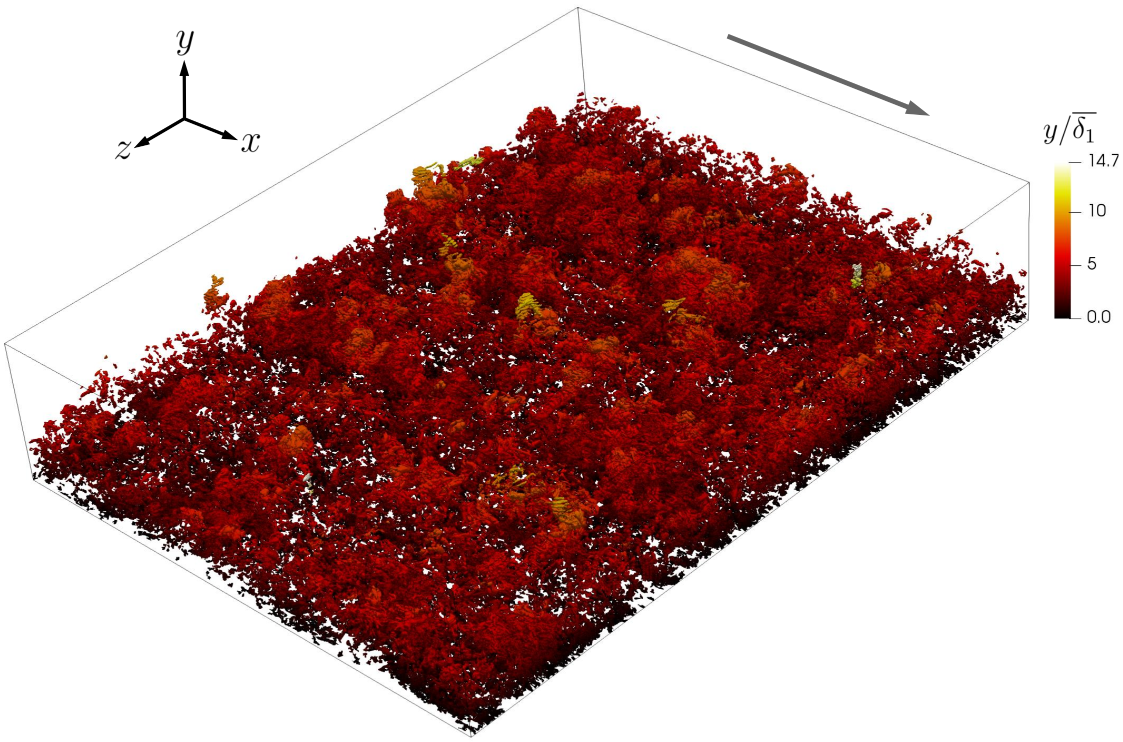

(a)

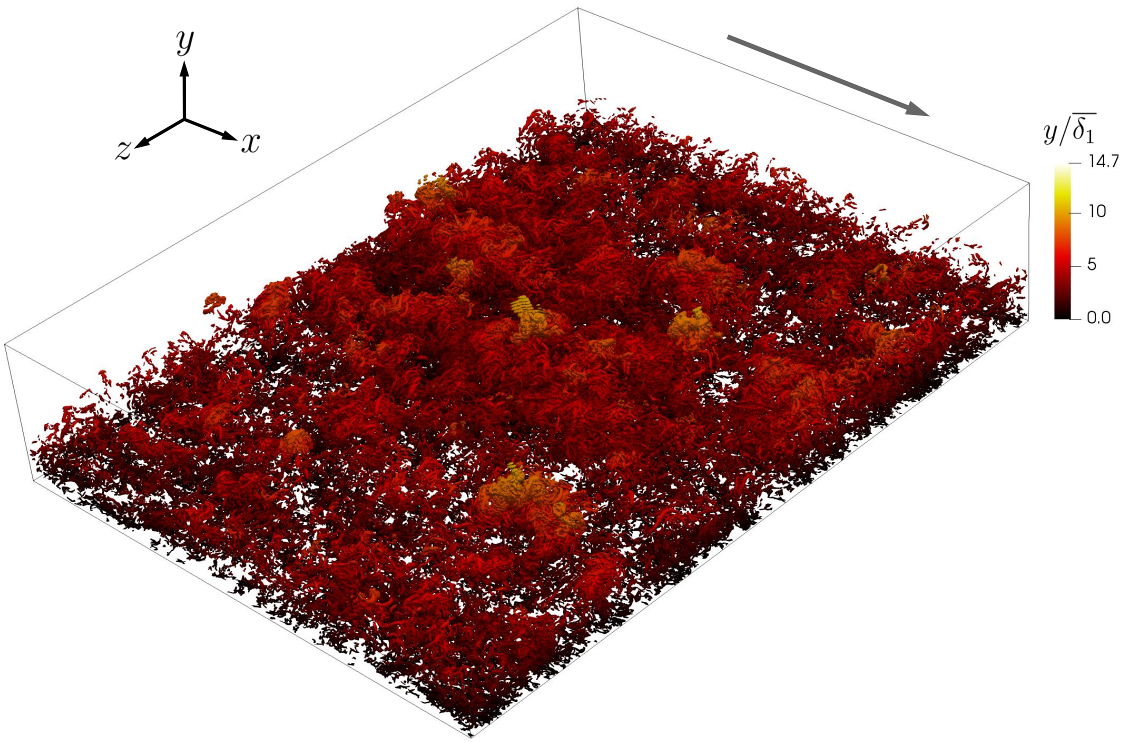

(b)

Figure 6.11: Instantaneous isosurfaces of (a) ω_{R+} and (b) ω_{R-} structures in the DoI of the ZPG TBL. The flow is from top-left to bottom-right as denoted by the arrow. The structures are coloured based on the distance from the wall. The size of the box in x, y and z directions are $54.4\overline{\delta_1}$, $14.7\overline{\delta_1}$ and $72.0\overline{\delta_1}$, respectively.

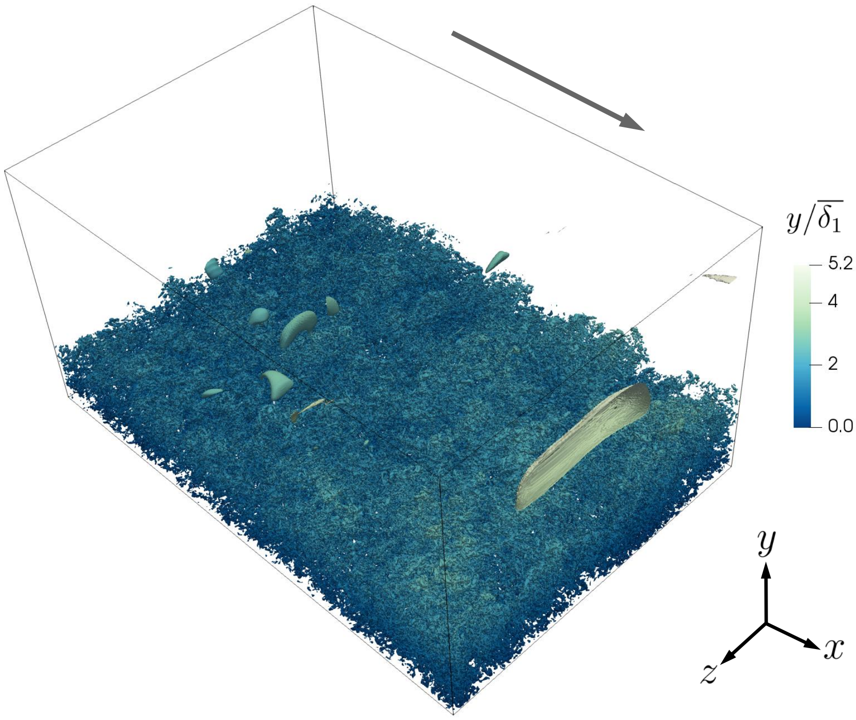

(a)

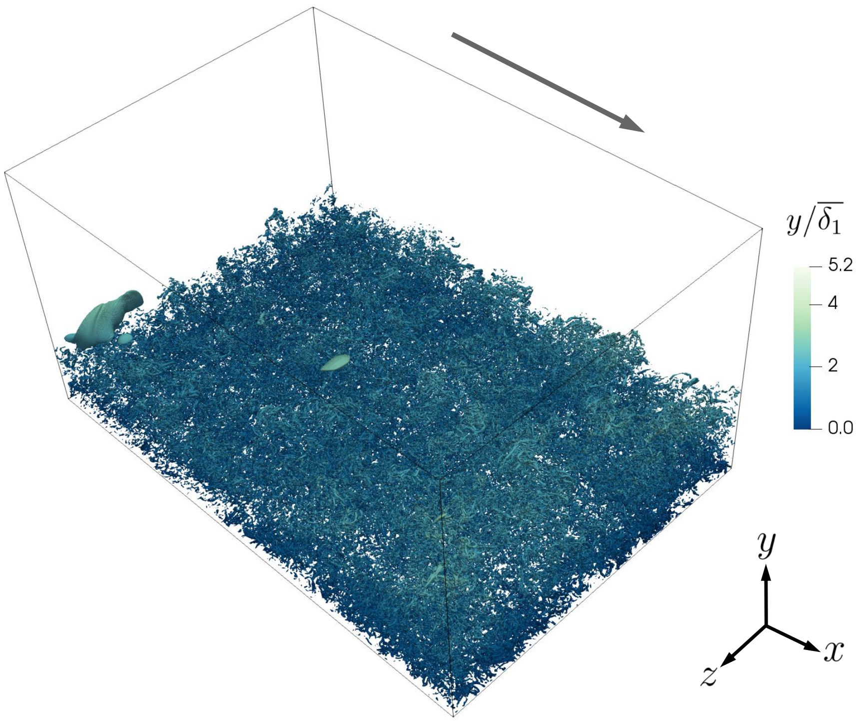

(b)

Figure 6.12: Instantaneous isosurfaces of (a) ω_{R+} and (b) ω_{R-} structures in the DoI and buffer domain of the strong APG TBL. The flow is from top-left to bottom-right as denoted by the arrow. The structures are coloured based on the distance from the wall. The size of the box in x, y and z directions are $11.3\overline{\delta_1}$, $5.9\overline{\delta_1}$ and $7.7\overline{\delta_1}$, respectively.

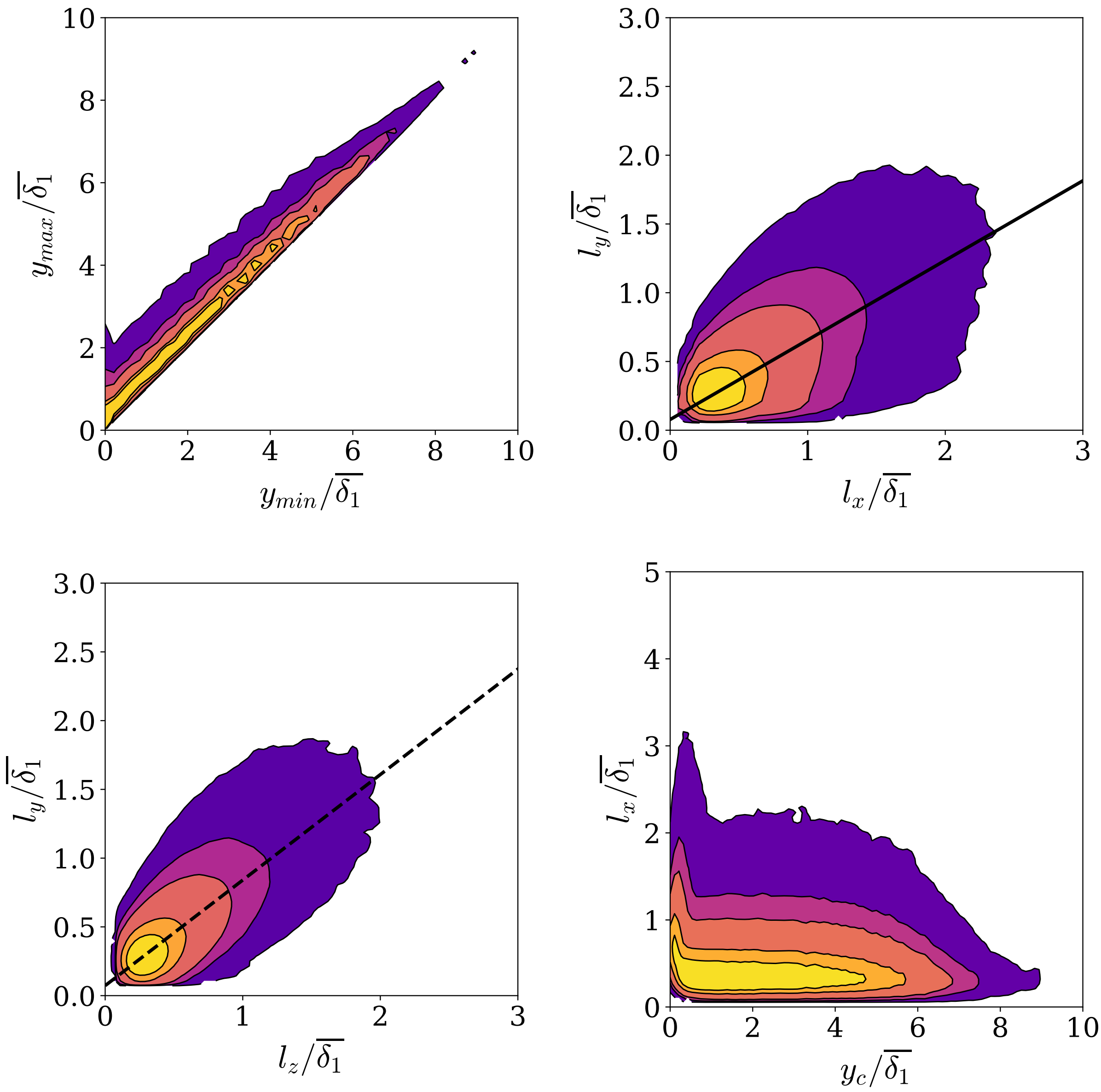

Figure 6.13: Geometrical characteristics of ω_{R+} structures in the ZPG TBL. The contour lines contain 50, 70, 90, 95, and 99% of the data. Solid line represents $l_y \approx 0.58 l_x$. Dashed line represents $l_y \approx 0.77 l_z$.

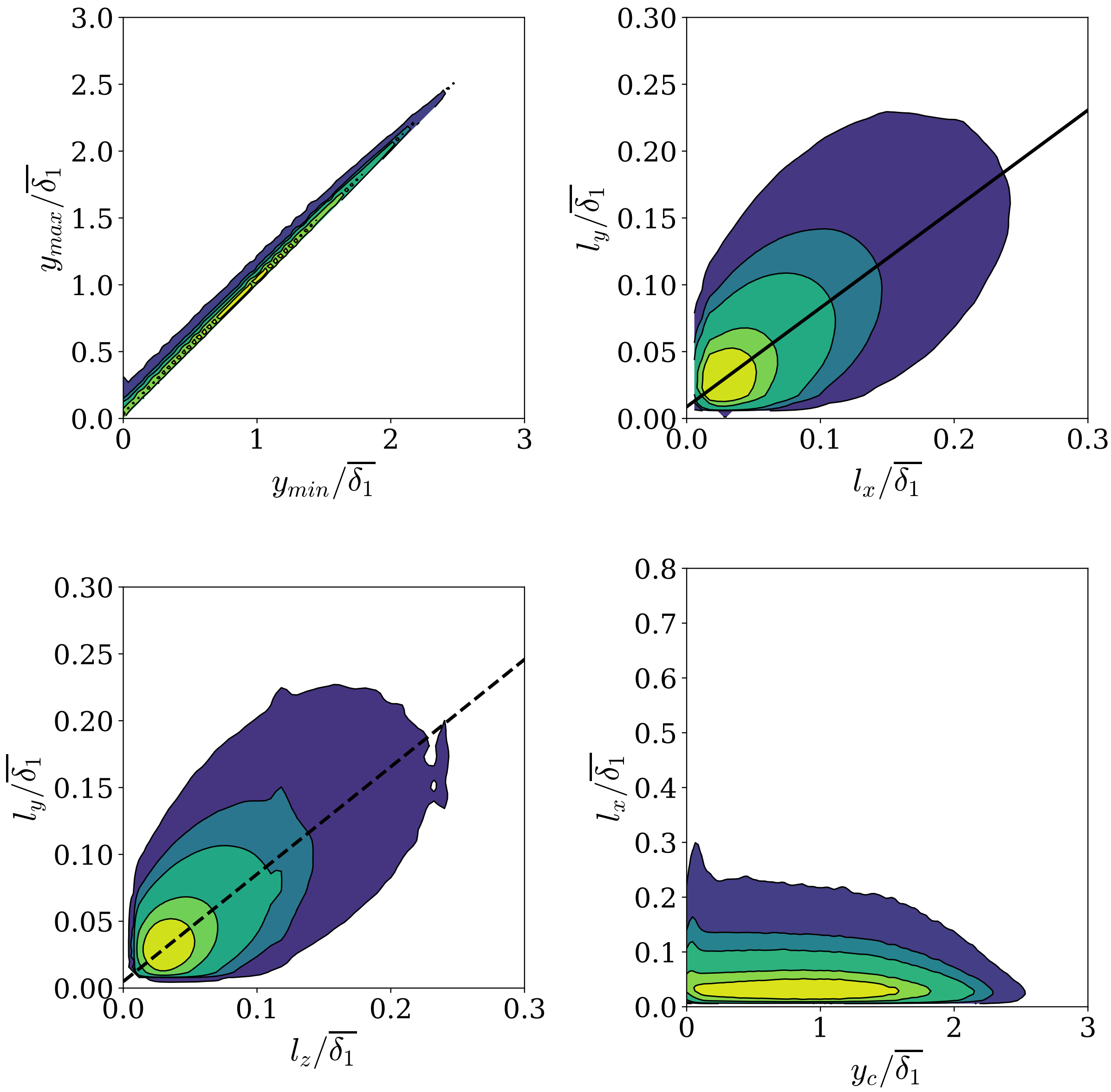

Figure 6.14: Geometrical characteristics of ω_{R+} structures in the strong APG TBL. The contour lines contain 50, 70, 90, 95, and 99% of the data. Solid line represents $l_y \approx 0.74 l_x$. Dashed line represents $l_y \approx 0.80 l_z$.

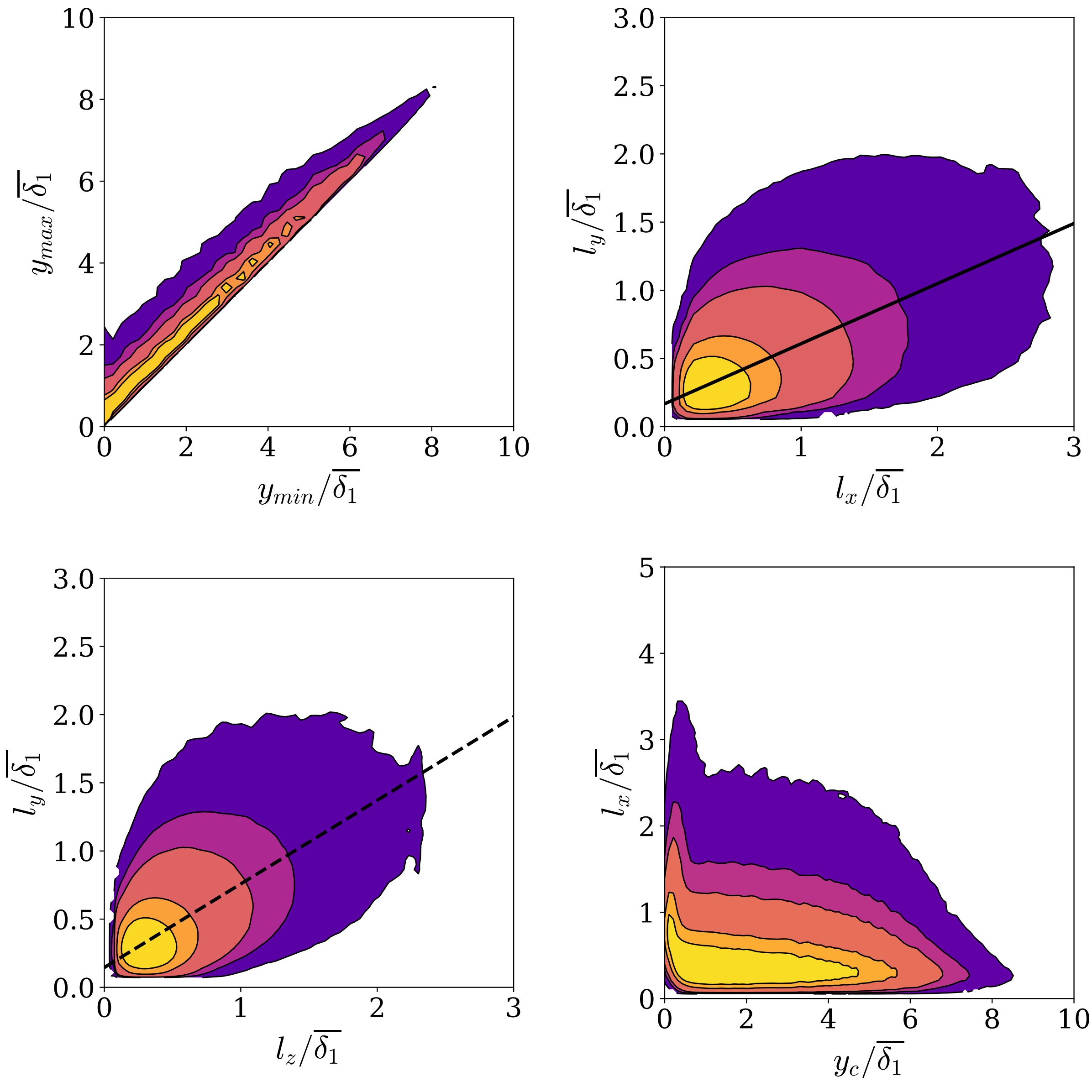

Figure 6.15: Geometrical characteristics of ω_{R-} structures in the ZPG TBL. The contour lines contain 50, 70, 90, 95, and 99% of the data. Solid line represents $l_y \approx 0.44 l_x$. Dashed line represents $l_y \approx 0.61 l_z$.

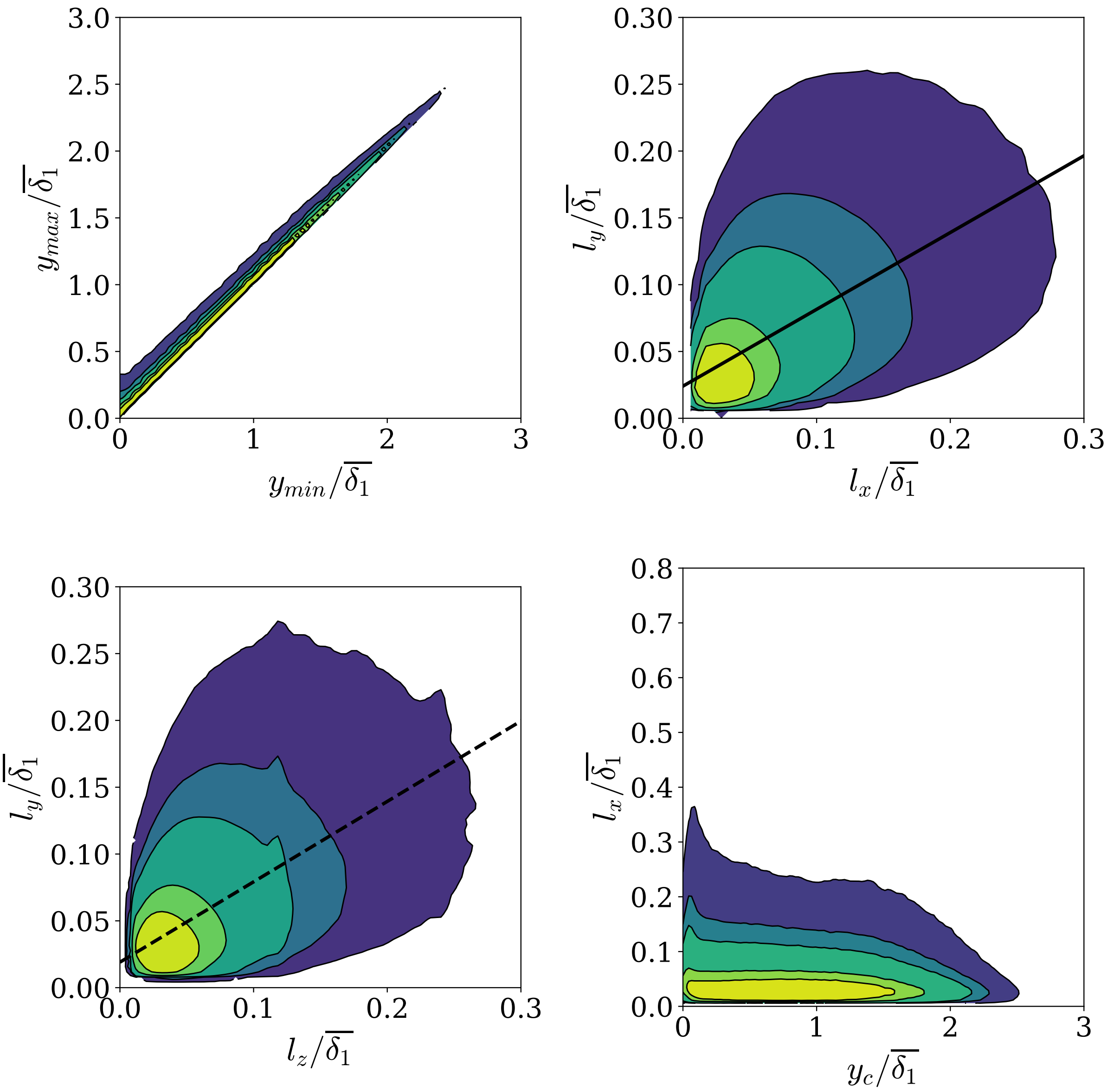

Figure 6.16: Geometrical characteristics of ω_{R-} structures in the strong APG TBL. The contour lines contain 50, 70, 90, 95, and 99% of the data. Solid line represents $l_y \approx 0.57 l_x$. Dashed line represents $l_y \approx 0.60 l_z$.

by the JPDFs of the ZPG TBL in figure 6.13, the ω_{R+} structures form a self-similar family of streamwise elongated structures with the aspect ratio of their sizes following the linear law $l_x \approx 1.7l_y \approx 1.3l_z$. However, as shown in figure 6.14, the ω_{R+} structures in the strong APG TBL are less streamwise extended than the ZPG TBL following the ratio $l_x \approx 1.4l_y$, while the relationship between the wall-normal and spanwise extents remains the same as $l_y \approx 0.8l_z$. As illustrated by the JPDF of l_x and y_c, it is less likely to find the streamwise elongated ω_{R+} structures closer to the wall in the strong APG TBL than in the ZPG TBL, which is consistent with the higher relative volume of the detached s_{R+} objects (85.2% of $V_{tot,\omega_{R+}}$) in the strong APG TBL.

In the ZPG TBL, the wall-attached ω_{R-} structures represent 36.2% of the total volume of the ω_{R-} structures as shown in table 6.5. In the strong APG TBL, the relative volume of the wall-attached ω_{R-} structures has decreased to 14.4%, showing that the volume proportion of the detached ω_{R-} structures have increased in the strong APG TBL. The JPDFs associated with the ω_{R-} structures in the ZPG TBL and the strong APG TBL are shown in figures 6.15 and 6.16, respectively. Similar to the ω_{R+} structures, the sizes of the ω_{R-} structures in the ZPG TBL, relative to the mean displacement thickness ($\overline{\delta_1}$), are generally bigger in all the directions than the structures in the strong APG TBL. As illustrated by the JPDFs of the ZPG TBL in figure 6.15, the ω_{R-} structures follow the law $l_x \approx 2.3l_y \approx 1.4l_z$. However, as shown in figure 6.16, the ω_{R-} structures in the strong APG TBL are less streamwise extended than the ZPG TBL following the ratio $l_x \approx 1.7l_y \approx 1.0l_z$. Similar to the ω_{R+} structures, as illustrated by the JPDF of l_x and y_c, it is less likely to find the streamwise elongated ω_{R-} structures closer to the wall in the strong APG TBL than in the ZPG TBL, which is consistent with the higher relative volume of the detached s_{R-} structures (85.6% of $V_{tot,\omega_{R-}}$) in the strong APG TBL.

6.3.3 Geometric characters of the intense Reynolds stress structures

With the present identification methodology, a total of 1.24×10^6 Q_{uv} structures are identified in the ZPG TBL and 1.35×10^6 Q_{uv} structures in the strong APG TBL.

The relative volume and number of the intense Reynolds stress structures are summarised in table 6.6, where $V_{tot,Q_{uv}}$ is the total volume occupied by the Q_{uv} structures (Q1, Q2, Q3, and Q4), and $N_{Q_{uv}}$ is the total number of identified intense structures in all the four quadrants. In the ZPG TBL, the Q_{uv-} structures occupy 44.9% of the total volume occupied by all the intense Reynolds stress structures, while the Q_{uv+} structures represent 55.1% of $V_{tot,Q_{uv}}$. However, in the strong APG TBL, the Q_{uv-} and Q_{uv+} structures represent almost equal volume proportions (50.3% and 49.7% of $V_{tot,Q_{uv}}$, respectively). The

Case	ZPG	strong APG
Q1	27.0% of $V_{tot,Q_{uv}}$ 31.8% of $N_{Q_{uv}}$	25.9% of $V_{tot,Q_{uv}}$ 36.9% of $N_{Q_{uv}}$
Q2	22.1% of $V_{tot,Q_{uv}}$ 16.5% of $N_{Q_{uv}}$	19.5% of $V_{tot,Q_{uv}}$ 19.9% of $N_{Q_{uv}}$
Q3	28.1% of $V_{tot,Q_{uv}}$ 34.4% of $N_{Q_{uv}}$	23.8% of $V_{tot,Q_{uv}}$ 23.1% of $N_{Q_{uv}}$
Q4	22.8% of $V_{tot,Q_{uv}}$ 17.3% of $N_{Q_{uv}}$	30.8% of $V_{tot,Q_{uv}}$ 20.1% of $N_{Q_{uv}}$
Q2+Q4 (Q_{uv-})	44.9% of $V_{tot,Q_{uv}}$ 33.8% of $N_{Q_{uv}}$	50.3% of $V_{tot,Q_{uv}}$ 40.0% of $N_{Q_{uv}}$
attached Q2+Q4	75.0% of $V_{tot,Q2+Q4}$ 39.6% of N_{Q2+Q4}	60.3% of $V_{tot,Q2+Q4}$ 21.0% of N_{Q2+Q4}
Q1+Q3 (Q_{uv+})	55.1% of $V_{tot,Q_{uv}}$ 66.2% of $N_{Q_{uv}}$	49.7% of $V_{tot,Q_{uv}}$ 60.0% of $N_{Q_{uv}}$
attached Q1+Q3	58.7% of $V_{tot,Q1+Q3}$ 29.3% of N_{Q1+Q3}	25.5% of $V_{tot,Q1+Q3}$ 16.1% of N_{Q1+Q3}
Q_{uv}	15.91% of V_{BL}	2.68% of V_{BL}

Table 6.6: Number and volume proportion of the intense Reynolds stress structures (Q1, Q2, Q3, and Q4) in the ZPG TBL and the strong APG TBL, where $V_{tot,Q_{uv}}$ is the total volume occupied by the intense structures in all the quadrants.

relative number of identified Q_{uv+} structures is higher in both the TBLs than the Q_{uv-} structures as shown in table 6.6. Figure 6.17 shows instantaneous 3D isosurfaces of the Q_{uv-} (Q2 and Q4) structures in the ZPG TBL and similarly, figure 6.18 shows the Q_{uv-} structures in the strong APG TBL.

In the ZPG TBL, the volume occupied by the Q_{uv} structures is 15.91% of V_{BL} as given in table 6.6 and it has reduced to 2.68% of V_{BL} in the strong APG TBL. However, the number of identified Q_{uv} structures ($N_{Q_{uv}}$) in the ZPG TBL is 1.24×10^6 and it has increased to 1.35×10^6 in the strong APG TBL. This shows that the intense Reynolds stress structures have also become finer in the strong APG TBL.

As shown in table 6.6, in the ZPG TBL, the wall-attached Q_{uv-} structures represent

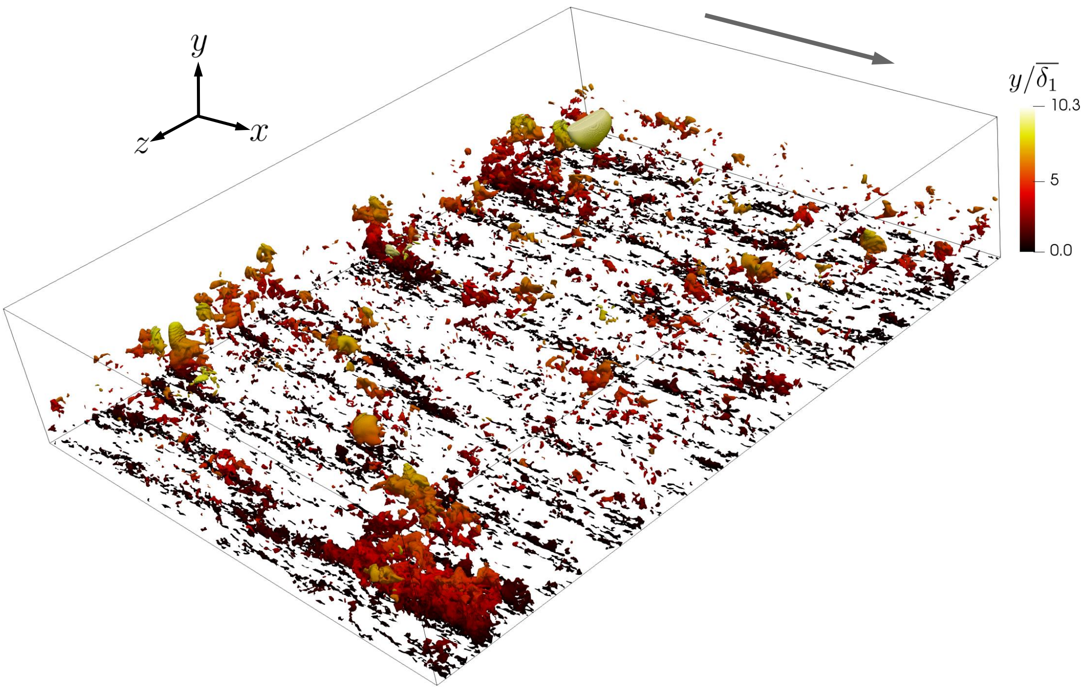

(a)

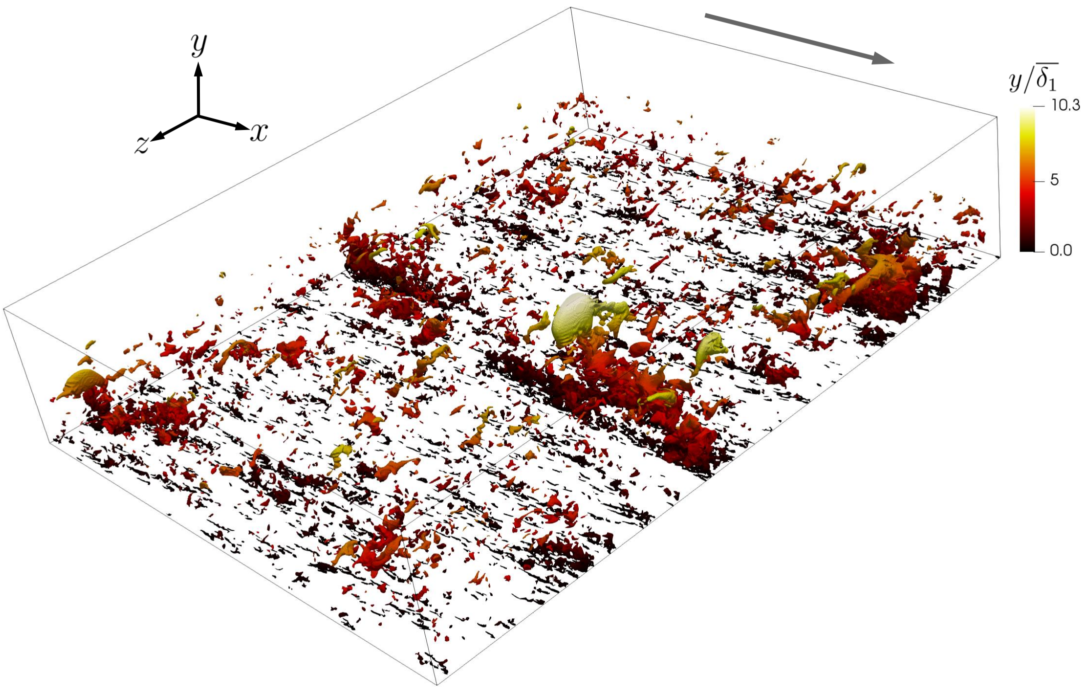

(b)

Figure 6.17: Instantaneous isosurfaces of the (a) Q2 and (b) Q4 Reynolds stress structures in the DoI of the ZPG TBL. The flow is from top-left to bottom-right as denoted by the arrow. The structures are coloured based on the distance from the wall. The size of the box in x, y and z directions are $54.4\overline{\delta_1}$, $14.7\overline{\delta_1}$ and $72.0\overline{\delta_1}$, respectively.

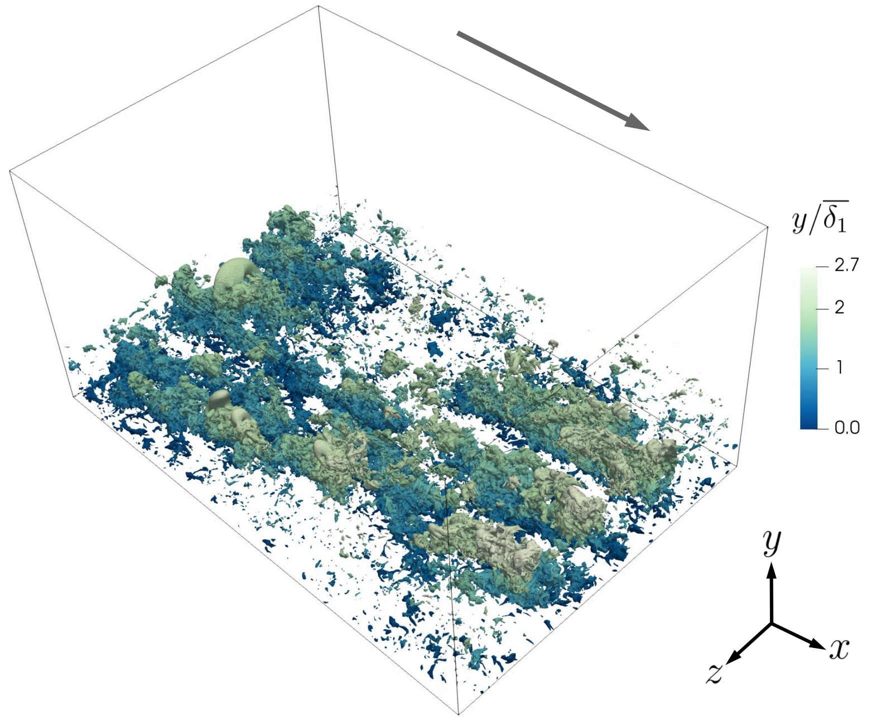

(a)

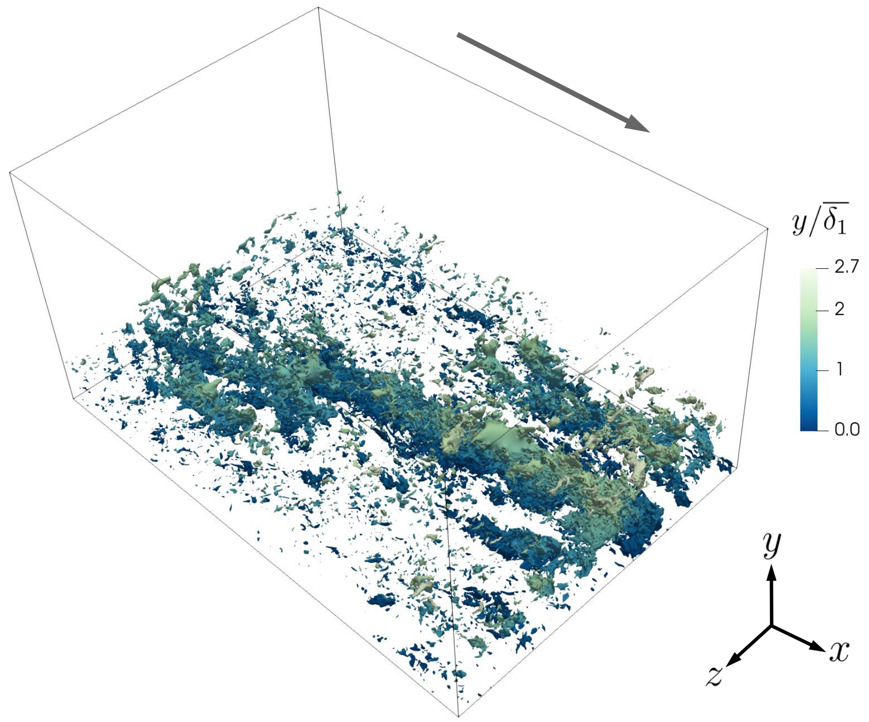

(b)

Figure 6.18: Instantaneous isosurfaces of the (a) Q2 and (b) Q4 structures in the DoI and buffer domain of the strong APG TBL. The flow is from top-left to bottom-right as denoted by the arrow. The structures are coloured based on the distance from the wall. The size of the box in x, y and z directions are $11.3\overline{\delta_1}$, $5.9\overline{\delta_1}$ and $7.7\overline{\delta_1}$, respectively.

75.0% of the total volume of the Q_{uv-} structures. In the strong APG TBL, the relative volume of the wall-attached structures has decreased to 60.3%, showing that the volume proportion of the detached Q_{uv-} structures (Q2 and Q4) have increased in the strong APG TBL. The JPDFs associated with the Q_{uv-} structures in the ZPG TBL and the strong APG TBL are shown in figures 6.19 and 6.20, respectively. Similar to the intense topological structures, the sizes of the Q_{uv-} structures, relative to the mean displacement thickness ($\overline{\delta_1}$), are generally bigger in all the directions when compared to those in the strong APG TBL. As illustrated by the JPDFs of the ZPG TBL in figure 6.19, the Q_{uv-} structures form a self-similar family of streamwise elongated structures with the aspect ratio of their sizes following the linear law $l_x \approx 3.4 l_y \approx 2.8 l_z$. However, as shown in figure 6.20, the Q_{uv-} structures in the strong APG TBL are less streamwise extended than the ZPG TBL following the ratio $l_x \approx 1.6 l_y$, while the relationship between the wall-normal and spanwise extents remains almost the same as $l_y \approx 0.8 l_z$. This result is also similar to that reported by Maciel et al. (2017b), who observed less streamwise elongation in the attached Q_{uv-} structures in their APG TBL when compared to those in their ZPG TBL. As illustrated by the JPDF of l_x and y_c, it is likely to find the intense Q_{uv-} structures with streamwise extent as long as $5\overline{\delta_1}$ closer to the wall in the ZPG TBL. However, it is less likely to find the streamwise elongated Q_{uv-} structures closer to the wall in the strong APG TBL than in the ZPG TBL, which is consistent with the higher volume proportion of detached Q_{uv-} objects (39.7% of $V_{tot,Q_{uv-}}$) in the strong APG TBL.

In the ZPG TBL, the wall-attached Q_{uv+} structures represent 58.7% of the total volume of the Q_{uv+} structures as shown in table 6.6. In the strong APG TBL, the relative volume of the wall-attached Q_{uv+} structures has decreased to 25.5%, showing that the volume proportion of the detached Q_{uv+} structures (Q1 and Q3) have increased in the strong APG TBL. The JPDFs associated with the Q_{uv+} structures in the ZPG TBL and the strong APG TBL are shown in figures 6.21 and 6.22, respectively. Similar to the intense Q_{uv-} structures, the sizes of the Q_{uv+} structures, relative to the mean displacement thickness ($\overline{\delta_1}$), are generally bigger in all the directions when compared to those in the strong APG TBL. As illustrated by the JPDFs of the ZPG TBL in figure 6.21, the Q_{uv+} structures follow the law $l_x \approx 2.4 l_y \approx 1.6 l_z$. However, as shown in figure 6.22, the Q_{uv+} structures in the strong APG TBL are less streamwise extended than the ZPG TBL following the ratio $l_x \approx 1.5 l_y \approx 0.9 l_z$. Similar to the Q_{uv-} structures, as illustrated by the JPDF of l_x and y_c, it is likely to find the intense Q_{uv+} structures with streamwise extent as long as $5\overline{\delta_1}$ closer to the wall in the ZPG TBL. However, it is less likely to find the streamwise elongated Q_{uv+} structures closer to the wall in the strong APG TBL than in the ZPG TBL, which is consistent with the higher volume proportion of detached Q_{uv+} objects (74.5% of $V_{tot,Q_{uv+}}$) in the strong APG TBL.

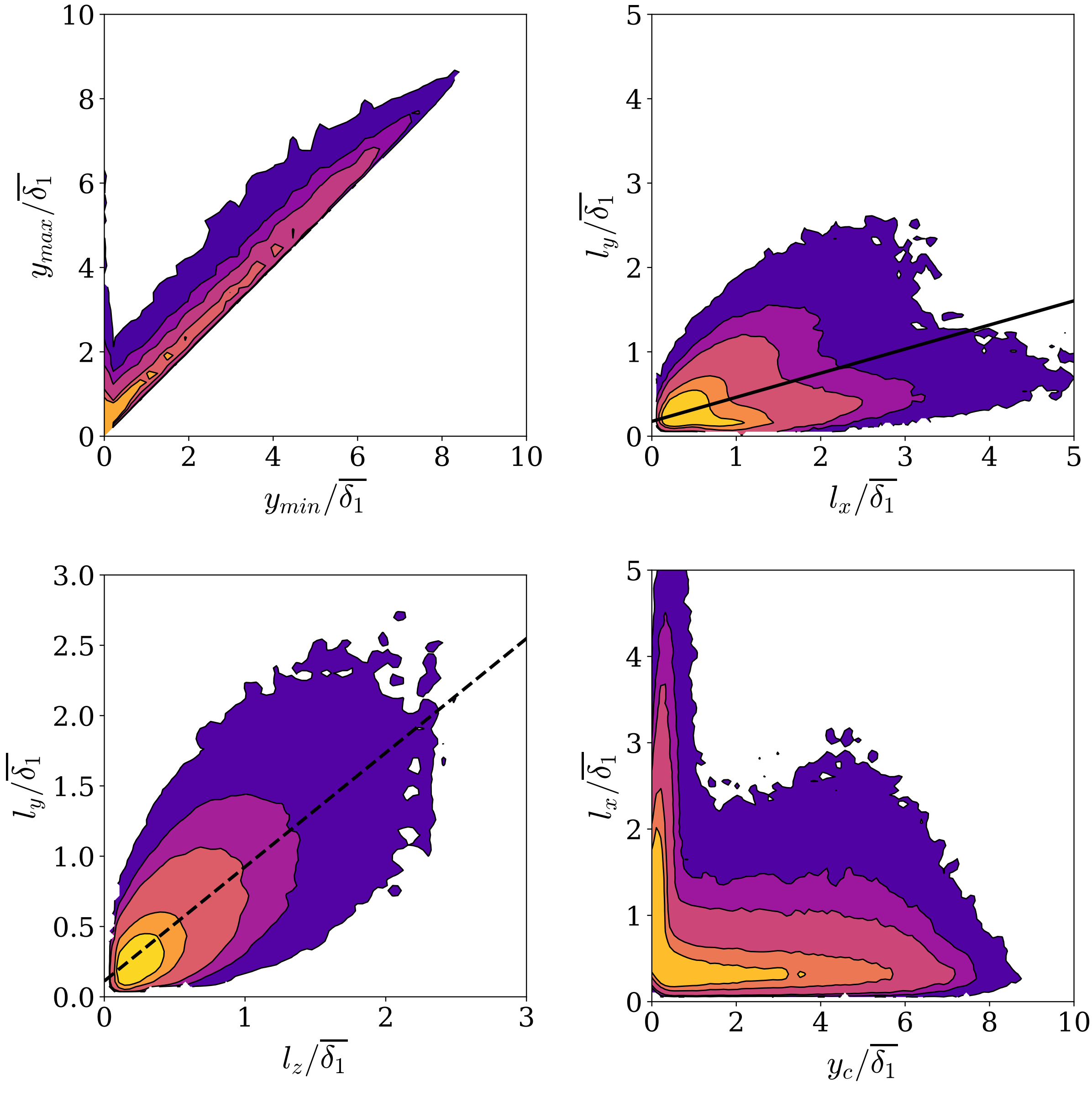

Figure 6.19: Geometrical characteristics of the intense Q_{uv-} structures (Q2 and Q4) in the ZPG TBL. The contour lines contain 50, 70, 90, 95, and 99% of the data. Solid line represents $l_y \approx 0.29 l_x$. Dashed line represents $l_y \approx 0.81 l_z$.

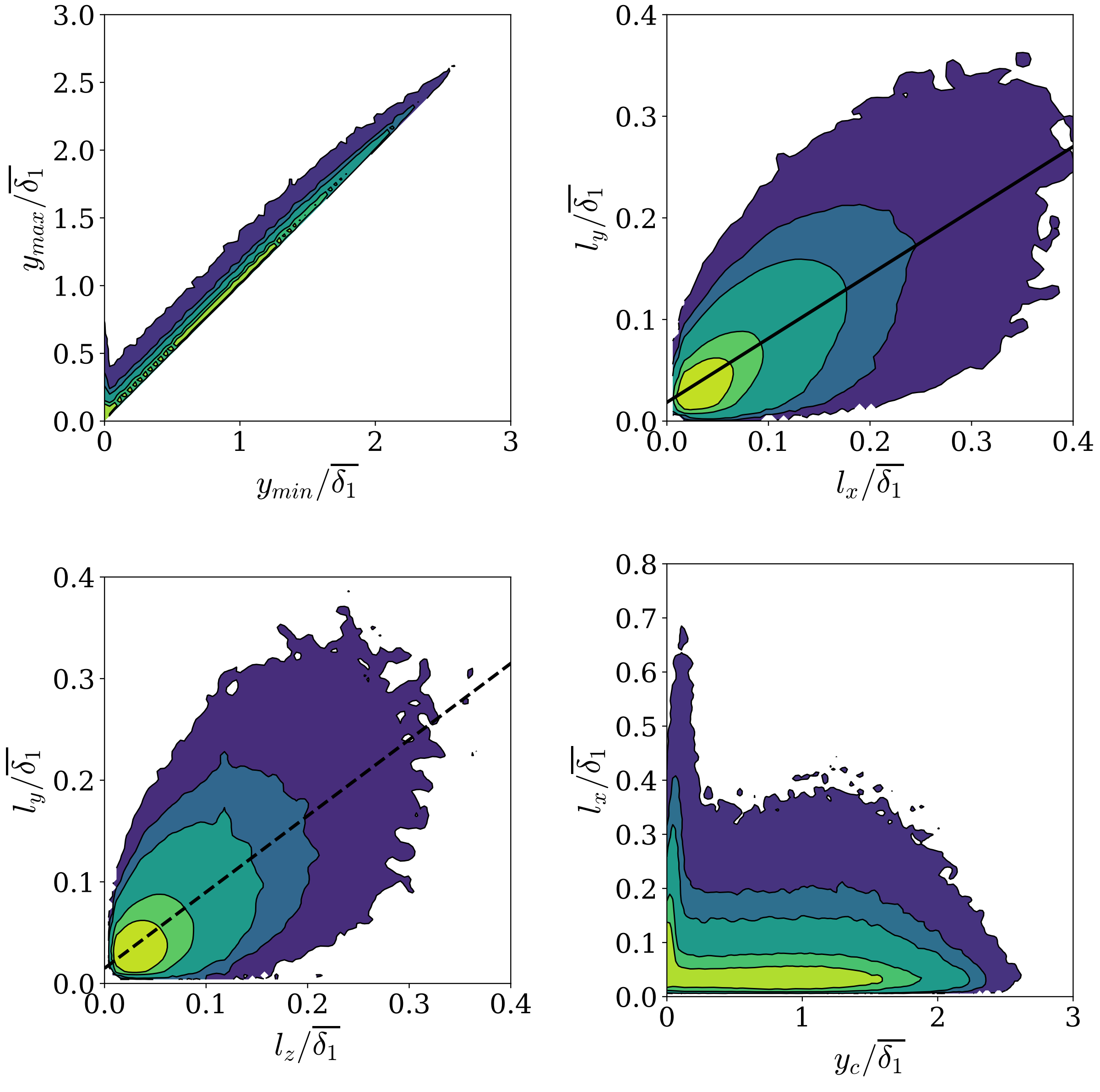

Figure 6.20: Geometrical characteristics of the intense Q_{uv-} structures (Q2 and Q4) in the strong APG TBL. The contour lines contain 50, 70, 90, 95, and 99% of the data. Solid line represents $l_y \approx 0.63 l_x$. Dashed line represents $l_y \approx 0.75 l_z$.

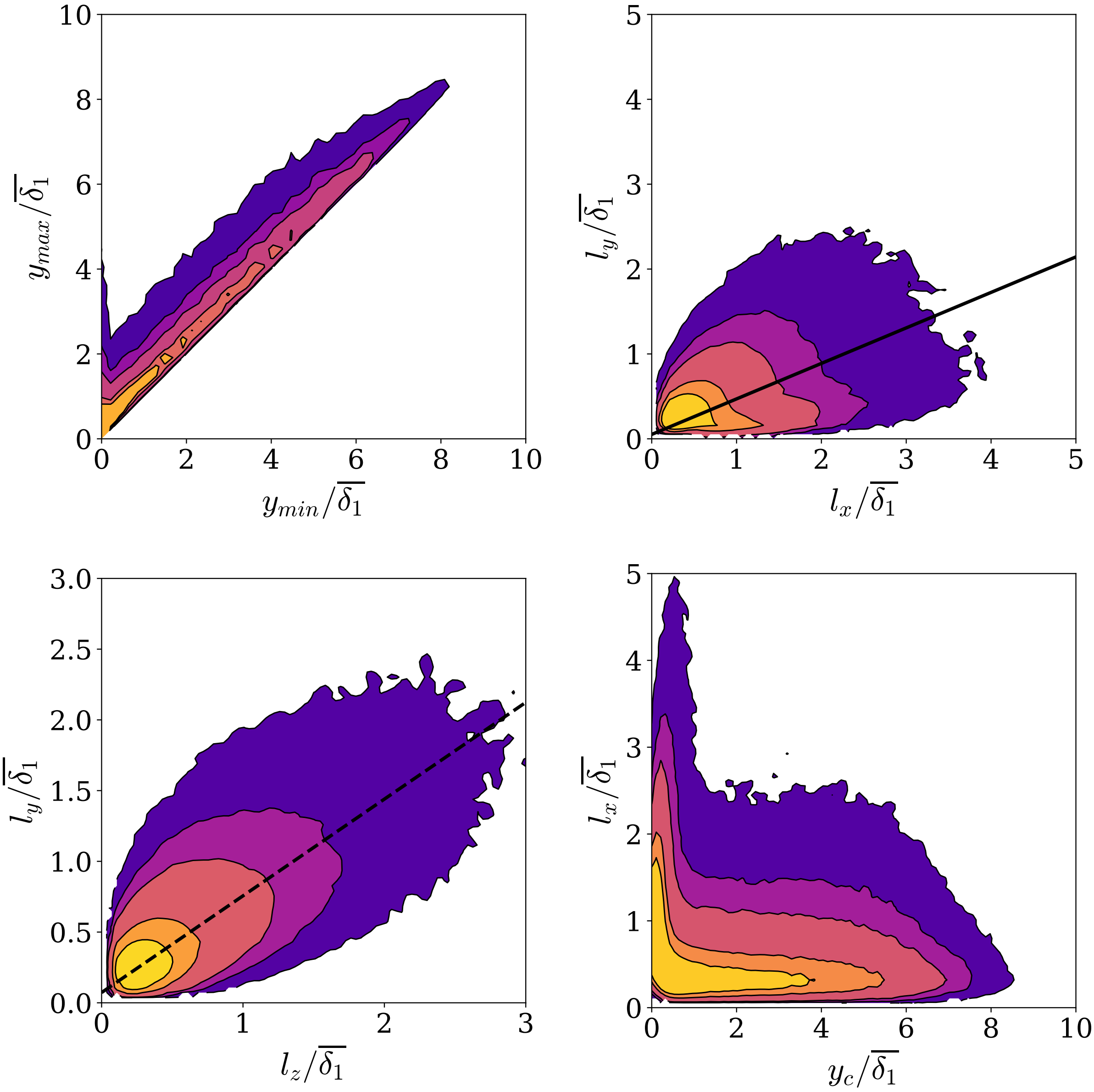

Figure 6.21: Geometrical characteristics of the intense Q_{uv+} structures (Q1 and Q3) in the ZPG TBL. The contour lines contain 50, 70, 90, 95, and 99% of the data. Solid line represents $l_y \approx 0.42 l_x$. Dashed line represents $l_y \approx 0.68 l_z$.

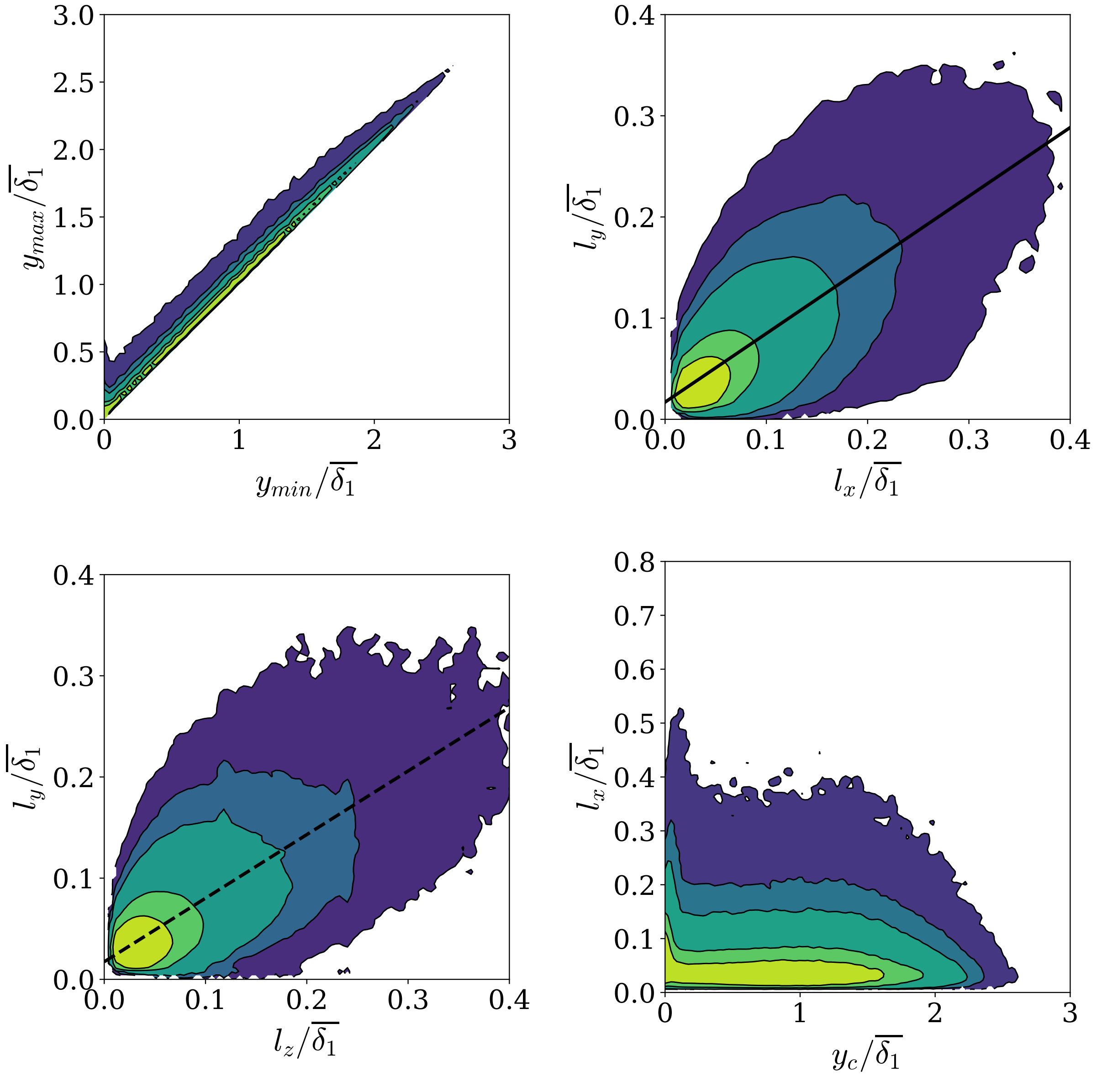

Figure 6.22: Geometrical characteristics of the intense Q_{uv+} structures (Q1 and Q3) in the strong APG TBL. The contour lines contain 50, 70, 90, 95, and 99% of the data. Solid line represents $l_y \approx 0.68 l_x$. Dashed line represents $l_y \approx 0.63 l_z$.

6.3.4 Summary of the geometric characters of the intense structures

In both the TBLs, there is a propensity for the topological structures with positive R_A values (s_{R+} and ω_{R+}) when compared to those with negative R_A values (s_{R-} and ω_{R-}), which can be seen from the higher values of their relative volumes and numbers given in tables 6.4 and 6.5. This propensity towards the intense topological structures with positive R_A values is apparent in the case of the dissipative structures in both the TBLs as the s_{R-} structures occupy only 16.4% of the total volume occupied by all the dissipative structures in the ZPG TBL, while its volume has decreased further to 11.0% of $V_{tot,s_{R,both}}$ in the strong APG TBL.

Case	ZPG ($\beta = 0$)	strong APG ($\beta = 39$)
s_{R+}	$l_x \approx 1.8l_y \approx 1.3l_z$ $l_y \approx 0.7l_z$	$l_x \approx 1.4l_y \approx 1.0l_z$ $l_y \approx 0.7l_z$
s_{R-}	$l_x \approx 1.4l_y \approx 1.0l_z$ $l_y \approx 0.7l_z$	$l_x \approx 2.2l_y \approx 1.0l_z$ $l_y \approx 0.5l_z$
ω_{R+}	$l_x \approx 1.7l_y \approx 1.3l_z$ $l_y \approx 0.8l_z$	$l_x \approx 1.4l_y \approx 1.1l_z$ $l_y \approx 0.8l_z$
ω_{R-}	$l_x \approx 2.3l_y \approx 1.4l_z$ $l_y \approx 0.6l_z$	$l_x \approx 1.7l_y \approx 1.0l_z$ $l_y \approx 0.6l_z$
Q_{uv-} (Q2 and Q4)	$l_x \approx 3.4l_y \approx 2.8l_z$ $l_y \approx 0.8l_z$	$l_x \approx 1.6l_y \approx 1.2l_z$ $l_y \approx 0.75l_z$
Q_{uv+} (Q1 and Q3)	$l_x \approx 2.4l_y \approx 1.6l_z$ $l_y \approx 0.7l_z$	$l_x \approx 1.5l_y \approx 0.9l_z$ $l_y \approx 0.6l_z$

Table 6.7: Summary of the aspect ratios of the intense structures in the ZPG TBL and the strong APG TBL.

The intense structures of all the types in the strong APG TBL have become finer than the ZPG TBL as shown by the reduction in their volumes and increase in their numbers. All of the intense structures are wider in the spanwise direction than how tall they are in the wall-normal direction. In the strong APG TBL, the structures are less streamwise elongated than the ZPG TBL. The strong APG TBL shows a propensity for detached intense structures than the ZPG TBL. The aspect ratios of the intense topological structures and the intense Reynolds stress structures in the ZPG TBL and the strong APG TBL are summarised in table 6.7.

As discussed in section 6.2, the topological structures are identified based on the invariants of the velocity gradient tensor (A_{ij}) in the (R_A,Q_A)-plane, while the Reynolds stress structures are identified based on the (u',v')-space. As the identification methodologies for these structure types are different, a point in the flow can simultaneously belong to a topological structure as well as a Reynolds stress structure. Therefore, the common volume or overlapping volume between these structure types can be computed. The common volume between the intense topological structures (s_{R+},s_{R-},ω_{R+},ω_{R-}) and the intense Reynolds stress structures (Q_{uv}) in the ZPG TBL and the strong APG TBL are given in table 6.8. Out of the four topological structures in the ZPG TBL, the highest common volume with the intense Reynolds stress structures is found for the ω_{R+} and ω_{R-} structures, whose common volumes are similar (0.97% of V_{BL}) as given in table 6.8. In the case of the strong APG TBL, the s_{R+} and ω_{R+} structures have the highest common volume with the intense Reynolds stress structures, whose values are also similar (0.11% of V_{BL}).

Case	$s_{R+} \cap Q_{uv}$	$s_{R-} \cap Q_{uv}$	$\omega_{R+} \cap Q_{uv}$	$\omega_{R-} \cap Q_{uv}$
ZPG	15.4% of $V_{tot,s_{R+}}$	15.8% of $V_{tot,s_{R-}}$	15.8% of $V_{tot,\omega_{R+}}$	16.9% of $V_{tot,\omega_{R-}}$
	0.780% of V_{BL}	0.157% of V_{BL}	0.972% of V_{BL}	0.971% of V_{BL}
strong APG	8.1% of $V_{tot,s_{R+}}$	9.8% of $V_{tot,s_{R-}}$	5.0% of $V_{tot,\omega_{R+}}$	4.3% of $V_{tot,\omega_{R-}}$
	0.110% of V_{BL}	0.015% of V_{BL}	0.106% of V_{BL}	0.056% of V_{BL}

Table 6.8: The common volume between the intense topological structures and the intense Reynolds stress structures in the ZPG TBL and the strong APG TBL.

6.4 Contribution of intense structures to the skin friction

As discussed in chapter 4, the Reynolds shear stress term in the RD identity is the dominant positive contributor to the skin friction in TBL flows irrespective of the streamwise pressure gradient in the flow. Therefore, it is important to quantify the turbulent contribution of the intense structures to the skin friction using the Reynolds shear stress term (C_{f_b}) in the RD identity. The RD identity proposed by Renard and Deck (2016) is defined in Equation 3.1.

The Reynolds shear stress carried by any structure of type 'k' can be defined as

$$\langle u'v' \rangle|_k = \frac{1}{n_f L_z} \sum_{m=1}^{n_f} \int_0^{L_z} W_k(x,y,z,m)\ u'v'(x,y,z,m)\ dz, \tag{6.12}$$

where L_z is the extent of the computational domain in the homogeneous spanwise direction and W_k is the weighting function for any instantaneous flow field 'm' defined as

$$W_k(x,y,z,m) = \begin{cases} 1 & \text{if the point belongs to a structure of type '}k\text{',} \\ 0 & \text{otherwise.} \end{cases} \tag{6.13}$$

Here, the subscript 'k' refers to each of the intense structure type considered in the present study, namely intense dissipative structures, intense vortical structures and intense Reynolds stress structures. Substituting the conditional Reynolds stress ($\langle u'v' \rangle|_k$) into the term C_{f_b} in Equation 3.1 leads to

$$C_{f_b|k} = \frac{2}{U_e^3} \int_0^{\infty} -\langle u'v' \rangle|_k \frac{\partial \langle u \rangle}{\partial y}\ dy. \tag{6.14}$$

The term $C_{f_b|k}$ refers to the turbulent contribution to the skin friction from the intense structures. In the following sections, the premultiplied integrands of C_{f_b} and $C_{f_b|k}$ are denoted by the subscript of *. The wall-normal position is non-dimensionalised by the local values of the outer scale δ_1. The profiles of the premultiplied integrands are streamwise averaged in the scaled coordinates within the DoI. Note that the premultiplied integrand of the term C_{f_b} (I_{b*}) is scaled down by 10 times in all the figures to compare with the premultiplied integrands of the term $C_{f_b|k}$.

6.4.1 Contribution of intense dissipative structures to the skin friction

The premultiplied integrands of the term $C_{f_b|k}$ corresponding to the intense dissipative structures (s_{R+} and s_{R-}) in the ZPG and the strong APG TBLs are illustrated in figure 6.23. The premultiplied integrand $I_{b|s_{R+*}}$ in the ZPG TBL exhibits an inner peak as well as an outer peak that are located around the same height of the peaks of I_{b*} as shown in figure 6.23a. The inner peak of $I_{b|s_{R+*}}$ in the ZPG TBL is more prominent than its outer peak. The premultiplied integrand $I_{b|s_{R-*}}$ exhibits a tiny outer peak around the similar position of I_{b*}. However, the overall contribution of the s_{R-} structures is not significant when compared to the s_{R+} structures in the ZPG TBL. The premultiplied integrands in the ZPG TBL span over a wider part of the boundary layer, whereas their contribution is from a narrow outer peak in the case of the strong APG TBL as illustrated in figure 6.23b.

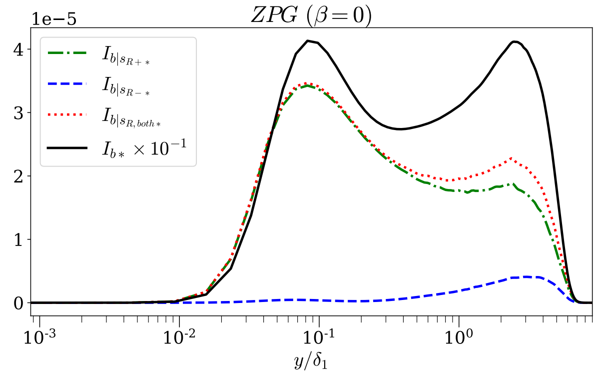

(a)

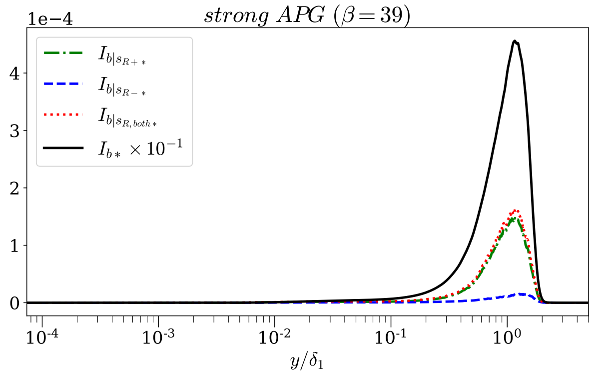

(b)

Figure 6.23: Premultiplied integrand of the term C_{f_b} conditioned for the intense dissipative structures (s_{R+} and s_{R-}) in (a) the ZPG TBL and (b) the strong APG TBL.

Similar to the ZPG TBL, the contribution from the s_{R-} structures is negligible when compared to the s_{R+} structures in the strong APG TBL. In the strong APG TBL, there is a clear outer peak in the profile of the premultiplied integrand $I_{b|s_{R+*}}$, which coincides with the location of the outer peak of the premultiplied integrand I_{b*} around the height of the displacement thickness ($y = \delta_1$).

Case	ZPG	strong APG
$C_{f_b\|s_{R+}} \times 10^4$	1.21	1.37
$C_{f_b\|s_{R-}} \times 10^4$	0.077	0.165
$C_{f_b\|s_{R,both}} \times 10^4$	1.29	1.54

Table 6.9: The streamwise averaged values of the turbulent contribution ($C_{f_b|k}$) from the intense dissipative structures (s_{R+} and s_{R-}) within the DoI in the ZPG TBL and the strong APG TBL.

The streamwise averaged values of the turbulent contribution from the intense dissipative structures within the DoI are given in table 6.9. The streamwise averaged values of the fractional contribution from the s_{R+} and s_{R-} structures within the DoI are given in table 6.10. The turbulent contribution of the s_{R+} and s_{R-} structures have increased in the strong APG TBL when compared to the ZPG TBL as shown in table 6.9. However, the fractional contribution of both of the dissipative structures given in table 6.10 have decreased for the strong APG TBL than the ZPG TBL. This is consistent with the reduction in their volume, $V_{tot,s_{R,both}}$, relative to V_{BL} as shown in table 6.4.

In the ZPG TBL, the fractional contribution of the s_{R-} structures is 15.8 times smaller than the s_{R+} structures, which is consistent with the smaller volume proportion of the s_{R-}

Case	ZPG	strong APG
$C_{f_b\|s_{R+}}/C_{f_b}$	7.09%	3.15%
$C_{f_b\|s_{R-}}/C_{f_b}$	0.45%	0.38%
$C_{f_b\|s_{R,both}}/C_{f_b}$	7.54%	3.53%

Table 6.10: The streamwise averaged values of the fractional contribution ($C_{f_b|k}/C_{f_b}$) from the intense dissipative structures (s_{R+} and s_{R-}) within the DoI in the ZPG TBL and the strong APG TBL.

structures (16.4% of $V_{tot,s_{R,both}}$) as given in table 6.4 and also clear from the instantaneous isosurfaces of the s_{R-} structures in the ZPG TBL as illustrated in figure 6.5b. Similarly, in the strong APG TBL, the fractional contribution of the s_{R-} structures is 8.3 times smaller than the s_{R+} structures, which is inline with the smaller volume proportion of the s_{R-} structures in the strong APG TBL (11.0% of $V_{tot,s_{R,both}}$) as given in table 6.4 and also apparent from the instantaneous isosurfaces of the s_{R-} structures shown in figure 6.6b.

6.4.2 Contribution of intense vortical structures to the skin friction

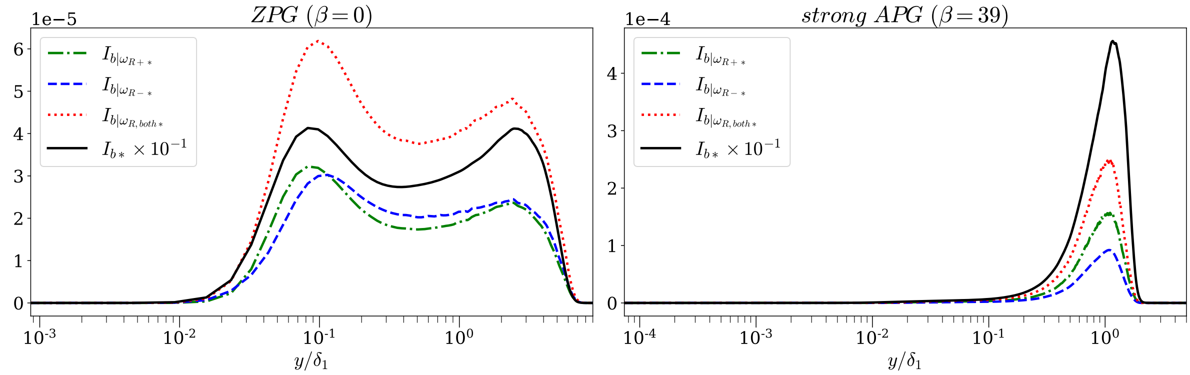

(a) (b)

Figure 6.24: Premultiplied integrand of the term C_{f_b} conditioned for the intense vortical structures (ω_{R+} and ω_{R-}) in (a) the ZPG TBL and (b) the strong APG TBL.

The premultiplied integrands of the term $C_{f_b|k}$ corresponding to the intense vortical structures (ω_{R+} and ω_{R-}) in the ZPG and strong APG TBLs are illustrated in figure 6.24. These premultiplied integrands exhibit two peaks in the ZPG TBL as illustrated in figure 6.24a. The inner and the outer peaks of the premultiplied integrands $I_{b|\omega_{R+*}}$ and $I_{b|\omega_{R-*}}$ are around the same height of the two peaks in the premultiplied integrand I_{b*} in the ZPG TBL. As observed in the contribution of the s_{R+} structures, the inner peak of the premultiplied integrands $I_{b|\omega_{R+*}}$ and $I_{b|\omega_{R-*}}$ is more significant than its outer peak. The profiles of the premultiplied integrands $I_{b|\omega_{R+*}}$ and $I_{b|\omega_{R-*}}$ are broader in the ZPG TBL, whereas their major contributions are from prominent outer peaks in the case of the strong APG TBL as illustrated in figure 6.24b. Similar to the intense dissipative structures in the strong APG TBL, the outer peaks in the profiles of the intense vortical structures coincide with the outer peak in I_{b*} around the displacement thickness height ($y = \delta_1$).

Case	ZPG	strong APG
$C_{f_b\|\omega_{R+}} \times 10^4$	1.11	1.58
$C_{f_b\|\omega_{R-}} \times 10^4$	1.15	0.91
$C_{f_b\|\omega_{R,both}} \times 10^4$	2.26	2.49

Table 6.11: The streamwise averaged values of the turbulent contribution ($C_{f_b|k}$) from the intense vortical structures (ω_{R+} and ω_{R-}) within the DoI in the ZPG TBL and the strong APG TBL.

Case	ZPG	strong APG
$C_{f_b\|\omega_{R+}}/C_{f_b}$	6.54%	3.61%
$C_{f_b\|\omega_{R-}}/C_{f_b}$	6.73%	2.08%
$C_{f_b\|\omega_{R,both}}/C_{f_b}$	13.27%	5.69%

Table 6.12: The streamwise averaged values of the fractional contribution ($C_{f_b|k}/C_{f_b}$) from the intense vortical structures (ω_{R+} and ω_{R-}) within the DoI in the ZPG TBL and the strong APG TBL.

The streamwise averaged values of the turbulent contribution from the intense vortical structures and their fractional contributions within the DoI are given in table 6.11 and table 6.12, respectively. The turbulent contribution of the ω_{R+} structures has increased in the strong APG TBL when compared to the ZPG TBL, while the turbulent contribution of the s_{R-} structures has slightly decreased in the strong APG TBL as shown in table 6.11. However, the total fractional contribution of these structures to C_{f_b} has reduced in the strong APG TBL by 2.3 times. This is consistent with the reduction in their volume, $V_{tot,\omega_{R,both}}$, relative to V_{BL} as shown in table 6.5.

6.4.3 Contribution of intense Reynolds stress structures to the skin friction

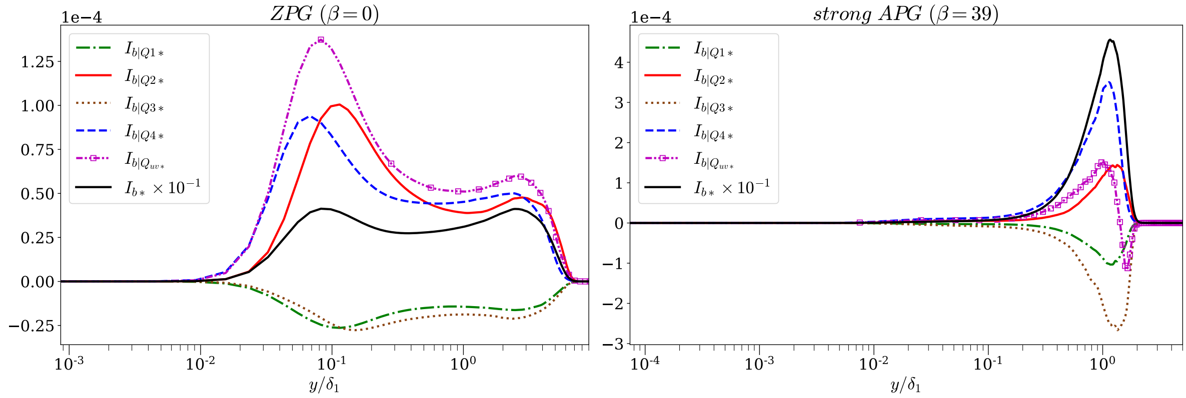

(a) (b)

Figure 6.25: Premultiplied integrand of the term C_{f_b} conditioned for the intense Reynolds stress structures in (a) the ZPG TBL and (b) the strong APG TBL.

The premultiplied integrands of the term $C_{f_b|k}$ for the intense Reynolds stress structures in the ZPG and the strong APG TBLs are illustrated in figure 6.25. In both the TBLs, the Q_{uv-} (Q2 and Q4) structures provide a positive contribution, while the Q_{uv+} (Q1 and Q3) structures reduce the skin friction by yielding a negative contribution to C_{f_b}. In the ZPG TBL, the premultiplied integrands of all the four quadrant structures exhibit an inner peak and an outer peak, which are located around the same height of the peaks of I_{b*} as illustrated in figure 6.25a. The inner peak of the Q_{uv-} structures are more prominent than their outer peaks in the ZPG TBL, whereas both the peaks are of similar magnitude for the Q_{uv+} structures. Similar to the intense topological structures in the ZPG TBL, the premultiplied integrands of the Q_{uv} structures cover a broader part of the boundary layer. However, the contribution of the Q_{uv} structures in the strong APG TBL are from the prominent peaks in the outer region as illustrated in figure 6.25b.

The streamwise averaged values of the turbulent contribution from the intense Reynolds stress structures and their fractional contributions within the DoI are given in table 6.13 and table 6.14, respectively. As given in table 6.6, in the ZPG TBL, the volume occupied by the Q_{uv-} structures (44.9% of $V_{tot,Q_{uv}}$) is less than that of the Q_{uv+} structures. In the strong APG TBL, the volume occupied by the Q_{uv-} and Q_{uv+} structures are nearly the same (50.3% and 49.7% of $V_{tot,Q_{uv}}$, respectively). However, in both the TBLs, the contribution of the Q_{uv-} structures to C_{f_b} is higher than the corresponding Q_{uv+} structures as shown in tables 6.13 and 6.14. This indicates that the Q_{uv-} structures are more intense than the Q_{uv+} structures in both the TBLs. A similar observation was also noted by Maciel et al. (2017a) in their APG TBL. The contribution of the Q_{uv-} structures to the

Case	ZPG	strong APG
$C_{f_b\|Q1}$ $\times 10^5$	-9.16	-10.06
$C_{f_b\|Q2}$ $\times 10^5$	29.31	14.43
$C_{f_b\|Q3}$ $\times 10^5$	-10.28	-26.52
$C_{f_b\|Q4}$ $\times 10^5$	30.09	36.25
$C_{f_b\|Q_{uv-}}$ $\times 10^5$	59.40	50.68
$C_{f_b\|Q_{uv+}}$ $\times 10^5$	-19.44	-36.58
$C_{f_b\|Q_{uv}}$ $\times 10^5$	39.96	14.10

Table 6.13: The streamwise averaged values of the turbulent contribution ($C_{f_b|k}$) from the intense Reynolds stress structures (Q1, Q2, Q3 and Q4) within the DoI in the ZPG TBL and the strong APG TBL.

Case	ZPG	strong APG
$C_{f_b\|Q1}/C_{f_b}$	-5.37%	-2.31%
$C_{f_b\|Q2}/C_{f_b}$	17.18%	3.31%
$C_{f_b\|Q3}/C_{f_b}$	-6.03%	-6.07%
$C_{f_b\|Q4}/C_{f_b}$	17.64%	8.32%
$C_{f_b\|Q_{uv-}}/C_{f_b}$	34.82%	11.63%
$C_{f_b\|Q_{uv+}}/C_{f_b}$	-11.40%	-8.38%
$C_{f_b\|Q_{uv}}/C_{f_b}$	23.42%	3.26%

Table 6.14: The streamwise averaged values of the fractional contribution ($C_{f_b|k}/C_{f_b}$) from the intense Reynolds stress structures (Q1, Q2, Q3 and Q4) within the DoI in the ZPG TBL and the strong APG TBL.

skin friction is 3.05 times the Q_{uv+} structures in the ZPG TBL, whereas the contribution of the Q_{uv-} structures is 1.39 times the Q_{uv+} structures in the strong APG TBL.

In the ZPG TBL, the fractional contribution of the intense ejection (Q2) and sweep (Q4) structures to C_{f_b} are nearly equal (17.18% and 17.64%, respectively). This is consistent with their volume proportions (22.1% and 22.8% of $V_{tot,Q_{uv}}$, respectively) being nearly similar as given in table 6.6. In the strong APG TBL, the fractional contribution of Q2 structures is lesser than the Q4 structures, which is consistent with the reduced volume proportion of the Q2 structures when compared to that of the Q4 structures as shown in table 6.6. The total turbulent contribution of all the four quadrant structures (Q_{uv}) has decreased in the strong APG TBL when compared to the ZPG TBL as shown in table 6.13. Similarly, the fractional contribution of the Q_{uv} structures to C_{f_b} has reduced in the strong APG TBL by 7.2 times, which is consistent with the reduction in their volume ($V_{tot,Q_{uv}}$) relative to V_{BL} as shown in table 6.6.

6.4.4 Summary of the contribution of intense structures to the skin friction

When comparing the two types of dissipative structures, it is found that the fractional contribution of the s_{R+} structures ($R_A > 0$) to C_{f_b} is more dominant than that of the s_{R-} structures in both the TBLs as shown in table 6.10. When comparing the two types of vortical structures in the strong APG TBL, the fractional contribution of the ω_{R+} structures ($R_A > 0$) is greater than that of the ω_{R-} structures, while their contributions are almost the same in the ZPG TBL as shown in table 6.12.

The s_{R+} structures have the highest fractional contribution to C_{f_b} (7.1%) when compared to the other topological structures in the ZPG TBL. In the strong APG TBL, the ω_{R+} structures have the highest fractional contribution to C_{f_b} (3.6%) when compared to the other topological structures. In the ZPG TBL, the contribution of the ω_{R+} and ω_{R-} are nearly the same (5.7%), which is consistent with the common volumes between these topological structures and the intense Reynolds stress structures being the same (0.972% of V_{BL}) as shown in table 6.8. Similarly, in the strong APG TBL, the contribution of the s_{R+} and ω_{R+} are around 3.6% and this result is consistent with their common volumes with the intense Reynolds stress structures being almost the same (0.110% of V_{BL}) as shown in table 6.8.

When comparing all the intense structure types in the ZPG TBL (s_{R+}, s_{R-}, ω_{R+}, ω_{R-}, Q_{uv}), the intense Reynolds stress structures have the highest fractional contribution (23.42%) to the term C_{f_b} as shown in table 6.14. Similarly, the highest fractional contribution in the strong APG TBL (3.26%) is also from the Q_{uv} structures.

6.5 Conclusion

The turbulent contribution of the intense structures to the skin friction are investigated in the ZPG TBL ($\beta = 0$) and the strong APG TBL ($\beta = 39$). The intense structures investigated in the present study are intense dissipative structures (s_{R+} and s_{R-}), intense vortical structures (ω_{R+} and ω_{R-}), and intense Reynolds stress structures (Q1, Q2, Q3 and Q4). The turbulent contribution of these intense structures to the skin friction are computed using the term C_{f_b} in the RD identity (Renard and Deck, 2016).

The intense structures of all the types in the strong APG TBL have become finer than those in the ZPG TBL as shown by the reduction in their relative volumes and increase in their numbers. All of the intense structures in both the TBLs are elongated in the streamwise direction. In the strong APG TBL, all of the intense structures (except s_{R-}) are less streamwise elongated than those in the ZPG TBL. In general, the strong APG TBL shows a greater propensity for detached intense structures of all types (except s_{R-}) than the ZPG TBL. In both the TBL cases, there is more inclination towards the topological structures with positive R_A values (s_{R+} and ω_{R+}) when compared to those with negative R_A values (s_{R-} and ω_{R-}), which is evident from the higher values of their relative volumes and numbers.

For all the intense structures in the ZPG TBL, the contribution to the skin friction ($C_{f_b|k}$) is from a wider part of the boundary layer, whereas, in the strong APG TBL, their contribution is from a dominant outer peak. With increasing pressure gradient, the fractional contribution of the structures to the skin friction ($C_{f_b|k}/C_{f_b}$) decreases for all the types of intense structures, which is consistent with the reduction in their volume relative to the mean boundary layer thickness based volume (V_{BL}). As the premultiplied integrands I_{b*} as well as $I_{b|k*}$ display a dominant outer peak in the strong APG TBL for all the intense structure types, this shows that the outer layer dynamics becomes more important with increasing pressure gradient in regards to the Reynolds shear stress contribution to the skin friction.

Experience is what you get when you didn't get what you wanted. And experience is often the most valuable thing you have to offer.

–Randy Pausch

Chapter 7

Conclusions

In this study, direct numerical simulations (DNSs) of three TBL cases with different streamwise pressure gradients are considered. The TBL cases are classified based on the non-dimensional pressure gradient β, which is defined as $\beta = \delta_1 P_{e,x}/\tau_w$, where δ_1 is the displacement thickness, τ_w is the mean wall shear stress and $P_{e,x}$ is the far-field streamwise pressure gradient. The three TBL cases are a zero pressure gradient (ZPG), a mild adverse pressure gradient (mild APG), and a strong adverse pressure gradient (strong APG) TBLs. The nominal values of β within the domain of interest (DoI) are 0, 1 and 39 for the ZPG, mild APG and strong APG TBLs, respectively. The various factors and the coherent structures that influence the skin friction in the TBL flows have been investigated in the present study.

The RD identity (Renard and Deck, 2016) has been used to investigate the contribution of the viscous effects and Reynolds shear stress to the skin friction, and their variation with the pressure gradient. In the ZPG TBL, all three components of the RD identity increase the skin friction by providing a positive contribution. However, in the mild APG and strong APG cases, the third term C_{f_c} decreases the skin friction by providing a negative contribution. The inner peak of the viscous term (C_{f_a}) diminishes with increasing pressure gradient and its contribution becomes almost negligible in the strong APG TBL case. This shows that the role of viscous effects becomes less significant with increasing pressure gradient.

It is found that the Reynolds shear stress plays a crucial role in the mechanism of skin friction generation in all the TBL cases. The contribution of the Reynolds shear stress (C_{f_b}) to the skin friction continues to increase with the pressure gradient and it remains as the dominant positive contributor irrespective of the pressure gradient in the flow. In the ZPG TBL, the contribution of the term C_{f_b} is from a broader region of the boundary layer. Whereas, with increasing pressure gradient, the inner peak of the premultiplied integrand I_{b*} decreases, while the outer peak grows. Especially, in the strong APG TBL, the predominant contribution of I_{b*} is from a clear peak located in the outer region, while its contribution from the inner region is negligible. It is also found in the strong APG case that the peak of the Reynolds shear stress ($\langle u'v' \rangle$), the peak of the premultiplied integrand I_{b*} (Reynolds shear stress contribution), the outer inflection point of the mean streamwise velocity, and the peaks of the turbulent production ($\mathcal{P}$) and dissipation ($\mathcal{D}$) coincide in the outer region around the displacement thickness height ($y/\delta_1 = 1$ or $y/\delta_\Omega = 0.2$). This emphasizes the significance of the outer layer dynamics with increasing pressure gradient. It is also supported by the fact that the FIK identity (Fukagata et al., 2002) has also captured the dominant outer peak contribution from the Reynolds shear stress around the displacement thickness height ($y/\delta_1 = 1$) in the strong APG TBL.

The contribution of the velocity-vorticity correlations to the skin friction has been investigated using the YAHS identity (Yoon et al., 2016). For all the pressure gradient cases, advective vorticity transport (contribution of $\langle v'\omega_z' \rangle$) decreases the skin friction, while vortex stretching (contribution of $-\langle w'\omega_y' \rangle$) increases the skin friction by providing a positive contribution. It is found that across the entire boundary layer in all the three pressure gradient cases, the combined effect of the velocity-vorticity correlations $\langle v'\omega_z' \rangle$ and $-\langle w'\omega_y' \rangle$ is the dominant contributor to the gradient $-\partial\langle u'v' \rangle/\partial y$. The contribution of $-\partial\langle u'v' \rangle/\partial y$ to the skin friction ($C_{f_{12b}}$) has an inner peak which diminishes with increasing pressure gradient, while its outer peak continues to grow. It is also found that for all the pressure gradient cases, the combined effect of the advective vorticity transport term (C_{f_1}) and the vortex stretching term (C_{f_2}) represents the contribution from the Reynolds shear stress with a constant wall-normal weight ($C_{f_{12c}}$). The premultiplied integrand of the term $C_{f_{12c}}$ also exhibits an outer peak around the height of 20% of boundary layer thickness ($y/\delta_\Omega = 0.2$ or $y/\delta_1 = 1$), which coincides with the outer peak of the Reynolds stress terms in the RD identity (C_{f_b}) and the FIK identity ($C_{f_{II}}$). This again emphasizes that the impact of the outer layer on the skin friction generation is higher with increasing pressure gradient, as the majority of the turbulence activity is in the outer layer.

The turbulent contribution of the intense structures to the skin friction has been quantified using the Reynolds stress term C_{f_b} in the RD identity. The types of intense structures considered in the present study are intense topological structures (dissipative and vortical) and intense Reynolds stress structures. Intense structures of all the types in the ZPG TBL as well as in the strong APG TBL are streamwise elongated with their width being larger than their height. However, in the strong APG TBL, the intense structures are less streamwise elongated when compared to those structures in the ZPG TBL. Intense structures of all the types in the strong APG TBL are smaller in scale than those in the ZPG TBL, which is evident from the reduction in their volume relative to the mean boundary layer volume (V_{BL}) and increase in their numbers. There is a greater propensity for detached intense structures in the strong APG TBL than in the ZPG TBL. The fractional contribution of the intense structures to the skin friction ($C_{f_b|k}/C_{f_b}$) decreases with increasing pressure gradient, which is also consistent with the reduction in their volume relative to V_{BL}. It is found that the contribution of all the intense structure types in the ZPG TBL is from a broader part of the boundary layer. However, in the strong APG TBL, the contribution of the intense structures is from a distinct peak in the outer region around the displacement thickness height ($y/\delta_1 = 1$). In conclusion, the outer layer dynamics becomes more important with increasing adverse pressure gradient, as it pertains to the contribution of the Reynolds shear stress ($\langle u'v' \rangle$) and its negative wall-normal gradient ($-\partial\langle u'v' \rangle/\partial y$) to the mechanism of the mean skin friction generation.

We cannot solve our problems with the same thinking we used when we created them.

–Albert Einstein

Appendix A

Analysis of the spanwise extent and time persistence of uniform momentum zones

As an additional part of the present research, the characteristics of the uniform momentum zones (UMZs) and their variation with the pressure gradient are investigated. The UMZs are one of the types of coherent structures found in wall-bounded turbulent flows. The UMZs are irregular regions in the flow with similar streamwise momentum and the interfaces between these zones are similar to shear layers. In the current study, time-resolved velocity fields are used to investigate the spanwise extent and the time persistence of the UMZs in the ZPG TBL and the strong APG TBL. This work is presented in the form of a journal paper published in the *Journal of Physics: Conference Series* (Senthil et al., 2020a). A part of this work was performed during the *Fourth Madrid Turbulence Workshop* during June-July, 2019 at the Universidad Politécnica de Madrid, Madrid, Spain (`https://torroja.dmt.upm.es/summer19/group_foto.jpg`).

PAPER • OPEN ACCESS

Analysis of the spanwise extent and time persistence of uniform momentum zones in zero pressure gradient and adverse pressure gradient turbulent boundary layers

To cite this article: Shevarjun Senthil *et al* 2020 *J. Phys.: Conf. Ser.* **1522** 012013

Journal of Physics: Conference Series **1522** (2020) 012013 doi:10.1088/1742-6596/1522/1/012013

Analysis of the spanwise extent and time persistence of uniform momentum zones in zero pressure gradient and adverse pressure gradient turbulent boundary layers

Shevarjun Senthil[1], **Callum Atkinson**[1], **and Julio Soria**[1,2]

[1]Laboratory for Turbulence Research in Aerospace and Combustion, Department of Mechanical and Aerospace Engineering, Monash University, Melbourne 3800, Australia
[2]Department of Aeronautical Engineering, King Abdulaziz University, Jeddah 21589, Kingdom of Saudi Arabia

E-mail: `shevarjun.senthil@monash.edu`

Abstract. Time-resolved velocity fields from direct numerical simulations (DNS) are used to investigate the spanwise extent and the time persistence of uniform momentum zones (UMZs) in a zero pressure gradient turbulent boundary layer (ZPG-TBL) and a self-similar adverse pressure gradient turbulent boundary layer (APG-TBL) at the verge of separation. The instantaneous detection methodology introduced by Adrian et al. [1] is used to detect the UMZs and is extended to take into account the spanwise domain length and the temporal evolution of the UMZs. The Reynolds number based on friction velocity (Re_τ) ranges from 1176 to 1277 for the ZPG-TBL and from 1652 to 1745 for the self-similar APG-TBL within the domain of interest. For both the TBL cases, probability density functions (PDFs) of the number of UMZs are computed as a function of the streamwise extent, spanwise extent and time extent. For the ZPG-TBL, when the streamwise length of the domain is greater than or equal to 3 boundary layer thickness, the probability of finding 4 UMZs becomes almost negligible. For the APG-TBL, even when the streamwise domain length is taken as large as 1.3 boundary layer thickness, the probability of finding 4 UMZs is still significant. The spanwise extent of the UMZs is found to be shorter than their streamwise extent regardless of the pressure gradient in the flow. In the ZPG-TBL flow, the majority of the UMZs have a spanwise extent of the order of one-tenth of a boundary layer thickness while for the APG-TBL, it is found to be on the order of one-hundredth of a boundary layer thickness. In the ZPG-TBL, the probability of finding 2 UMZs that persist over a time period of 2 integral time scale is around 50%. Similarly, for the APG-TBL, the probability of finding 2 UMZs with a time persistence of 0.4 integral time scale is over 50%. In the case of the ZPG-TBL, it is observed that some of the UMZs with higher persistence in time have higher streamwise momentum and are found to be closer to the free-stream in general. This result is consistent with the previous observations by Laskari et al. [2]. In contrast, for the APG-TBL, UMZs with longer time persistence are found closer to the wall with lower streamwise momentum.

1. Introduction

Wall-bounded flows have different types of coherent structures like low-speed streaks, sweeps and ejections, and hairpin vortices [3–5]. One of the many coherent structures in wall-bounded

Journal of Physics: Conference Series **1522** (2020) 012013 doi:10.1088/1742-6596/1522/1/012013

flows are uniform momentum zones (UMZs), which are uneven regions in the flow with similar streamwise momentum and varying shape with time. Meinhart & Adrian [6] were the first to report the existence of these zones. The UMZs are separated from each other by layers which have high values of the local wall-normal gradient of the streamwise velocity with spanwise vorticity clustered along these boundaries [6]. The interfaces between the UMZs are similar to a shear layer. Adrian et al. [1] proposed a method to identify the instantaneous UMZs based on the probability density function (PDF) of the instantaneous streamwise velocity. Kwon et al. [7] identified the presence of a large core with uniform velocity and low turbulence levels in a turbulent channel flow. Similar experimental studies on turbulent boundary layers using particle image velocimetry have also revealed regions of relatively uniform streamwise velocity [8, 9]. More recently, Laskari et al. [2] investigated the UMZs in a streamwise wall-normal plane of a turbulent boundary layer using time-resolved particle image velocimetry. Laskari et al. [2] found that the presence of higher number of UMZs is linked with the large-scale ejection events, whereas the lower number of UMZs is related to large-scale sweep events. The focus of the present study is to investigate the spanwise extent and time persistence of the UMZs in a zero pressure gradient and an adverse pressure gradient turbulent boundary layer. To the best of the authors' knowledge, the present analysis is the first to investigate the time persistence of the UMZs as well as the spanwise extent using three dimensional (3D) velocity fields to construct the PDFs.

2. Details of the direct numerical simulation

The turbulent boundary layer (TBL) datasets were computed by solving the incompressible Navier-Stokes equation for velocity and pressure fields [10, 11]. The TBL flows are solved in a Cartesian coordinate system with the flow directions as streamwise (x), wall-normal (y) and spanwise (z). The mean velocity components are represented by ($\langle u\rangle, \langle v\rangle, \langle w\rangle$) while the corresponding fluctuating components are represented by (u', v', w').

The first version of the code was developed by Simens et al. [10, 11] which was subsequently optimized by Borrell et al. [12] by adding OpenMP (Open Multi-Processing) to the MPI Parallelization. The current version of the code is the one presented in Kitsios et al. [13, 14] modified to enable the simulation of adverse pressure gradient turbulent boundary layer flow. The governing equations are solved using the fractional step method [15, 16]. The grid is staggered only in the streamwise and the wall-normal directions. The spanwise direction is periodic while compact finite difference is used for spatial discretization in the x and y directions [17]. Time stepping is achieved using a 3-step Runge Kutta method [11]. The fluid density ($\rho = 1$) and kinematic viscosity (ν) are taken as constants. Further details on the DNS code and the parallelisation techniques used in it can be found in Sillero [18] and Borrell et al. [12]. The desired pressure gradient is applied via the far-field boundary condition using the methodology developed by Kitsios et al. [13, 14].

The non-dimensional pressure gradient (β) is given by

$$\beta = \frac{\delta_1}{{u_\tau}^2}\frac{P_{e,x}}{\rho} = \delta_1\frac{P_{e,x}}{\tau_w}, \tag{1}$$

where $u_\tau = \sqrt{\tau_w/\rho}$ is the friction velocity, τ_w is the mean wall shear stress, ρ is the fluid density, $P_{e,x}$ is the far-field streamwise pressure gradient and δ_1 is the displacement thickness.

The displacement thickness (δ_1), based on the definition of Spalart & Watmuff [19], is given by

$$\delta_1(x) = \frac{-1}{U_e}\int_0^{\delta_\Omega} y\langle\Omega_z\rangle(x, y)dy, \tag{2}$$

where U_e is the outer reference velocity, $\langle\Omega_z\rangle$ is the mean spanwise vorticity, and δ_Ω is the wall-normal position or the boundary layer thickness at which $\langle\Omega_z\rangle$ has decayed to 0.2% of the mean

Table 1: Numerical details of the ZPG and the APG-TBLs in their respective domain of interest (DoI). $\delta_{\Omega*}$ is δ_Ω at the start of the DoI and $\langle u\rangle_{\infty*}$ is the far-field mean streamwise velocity at the start of the DoI. The integral time scale is defined as $\delta_{\Omega*}/\langle u\rangle_{\infty*}$.

		ZPG	APG
Nominal non-dimensional pressure gradient	β	0	39
Streamwise data points	n_x	1035	1001
Wall-normal data points	n_y	315	1000
Spanwise data points	n_z	2048	2048
Streamwise domain size	$l_x/\delta_{\Omega*}$	9.32	1.28
Wall-normal domain size	$l_y/\delta_{\Omega*}$	3.49	2.55
Spanwise domain size	$l_z/\delta_{\Omega*}$	12.34	1.76
Friction velocity based Reynolds number	Re_τ	1176 $\rightarrow$ 1277	1652 $\rightarrow$1745
Displacement thickness based Reynolds number	Re_{δ_1}	4678 $\rightarrow$ 5098	22182 $\rightarrow$28789
Momentum thickness based Reynolds number	Re_{δ_2}	3360 $\rightarrow$ 3679	9857 $\rightarrow$12101
Mean boundary layer thickness	$\overline{\delta_\Omega}/\delta_{\Omega*}$	1.05	1.15
Mean friction velocity	$\overline{u_\tau}$	0.039	0.007
Total time period for 200 fields	$t\langle u\rangle_{\infty*}/\delta_{\Omega*}$	3.2	0.47

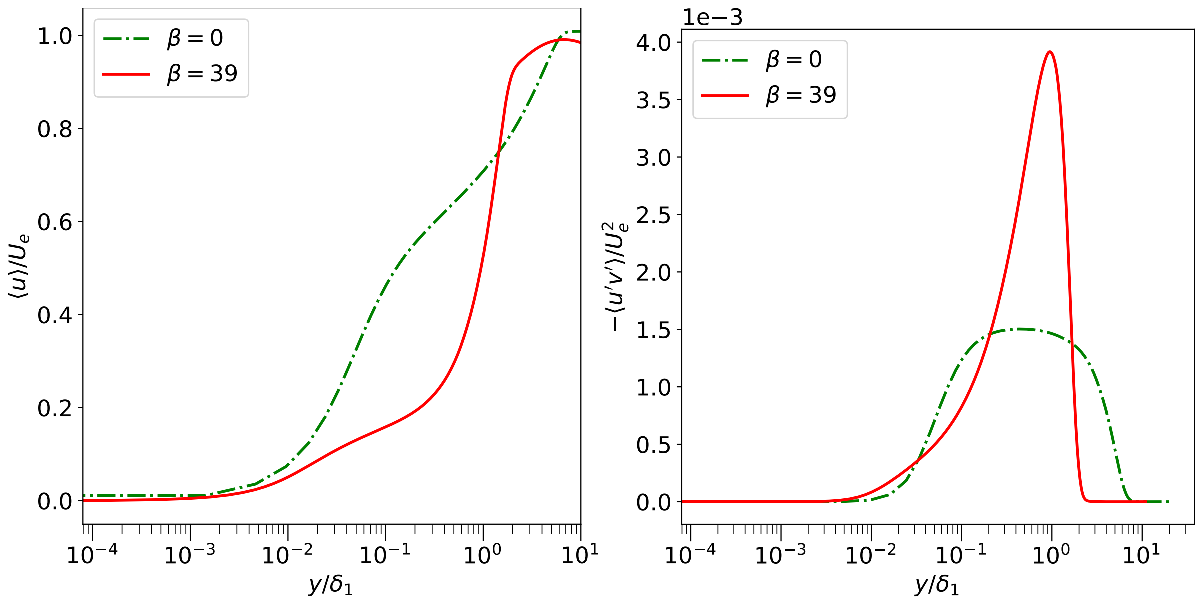

(a) (b)

Figure 1: Profiles of (a) mean streamwise velocity ($\langle u\rangle$), and (b) Reynolds shear stress ($\langle u'v'\rangle$) for both the TBL cases. The profiles are averaged in streamwise direction within DoI and are non-dimensionalised by δ_1.

vorticity at the wall. The outer velocity (U_e), based on the definition of Lighthill [20], is given by

$$U_e(x) = U_\Omega(x, \delta_\Omega), \tag{3}$$

where

$$U_\Omega(x,y) = -\int_0^y \langle \Omega_z \rangle (x,\tilde{y})\ d\tilde{y}. \tag{4}$$

In the present study of the UMZs, a time-resolved DNS of a zero pressure gradient turbulent boundary layer (ZPG-TBL) and a self-similar adverse pressure gradient turbulent boundary layer (APG-TBL) at the verge of separation are considered. For the APG-TBL, a self-similar domain is considered to minimise the influence of the history effects and β has an average value of 39 within the domain of interest (DoI). Profiles of the mean streamwise velocity ($\langle u \rangle$) and the Reynolds shear stress ($\langle u'v' \rangle$) for both the TBL cases are compared in Figure 1. For the ZPG-TBL, the Reynolds shear stress has a broader profile whereas its profile is confined to a much narrower region in the case of the APG-TBL. For the APG-TBL, the peak of the Reynolds shear stress in Figure 1b and the inflection point of the mean streamwise velocity in Figure 1a coincide at an approximate height of the displacement thickness ($y/\delta_1 = 1$). Profiles of the kinetic energy budgets and the momentum balances for both the TBLs can be found in Kitsios et al. [13, 14]. Numerical details of the two TBL cases in their respective DoI are given in Table 1. $\delta_{\Omega *}$ is δ_Ω at the start of the DoI and $\langle u \rangle_{\infty *}$ is the far-field mean streamwise velocity at the start of the DoI. For the APG-TBL, the available streamwise domain size relative to the boundary layer thickness ($l_x/\delta_{\Omega *}$) is shorter because of the higher boundary layer thickness. The profiles of the boundary layer thickness ($\delta_\Omega/\delta_\Omega(x_I)$) for both the TBLs are given in Figure 2, where x_I is the position of the inlet plane. 200 time-resolved velocity fields are used in the investigation of the UMZs for both the TBL cases. The integral time scale is defined as $\delta_{\Omega *}/\langle u \rangle_{\infty *}$. The wall-normal domain size (l_y) used in all the analyses is fixed as $1.3\delta_{\Omega *}$ and $0.7\delta_{\Omega *}$ for the ZPG-TBL and the APG-TBL respectively. All the PDFs related to the ZPG case are in green while the ones corresponding to the APG-TBL are in red colour.

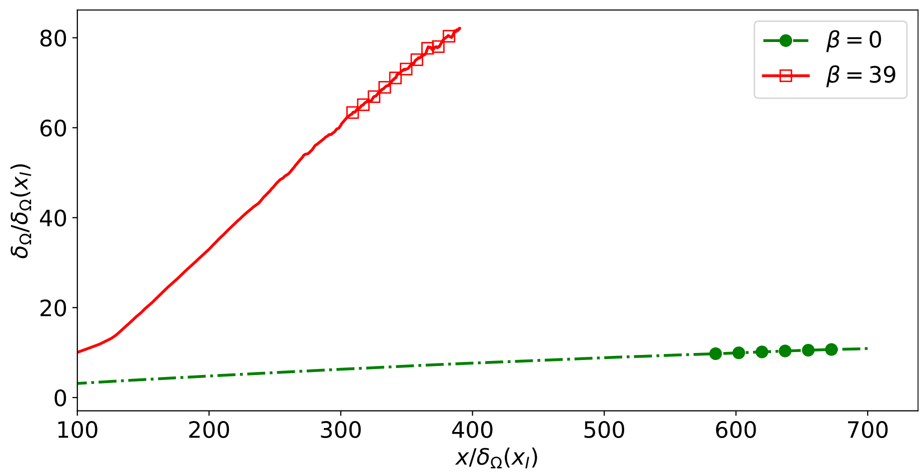

Figure 2: Profiles of the boundary layer thickness (δ_Ω) in the streamwise direction for both the TBL cases, where x_I is the position of the inlet plane.

3. UMZ detection methodology

The instantaneous UMZs and the boundaries that demarcate them are identified based on the method introduced by Adrian et al. [1]. This method is extended to consider the instantaneous three dimensional velocity fields and the temporal evolution of the UMZs [2]. In this method, the local maxima (peaks) and the local minima (troughs) in the probability density function (PDF) of the instantaneous streamwise velocity fields are detected. The modal velocity is defined as the velocity that corresponds to a local peak in the PDF. Similarly, the edge velocity is defined as

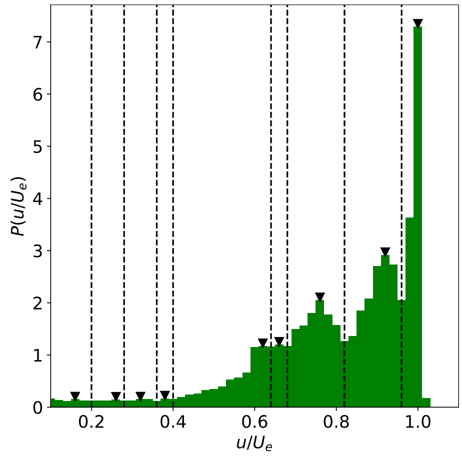

(a)

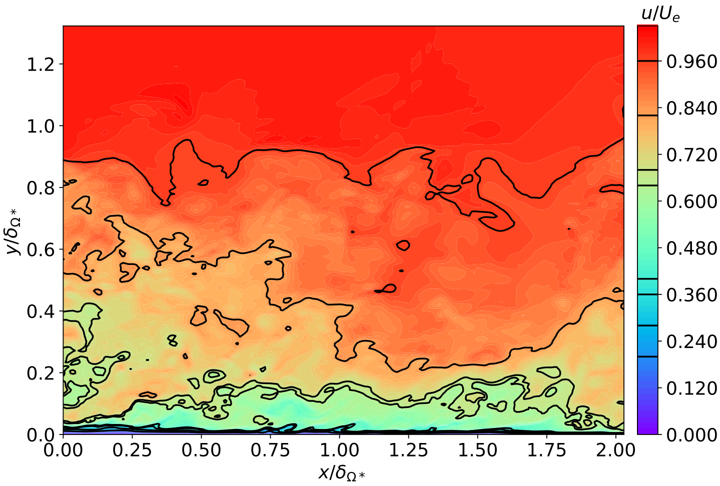

(b)

Figure 3: For the ZPG-TBL with no thresholds ($T_h = 0$, $T_p = 0$, and $T_d = 0$): (a) The PDF of u/U_e for an instantaneous 2D velocity field in the xy plane. The triangles represent all the detected peaks while the dashed lines refer to the edge velocities; (b) Corresponding contour plot of the instantaneous velocity field with the solid lines representing the contour lines of the edge velocities. $\delta_{\Omega*}$ is the boundary layer thickness at the start of the DoI. Non-dominant peaks with lower streamwise velocity have been detected as no thresholds are used.

the velocity associated with a local minimum in the PDF. The modal velocity can be considered as the characteristic velocity of each of the UMZs [1, 2, 8] and the contour lines of the edge velocities refer to the boundaries between the UMZs in physical space.

Laskari et al. [2] used different thresholds in their peak detection algorithm. In a similar way, three thresholds are defined for the current peak detection method. They are the minimum height required for a peak to be considered detectable (T_h), the minimum prominence of a peak compared to its troughs (T_p), and the minimum allowed distance between two peaks in terms of number of bins (T_d). These thresholds are used to reject non-dominant peaks. T_h is given by

$$T_h = \frac{P_i}{P_{NFS_{max}}}, \tag{5}$$

where P_i is any given peak in the PDF and $P_{NFS_{max}}$ is the maximum among the detected non-freestream (NFS) peaks in the PDF. P_i is normalised by $P_{NFS_{max}}$ to allow comparison of the peaks of the UMZs relative to each other and to ensure that the presence of the freestream peak in the PDF does not influence the detection methodology. T_p is given by

$$T_p = \frac{P_i - (E_i + E_{i+1})/2}{P_i}, \tag{6}$$

where E_i and E_{i+1} are the troughs in the PDF (the PDF values corresponding to the edge velocities) on both the sides of any given peak P_i in the PDF.

The number of bins (N_{bins}) used to construct the PDF is 50 for both the TBL cases. For the ZPG-TBL, $u/U_e \in [0.1,\ 1.1]$ with the bin width approximately equal to $0.5\overline{u_\tau}$. For the APG-TBL, the size of each bin is approximately equal to $3.1\overline{u_\tau}$ with $u/U_e \in [0.02,\ 1.1]$. The range of u/U_e is started slightly above zero to avoid the peak close to zero because of the no slip boundary condition. Figure 3 shows an example of a PDF and the identified UMZs in the

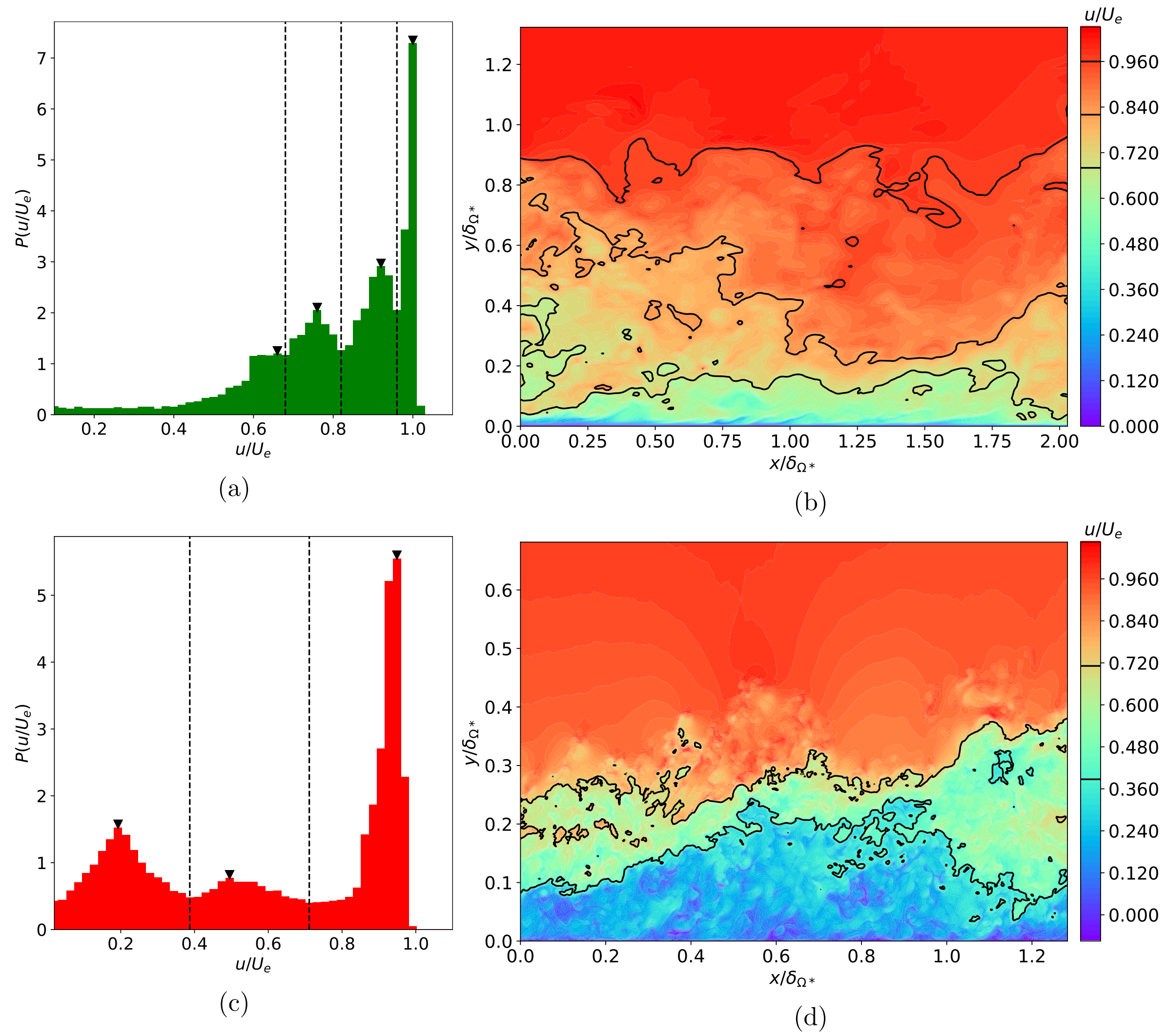

Figure 4: For the ZPG-TBL: (a) The PDF of u/U_e for an instantaneous 2D velocity field in the xy plane. The triangles represent all the detected peaks after applying the thresholds while the dashed lines refer to the edge velocities; (b) Corresponding contour plot of the instantaneous velocity field with the solid lines representing the edges between the UMZs. Similarly, for the APG-TBL: (c) and (d). The thresholds used are $T_h = 0.2$, $T_p = 0.2$, and $T_d = 2$ bins. $\delta_{\Omega*}$ is the boundary layer thickness at the start of the DoI.

ZPG-TBL when no thresholds are used. Non-dominant peaks with lower streamwise velocity are detected as all the thresholds are taken as zero.

In this study, for both the TBL cases, the values of the thresholds used to reject the non-dominant peaks in the PDF are $T_h = 0.2$, $T_p = 0.2$, and $T_d = 2$ bins. Peaks in the PDF are considered detectable if they have values above these thresholds. Figure 4 shows a representative example of a constructed PDF and the corresponding identified UMZs using the described detection methodology for both the TBL cases. Two dimensional (2D) velocity fields in the xy planes are used to generate the PDFs in the section 4 while three dimensional (3D) velocity fields are used to form the PDFs in all the other following sections.

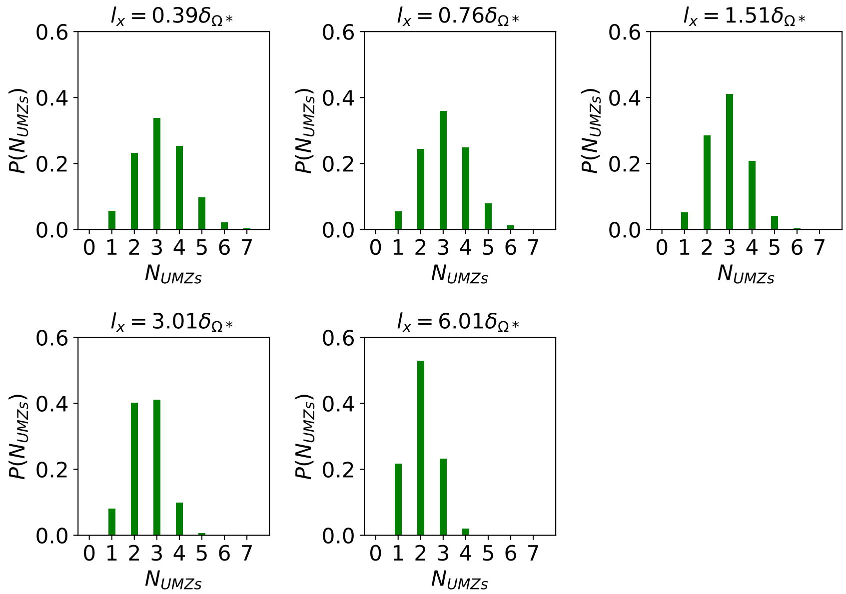

(a)

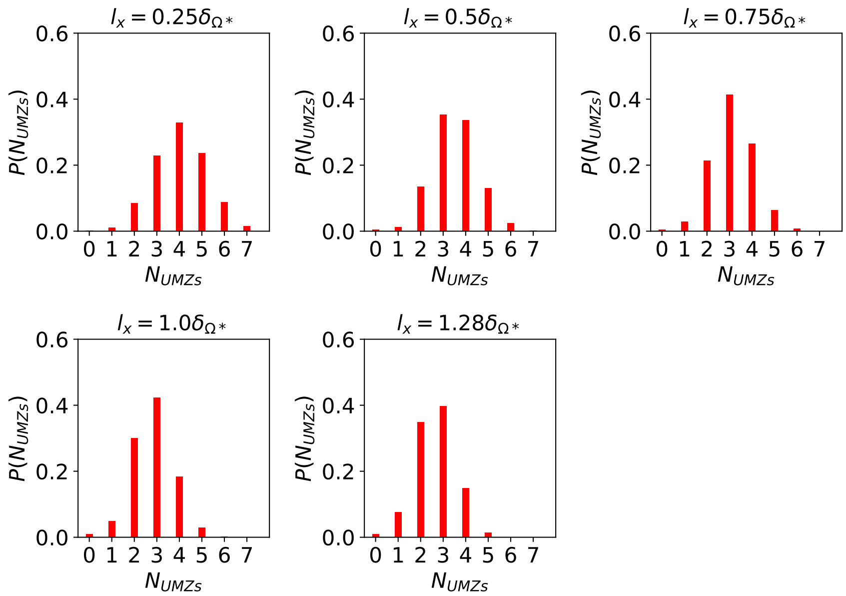

(b)

Figure 5: (a) PDFs of the number of UMZs (N_{UMZs}) as a function of the streamwise extent upto $l_x = 6.01\delta_{\Omega*}$ for the ZPG-TBL. The selected length is $l_x = 2\delta_{\Omega*}$. (b) Similarly, for the APG-TBL upto $l_x = 1.28\delta_{\Omega*}$. The selected length is $l_x = 1.28\delta_{\Omega*}$.

4. Streamwise extent of UMZs

For a given streamwise domain length (l_x), the instantaneous PDFs of the streamwise velocity (u/U_e) are constructed using the various 2D xy planes available in all the fields. Using these velocity PDFs, the number of UMZs (N_{UMZs}) for each of the 2D xy planes are calculated. Then, the PDF of N_{UMZs} is computed for that streamwise extent. This process is repeated for different streamwise lengths. Following this approach, the PDF of N_{UMZs} as a function of extent in the streamwise direction is obtained, which is illustrated in Figure 5 for both the cases.

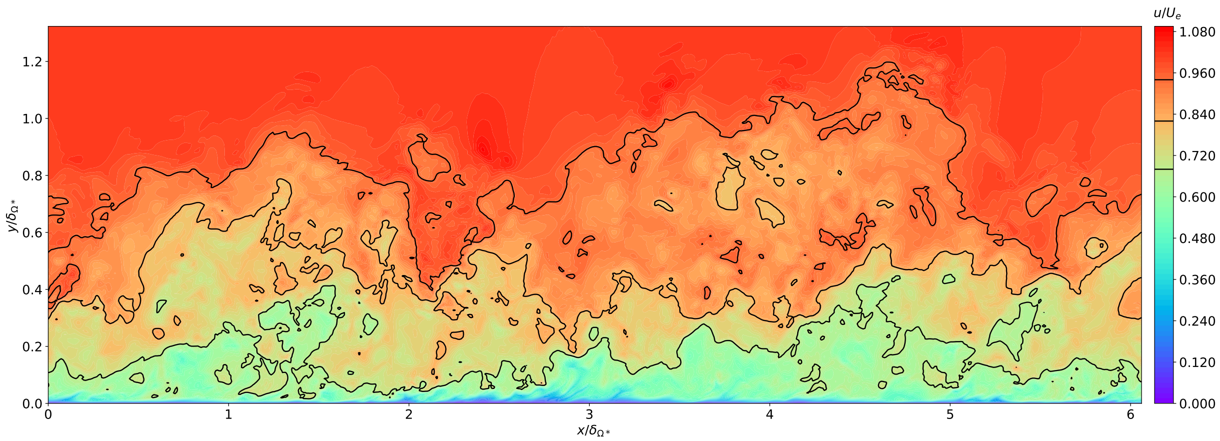

Figure 6: An example of "super-structures" identified in the ZPG-TBL with the streamwise extent (l_x) as long as 6 boundary layer thickness. 3 UMZs are detected in this xy plane. $\delta_{\Omega*}$ is the boundary layer thickness at the start of the DoI

In Figure 5, the number of samples used to construct each of the PDFs is 409,600. The aim of this approach is to select a domain length which will maximise the probability of finding more number of zones. The streamwise extent is varied upto $6.01\delta_{\Omega*}$ and $1.28\delta_{\Omega*}$ for the ZPG-TBL and the APG-TBL respectively. As the streamwise extent is increased, the probability of finding more number of zones reduces for both the TBLs.

In the case of the ZPG-TBL in Figure 5a, for $l_x = 0.39\delta_{\Omega*}$, the probability of finding 4 UMZs is over 20%, while it drops down to less than 10% and becomes insignificant for $l_x \geq 3.01\delta_{\Omega*}$. Hence, an extent of $l_x = 2\delta_{\Omega*}$ is chosen, which has a probability of over 10% in finding 4 UMZs. Therefore, for the ZPG-TBL, the streamwise extent is fixed as $l_x = 2\delta_{\Omega*}$ for all the subsequent analysis, which is the streamwise length that has also been used in previous studies [8]. It is also worth mentioning that there are few UMZs which have a streamwise extent as long as $6\delta_{\Omega*}$. An example of such "super-structures" is shown in Figure 6.

For the APG-TBL in Figure 5b, the probability of finding 4 UMZs is over 30% for $l_x = 0.25\delta_{\Omega*}$. When the streamwise extent is increased to $l_x = 1.28\delta_{\Omega*}$, the probability of finding 4 UMZs is still significant and over 10%. Therefore, for the APG-TBL, the entire available streamwise extent $l_x = 1.28\delta_{\Omega*}$ is chosen to be used in all the analyses.

5. Spanwise extent of UMZs

The spanwise extent of the UMZs are investigated by considering 3D velocity fields with the streamwise length $l_x = 2\delta_{\Omega*}$ for the ZPG-TBL and $l_x = 1.28\delta_{\Omega*}$ for the APG-TBL. For a given spanwise length (l_z), the number of UMZs in different 3D sub-domains is computed by varying the location of the domain in the spanwise direction of an instantaneous field. In a similar way, N_{UMZs} can be computed for all the sub-domains in the available 200 fields, which results in the PDF of N_{UMZs} for that spanwise length. This process is repeated for different spanwise lengths to obtain the PDF of N_{UMZs} as a function of the spanwise extent. As shown in Figure 7, the spanwise extent is varied up to $1.6\delta_{\Omega*}$ for both the TBLs. The probability of finding higher number of UMZs decreases with increasing spanwise length. It is apparent right away that the spanwise extent of the UMZs are much shorter than their streamwise extent for both the TBL cases as the results in Figure 7 show.

For the ZPG-TBL, when $l_z = 0.05\delta_{\Omega*}$, the probability of finding 3 UMZs is over 25% and it becomes almost negligible for $l_z \geq 0.2\delta_{\Omega*}$. This shows that most of the UMZs have a spanwise extent of the order of one-tenth of a boundary layer thickness. Therefore, for the ZPG-TBL, the spanwise extent is chosen as $l_z = 0.1\delta_{\Omega*}$ for the subsequent analysis. In the case of the APG-TBL, the probability of finding 3 UMZs is over 25% for $l_z = 0.01\delta_{\Omega*}$ and it becomes insignificant for $l_z \geq 0.1\delta_{\Omega*}$. The spanwise length of most of the UMZs is around the order of one-hundredth of a boundary layer thickness. Hence, the spanwise extent is selected as $l_z = 0.05\delta_{\Omega*}$ for the APG-TBL. It is important to note that when the pressure gradient increases from the ZPG case to the point of verge of separation in the APG case, the spanwise extent of the majority of the UMZs decreases.

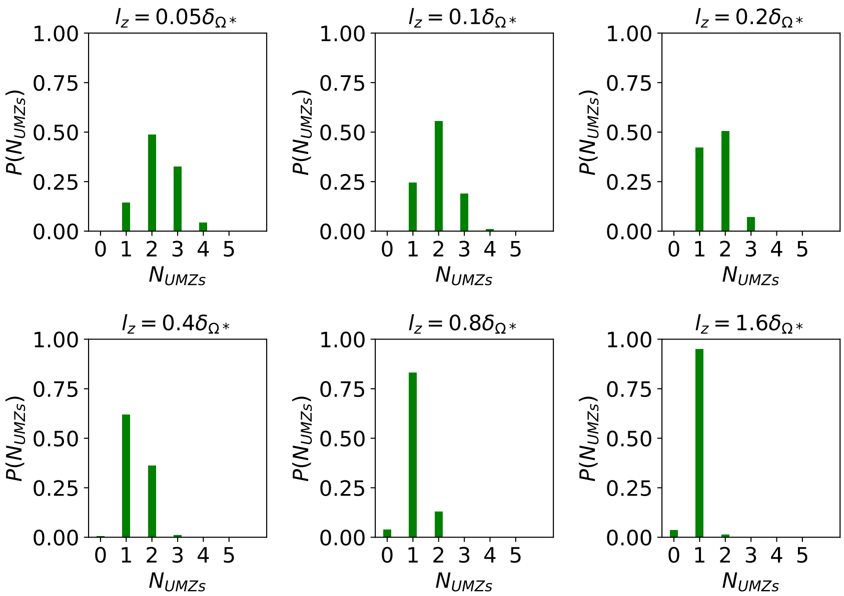

(a)

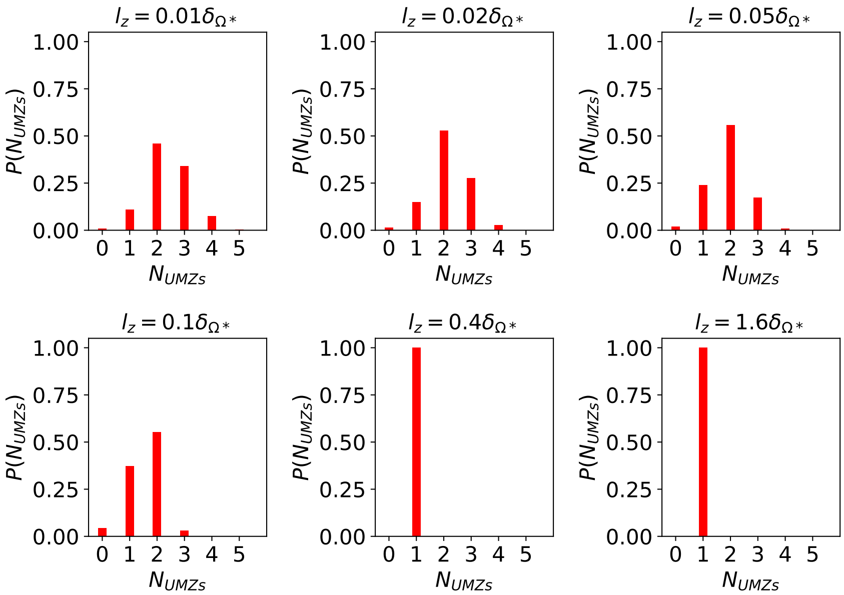

(b)

Figure 7: (a) PDFs of the number of UMZs (N_{UMZs}) as a function of the spanwise extent upto $l_z = 1.6\delta_{\Omega*}$ for the ZPG-TBL. (b) Similarly, for the APG-TBL upto $l_z = 1.6\delta_{\Omega*}$.

6. Time persistence and time evolution of UMZs

For the ZPG-TBL, the time extent (l_t) over which the UMZs persist are investigated by using 3D velocity fields with the domain lengths $l_z = 0.1\delta_{\Omega*}$, $l_y = 1.3\delta_{\Omega*}$ and $l_x = 2\delta_{\Omega*}$, chosen based on the results of sections 4 and 5. Similarly, for the APG-TBL, the selected domain lengths are $l_z = 0.05\delta_{\Omega*}$, $l_y = 0.7\delta_{\Omega*}$ and $l_x = 1.28\delta_{\Omega*}$. 200 time-resolved velocity fields are used in this analysis. For a particular time extent (l_t), the total time period is divided into different time subsets. For a particular z sub-domain in a time subset, velocity PDF is constructed to calculate the number of UMZs (N_{UMZs}) in that sub-domain. In a similar way, N_{UMZs} are computed for the same z sub-domain in the other time subsets. This process can be repeated for all the z sub-domains in all the time subsets to get the PDF of N_{UMZs} for that particular time extent (l_t). Following this approach, the PDF of N_{UMZs} are computed for different time extents as illustrated in Figure 9. The time extent is varied up to $2\delta_{\Omega*}/\langle u\rangle_{\infty*}$ and $0.4\delta_{\Omega*}/\langle u\rangle_{\infty*}$ for the ZPG-TBL and the APG-TBL respectively. In the case of the ZPG-TBL, the probability of finding 2 UMZs is around 50% for all the time extents. This shows that most of the UMZs in the ZPG-TBL persist for a time period of 2 integral time scale. Similarly, for the APG-TBL, the probability of finding 2 UMZs is around 50% for all the time extents considered. This shows that most of the UMZs in the APG-TBL persist over the entire available time period of 0.4 integral time scale.

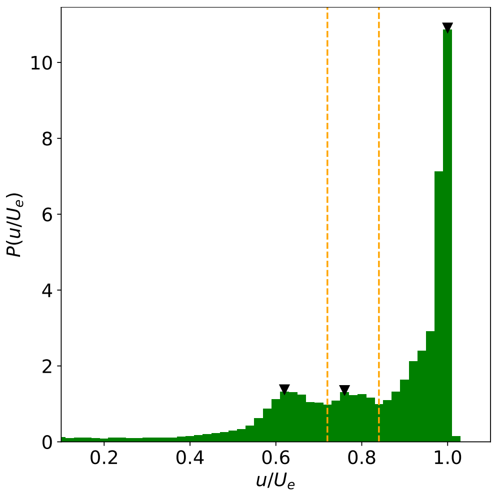

(a)

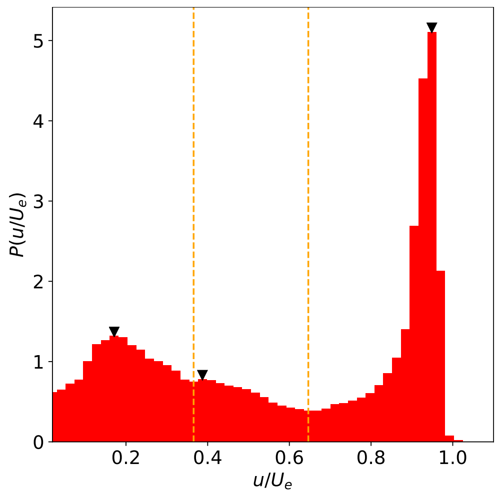

(b)

Figure 8: The instantaneous PDFs of u/U_e constructed using 3D fields from the domains of selected size in section 6 for (a) the ZPG-TBL; (b) the APG-TBL.

The time evolution of the UMZs is investigated for both the TBL cases in a similar manner to Laskari et al. [2]. This is done by following a particular z sub-domain over consecutive time steps. Figure 8 shows an example of the instantaneous PDFs generated using 3D fields from a random domain of the chosen size for both the cases. Figure 10 shows the time evolution of the UMZs in that domain for both the cases in terms of the integral time scale. The contours represent the PDF of u/U_e and the squares refer to the modal velocities of each of the detected UMZs. In case of the ZPG-TBL in Figure 10a, the results indicate that the UMZs having higher time persistence are closer to the free-stream and have higher streamwise momentum relative to the other detected UMZs. This behaviour of higher momentum zones having more persistence in time was also noted by Laskari et al. [2]. For the APG-TBL in Figure 10b, the important difference to be noted is that the UMZs with higher time persistence are found closer to the plate. When the flow reaches the point of the verge of separation in the APG-TBL, the results

Journal of Physics: Conference Series **1522** (2020) 012013 doi:10.1088/1742-6596/1522/1/012013

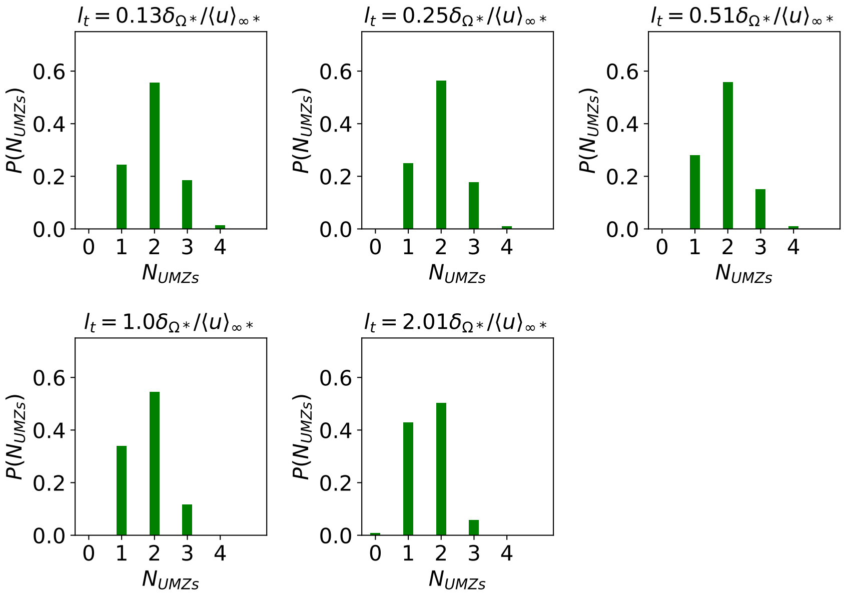

(a)

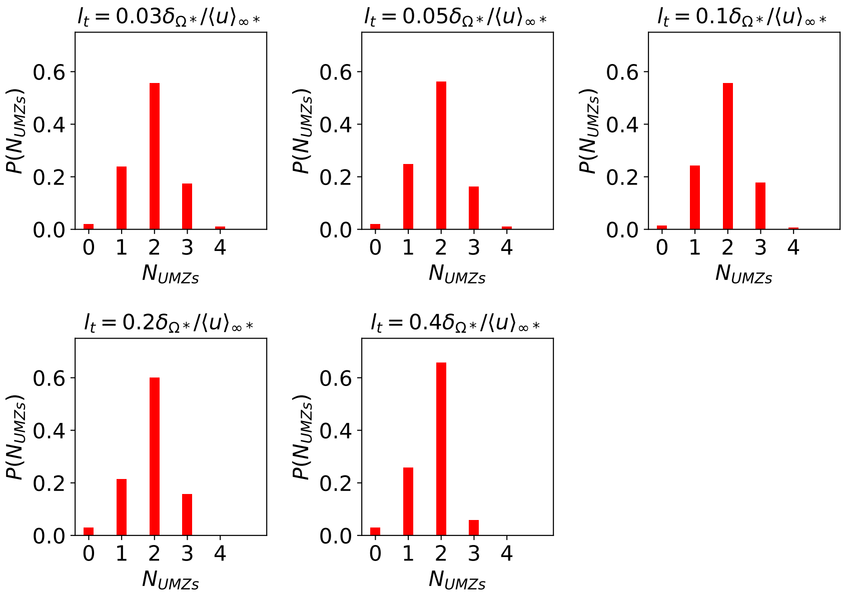

(b)

Figure 9: (a) PDFs of the number of UMZs (N_{UMZs}) as a function of the time extent up to $l_t = 2\delta_{\Omega*}/\langle u\rangle_{\infty*}$ for the ZPG-TBL. (b) Similarly, for the APG-TBL upto $l_t = 0.4\delta_{\Omega*}/\langle u\rangle_{\infty*}$.

indicate that the UMZs with lower streamwise momentum have more persistence in time relative to the higher momentum UMZs in the flow.

7. Concluding remarks

The 3D time persistence and evolution of the uniform momentum zones (UMZs) have been investigated in a ZPG-TBL and a self-similar APG-TBL at the verge of separation. 200 time-resolved velocity fields from two DNS were used in this study. The instantaneous detection methodology introduced by Adrian et al. [1], which is based on the PDFs of the streamwise

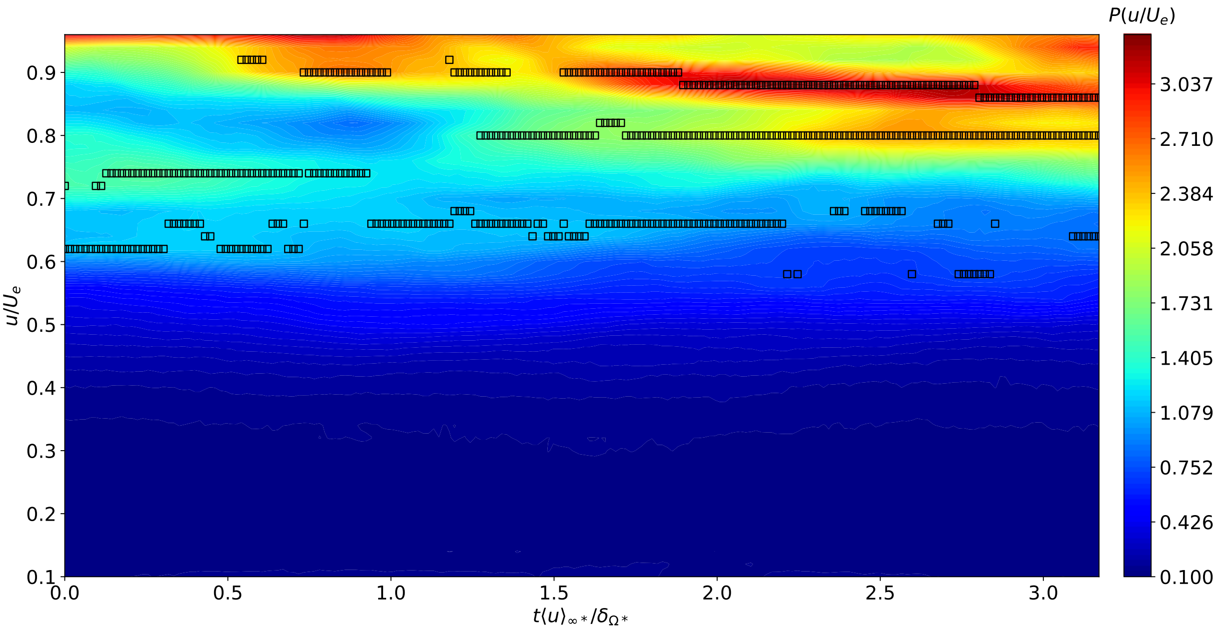

(a)

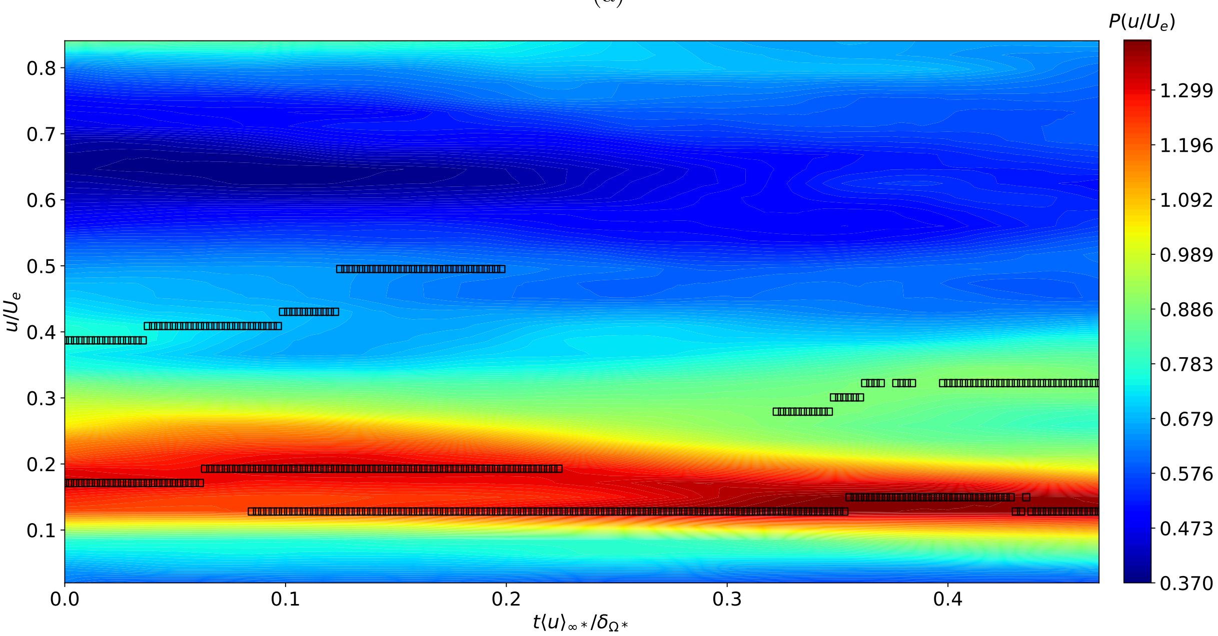

(b)

Figure 10: (a) Time evolution of the UMZs in the ZPG-TBL for 200 consecutive velocity fields. The squares refer to the modal velocities of each of the detected UMZs and the contour represents the PDF of u/u_∞. The time (t) is expressed in terms of the integral time scale defined based on $\delta_{\Omega*}$ and $\langle u\rangle_{\infty*}$. (b) Similarly, for the APG-TBL. Modal velocities corresponding to the free stream is not shown here.

velocity is used in the present study and is extended to account for the spanwise extent and the temporal evolution of the UMZs [2].

For the ZPG-TBL, when the streamwise domain length (l_x) is greater than or equal to $3\delta_{\Omega*}$, the probability of finding 4 UMZs become negligible. In the case of the APG-TBL, even when the streamwise domain length is chosen as high as $1.28\delta_{\Omega*}$, the probability of finding 4 UMZs does not become insignificant. The spanwise extent (l_z) of the predominant number of UMZs are shorter than their streamwise extent irrespective of the pressure gradient in the flow. For the ZPG case, the majority of the UMZs have a spanwise extent of the order of one-tenth of a boundary layer thickness ($\delta_{\Omega*}$), whereas, for the APG case, the spanwise extent of most of the UMZs is found to be shorter with values of the order of one-hundredth of a boundary layer thickness.

In the ZPG-TBL, the probability of finding 2 UMZs of size $l_z = 0.1\delta_{\Omega*}$, $l_y = 1.3\delta_{\Omega*}$ and $l_x = 2\delta_{\Omega*}$ with a time persistence of 2 integral time scale is around 50%. Similarly, for the APG-TBL, the probability of finding 2 UMZs of size $l_z = 0.05\delta_{\Omega*}$, $l_y = 0.7\delta_{\Omega*}$ and $l_x = 1.28\delta_{\Omega*}$ with a time persistence of 0.4 integral time scale is over 50%. For the ZPG-TBL, based on the time evolution of a single sample, it is observed that some of the UMZs with larger time persistence are the zones with higher streamwise momentum and are found closer to the free stream. This result is also consistent with the previous observations made by Laskari et al. [2]. In contrast to the ZPG-TBL, for the APG-TBL at the verge of separation, the UMZs with higher time persistence are found to be the lower momentum zones that are closer to the wall.

8. Acknowledgements

The authors would like to acknowledge the research funding from the Australian Government through the Australian Research Council. This work was supported by the computational resources provided by the Pawsey Supercomputing Centre, the National Computational Infrastructure (NCI) and the Multi-modal Australian ScienceS Imaging and Visualisation Environment (MASSIVE) through the National Computational Merit Allocation Scheme (NCMAS) funded by the Australian Government. This work was also funded in part by the Coturb program of the European Research Council. We are grateful to A.G. Gungor for her careful reviewing of the manuscript.

References

[1] R J Adrian, C D Meinhart, and C D Tomkins. Vortex organization in the outer region of the turbulent boundary layer. *J. Fluid Mech.*, 422:1–54, 2000.

[2] A Laskari, R de Kat, R J Hearst, and B Ganapathisubramani. Time evolution of uniform momentum zones in a turbulent boundary layer. *J. Fluid Mech.*, 842:554–590, 2018.

[3] S J Kline, W C Reynolds, F A Schraub, and P W Runstadler. The structure of turbulent boundary layers. *J. Fluid Mech.*, 30:741–773, 1967.

[4] M R Head and P Bandyopadhyay. New aspects of turbulent boundary-layer structure. *J. Fluid Mech.*, 107:297–338, 1981.

[5] E R Corino and R S Brodkey. A visual investigation of the wall region in turbulent flow. *J. Fluid Mech.*, 37:1–30, 1969.

[6] C D Meinhart and R J Adrian. On the existence of uniform momentum zones in a turbulent boundary layer. *Phys. Fluids*, 7:694–696, 1995.

[7] Y S Kwon, J Philip, C M de Silva, N Hutchins, and J P Monty. The quiescent core of turbulent channel flow. *J. Fluid Mech.*, 751:228–254, 2014.

[8] C M de Silva, N Hutchins, and I Marusic. Uniform momentum zones in turbulent boundary layers. *J. Fluid Mech.*, 786:309–331, 2016.

[9] C M de Silva, J Philip, N Hutchins, and I Marusic. Interfaces of uniform momentum zones in turbulent boundary layers. *J. Fluid Mech.*, 820:451–478, 2017.

[10] M P Simens, J Jiménez, S Hoyas, and Y Mizuno. A high-resolution code for turbulent boundary layers. *J. Comput. Phys.*, 228:4218–4231, 2009.

[11] M P Simens. *The study and control of wall bounded flows.* PhD thesis, Univ. Politécnica de Madrid, 2008.

[12] G Borrell, J A Sillero, and J Jiménez. A code for direct numerical simulation of turbulent boundary layers at high Reynolds numbers in BG/P supercomputers. *Comput. Fluids*, 80:37–43, 2013.

[13] V Kitsios, C Atkinson, J A Sillero, G Borrell, A G Gungor, J Jiménez, and J Soria. Direct numerical simulation of a self-similar adverse pressure gradient turbulent boundary layer. *Int. J. Heat Fluid Fl.*, 61:129–136, 2016.

[14] V Kitsios, A Sekimoto, C Atkinson, J A Sillero, G Borrell, A G Gungor, J Jiménez, and J Soria. Direct numerical simulation of a self-similar adverse pressure gradient turbulent boundary layer at the verge of separation. *J. Fluid Mech.*, 829:392–419, 2017.

[15] F H Harlow and J E Welch. Numerical calculation of time-dependent viscous incompressible flow of fluid with free surface. *Phys. Fluids*, 8:2182–2189, 1965.

[16] J B Perot. An analysis of the fractional step method. *J. Comput. Phys.*, 108:51–58, 1993.

[17] S K Lele. Compact finite difference schemes with spectral-like resolution. *J. Comput. Phys.*, 103:16–42, 1992.

[18] J A Sillero. *High Reynolds number turbulent boundary layers*. PhD thesis, Univ. Politécnica de Madrid, 2014.

[19] P R Spalart and J H Watmuff. Experimental and numerical study of a turbulent boundary layer with pressure gradients. *J. Fluid Mech.*, 249:337–371, 1993.

[20] M. J. Lighthill. Introduction. Boundary layer theory. In L. Rosenhead, editor, *Laminar Boundary Layers*, chapter 2. Oxford Univ. Press, 1963.

Bibliography

Adrian, R. J. (2007). Hairpin vortex organization in wall turbulence. *Physics of Fluids*, 19(4):041301.

Adrian, R. J., Meinhart, C. D., and Tomkins, C. D. (2000). Vortex organization in the outer region of the turbulent boundary layer. *Journal of fluid Mechanics*, 422:1–54.

Anderson Jr, J. D. (2010). Brief history of the early development of theoretical and experimental fluid dynamics. *Encyclopedia of Aerospace Engineering*.

Blackburn, H. M., Mansour, N. N., and Cantwell, B. J. (1996). Topology of fine-scale motions in turbulent channel flow. *Journal of Fluid Mechanics*, 310:269–292.

Blackwelder, R. and Kaplan, R. (1976). On the wall structure of the turbulent boundary layer. *Journal of Fluid Mechanics*, 76(1):89–112.

Bogard, D. and Tiederman, W. (1986). Burst detection with single-point velocity measurements. *Journal of Fluid Mechanics*, 162:389–413.

Borrell, G. (2015). *Entrainment Effects in Turbulent Boundary Layers*. PhD thesis, Universidad Politécnica de Madrid.

Borrell, G., Sillero, J. A., and Jiménez, J. (2013). A code for direct numerical simulation of turbulent boundary layers at high reynolds numbers in bg/p supercomputers. *Computers & Fluids*, 80:37–43.

Chacin, J. M. and Cantwell, B. J. (2000). Dynamics of a low reynolds number turbulent boundary layer. *Journal of Fluid Mechanics*, 404:87–115.

Chong, M. S., Perry, A. E., and Cantwell, B. J. (1990). A general classification of three-dimensional flow fields. *Physics of Fluids A: Fluid Dynamics*, 2(5):765–777.

Chong, M. S., Soria, J., Perry, A., Chacin, J., Cantwell, B., and Na, Y. (1998). Turbulence structures of wall-bounded shear flows found using dns data. *Journal of Fluid Mechanics*, 357:225–247.

Clauser, F. H. (1954). Turbulent boundary layers in adverse pressure gradients. *Journal of the Aeronautical Sciences*, 21(2):91–108.

Corino, E. R. and Brodkey, R. S. (1969). A visual investigation of the wall region in turbulent flow. *Journal of Fluid Mechanics*, 37(1):1–30.

Davidson, P. A., Kaneda, Y., Moffatt, K., and Sreenivasan, K. R. (2011). *A voyage through turbulence*. Cambridge University Press.

Del Álamo, J. C., Jimenez, J., Zandonade, P., and D MOSER, R. (2006). Self-similar vortex clusters in the turbulent logarithmic region. *Journal of Fluid Mechanics*, 561:329.

Fukagata, K., Iwamoto, K., and Kasagi, N. (2002). Contribution of reynolds stress distribution to the skin friction in wall-bounded flows. *Physics of Fluids*, 14(11):L73–L76.

George, W. K. and Castillo, L. (1993). Boundary layers with pressure gradient- another look at the equilibrium boundary layer. *Near-wall turbulent flows*, pages 901–910.

Harlow, F. H. and Welch, J. E. (1965). Numerical calculation of time-dependent viscous incompressible flow of fluid with free surface. *The physics of fluids*, 8(12):2182–2189.

Head, M. and Bandyopadhyay, P. (1981). New aspects of turbulent boundary-layer structure. *Journal of Fluid Mechanics*, 107:297–338.

Hinze, J. (1975). Turbulence. 2nd edn. *New York: McGraw-Hill.*

Hoshen, J. and Kopelman, R. (1976). Percolation and cluster distribution. i. cluster multiple labeling technique and critical concentration algorithm. *Physical Review B*, 14(8):3438.

Jiménez, J. (2012). Cascades in wall-bounded turbulence. *Annual Review of Fluid Mechanics*, 44:27–45.

Jiménez, J. (2013). Near-wall turbulence. *Physics of Fluids*, 25(10):101302.

Jiménez, J. and Moser, R. D. (2007). What are we learning from simulating wall turbulence? *Philosophical Transactions of the Royal Society A: Mathematical, Physical and Engineering Sciences*, 365(1852):715–732.

Kim, H., Kline, S., and Reynolds, W. (1971). The production of turbulence near a smooth wall in a turbulent boundary layer. *Journal of Fluid Mechanics*, 50(1):133–160.

Kim, J. (1985). Turbulence structures associated with the bursting event. *The Physics of fluids*, 28(1):52–58.

Kim, J. (2011). Physics and control of wall turbulence for drag reduction. *Philosophical Transactions of the Royal Society A: Mathematical, Physical and Engineering Sciences*, 369(1940):1396–1411.

Kim, J., Moin, P., and Moser, R. (1987). Turbulence statistics in fully developed channel flow at low reynolds number. *Journal of fluid mechanics*, 177:133–166.

Kitsios, V., Atkinson, C., Sillero, J. A., Borrell, G., Gungor, A. G., Jiménez, J., and Soria, J. (2016). Direct numerical simulation of a self-similar adverse pressure gradient turbulent boundary layer. *International Journal of Heat and Fluid Flow*, 61:129–136.

Kitsios, V., Sekimoto, A., Atkinson, C., Sillero, J. A., Borrell, G., Gungor, A. G., Jiménez, J., and Soria, J. (2017). Direct numerical simulation of a self-similar adverse pressure gradient turbulent boundary layer at the verge of separation. *Journal of Fluid Mechanics*, 829:392–419.

Klewicki, J. (1989). Velocity–vorticity correlations related to the gradients of the reynolds stresses in parallel turbulent wall flows. *Physics of Fluids A: Fluid Dynamics*, 1(7):1285–1288.

Klewicki, J., Murray, J., and Falco, R. (1994). Vortical motion contributions to stress transport in turbulent boundary layers. *Physics of Fluids*, 6(1):277–286.

Kline, S. J., Reynolds, W. C., Schraub, F., and Runstadler, P. (1967). The structure of turbulent boundary layers. *Journal of Fluid Mechanics*, 30(4):741–773.

Kolmogorov, A. N. (1941). The local structure of isotropic turbulence in an incompressible viscous fluid. In *Dokl. Akad. Nauk SSSR*, volume 30, pages 301–305.

Lele, S. K. (1992). Compact finite difference schemes with spectral-like resolution. *Journal of computational physics*, 103(1):16–42.

Lighthill, M. J. (1963). *Introduction. Boundary layer theory. In Laminar Boundary Layers (L. Rosenhead, ed.).* Oxford University Press.

Lozano-Durán, A., Flores, O., and Jiménez, J. (2012). The three-dimensional structure of momentum transfer in turbulent channels. *Journal of Fluid Mechanics*, 694:100–130.

Lu, S. and Willmarth, W. (1973). Measurements of the structure of the reynolds stress in a turbulent boundary layer. *Journal of Fluid Mechanics*, 60(3):481–511.

Lumley, J. (1992). Some comments on turbulence. *Physics of Fluids A: Fluid Dynamics*, 4(2):203–211.

Maciel, Y., Gungor, A. G., and Simens, M. (2017a). Structural differences between small and large momentum-defect turbulent boundary layers. *International Journal of Heat and Fluid Flow*, 67:95–110.

Maciel, Y., Simens, M. P., and Gungor, A. G. (2017b). Coherent structures in a non-equilibrium large-velocity-defect turbulent boundary layer. *Flow, Turbulence and Combustion*, 98(1):1–20.

Martın, J., Ooi, A., Chong, M. S., and Soria, J. (1998). Dynamics of the velocity gradient tensor invariants in isotropic turbulence. *Physics of Fluids*, 10(9):2336–2346.

Marusic, I. and Monty, J. P. (2019). Attached eddy model of wall turbulence. *Annual Review of Fluid Mechanics*, 51:49–74.

Mehdi, F., Johansson, T. G., White, C. M., and Naughton, J. W. (2014). On determining wall shear stress in spatially developing two-dimensional wall-bounded flows. *Experiments in fluids*, 55(1):1656.

Mehdi, F. and White, C. M. (2011). Integral form of the skin friction coefficient suitable for experimental data. *Experiments in Fluids*, 50(1):43–51.

Meinhart, C. D. and Adrian, R. J. (1995). On the existence of uniform momentum zones in a turbulent boundary layer. *Physics of Fluids*, 7(4):694–696.

Mellor, G. and Gibson, D. (1966). Equilibrium turbulent boundary layers. *Journal of Fluid Mechanics*, 24(2):225–253.

Mellor, G. L. (1966). The effects of pressure gradients on turbulent flow near a smooth wall. *Journal of Fluid Mechanics*, 24(2):255–274.

Moisy, F. and Jiménez, J. (2004). Geometry and clustering of intense structures in isotropic turbulence. *Journal of fluid mechanics*, 513:111.

Na, Y. and Moin, P. (1998). Direct numerical simulation of a separated turbulent boundary layer. *Journal of Fluid Mechanics*, 374:379–405.

Ooi, A., Martin, J., Soria, J., and Chong, M. S. (1999). A study of the evolution and characteristics of the invariants of the velocity-gradient tensor in isotropic turbulence. *Journal of Fluid Mechanics*, 381:141–174.

Perot, J. B. (1993). An analysis of the fractional step method. *Journal of Computational Physics*, 108(1):51–58.

Pope, S. B. (2000). *Turbulent Flows.* Cambridge University Press, Cambridge.

Renard, N. and Deck, S. (2016). A theoretical decomposition of mean skin friction generation into physical phenomena across the boundary layer. *Journal of Fluid Mechanics*, 790:339–367.

Reynolds, O. (1883). An experimental investigation of the circumstances which determine whether the motion of water shall be direct or sinuous, and of the law of resistance in parallel channels. *Philosophical Transactions of the Royal society of London. A*, 174:935–982.

Reynolds, O. (1895). On the dynamical theory of incompressible viscous fluids and the determination of the criterion. *Philosophical Transactions of the Royal society of London. A*, 186:123–164.

Richardson, L. F. (1922). *Weather prediction by numerical process.* Cambridge university press.

Robinson, S. K. (1991). Coherent motions in the turbulent boundary layer. *Annual Review of Fluid Mechanics*, 23(1):601–639.

Senthil, S., Atkinson, C., and Soria, J. (2020a). Analysis of the spanwise extent and time persistence of uniform momentum zones in zero pressure gradient and adverse pressure gradient turbulent boundary layers. In *Journal of Physics: Conference Series*, volume 1522, page 012013. IOP Publishing.

Senthil, S., Kitsios, V., Sekimoto, A., Atkinson, C., and Soria, J. (2020b). Analysis of the factors contributing to the skin friction coefficient in adverse pressure gradient turbulent boundary layers and their variation with the pressure gradient. *International Journal of Heat and Fluid Flow*, 82:108531.

Sillero, J. A. (2014). *High Reynolds number turbulent boundary layers.* PhD thesis, Universidad Politénica de Madrid.

Simens, M. P. (2008). *The study and control of wall bounded flows.* PhD thesis, Universidad Politénica de Madrid.

Simens, M. P., Jiménez, J., Hoyas, S., and Mizuno, Y. (2009). A high-resolution code for turbulent boundary layers. *Journal of Computational Physics*, 228(11):4218–4231.

Skåre, P. E. and Krogstad, P.-Å. (1994). A turbulent equilibrium boundary layer near separation. *Journal of Fluid Mechanics*, 272:319–348.

Smits, A. J. and Marusic, I. (2013). Wall-bounded turbulence. *Phys. Today*, 66(9):25–30.

Smits, A. J., McKeon, B. J., and Marusic, I. (2011). High–reynolds number wall turbulence. *Annual Review of Fluid Mechanics*, 43.

Soria, J. (2020). Derivation of decomposition of skin friction in terms of velocity-vorticity correlations. Technical Report 1, Monash University. `https://ltrac.eng.monash.edu.au/techreports/`.

Soria, J., Atkinson, C., Kitsios, V., Sekimoto, A., Senthil, S., and Jiménez, J. (2019). Statistics of Beta = 0, 1, 39 Turbulent Boundary Layer DNS. `https://bridges.monash.edu/articles/dataset/Statistics_of_Beta_0_1_39_Turbulent_Boundary_Layer_DNS/8790785`.

Soria, J. and Cantwell, B. J. (1994). Topological visualisation of focal structures in free shear flows. *Applied scientific research*, 53(3):375–386.

Soria, J., Kitsios, V., and Atkinson, C. (2016). On the identification of intense reynolds stress structures in wall-bounded flows using information-limited two-dimensional planar data. *European Journal of Mechanics-B/Fluids*, 55:279–285.

Soria, J., Sondergaard, R., Cantwell, B., Chong, M., and Perry, A. (1994). A study of the fine-scale motions of incompressible time-developing mixing layers. *Physics of Fluids*, 6(2):871–884.

Spalart, P. R. and Watmuff, J. H. (1993). Experimental and numerical study of a turbulent boundary layer with pressure gradients. *Journal of Fluid Mechanics*, 249:337–371.

Stratford, B. (1959). An experimental flow with zero skin friction throughout its region of pressure rise. *Journal of Fluid Mechanics*, 5(1):17–35.

Townsend, A. (1960). The development of turbulent boundary layers with negligible wall stress. *Journal of Fluid Mechanics*, 8(1):143–155.

Townsend, A. (1961). Equilibrium layers and wall turbulence. *Journal of Fluid Mechanics*, 11(1):97–120.

Wallace, J. M., Eckelmann, H., and Brodkey, R. S. (1972). The wall region in turbulent shear flow. *Journal of Fluid Mechanics*, 54(1):39–48.

Willmarth, W. and Lu, S. (1972). Structure of the reynolds stress near the wall. *Journal of Fluid Mechanics*, 55(1):65–92.

Yoon, M., Ahn, J., Hwang, J., and Sung, H. J. (2016). Contribution of velocity-vorticity correlations to the frictional drag in wall-bounded turbulent flows. *Physics of Fluids*, 28(8):081702.

Yoon, M., Hwang, J., Yang, J., and Sung, H. J. (2020). Wall-attached structures of streamwise velocity fluctuations in an adverse-pressure-gradient turbulent boundary layer. *Journal of Fluid Mechanics*, 885.